NOVEL HYDROXIDE PRECURSORS FOR SYNTHESIS OF SELECTED OXIDES AND THEIR CHARACTERIZATION

A thesis submitted to the

University of Pune

for the award of degree of

Doctor of Philosophy** in **chemistry

in faculty of science

By

H. Muthurajan

Physical and Materials Chemistry Division
National Chemical Laboratory
Pune-411 008, India

February 2011

राष्ट्रीय रासायनिक प्रयोगशाला
(वैज्ञानिक तथा औद्योगिक अनुसंधान परिषद)
डॉ. होमी भाभा मार्ग पुणे - 411 008. भारत
NATIONAL CHEMICAL LABORATORY
(Council of Scientific & Industrial Research)
Dr. Homi Bhabha Road, Pune - 411 008. India.

Date: 17 February 2011

CERTIFICATE

This is to certify that the thesis entitled **"Novel hydroxide Precursors for Synthesis of selected oxides and their Characterization"** describe the original research work done by **Mr. H.Muthurajan** under my supervision for the degree of **Doctor of Philosophy** in **Chemistry** under the faculty of science of the **University of Pune**. Such material as has been obtained from other sources has been duly acknowledged in this thesis.

Dr. V. Ravi
Scientist
Physical and Materials Chemistry Division
National Chemical Laboratory
Pune-411 008, India

Communication Channels
☎
NCL Level DID : 2590
NCL Board No. : +91-20-25902000
EPABX : +91-20-25893300
+91-20-25893400

FAX
Director's Office : +91-20-25902601
COA's Office : +91-20-25902660
COS&P's Office : +91-20-25902664

WEBSITE
www.ncl-india.org

CANDIDATE'S DECLARATION

I hereby declare that the thesis entitled **"Novel hydroxide Precursors for Synthesis of selected oxides and their Characterization"** submitted for the degree of Doctor of Philosophy in Chemistry to the University of Pune, has not been submitted by me to any other university or institution. This work was carried out at the National Chemical Laboratory, Pune, India.

Physical and Materials Chemistry Division H. Muthurajan
National Chemical Laboratory
Pune 411008

February 2011

Acknowledgement

I gratefully acknowledge my guide, ***Dr. V. Ravi****, for his valuable suggestions, timely help and contribution of time and energy to work. It is a great pleasure in thanking him for his excellent guidance, without which this work would not have reached its goal.*

I also wish to acknowledge the help and co-operation I received from all the staffs of Physical and Materials Chemistry Division, National Chemical Laboratory with special mention to Dr Pankaj Poddar, Dr S.P. Gokhale, N. Natarajan and Ms Violet Samuel, Catalysis division.

I gratefully acknowledge SR Madhavan for extending me his constant encouragement and moral support at all times.

I would also like to thank all the staffs from DRDO Centre for Piezoceramics and Devices of Armament Research and Development Establishment with special mention to HH Kumar, Dr DK Kharat, Praveen Kumar.

My sincere thanks to Prof Ang How Ghee, Director, Energetics Research Institute, Nanyang Technological University for his valuable support and extending the thermal analysis facility for characterization.

I am thankful to each and every person who helped and supported me during this research work.

I express my sincere thanks to Dr Li Tao, School of Materials Science and Engineering, Nanyang Technological University for allowing me to carry out Impedance measurements in their lab and for useful discussions.

I like to thank G. Mugunthan, for being a close friend and giving me the support I need.

My sincere thanks to my friends N. Koteswara Rao, Upendra Nath Gupta, Sanjay Patil, Nagarajan, Sivaram Pradha and, B. Rituraj Raj and M Chidambaram from Catalysis division of National Chemical Laboratory for their valuable help during my research works at NCL.

I am thankful to Head, Physical and Materials Chemistry Division and Director, National Chemical Laboratory for allowing to submit this work in the form of Ph. D. thesis.

Last but not the least, I would like to thank my Parents, all my family members and friends, who inspite of their own difficulties, have stood as a constant source of inspiration in every stage and shown moral support to carry out this research work successfully.

H. Muthurajan

List of abbreviations

Å	Angstrom
ε'	Dielectric Constant
E_a	Activation energy
°C	Degree centigrade
C	Capacitance, unit Farad
f	Frequency
min	Minutes
hr	Hours
K	Kelvin (temperature in Kelvin scale)
RT	Room Temperature
T	Temperature
Hz	Hertz, Unit of frequency
kHz	Kilo Hertz
MHz	Mega Hertz
tanδ	Dielectric Loss tangent
C	Capacitance
I	Current
V	Voltage
R	Resistance (Ω)
ω	Angular frequency (S^{-1})

Z	Impedance (Ω)
Z`	Real component of Z (Ω)
Z``	Imaginary component of Z (Ω)
|Z|	Modulus of Z (Ω)
λ	Wavelength of X-ray radiation
θ	Angle of diffraction
AC	Alternating Current
DSC	Differential Scanning Calorimetry
EDX or EDS	Energy Dispersive X-Ray Spectroscopy
FWHM	Full Width at Half Maximum
LN	Lithium Niobate ($LiNbO_3$)
LT	Lithium Tantalate ($LiTaO_3$)
NN	Sodium Niobate ($NaNbO_3$)
NT	Sodium Tantalate ($NaTaO_3$)
PID	Proportion Integration Differentiation
SEM	Scanning Electron Microscope
SN	Strontium Niobate ($SrNb_2O_6$)
ST	Strontium Tantalate ($SrTa_2O_6$)
TEM	Transmission Electron Microscope
TGA	Thermogravimetry Analysis
XRD	X-Ray Diffraction

Contents

Chapter 1 Introduction

Chapter 2 Experimental

Chapter 3 Synthesis and Characterization of Lithium Niobate and Tantalate

Chapter 4 Synthesis and Characterization of Sodium Niobate and Tantalate

Chapter 5 Synthesis and Characterization of Strontium Niobate and Tantalate

Chapter 1

Introduction

This chapter is comprised of general introduction about electroceramics and the importance of the present investigation for its potential application. As the physical properties generally arise from the crystal chemistry, the structural aspects of electroceramics based on Pervoskite (ABO_3) and Columbite (AB_2O_6) form is discussed in this chapter. This chapter has detailed survey on the most important application of ceramic oxides in various fields. The syntheses techniques for various ceramic oxides as well as research on advanced ceramics and market analysis are described in this chapter.

1. Introduction

An oxide is an anion of oxygen in the oxidation state of -2 or a chemical compound formally containing an oxygen in this state. ABO_3-type perovskite oxides display a wide spectrum of physical properties of technical importance such as ferroelectricity, antiferroelectricity, piezoelectricity, insulating behaviour, semiconductivity, metallic conductivity, superconductivity, ferromagnetism, antiferromagnetism etc. The ferroelectric properties are mostly controlled by the relative sizes of the ions. The electrical and magnetic properties are mainly dependent on the electronic configuration of the ions. Dopants and substituents have a profound influence on the properties of the ABO_3 oxides [1].

Oxide materials having a composition ABO_3 form an important class since they are useful in several device applications, some examples of which follow. These materials are used in special ceramic capacitors. Piezoelectric PLZT ceramic discs made from ABO_3 type oxides are well known for their use in a variety of transducer devices such as phonograph pick-ups, strain gauges, ultrasonic equipment etc. [2]. Some doped ABO_3-type oxides find applications in switching devices [3,4]. $LaCoO_3$ can be used instead of platinum as a catalyst in the oxidation of CO in automobile exhaust gases [5] and is also useful as an ohmic-loss-free electrode [6,7]. $LiNbO_3$ has been used in the development of materials for generating and detecting surface acoustic waves and also in optical memory devices [8,9]. $YA1O_3$ is a laser host material [10]. Rare earth orthoferrites are used in magnetic bubble domain devices because of their strong anisotropic properties [11, 12]. Perovskite is one of the most frequently encountered structures in solid-state inorganic chemistry, and it accommodates most of the metallic ions in the periodic table with a significant number of different anions [11].

Although there has been considerable amount of work in the area of dielectric oxides in the past fifty years, dielectric materials continue to remain a hot area of scientific research due to their wide ranging applications. They include capacitors, piezoelectrics, and electronic IC packages. In addition high permittivity microwave ceramics have a large market for passive ceramic components for mobile communications and satellite broadcasting, such as resonators for stabilisation of oscillators and for frequency filters [13]. Most of these dielectric materials are oxides with metal - oxygen octahedra connected to each other to form mainly three dimensional structures.

Among them the ABO_3 type perovskite oxides and the AB_2O_6 (columbite) type of oxides where B is either Nb or Ta have been pursued vigorously in the recent past [14 – 16]. There is a continuous interest to optimise the dielectric properties by suitable doping at the A-site, B-site [17].

1.1 Advanced Electroceramic – An overview

Ceramics, by definition, comprise inorganic, non-metallic, water insoluble compounds that show ionic contributions in their chemical bonds. Along with the revolutionary development of electronics in the second half of the twentieth century, the huge potential of ceramic materials has been unfolded and introduced into a fascinatingly wide spectrum of electrical and microelectronic devices and applications [18]. Electroceramics represent an important technology which has considerable impact for a large variety of industries, branches and markets. It is considered as an enabling technology which has potential to deliver high-value contributions for solving the challenges of our future [19]. Ceramic oxides are finding a wide range of application as materials for electronic systems in the modern world. They are used as electrodes and electrolytes in fuel cells and oxygen sensors, and as magnetic and dielectric materials in control devices, to mention only a few examples. Because of their nature, the fabrication of components incorporating ceramic oxides is usually carried out at high temperatures.

The “Advanced Ceramics” industry is fundamentally different from the silicon microelectronics industry, due to its higher diversity, higher interdisciplinarity, very different processing technologies and variety of application [19]. This means that a straightforward anticipation of the ever increasing cost benefits from economy of scale and the continuous improvement of yield is inappropriate in the case of advanced ceramics. Advanced ceramics represent an important technology which has considerable impact for a large variety of industries, branches and markets. It is considered as an enabling technology which has potential to deliver high-value contributions for solving the challenges of our future.

Modern electronic equipment from computers to microwave ovens makes use of electroceramic materials as sensors, components of electronic circuitry and industrial control systems. The wide variety of ceramic oxides which is being used for these functions draws cation components from most groups of the periodic table, arranged in diverse crystalline structures with oxygen anions [20]. Historically, developments in the various subclasses of Electroceramics have paralleled the growth of new technologies. Examples include: Ferroelectrics - high dielectric capacitors, non-volatile memories; Ferrites-data and information storage; Solid Electrolytes - energy storage and conversion; Piezoelectrics-sonar; Semiconducting Oxides - environmental monitoring. The performance of electroceramics materials and devices depends on the complex interplay between processing, chemistry, structure at many levels and device physics and therefore it requires a truly interdisciplinary effort by individuals from many fields. Articles in the professional literature tend to deal with the processing, characterization, structure, properties, modeling and performance of electroceramics [20]. The transport properties and redox properties of the constituent ions in these materials therefore play a significant role in determining the ease of fabrication as well as the scope of application of devices.

Electroceramic materials are following in the footsteps of conventional semiconductors with respect to further miniaturization, and are experiencing the same evolution from microtechnology towards nanotechnology. Nanosize effects and nanotechnology issues are therefore gaining importance. While ceramics have traditionally been admired for their mechanical and thermal stability, their unique electrical, optical and magnetic properties have become of increasing importance in many key technologies including communications, energy conversion and storage, electronics and automation. Such materials are now classified under *Electroceramics* as distinguished from other functional ceramics such as advanced structural ceramics. With the development and commercialization of new technologies such as mobile communication, personal computers and the internet, came the need for miniaturization and high-performance electroceramics.

It appears that the field is still open to many new developments, largely because of the wide range of cationic mixtures which can be sustained in the structural and stability properties of these materials [20]. Electroceramics research is driven by technology and device applications. This growing field includes a vast number of magnetic, dielectric, ionically conducting, semiconducting, and superconducting ceramics used in domains as diverse as transportation, industrial production, power engineering, medicine and health care, consumer electronics, and communication. At the turn of the decade, three major trends are gaining importance.

1.2 Structure

1.2.1 Perovskite (ABO_3)

Among the large family of metal oxides, polar oxides play an outstanding role in science and technology owing to their dielectric, optic, piezoelectric, and pyroelectric properties [21]. The most important class of polar oxides are those possessing the perovskite structure, because distortion from the ideal ABO_3 cubic symmetry allows to change the physical properties on application of an external stimulus [22].

As the physical properties generally arise from the crystal chemistry, the formation of pure, stoichiometric, homogeneous, and crystalline materials with controlled crystal size is crucial [22]. Although size effects on the nanometer scale have long been investigated in ceramics, it is a relatively new trend to utilize them in a controlled way to improve the properties of nanocrystalline materials [23–25]. The conventional synthesis of perovskite materials involves solid-state reactions between the individual metal oxide or carbonate powders at temperatures between 1000 and 1250^0C. In order to bring the reaction partners sufficiently close together and to provide high mobility, these solid-state reactions require a high temperature and small particle sizes. However, these harsh conditions ruin any opportunity for suitable control of the reactions and often prevent the formation of thermally labile and metastable solids [26]. It is obvious that for the synthesis of nanoparticles, whose size and shape are crucial factors in determining the properties, other preparation methodologies have to be developed. The most promising alternatives are soft-chemistry routes [27–29], where good control from the molecular precursor to the final product is achieved, offering high purity and homogeneity and low processing temperatures.

Perovskite is also the name of a more general group of crystals which take the same structure. See perovskite structure for details. The basic chemical formula follows the pattern ABO_3, where A and B are cations of different sizes (for example, $LaMnO_3$). The idealized structure is primitive cube, but differences in ratio between the A and B cations can distort the structure to a number of different so-called distortions, of which tilting is the most common one. The A cation is the cation in the middle of the cube and B is on the corners. The oxygen ions are on the centres of the unit cell faces. There are also complex perovskites which contain two different B-site cations. This results in ordered and disordered variants. The ordered structure can be indexed by a trigonal unit cell, with the B-site ions at the centre of the oxygen octahedra.

Its most common mineral, perovskite, lends its name to this important group of oxides. The importance of this group is two fold. First, every member of this group has rare earth metals as trace elements in their structures and second, the structure of this group is unique and many ceramic, synthetic and useful substances can be created using the structure. The Perovskite Group is a group of oxides with a general formula of AXO_3. The A can be either cerium, calcium, sodium, strontium, lead and/or various rare earth metals. The X site can be occupied by titanium, niobium and/or iron. All members of this group have the same basic structure.

The XO_3 atoms form a framework of interconnected octahedrons. Each octahedron has at its center an X ion and at their corners are six oxygens which are in themselves a corner of yet another octahedron. In the mineral perovskite's case, each oxygen (-2 charge) is connected to two titanium ions which have a charge of (+4) and are in themselves connected to six oxygens for a ratio of 1/3. The result is an imbalance of a -2 charge (as in $(+4) + 3(-2) = -2$) which must be counter balanced with a calcium ion (+2) situated between eight TiO_3 octahedrons. If the X ion is niobium (+5) or iron (+2 or +3) then the A ions must have a charge appropriate for balancing the formula.

This simplified ideal structure is isometric in symmetry. Members of this group would all be isometric if it were not for the fact that the octahedrons of most of the natural members of the group are twisted or rotated so as to kink or bend the structure. The twisting or bending is to accommodate the large ions between the octahedrons. The result is a variety of symmetries from isometric to tetragonal to orthorhombic to monoclinic depending on the degree of distortion to the basic ideal structure. Most perovskite minerals show some pseudocubic tendencies due to the close to, but not quite, isometric structure.

There are several synthetic crystals that have been made with the perovskite structure. These synthetics have a wide range of electrical ceramic uses from insulators right on through to superconducting material. Due to these uses and the increasing need for rare earth metals, the Perovskite Group will continue to be important and intensely studied. The perovskite structure shares the property of ferroelectricity with garnet and olivine. Many superconducting ceramic materials have perovskite-like structures.

Perovskite is an increasingly economically important, and in some rocks a rather common, mineral. It is sought after for its rare earth metal content. Often perovskite is enriched in cerium, niobium, thorium, lanthanum, neodymium and other rare earth metals. Rare earth metals are becoming rather attractive for prospectors due to their growing value to industry. The titanium derived from perovskite is recovered as well.

Crystals of perovskite appear as cubes, but this is deceiving. Perovskite is actually pseudocubic (or "falsely shaped" in a loose translation from the Greek). It is really orthorhombic in symmetry, but its structure is very close to isometric. The titaniums and oxygens compose a framework structure in which TiO_6 octahedrons are connected at each corner to other TiO_6 octahedrons. If the connections were at perfect 90 degree angles then the structure would be isometric. However the large ions, such as calcium and some rare earth metals that are needed to balance the formula, are too large to fit comfortably between the octahedrons. This causes a bending or twisting of the octahedrons and a distortion of the structure to orthorhombic symmetry. But the structure is still close to being isometric and it can therefore create crystals that are close to being cubes. Specimens can remind one of darkly colored cubes of galena. But galena's better metallic luster, greater density and perfect cleavage will give nobody any trouble in permanently confusing the two.

Perovskite is named for a Russian mineralogist, Count Lev Aleksevich von Perovski. The mineral was discovered and named by Gustav Rose in 1839 from samples found in the Ural Mountains. Now it is a well known and recognized as a common mineral in aluminum and silica poor rock types such as nepheline syenites, carbonatites, kimberlites and melilites as well as some contact metamorphic marbles.

The perovskite structure is adopted by many oxides with formula ABO_3 and is very versatile having many useful technological applications such as ferroelectrics, catalysts, sensors and superconductors. The general crystal structure is a primitive cube, with the A-cation in the middle of the cube, the B-cation in the corner and the anion, commonly oxygen, in the centre of the edges. The structure is stabilized by the 6 coordination of the B-cation (octahedron) and 12 of the A cation. The packing of the ions can be thought of the A and O ions together form a cubic close packed array, where the B ions occupy a quarter of the octahedral holes. When the ratio of the ionic radii differs too much of the so-called tolerance factor often distortions occur of which tilting is the most common one. With perovskite tilt the BO_6 octahedron twist along one or more independent axe to accommodate the ratio-difference.

Perovskite (calcium titanium oxide, $CaTiO_3$) is a relatively rare mineral occurring in orthorhombic (pseudocubic) crystals. Perovskite is found in contact metamorphic rocks and associated mafic intrusives, nepheline syenites, and rare carbonatites. This structure takes it name from the mineral perovskite ($CaTiO_3$). Perovskite was discovered in the Ural mountains of Russia by Gustav Rose in 1839 and named for Russian mineralogist, L. A. Perovski (1792-1856). Under the high pressure conditions of the mantle the pyroxene enstatite, $MgSiO_3$, is a perovskite polymorph and may be the most common mineral in the Earth.

The perovskite structure shares the property of ferroelectricity with garnet and olivine. Many superconducting ceramic materials have perovskite-like structures.

In Perovskite structure the higher symmetry is cubic and lower distorted perovskite structure (fig 1.1) is as follows:-

Tetragonal	Slightly distorted
Orthorhombic	↓
Rombohyderal or hexagonal	↓
Monoclinic	↓
Triclinic	Highly distorted

Ideal Perovskite Structure

Distorted Perovskite ($CaTiO_3$)

Tetragonal Perovskite ($CaSiO_3$)

Monoclinic Perovskite ($Pr_{0.6}Sr_{0.4}MnO_3$)

Figure 1.1 Perovskite structures of ABO_3 compounds

The perovskite structure ABO_3 is very accommodating to a whole range of cationic mixtures on both the A and B sites. In the barium titanate family of dielectric materials, the transformation from ferroelectric to antiferroelectric behavior can be made by substituting zirconium for titanium on the B sites and the order- disorder transformation temperature to paraelectric behavior can be increased by introducing lead in exchange for barium. The dielectric properties of $BaTiO_3$ and $BaZrO_3$ arise from the displacement of the Ti^{4+} or Zr^{4+} ion from the center of the octahedral oxygen coordination shell. In the titanate this leads to ferroelectric behavior where these displacements are lined up in the presence of an external field leading to a high dielectric constant. In the zirconate the effect of the external field is the opposite, leading to alternate planes of Zr^{4+} ions having opposite displacements, and this material is designated as "antiferroelectric". The shape of the hysteresis loop in both the ferromagnetic spinels and the ferroelectric titanates can be affected by substitution of small amounts of aliovalent ions on two cation sublattices. The substitution of lanthanum or neodymium for barium produces a "softer" dielectric material, i.e. one having a smaller coercive field than pure $BaTiO_3$. The exchange of the trivalent La^{3+} ion for divalent Pb^{2+} leads to the formation of vacancies on the cation sublattice, but the major effect is due to the reduction of the p-type semiconduction, and hence a decrease in the electrical conductivity. In this context, the aliovalent ion is termed a "donor", although n-type semiconduction is not introduced with this substitution. The substitution of trivalent ions for the tetravalent Ti^{4+} or Zr^{4+} ions on the B sites leads to "harder" materials. This is thought to be due to the introduction of vacant oxygen sites which cluster around the trivalent ion, impeding domain wall rotation [20].

Because the oxygen ion has a much higher diffusion coefficient in the perovskites than the corresponding cations, the oxygen vacancy can diffuse more rapidly than the cation vacancy, and forms dipoles with La^{3+} substituted ions. These are thought to impede domain wall rotation and hence to "harden" the ferroelectric behavior. It should be noted that polycrystalline materials, which probably contain pores at the grain boundary, also show a broader hysteresis loop than the corresponding single crystal, probably for the same reason [20, 30].

The perovskite structure has also been used to develop new oxide electrolytes which contain ions which are less reducible than zirconium, and hence can be used in oxygen sensors at low oxygen pressures to replace thorium oxide. Lanthanum yttrium oxide and lanthanum aluminium oxide have been found to function satisfactorily when alkaline earth oxide additions such as SrO on the A sites and CaO or MgO on the B sites are made. The electrolytes show unit transport number for oxygen ions down to the oxygen potential of the Ta-Ta_2O_5 system at least and up to a temperature of 1000°C [31].

Perovskites based on Ce^{4+} ions on the B sites have been used to develop hydrogen sensors. For example, if $BaCeO_3$ is doped with Nd_2O_3 to create oxygen vacancies, the resulting material can be used as a solid electrolyte in a hydrogen electrochemical cell [32]. One potential perovskite oxide solid electrolyte is doped $LaA1O_3$, which has a melting point of 2110°C [33] and can thus be used in high temperature applications [31]. BT, BNT and BKT are well known ferroelectrics with the perovskite structure. BT is expected to be one of the superior candidates for lead-free piezoelectrics, however, the Curie temperature, Tc, of BT is too low at 135°C, limiting the working temperature range. BNT [34–36] also has high potential for lead-free piezoelectrics, however, the depolarization temperature, Td, occurs at about 200 °C. $KNbO_3$ (KN) is also well known lead-free piezoelectric material having a large piezoelectricity and high Tc [37–39].

The structure of perovskite can be maintained by controlling the tolerance factor (τ), a quantity first suggested in 1926 by Goldschmidt [40] and this is mathematically given by equation below

$$\tau = \frac{R_A + R_O}{\sqrt{2}\left(R_B + R_O\right)}$$

Where R_A and R_B stand for the radii of A and B site cations respectively and R_O stands for the X-site anions. For ideal perovskite structure (cubic) $\tau = 1$, however; the structures other than the cubic remain stable in the range $0.75 < \tau < 1$ i.e. Materials with a lower tolerance factor exhibit a lower symmetry and vice versa [41–43].

Goldschmidt's tolerance factor τ has been widely accepted as a criterion for the formation of the perovskite structure, a number of researchers have used it to discuss the perovskite stability, including oxides [44–48], fluorides [49–51], chlorides [52].

The perovskite structure is shown to be the single most versatile ceramic host. By appropriate changes in composition one can modify the most significant electroceramic dielectric ($BaTiO_3$ and its relatives) phase in industry, into metallic conductors, superconductors or the highest pressure phases in the earth [53].

Although majority of the perovskite compounds are oxides or fluorides, other forms like heavier halides, sulphides, hydrides, cyanides, oxyfluorides and oxynitrides are also reported [54, 11]. Perovskite and perovskite-related materials are important crystal structure due to their diverse physical/chemistry properties [54–56] over a wide temperature range. For example, perovskite ceramics with ferroelectric and/or piezoelectric properties, such as $BaTiO_3$ and $Pb(ZrTi)O_3$ play a dominant role in the electroceramics industry. Other industry interests of perovskites are: colossal magnetoresistance ($(SrCaLa)MnO_3$), PTC thermistor ($BaTiO_3$), electrooptical modulator ($(PbLa)(ZrTi)O_3$, $BaTiO_3$), optical switch ($LiNbO_3$), battery Material (($Li_{0.5-x}La_xTiO_3$)), etc.

1.2.2 Columbite (AB_2O_6)

The columbite group of minerals has the general formula AB_2O_6, in which, most typically, A represents Fe^{2+}, Mn, and Mg, and B represents Nb and Ta. Members of the columbite group are subdivided on the basis of A and B-site chemistry; samples with Nb as the dominant B cation are loosely referred to as "columbite," and with Ta, as "tantalite." In the construction of species names, prefixes are used to describe A-site chemistry; thus, the species of "tantalite" with Mn dominant at the A site is manganotantalite. Columbite-group minerals show variable degrees of cation order. A range of structural states is possible, yet formal guidelines for structural subdivision of the group have not yet been devised [57]. For the purposes of the simplicity, samples with intermediate degrees of cation order are referred to as "partially ordered" in conjunction with the name of an ordered species. Thus, "fully disordered ferrocolumbite," "partially ordered ferrocolumbite," and "ferrocolumbite" would describe increasingly cation-ordered variants of the composition $FeNb_2O_6$.

Besides their economical importance these materials present interesting physical properties which have motivated investigations reported in the last two decades [58 -68]. Beyond economically important as niobium and tantalum ores [69], columbites display physical properties that make them adequate prototypes for oxide materials with relevant technological applications [70].

Columbites are typical pegmatite minerals with general formula $A^{2+}B^{5+}{}_2O_6$ where A represents essentially manganese plus iron and B, niobium plus tantalum[71]. MNb_2O_6 (where M = Mg, Zn, Ni, Ca, Cu, Mn and Co) columbite niobate [72] compounds of low sintering temperature and low cost have receivedmuch attention [73–76].

Minerals of the columbite group are the main source of niobium and tantalum, which are important because of their applications in high-technology products [77]. These oxide minerals have the general formula AB_2O_6, in which the A position is occupied mostly by Fe^{2+}, Mn^{2+}, and, to a lesser extent, Mg^{2+}; the B position is occupied mainly by Nb^{5+}, Ta^{5+}, and, occasionally, Ti^{4+} and Sn^{4+}. The end members of these orthorhombic minerals are ferrocolumbite $FeNb_2O_6$, manganocolumbite $MnNb_2O_6$, manganotantalite $MnTa_2O_6$, and magnocolumbite $MgNb_2O_6$. Ions at A and B sites are coordinated to six oxygen atoms that form distorted octahedra. Octahedra are stacked in a sequence of *ABBABB* layers; those of type A share corners, while those of type B share edges [77].

Although the 3*d* transition metals occupy mainly the *A* site, there exists a considerable degree of cation occupation disorder between sites *A* and *B*; i.e., Fe, Mn, Nb, or Ta are found to occupy both sites *A* and *B* in different proportions. The different cationic occupancy of sites from one member of the series to the other leads to changes in the unit cell dimensions and to distortions in the oxygen octahedra. Cerny and Ercit [78] observed that in several groups of cogenetic columbite-tantalites with variable composition and structural state, the degree of ordering increases with the enrichment in Mn. Komkov [79] found that the a/c ratio of columbite-tantalite is a suitable parameter to describe the cation order-disorder. Cerny and Turnock [80] found in an a vs c plot (3 x a for disordered phases) that the cell parameters correlate qualitatively with the degree of cationic order and with the approximate Fe/Mn ratio, but that no apparent relationship seems to exist with the Nb/Ta ratio. However, the diagram is of limited quantitative application because the range of cell parameters for fully disordered samples is not known and, in addition, impurity substituents have an unknown infuence on those parameters [81]. Columbite structure is based on a hexagonal closest packing of oxygen anions with cations filling half of the available octahedral interstices [71]. Occupied octahedra share two opposite edges and define zigzag chains along [001] that are further interconnected through corner sharing of the octahedra (Fig. 1.2). Closest packed planes are parallel to (100), being interleaved by A- or B-type cations in a sequence [ABB]. An empirical formula derived by Ercit to estimate the degree of cation order for columbite has been used on some occasions [80-82]. In particular, for single crystals of columbite-tantalite pegmatites, Wenger *et al*. [82] found that the degree of cationic disorder obtained after application of Ercit's formula [81] correlates well with the site occupancy obtained by refinement of single crystal X-ray diffraction data.

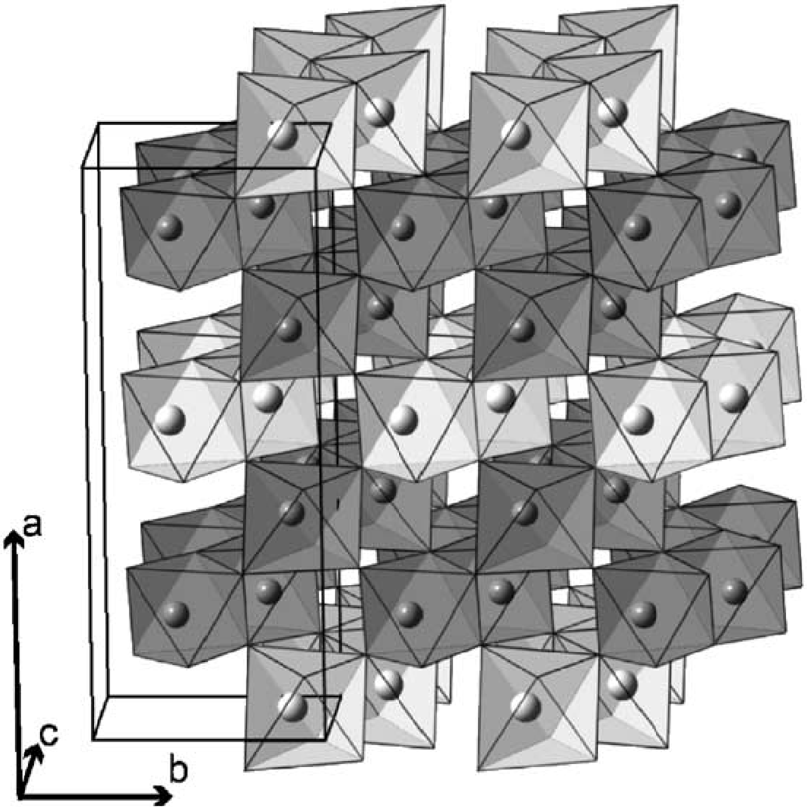

Fig. 1.2. Crystal structure of columbite-group minerals emphasizing the octahedral chains. Light grey, A-metals; dark grey, B-metals.

1.3 Synthesis of Ceramic Oxides

The synthetic approaches for preparing ceramic oxide nanostructures can be generally classified into several categories: solid-state growth, solution-phase growth, template-based methods, non-template-based methods, carbothermal reactions, solid liquid solid processes, solvothermal processes and vapor phase growth (including thermal evaporation, chemical vapor-phase deposition, metal-organic chemical vapor phase deposition, arc discharge and laser ablation). A wide variety of chemical methods for powder synthesis has been developed and optimized for preparing of electroceramic, including coprecipitation, sol–gel processes, and wet chemical methods using the hydrothermal synthesis and the polymeric precursor method. These advanced techniques of preparation are important, since they allow the preparation of stoichiometric, single phase, and highly specific surface-area powders. These characteristics have a high degree of influence on the improvement and reliability of the electrical and dielectrical behavior of the material. In this sense, the degree of densification of the sample exerts a significant influence on the electrical behavior.

The development and improvement of electronic systems must be preceded by the designing of new miniaturized and reliable electronic components. Although existing commercial components meet the engineering criteria, other new systems can be developed or existing ones can be perfected by introducing new components with improved characteristics. This development encourages the investigations of electronic materials, in particular the development of new dielectric materials with specific dielectric properties that are demanded by electronics engineers [83]. Compared with solid-state preparation, wet chemical methods have been confirmed to be a more efficient method in controlling the morphology and chemical composition of powders.

Alkali metal niobates powders are usually synthesized via a solid state reaction route using sodium and/or lithium carbonates and niobium pentoxide [84-87], One of the characteristics of this classical method is that it is rather difficult to achieve an homogeneous mixture of the components. Moreover, high sintering temperatures are required because of the low surface area of raw powders. Indeed, this method does not always allow for the production of dense, homogeneous single phase ceramics. High sintering temperatures can also enhance the volatilization of the alkali metal, which leads to stoichiometric variations in the sintered material. Increased sinterability of mixed powders and higher densification rate of green compacts were attained through pressure sintering and/or by adding selected sintering additives [88-91]. Fired densities ranging from 94 to 98% of the theoretical ones were thus reached. The firing temperature was decreased by one hundred degrees using pressure sintering. However, a calcinations step at a temperature of around 900^0C and a subsequent annealing in an oxygen flow were required [92,93].

1.3.1 Mechanochemical activation

Mechanochemical activation is away to modify the conditions in which chemical reactions usually take place [94]. During the mechanical treatment the particle size of the crystals is reduced, the homogeneity of the mixture is increased and, in most of the cases, the solid becomes more reactive [95]. Mechanical activation is usually a result of disorder of the crystal and generation of defects that cause the decrease of activation barrier for the reaction [96].

1.3.2 Solid State Reaction

Solid state route involves the many processes which includes preparation of composition, mixing and ball milling, calcining, ultrafine grinding, drying, binder addition and granulation, forming, drying and binder removal, sintering, lapping, electroding and poling. In the solid state reaction, mixing and milling are often carried out simultaneously, usually, by using ball mill. The aims of this process are to reduce particle size, to reduce agglomerates or aggregates in size and to achieve desired particle size distribution. For milling ball mill, bead mills ,sand mills, jet mills etc types of mills are available. The schematic diagram of ball mill is shown in fig 1.3.

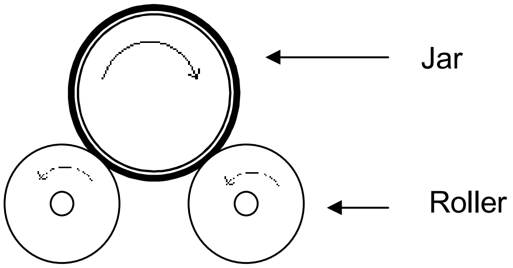

Fig 1.3 Schematic diagram of ball mill

The compound is usually synthesized at high temperature by solid-state reaction[97-99]. Although this method is simple, it takes long synthesis time and produces powders with irregular morphology, large particle size and broad particle size distribution[100]. In conventional solid-state reaction, for enhancing the diffusivity among solids, the prolonged high-temperature heating is required. However, the heating process will cause severe coarsening of the ceramic powders and also cause the volatilization of lithium compounds[101]. Furthermore, the homogeneity of the starting materials is low in the solid-state process and the conversion rate of the chemical reaction will decrease, rendering the stoichiometric deviation in the composition of the heated powders[102]. To overcome the above shortcomings, the hydroxide precrusior has been developed to synthesize ceramic powders having small particles and a narrow size distribution.

The conventional way to produce these materials involved the solid-state reaction of mixing with oxides or carbonates that contain lithium and manganese cations, and calcination at high temperature. However, the solid-state reaction requires a long heating time and followed by several grinding, annealing process, which has some inherent disadvantages, including chemical inhomo geneity, coarser particle size, and introduction of impurities during ball milling [103].

For commercial exploitation, it is desirable that the temperature of synthesis be as low as possible to produce bulk quantities of the material [104]. There are some factors such as particle size, surface morphology and homogeneity, which have an important influence on the electrochemical characteristics. It is difficult, however, to control such factors precisely using a conventional solid-state reaction which requires a high reaction temperature as high as 700–900°C [105–108], long and repeated heat treatments that lead to agglomeration of particles. Otherwise, abnormal grain growth and poor control of stoichiometry due to the nonhomogeneous composition distribution may lead to poor electrochemical performances[109].

1.3.3 Wet-Chemical Methods

In recent years, several low temperature preparation techniques such as sol–gel precipitation [110–112], Pechini process [113–114], electrochemical process [115,116] and hydrothermal process have been developed in which all the components can be homogeneously distributed to atomic scale, thus allowing a reduction of heating temperature and sintering time.

Solution technique is an alternative, in which all the components can be homogeneously distributed at the atomic–molecular level and the synthesis can be conducted at low temperatures for short periods [109].

The wet chemical process generally offers significant advantages in the fabrication of electronic materials, such as high purity, low cost, ease of composition control, relatively low-processing temperature and large deposition area [117]. In the wet chemical process, the preparation of high-quality materials depends strongly on the synthesis of an appropriate precursor [118].

1.3.4 Solvothermal Synthesis

Solvothermal method has been extensively examined as a possible solution route to prepare semiconductor nanowires and nanorods [119]. In this process, a solvent is mixed with certain metal precursors and possibly crystal growth regulating and templating agents such as amines. This solution mixture is then placed in an autoclave kept at relatively high temperature and pressure above the critical point to carry out the crystal growth and assembly process. The methodology seems to be quite versatile and has been demonstrated to produce many different crystalline semicondutor nanorods and nanowires [120].

1.3.5 Carbothermal Reactions

A variety of oxides, nitrides and elemental nanowires can also be synthesized by carbothermal reactions [121]. For example carbon mixed with an oxide produces oxide or sub oxide vapor species, which react with other reactants (O_2, N_2 or NH_3) to produce the desired nanowires. Yang et al. reported the synthesis of MgO, Al_2O_3, ZnO, and SnO_2 nanowires via a carbothermal reduction process [122].

1.3.6 Powder Metallurgy Method

Solid and molten state reaction at high temperature is the generally used method to obtain solid-state materials especially in ceramic processing. However, such synthetic routes always result in compositional inhomogeneity, shape-forming difficulty, and huge energy consumption[123]. Powder metallurgy method is a forming and fabrication technique consisting of three major processing stages. First, the primary material is physically powdered, divided into many small individual particles. Next, the powder is injected into a mold or passed through a die to produce a weakly cohesive structure (via cold welding) very near the dimensions of the object ultimately to be manufactured. Pressures of 10-50 tons per square inch are commonly used. Also, to attain the same compression ratio across more complex pieces, it is often necessary to use lower punches as well as an upper punch. Finally, the end part is formed by applying pressure, high temperature, long setting times (during which self-welding occurs), or any combination thereof.

1.3.7 Synthesis by Gas phase reactions

Using gas phase and or vacuum system to synthesize inorganic materials such as chemical vapor deposition (CVD) and sputtering also needs high energy and sophisticated instrumentation. Each of these techniques is neither economically nor environmentally friendly [123].

1.3.8 Thermal Evaporation

Thin films of oxides were prepared using thermal evaporation from a tungsten boat. The material was slowly out gassed before evaporation. The system was initially pumped to a base pressure of 10^{-4}Pa. The oxide films were deposited on The substrates can also be rotated during the deposition. The evaporation rate and thickness of the oxide films were generally controlled by a quartz crystal thickness monitor. However this method is not suitable for bulk synthesis of ceramic oxides [124, 125].

1.3.9 Hydrothermal synthesis

Hydrothermal synthesis includes the various techniques of crystallizing substances from high-temperature aqueous solutions at high vapor pressures; also termed "hydrothermal method". The term ‘hydrothermal’ came from the earth sciences, where it implied a regime of high temperatures and water pressures. Hydrothermal research was initiated in the middle of the 19th century by geologists and was aimed at laboratory simulations of natural hydrothermal phenomena. In the 20th century, hydrothermal synthesis was clearly identified as an important technology for materials synthesis, predominantly in the fields of hydrometallurgy and single crystal growth [126]. However, the severe (supercritical) reaction conditions required particularly for growing single crystals have discouraged extensive research and commercialization for many materials [127].

Hydrothermal synthesis is a process that utilizes single or heterogeneous phase reactions in aqueous media at elevated temperature (T>25ºC) and pressure (P>100 kPa) to crystallize ceramic materials directly from solution. However, researchers also use this term to describe processes conducted at ambient conditions. Syntheses are usually conducted at autogeneous pressure, which corresponds to the saturated vapor pressure of the solution at the specified temperature and composition of the hydrothermal solution. Upper limits of hydrothermal synthesis extend to over 1000ºC and 500 MPa pressure [128]. However, mild conditions are preferred for commercial processes where temperatures are less than 350ºC and pressures less than approximately 50 MPa. The transition from mild to severe conditions is determined mostly by corrosion and strength limits of the materials of construction that comprise the hydrothermal reaction vessels. Intensive research has led to a better understanding of hydrothermal chemistry, which has significantly reduced the reaction time, temperature, and pressure for hydrothermal crystallization of materials (T<200ºC, P<1.5 MPa) [126–131].

1.4 Applications of Electroceramics

Materials integration issues play an increasingly important role driven by the interest in integrating electroceramic functions into conventional semiconductor chips as well as by the evolution of multifunctional components and systems. The industrial production process currently is in a transition from empirical studies and physical demonstrators into virtual design and testing. To fit into this evolution, for integrated as well as for discrete electroceramic components, a rise in modeling and numerical simulation of material- and device-related properties presently occurs. A few functions, properties and application of the ceramics are listed in Table 1.1

Since these materials are intended for long-term service in each particular application, the thermodynamic stability is of major importance. Kinetic factors such as ionic diffusion and electrical current transport by ions, electrons or positive holes are important considerations in the choice of preparative reactions, and in optimizing the long-term stability and the electrical properties which are to be employed.

Table 1.2 lists typical applications of ceramic oxides in electrical devices, and it can be seen that the complexity of these materials ranges from the simple oxides for use in oxygen sensors, TiO_2 and SnO_2, to the very complex superconductors, e.g. $Ti_2Ca_2Ba_2Cu_3O_x$, which grow more complex in composition every year. In this respect, the ceramicist has followed the lead of the metallurgist in exploiting the development of alloys, or solid solutions, to modify and improve particular properties of materials.

Table 1.1. Advanced ceramics classification according to function properties and the corresponding applications.

Function	Properties	Application (example)
Thermal	Insulation	High temperature furnace lining for insulation (oxide fibers e.g. SiO_2, Al_2O_3 and ZrO_2
	Refractoriness	High temperature furnace lining for insulation and containment of molten metals and slags
	Thermal conductivity	Heat sinks for electronic packages (AlN)
Electrical and dielectric	Conductivity	Heating elements for furnace (SiC, ZrO_2, $MoSi_2$)
	Ferroelectricity	Capacitors (Ba-titanate based materials)
	Low-voltage insulator	Ceramic insulation (porcelain, steatite, forsterite)
	Electronic insulators	Substrate for electronic packaging and electrical insulators in general (Al_2O_3, AlN)
	Hostile environments insulators	Spark plugs (Al_2O_3)
	Ion-conducting	Sensors, fuel cells and solid electrolytes (ZrO_2, β-alumina, etc.)
	Semiconducting	Thermistors and heating elements (oxides of Fe, Co, Mn)
	Nonlinear I-V characteristic (varistor)	Current surge protector (SiC, ZnO, SnO_2)
	Gas-sensitivity	Gas sensors (SnO_2, ZnO)
Magnetic and superconductive	Hard magents	Ferrite magnets [$(Ba,Sr)O.6Fe_2O_3$]
	Soft magents	Transformer cores [$(Zn,M)Fe_2O_3$ with M=Mn, Co, Mg]: magnetic tapes (rare-earth garnets)
	Superconductivity	Wires and SQUID magnetometers ($Yba_2Cu_3O_7$)
Optical	Transparancy	Windows (soda-lime glasses), cables for optical communication (ultra-pure silica)
	Translucency and chemical inertness	Heat and corrosion-resitantmaterials, usually for Na lamps (Al_2O_3, MgO)
	Nonlinearity	Switching devices for optical computing ($LiNbO_3$)
	IR transparency	Infrared laser windows (CaF_2, SrF_2, NaCl)
Nuclear	Fission	Nuclear fuel (UO_3, UC), fuel cladding (C, SiC) neutron moderators (C, BeO)
	Fusion	Tritium breeder materials (Zirconates and Silicates of Li, Li_2O); fusion reactor lining (C, SiC, Si_3N_4, B_4C_3)
Chemical	Catalysis	Filters (Zeolites); purification of exaust gases
	Anticorrosion	Heat exchange (SiC), chemical equipments in corrosive eiviornments
	Biocompatility	Artificial joint prostheses (Al_2O_3)
Mechanical	Hardness	Cutting tools (SiC whisker-reinforced Al_2O_3, Si_3N_4)
	High-temperature strength retention	Stators and turbine blades, ceramic engine (Si_3N_4)
	Wear resistance	Bearings (Si_3N_4)

In all of these so-called "electroceramics" there are irregularities in the atomic arrangements of the metal ions which are deliberately introduced to produce a particular physical property. These irregularities can take the form of mixing of cationic species on one or more cation sub-lattices, or the introduction of vacancies either singly on the cation or the anion sublattices, or in agglomerated form to create voids. The resultant materials are normally polycrystalline, with small average grain size, containing a small fraction of porosity at the grain boundaries.

Table 1.2 Device potential applications of ceramic oxides

Device potential applications	Ceramic Oxides
Semiconducting probes and electrodes	TiO_{2-x}, SnO_{2-x} $(In, Sn)_2O_3$
Electrochemical oxygen probes	Y_2O_3-CeO_2, CaO-ZrO_2
Magnetic materials	Fe_3O_4, $(Mn,Zn)Fe_2O_4$, $Mn_3Fe_2Fe_3O_{12}$ garnets, BaO.6Fe_2O_3,magneto-plumbite
Dielectric and piezoelectric materials	$BaTiO_3$, $(Pb,La)(Zr,Ti)O_4$, $LiNbO_3$
Electrode, superconducting and catalytic materials	$(La,Sr)MO_3$ ($M \equiv$ Cr, Mn,Fe,Co,Ni), $Sr_2Fe_2O_5$, $(La,Sr,Ba)CuO_4$, $YBa_2Cu_3O_7$, (Bi,Pb)z $Ca_2Sr_2CuO_{10}$

The densities of these materials typically reach better than 95% of theoretical density. A brief explanation of some of the types of electroceramic materials is discussed in the following section.

1.4.1 Piezoelectric Materials

Piezoelectric materials are most widely used as sensors in different environments. They are often used to measure fluid compositions, fluid density, fluid viscosity, or the force of an impact. An example of a piezoelectric material in everyday life is the airbag sensor in your car. The material senses the force of an impact on the car and sends and electric charge deploying the airbag. Piezoelectricity is defined as a change in electric polarization with a change in applied stress (direct piezoelectric effect). The converse piezoelectric effect is the change of strain or stress produced in the material due to an applied electric field. Piezoelectricity was discovered in 1880 by Curie brothers who found generation of charge due to stresses in some of the crystalline materials like quartz, Rochelle salt, tourmaline etc.

First piezoelectric transducer was developed out of quartz crystal and demonstrated by Langevin in 1917 for underwater detection. In 1940, ferroelectric and electrostrictive ceramic $BaTiO_3$ was discovered. It was superior to quartz in many respect but difficult to sinter. Quarts has high strength but low permittivity and coupling coefficient, while Rochelle salt has high permittivity and coupling coefficient but is mechanically weak and temperature and humidity unstable. Because of their higher dielectric constant and greater sensitivity, they can be effectively used for measuring very small stresses than natural crystals like Quartz, Tourmaline etc.,. . Piezoelectricity is the ability of certain crystalline materials to develop an electric charge (voltage) proportional to a mechanical stress. This is referred as “generator effect”. The converse of this is also true i.e. when an electric field is applied to the material, it produces proportional mechanical strain. This is referred as “motor effect”. The generator (direct) and motor (converse) effects are depicted in fig 1.4 and fig 1.5 respectively.

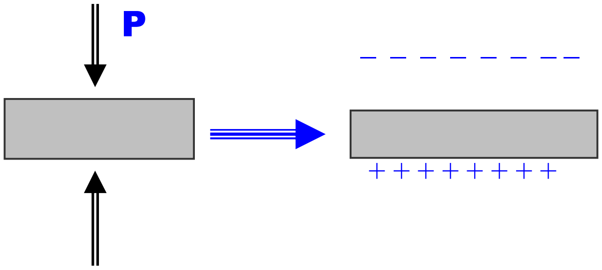

Figure 1.4 Direct piezoelectric effect

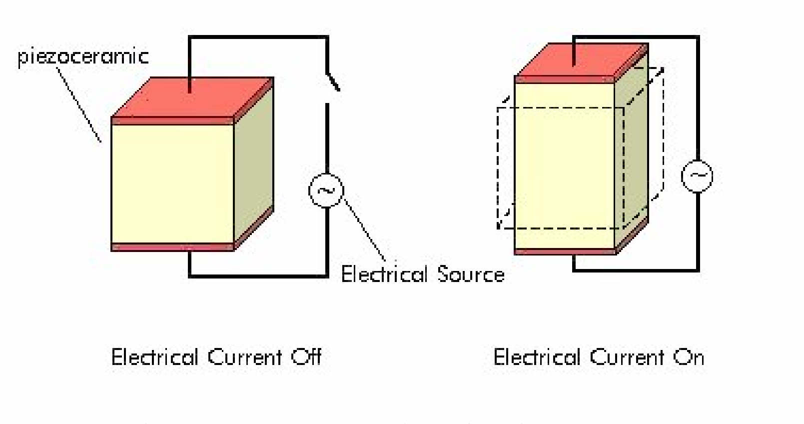

Figure 1.5. Converse piezoelectric effect

The microscopic origin of the piezoelectric effect is the displacement of ionic charges within a crystal structure. In the absence of external strain, the charge distribution within the crystal is symmetric and the net electric dipole moment is zero. However when an external stress is applied, the charges are displaced and the charge distribution is no longer symmetric and a net polarization is created. A material can be only piezoelectric, if the crystallographic unit cell has no center of inversion. Furthermore, a permanently-polarized material such as quartz (SiO_2) or barium titanate ($BaTiO_3$) will produce an electric field when the material changes dimensions as a result of an imposed mechanical force [132, 133]. The standard piezoelectric material commonly in use for medical imaging processes is lead zirconate titanate (PZT). In some cases a crystal posses a unique polar axis even in the unstrained condition. This can result in a change of the electric charge due to the uniform change in temperature. This is called the pyroelectric effect. One of the most common thermal sensors used in the infrared (IR) applications is the pyroelectric detector. Pyroelectric sensors made from lithium tantalate ($LiTaO_3$) generate electric charges with small temperature changes, and are stable, uniform and durable.

Table 1.3 Application of Piezo ceramic materials in various areas

Sr No	Major Area	Application of Piezoceramic materials
1	Automotive	Knock sensors, Wheel balancing machines, Radio filters, Seat belt buzzers, Air flow, Tyre pressure Indicators, Spark igniters, Audible alarms, keyless door entry etc.
2	Computer	Microactuators for hard disk, Transformers for notebook etc
3	Commercial	Ultrasonic cleaners, Ultrasonic probes, Ultrasonic welders, Ultrasonic touch sensors, Thickness gauges, Vibrators, Ink jet printers, Fans, Smart materials for aircraft wings etc.
4	Medical	Ultrasonic cataract remover, Ultrasonic therapy, Fetal heart detectors, Ultrasonic imaging, Nebulizers , Insulin pumps etc.
5	Consumer	Humidifiers, Gas grill igniters, Telephones, Jewelry cleaners, Musical instruments, Ultrasonic sewing machines etc.
6	Military	Hydrophones, Sonobuoys, Sonar, Depth Sounders, Targets, Fuze devices, Telephony, Ringers, Piezoelectric accelerometers as internal navigation, Deformable mirror – Adaptive optics, Acoustic Decoy System, Underwater Terrain mapping, Passive Surveillance Array System, Active Surveillance Towed Array Sensor System, Submarine detection, etc

The ability of piezoceramics to convert electrical signal to mechanical displacement and vice versa makes it one of the most useful components in transducer development. Piezoelectric materials are highly promising for naval applications as well as potential military applications such electronic fuze application, deformable mirrors, gyroscopes, and likely to play vital role in many fold. Considering the wide range of application of these materials both in military and civil, it is certain that, there is considerable scope for future development to enhance the performance of the device where it is employed. The piezoceramics are used for many applications, some of them are listed in table 1.3.

1.4.2 Ferroelectric applications

Ferroelectrics are materials that display an electric polarization in the absence of an external applied electric field, together with the property that the direction of the polarization may be reversed by an electric field. The study of the properties of ferroelectric materials and the attempt to understand the nature of the ferroelectric state constitute the field of ferroelectricity [134]. Ferroelectric materials are a sub-class of pyroelectric materials in which the direction of the electric dipole can be reversed by applying an electric field. The number of ferroelectric materials known today includes large number of ceramic solid solution compositions. Most outstanding feature of ferroelectric ceramic is its hysteresis loop (polarization vs electric field). It describes the nonlinear polarization switching behavior as a function of field. Example of ferroelectric ceramics are barium titanate, lead zirconate titanate (PZT), lead niobate, bismuth titanate, sodium potassium niobate, lead titanate relaxor ferroelectrics and polymer composites [135-140].

In ferroelectric materials, the relationship between the Ps (Polarization) and E**c** (Coercive Field) is represented by hysteresis loop as shown in fig-1.6 . Unpoled PZT crystal will show net dipole moment (Polarization) equal to zero due to their random orientation of dipoles. When a field applied to the crystal is increased slowly, in positive direction, Polarization will increase due to alignment of dipoles in the direction of field, reversal of dipoles and due to increase in the size of favourable domains. The curve OAB will be traced. After point B, though the field is increased polarization remains the same (curve BC), this is known as Saturation Polarization, Psat. When the field reduced zero the CD curve wiil be traced. The crystal will ramain polarised due to locking of dipoles known as Remanant Polarization, Pr (OD) . The extrapolation of the linear portion BC of the curve back to polarization axis is known as Spontaneous Polarization, Ps (OE). Ps is virtually equal to Pr in crystals.

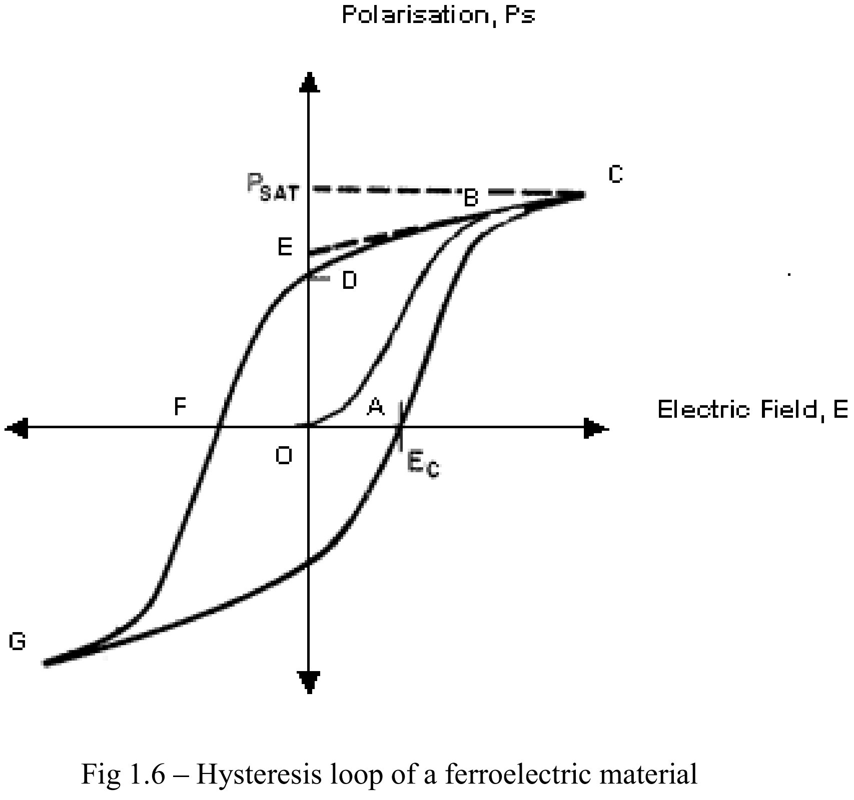

Fig 1.6 – Hysteresis loop of a ferroelectric material

In order to annihilate the overall polarization of the crystal an electric field is applied in the opposite(negative) direction. The value of field required to make the polarization equal to zero is known as Coercive field, Ec (OF). Further increasing the field, in negative direction, will reverse all the dipoles (FG). The cycle can be completed by reversing the field once again (in positive direction), curve GHC. Generally, piezoceramic compositions with high value of Pr shows usable piezoelectric effect .

1.4.3 Semiconductor Memories

Semiconductor memories such as dynamic random access memories (DRAMs) and static random access memories (SRAMs) currently dominate the market. However, the disadvantage of these memories is that they are volatile, i.e the stored information is lost when the power fails. The non-volatile memories available at this include complementary metal oxide semiconductors (CMOS) with battery backup and electrically erasable read only memories (EEROMs). These non-volatile memories are very expensive. The main advantages offered by ferroelectric random access memories (FeRAMs) include non-volatile and radiation hardened compatibility with CMOS and GaAs circuitry, high speed (30ns cycle time for read/erase/rewrite) and high density $(4\mu m)^2$ cell size) [141, 142].

The fabrication of ferroelectric thicn films is done by three methods including physical vapour deposition (PVD), chemical vapor deposition (CVD) and sol-gel processing. In PVD, precursors of the desired film composition are vaporized and deposited on the substrate by one of the sputtering techniques (i.e. r.f magnetron sputtering, pulsed vapor deposition (PLD) etc.) methods, molecular beam epitaxy (MBE) and laser ablation [143, 144].

1.4.4 Semiconducting Oxides

Many semiconducting oxides such as ZnO, SnO_2, In_2O_3, Ga_2O_3, CdO, and PbO_2 have been demonstrated to be highly useful for the fabrication of nanodevices such as field-effect transistors and gas sensors [145–150]. Of these, SnO_2 and ZnO are widely exploited because of their unique conductance properties and process flexibility. The characteristics of SnO_2 containing cations with mixed valencies and the adjustable oxygen deficiency enable tuning of their structure and properties. The wide direct band gap (3.37 eV), large exciton binding energy (60 meV), negative electron affinity, and high mechanical strength makes ZnO one of the promising photonic materials in the ultraviolet region and a good candidate for field emitter arrays of flat panel display devices.

1.4.5 Electrostriction materials

During the last 2 decades, the electrostriction phenomenon showed an increasing importance due to its various applications [153–157]. Electrostriction is the fundamental mechanism of electromechanical coupling in all insulator materials. Its magnitudes can range from very minute in low permittivity dielectrics to very large in ferro electrics [158]. In practical applications, electrostrictive stresses can cause breakdown in insulator materials in microelectronics and high voltage devices [159]. Electrostriction is defined as the quadratic coupling between strain (x) and electric field (E), or between strain and polarization (P) [160, 161]. Electrostriction has been known for long as a major source of internal stress developing in oxide films during anodizing [162, 163].

Electrostriction is also an another electromechanical effect that exists in ferroelectric ceramics. In electrostriction the sign of the deformation that occurs with an electric field is independent of the polarity of the field and is proportional to the even powers of the field [164]. The application of piezoelectric, pyroelectric and ferroelectric materials, for sensing and actuation spans in most of the industrial sectors. This includes medical diagnostics such as ultrasonic imaging, aerospace such as accelerometers and micro-positioners, automotive such as solid-state piezoelectric fuel injectors, and chemical and process control, which requires the use of thermal, strain and force sensors.

1.4.6 Dielectric materials

Dielectric materials play a important role as gate oxide in integrated circuits [165]. The word *dielectric* is derived from the prefix *dia*, originally from Greek, which means "through" or "across"; thus, the *dielectric* is referred to as a material that permits the passage of the electric field or electric flux, but not particles. This implies that the dielectric does not permit the passage of *any* kind of particles, including electrons. Thus, it should not conduct the electric current. However, a dielectric is generally considered a nonconducting or an insulating material. There is no ideal dielectric in this planet. The perfect vacuum may be considered to be close to the ideal dielectric, but a perfect vacuum cannot be obtained on Earth. A vacuum of 10^{-14} torr still consists of about 300 particles per cubic centimeter. All real dielectric materials are imperfect, and thus permit, to a certain degree, the passage of particles. We have to coexist with the imperfections [166]. Dielectric materials are insulators used for their exceptional dielectric properties. When a material is introduced between two plates of a capacitor, the total charge stored in the capacitor will change. The change depends on the ability of the material to polarize under an electric field. The dielectric constant or permitivity of a material determines the change in charge storage. For high capacity applications, a high dielectric constant is needed. Since the dielectric constant depends on the polarization in the material, ferroelectric materials are usually the materials of choice. High dielectric constant materials are also called high K materials. In some cases capacity is a side effect of the structure and needs to be minimized. For these applications material with a low dielectric constant is required. These materials are also referred to as low K materials.

This dielectric property is useful in capacitors, especially at radio frequencies. Dielectric materials are also used in the construction of radio-frequency transmission lines. In practice, most dielectric materials are solid. Examples include ceramic (typically alumina or aluminosilicates), mica, glass, plastics, and the oxides of various metals (for example, titanium, zirconium and hafnium oxides, or tantalum oxide) as well as multi-metallic oxides (for example barium strontium titanate) [167]. The dielelctric materials used for ceramic capacitor are classified as film capacitors, multilayer capacitor, barrier layer capacitor and grain boundary barrier layer (GBBL) capacitors [168–172].

1.4.7 Metal Oxide Gas Sensors

The simple metal oxides such as TiO_2 and SnO_2 are used as oxygen sensors in the automotive industry [173]. The response to the oxygen partial pressure in the engine exhaust is detected through the dependence of the n-type electrical conductivity of these oxides on oxygen potential. The conductivity is determined by the electron carrier concentration which is inversely related to the oxygen-to-metal ratio in the oxide. This can be calculated from an application of the mass action law to thermodynamic data providing the deficiency is very small, less than 0.1% of the oxygen ion sites being vacant. It is interesting to note that the electrical conductivity and the departure from stoichiometry vary as a function of oxygen potential in very closely the same manner. It follows that the electrical mobility of the current-carrying species produced as a result of departure from stoichiometry, is independent of the concentration of these species.

The limit on the use of these materials as oxygen sensors is determined by a significant departure of the conductivity from the simple mass action prediction at low oxygen pressures. In the case of TiO_{2-x} this is known to be due to the almost complete elimination of the oxygen vacancies, created by departure from stoichiometry, by a shear transformation in the solid. The resulting structure consists of islands of normal TiO_2 separated by shear planes of composition approximating to Ti_2O_3, and as the oxygen pressure is further reduced, the spacing between the shear planes, and hence the volume of the normal TiO_2 regions, decreases. This gives rise to the formation of a series of Magneli phases of general formula Ti_nO_{2n-1} with n decreasing as the oxygen potential decreases. The final member of this series is Ti_2O_3.

A surprising fact is that although SnO_{2-x} has been used as an oxygen sensor in a similar way for many applications over a long period of time, the precise relationship between stoichiometry and oxygen pressure has only recently been elucidated [174]. The lower limit of oxygen potential for the use of this material in an oxygen sensor is that at which there is the appearance of metallic tin. These two oxygen sensors must be coated with noble metal catalysts in order to respond in a sufficiently short time to changes in the oxygen atmosphere for practical application [175]. In further designs aimed at increasing the speed of response, considerable effort has been expended in producing porous sensors with a stable pore structure at operating temperatures, in order to optimize the gas-solid contact.

1.4.8 Thermistors

Thermistors which show a negative temperature coefficient of resistance are usually simple oxide solid solutions which can be designed to give a readily detected change in electrical conductivity for a small change in temperature. They are normally insensitive to oxygen pressure changes in the temperature range 0-200 °C where they are used. (This is because both types of semiconductivity depend on thermally activated conduction by small polaron motion.) Transition metal ions are used in the production of these materials, and both n- and p-type semiconduction has been applied for this purpose. This temperature dependence can be adequately described by the Arrhenius expression

$$\sigma_T = \sigma_o \, exp(-E/RT)$$

The simple solid solutions obey Raoult's law reasonably well and can thus be described by assuming that the random mixing of cations leads to an ideal entropy contribution to the stability. The practical advantage of using oxides as thermistors is that a relatively low conductivity, dependent on the current carrier concentration, can be blended with a high activation energy E, for polaron migration, to produce a sensitive temperature measuring device. Several commercial materials are based on the spinel Mn_3O_4 in which some substitution is made of nickel, cobalt or copper ions to provide the optimum values of these two parameters. Because of the sensitivity of the valency of these transition metal ionic species to the oxygen potential of the surrounding gaseous phase at the high temperatures used in the fabrication process, great care must be exercised in control of the atmosphere during production. Figure

1.7 shows a typical thermistor temperature curve compared to a typical 100 Ω RTD temperature curve.

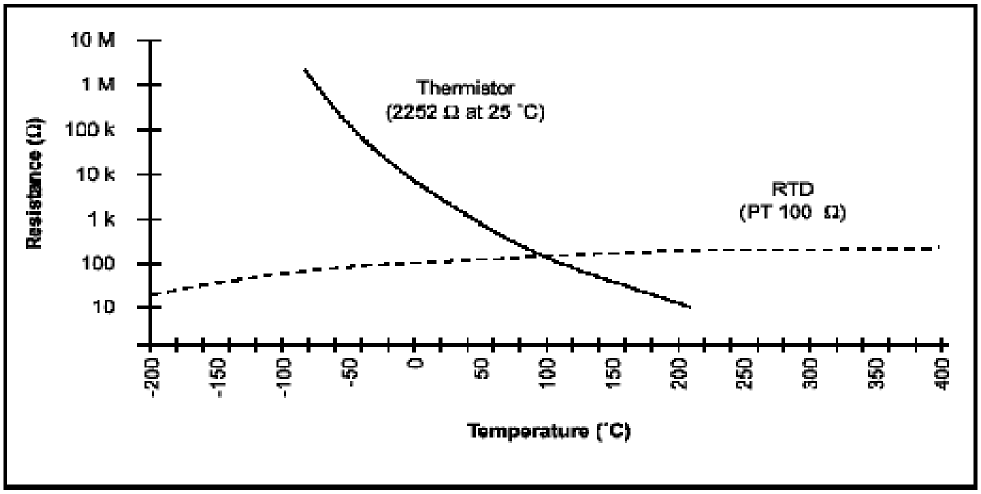

Figure 1.7. Resistance versus Temperature for a Typical Thermistor and RTD

1.4.9 Electro-optic applications

The electro-optic effect is the change in the refractive index as a function of an externally applied electric field. The requirements for using ferroelectric thin films of oxides for electro-optic application include an optically transparent film with a high degree of crystallinity. The electro-optic thin film devices are of two types; one in which the propagation of light is along the plane of the film for optical wave guides and the other in which the light passes through the film for optical memory and display applications.

An optical waveguide controls the propagation of light in a transparent material (ferroelectric thin film oxides) along a certain path. For the waveguide to work properly, the refractive index of the films should be higher than that of the substance. For light to propagate in the waveguide, the thin film should be optically transparent. This can be achieved by fabricating the film under clean conditions and aiming for a fine grain size with ultra-phase purity and high density. A great deal of work has been done on making ferroelectric thin film waveguides from $LiNbO_3$ and $Li(Na, Ta)_3$ using LPE and MBE methods. Lead zirconate Titanate (PZT) and Lead Lanthanum Zirconate Titanate (PLZT) thin films are even better candidates for optical waveguide applications because of their large electro-optic coefficient [176, 177].

In unisotropic materials the index of refraction depends on the direction of propagation and the direction of polarization of the light (optical birefingence). This means that the two components of light polarization can propagate at a different speed inside the material. This in turn causes a rotation of the overall polarization direction. Applying an electric field will change the index of refraction by a different amount for the two polarizations, causing further rotation of the polarization vector. By placing the electro-optic material between two polarizers one can control the amount of light passing through by changing the voltage. The electro-optic ceramic compositions are PLZT (La modified lead zirconate titanate) PSN (lead scandium niobate, $MgA1_2O_4$ (spinel), ALON (aluminium oxynitride), $A1_2O_3$-MgO (lucalox), MgO, MgF_2, CaO, CaF_2, Y_2O_3-ThO_2 (yttralox), etc. However, PLZT is the best optically-transparent ceramic material. The electrooptic properties of PLZT materials are intimately related to their ferroelectric properties. Consequently, varying the ferroelectric polarization with an electric field, such as in a hysteresis loop, also produces a change in the optical properties of the ceramic [164]. PLZT materials are also known to possess many special photosensitive phenomena that are directly linked to their microstructural, chemical, electronic and optical properties, including photoconductivity, photovoltaic properties, photo-assisted domain switching, ion-implantation-enhanced photosensitivity, photochromic effect, photomechanical (photostrictive) behavior, photorefractive effects and photoexcited space charge phenomena [178–181].

The use of optical techniques for both recording and read-out offers the capability of high-capacity, random-access memories without serious interconnection problems. The ideal storage medium allows insitu erasure information (for updating the memory), a resolution of about 1000 lines/mm, long storage time, high recording sensitivity, high signal to noise ratio and linear exposure characteristics. Holographic storage with a resolution of 500 lines/mm has been accomplished with $Bi_4Ti_3O_{12}$ ferroelectric-photoconductor sandwich structures.

1.4.10 Oxides for Photovoltaics

The traditional concept of Photovoltaics (PV) or solar cells is that of a solid-state device that produces useful electricity (direct current and voltage) from the Sun's energy via the photovoltaic effect. When sunlight strikes the cell, the part of the solar spectrum with energy above the bandgap of the semiconductor material imparts enough energy to create electron hole pairs. A junction formed between dissimilarly doped semiconductor layers sets up a potential barrier in the cell, which separates the light-generated carriers. This induces a fixed electric current (dependent on cell area) and a voltage (dependent on the nature of the doped layers) in the device. The electricity is collected and transported by metallic contacts on the top and bottom surfaces of the cell. More than 30 years of worldwide research on terrestrial PV has resulted in significant advances in research and the markets, as well as in significant cost reductions for PV systems and improvements in the reliability of all system components. One of the most significant trends is the continuous improvement of solar cell efficiencies for all technologies

Corrosion protection of metals and alloys is achieved by the formation of passive metal oxide, which usually exhibits semiconductive properties. Photovoltaics, the conversion of sunlight to electrical power has been dominated by solid-state junction devices, often made of silicon [183]. To improve the properties of transparent conductive oxide (TCO) glass, which is commonly used as a front contact in thin film silicon PV modules, is believed to be one of the most effective approaches to increase conversion efficiency and decrease production cost [184, 185]. Besides the silicon absorber layers, transparent conducting oxide (TCO) films are also important components of thin film Si solar cells (photovoltics). Such highly conducting TCO layers are commonly used as contact layers of pin solar cell structures [186–190]. Schematic diagram of a solar cell structure having TCO films which are key for the improving efficiency of thin film solar cells along with function of other layers is given in figure 1.8.

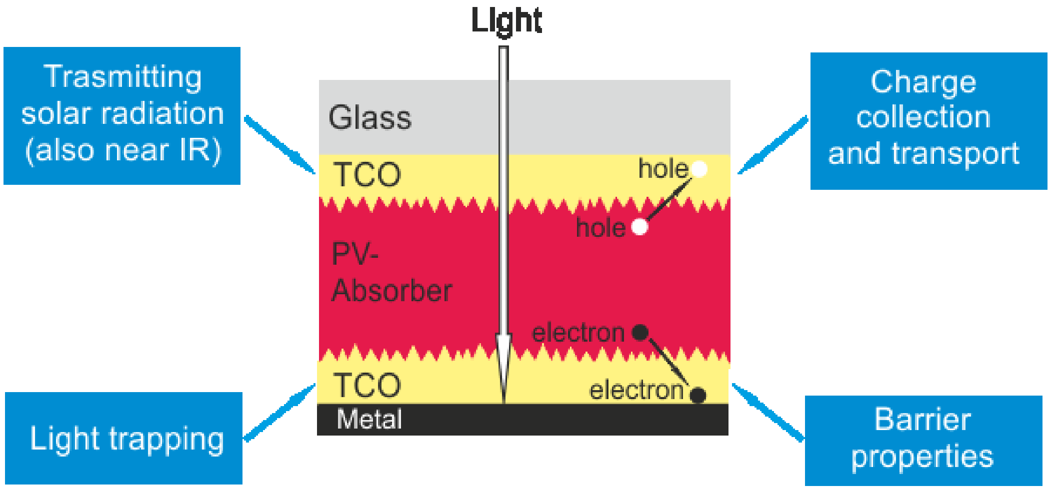

Figure 1.8. Transparent conductive oxide (TCO films) in solar cell structure

Since the lateral conductance of doped p/n silicon layers is not sufficient to prevent resistive losses over typical distances in the range of 1 cm, a TCO front layer is used to avoid a high series resistance [186]. Furthermore, front contact TCO layers serve the purpose of (i) an effective coupling of light into the solar cell by refractive index matching and (ii) an efficient trapping of light scattered into the solar cell at the rough TCO/silicon interface. Also at the rear contact of the solar cell, TCO layers are applied in order to obtain current extraction similar as the TCO front contact [189, 191], and /or the improvement of optical properties of the metal back contact. Direct contact of the metal (usually silver or aluminium) with silicon is known to cause optical absorption losses [192]. Furthermore, the long-term stability of the ZnO/Ag rear contact is superior to the Ag layer in direct contact with silicon [188,193]. Furthermore most current cells are also based on an inorganic transparent conductor, such as indium tin oxide.

1.4.11 Ionic conductors and mixed conductors

Most structural ceramics are known for their high resistance to charge transfer, and are therefore useful as electric insulators. Some electroceramics, however, are very useful for the exact opposite reason that they can accommodate charge transfer. There are several methods of conducting in ceramic materials. The first is electronic conduction, similar to that of metals, and the second is ionic conduction, where charged atoms serve as carriers. As mentioned before, ionic conduction is achieved by the movement of ions (atoms of positive or negative charge) through the solid. This transfer is usually done via point defects called vacancies in the crystal lattice. Such movement can require high energy, making ionic conduction very strongly dependent on temperature. Ionic conductors are useful in gas sensors, fuel cells and batteries. Materials that can accomodate electron conductivity as well as ionic conductivity are known as mixed conductors.

1.4.12 Microwave Ceramic oxides

Commercial wireless technologies, such as cellular phones, direct broadcasting satellites and global position systems have been making rapid progress due to the improved performance of dielectric resonators at microwave frequencies [194]. The dielectric resonator requires a high dielectric constant (ε_r) for possible size miniaturization, a low dielectric loss for frequency selectivity and low signal attenuation and a near zero temperature coefficient at resonant frequency [195,196]. Several compounds such as $Ba(Mg_{1/3}Ta_{2/3})O_3$, $(Mg,Ca)TiO_3$ and $Ba(Zn_{1/3}Ta_{2/3})O_3$ have therefore been developed for microwave applications [197, 198].

Recently, the binary niobate and tantalate compounds with general formula AB_2O_6 (where A = Ca, Mg, Zn, Co, Ni, Cu, Mn and B = Nb, Ta) were found to be promising candidates for application in microwave devices due to that the evaluations of the microwave dielectric properties of these compounds reveal a high quality factor ($Q \times f$) and a high dielectric constant (ε_r) [15, 197–202]. These materials have good quality factors, especially considering low cost and simplicity of the materials compared with complex perovskites [203]. The requirements of ceramic resonators used at microwave frequencies are high dielectric constant, a high Q value (reciprocal of dielectric loss) and a low temperature coefficient of resonant frequency [16].

1.4.13 Magnetic materials and superconductors

Ceramics based materials compose a major share of both hard and soft magnetic materials. Permanent magnet applications are found in the aerospace, automotive, computer electronics, instrumentation, medical, telecommunications etc. These permanent or hard ferrite materials are part of family of complex oxide having the general composition MO.6Fe_2O_3 (eg: SrO.6Fe_2O_3, BaO.6Fe_2O_3) The performance characteristics of the ferrites are being improved following many chemical approaches. Soft magnets are important in many electrical and electronic systems. Soft ferrites can be classified further according to the frequency of use and crystal structure Mn-Zn, Ni-Zn and Mg-Zn ferrites are widely used soft ferrites depending on the frequency of interest. Under some conditions, such as extremely low temperature, some ceramics exhibit superconductivity. The exact reason for this is not known, but there are two major families of superconducting ceramics [204].

1.4.14 Smart materials

Smart materials have one or more properties that can be dramatically altered. Smart materials respond to environmental stimuli with particular changes in some variables. For that reason they are often also called responsive materials. Depending on changes in some external conditions, smart materials change their properties (mechanical, electrical, appearance), their structure or composition, or their functions. Mostly, smart materials are embedded in systems whose inherent properties can be favorably changed to meet performance needs [205, 206]. To address the problems of deteriorating civil infrastructure, research is very essential on smart materials. The peculiar properties of the shape memory alloys for smart structures render a promising area of research in this field. Smart systems and smart materials Smart structures are a new emerging materials system which combines contemporary materials science with information science. The smart system is composed of sensing, processing, actuating, feedback, self-diagnosing and self-recovering subsystems. The system uses the functional properties of advanced materials to achieve high performances with capabilities of recognition, discrimination, and adjustification in response to a change of its environment.

Smart materials cover a wide and developing range of technologies. A particular type of smart material, known as chromogenics, can be used for large area glazing in buildings, automobiles, planes, and for certain types of electronic display. These technologies consist of electrically-driven media including electrochromism, suspended particle electrophoresis, polymer dispersed liquid crystals, electrically heated thermotropics, and gaschromics.

1.4.15 Multilayer ceramic oxides

Multilayer ceramic technology (MLC) is one of the most challenging growth areas in the ceramic industry today. The technology lends itself to computer control of the process, including the design and artwork, and this has become one of the most sophisticated ceramic technologies yet developed. Successful design of an MLC substrate depends on complete understanding of the green and fired properties of the ceramic and the metallurgy used and careful matching of shrinkage curves between metal and ceramic during firing.

With the advent of advanced electronic circuits, the demand for surface mountable chip components continues to increase. Under these circumstances, the principal developments in the multilayer ceramic capacitors industry are miniaturization, improvement of volumetric efficiency, cost reduction, improvement in reliability, and the design of new products with improved performance. Schematic diagram of a Multilayer ceramic technology (MLC) is illustrated in fig 1.9. Advanced technologies for fine oxide powder synthesis, thin film preparation, and the stacking of a high layer count (~300) have led to a high volumetric efficiency comparable to that of tantalum electrolytic capacitors [207]. One of the most critical material processing parameters is the degree of homogeneous mixing of additives in the slurry. Miniaturized highly reliable chip components are required to design compact and reliable electrical equipment. MLCs are typical passive electronic components which have steadily decreased in size year by year.

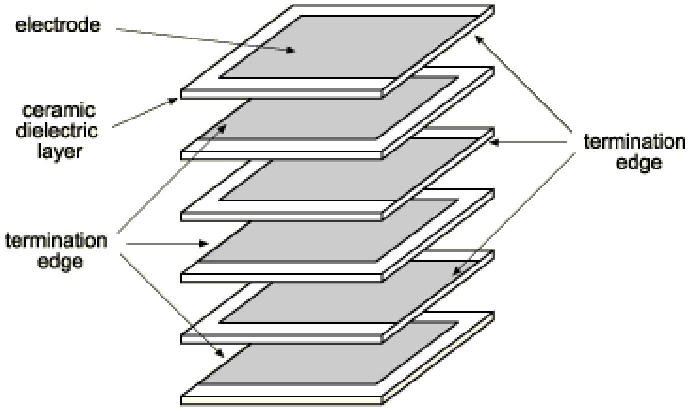

Figure 1.9 Schematic diagram of a Multilayer ceramic technology (MLC)

1.4.16 Ceramics oxides in MEMS

The electroceramic oxides are proving most promising for use in miniature devices for industrial and commercial applications, because of their unique properties [208, 209]. Miniaturization of electroceramics has shown an increasing trend for the design of useful electromechanical devices such as microelectromechanical systems (MEMS) in the last decade. Currently, MEMS primarily use silicon technology and have typical feature sizes of the order of microns or smaller [210].

The excellent micromachinability of silicon added new perspectives in sensor design, micromachined silicon structures such as cantilever beams, free-standing bridges, membranes, and channels led to novel structures of miniature transducers resulting in the emergence of the new field of microelectromechanical systems (MEMS). MEMS are miniature devices or arrays of devices that combine electronics with other components such as sensors, transducers and actuators, and are fabricated by IC processing techniques. For a number of applications the MEMS concept facilitates better device quality (e.g. higher sensitivity, better reproducibility, and faster response), and involve low costs with, very often, lower power consumption in comparison with discrete devices. Examples of MEMS products are the air-bag accelerometer, which reached the market at the beginning of the 1990s, and the more recent digital micromirror display (TV screen) in which a large array of electronically controlled mirrors etched onto a MEMS converts video data into high-resolution TV images. The integration of functional ceramics, in the form of thin or thick films, with silicon promises to add versatility to the MEMS leading to new functionalities. Research in this direction increased in importance in very recent years, and is very likely to continue to grow in the future [18].

1.4.17 Ceramic voltage sensors or varistors oxides

A device which performs the duty of protecting electronic/electrical device is called the voltage sensors/Voltage dependent resistors (VDR) or transient voltage suppressor or surge arrestors or more popularly called the Varistor. Varistors (Variable Resistors) are voltage-dependent resistors with a symmetrical *V*/*I* characteristic curve (figure 1.10) whose resistance decreases with increasing voltage. Connected in parallel with the electronic device or circuit that is to be guarded, they form a low-resistance shunt when voltage increases and thus prevent any further rise in the over voltage. Despite its many benefits, one of the few drawbacks of semiconductor technology is the vulnerability of solid-state devices to over voltages.

Even voltage pulses of very low energy can produce interference and damage, sometimes with far-reaching consequences. So, as electronics makes its way into more and more applications, optimum over voltage or transient suppression becomes a design factor of decisive importance. The power fluctuations/over-voltage usually encountered due to natural lightning and switching operations can permanently damage the electronic/electrical devices.

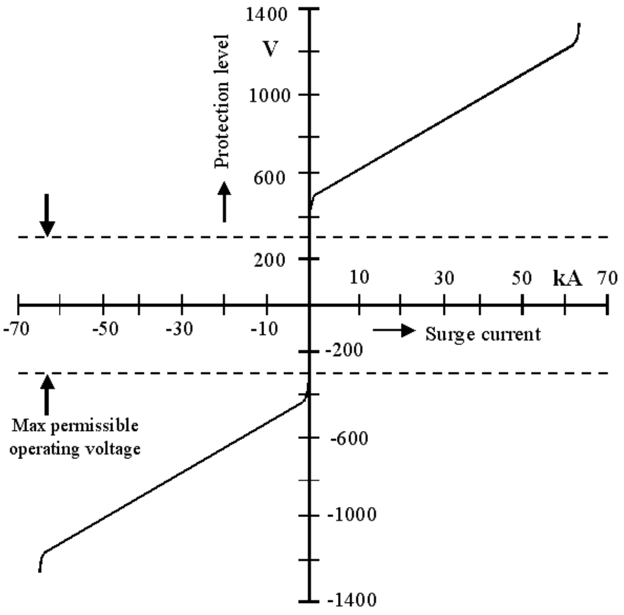

Figure. 1.10 Typical I-V characteristics of varistors on linear scale.

It is essential to suppress/bypass these over voltages to protect the sensitive components/device. In early days, spark gaps were used for over voltage protection and guarding the sensitive device. Spark gaps and gas tubes are crowbar devices that change from an insulator to an almost ideal conductor during an over voltage. These spark gaps remains short-circuited after the first spark and hence were not repeatedly usable. The development of Silicon carbide (SiC) based voltage sensors have occurred around 1930 [211]. Silicon carbide varistors [212] were the most common type of varistor used before the metal oxide varistors. Made from specially processed silicon carbide, they handle high-power, high-voltage surge arrester applications. However, the relatively low impedance values of this material produce one of the following two results. Either the protective level is too high for a device capable of withstanding line voltage or for a device producing an acceptable protective level, excessive standby current would be drawn at normal voltage if directly connected across the line. Therefore, they require a series gap to block the normal voltage. Silicon avalanche diodes find use in both low-voltage dc applications and in higher voltage ac mains protection. Avalanche diodes have a wider junction than a standard zener diode, which gives them a greater ability than a zener to dissipate energy. The biggest disadvantage to using the avalanche diode as a transient suppressor on an ac mains line is its low peak current handling capability.

The main breakthrough in the field of over voltage protectors/limiters came when in 1969 Matsuoka et al [213] announced the development of varistors based on Zinc oxide compositions. His more detailed paper describes many of the essential features of varistors, as we know them today [214]. When exposed to surges, the zinc oxide material exhibits a bulk action characteristic, permitting it to conduct large amounts of current without damage. Metal oxide varistor (MOV) are cost and size effective, are widely available, and do not have a significant amount of overshoot. They have no follow-on current and their response time is often sufficient for the types of transients encountered in the ac mains environment.

1.4.18 Ceramic capacitors

A capacitor consists of a dielectric material sandwiched between two electrodes. The total capacitance of this device is given by

$$C = \frac{\varepsilon_o \varepsilon_r A}{d}$$

where ‘C’ is the capacitance

ε_o is the permittivity of free space

ε_r is the relative dielectric permittivity

‘d’ is the distance between the electrodes

‘A’ is the area of electrodes.

To get a high volumetric efficiency (capacitance per unit volume) the dielectric material between the electrodes would have a large dielectric constant, a large area and a small thickness. ABO_3 based ceramics having a perovskite type structure show dielectric constant values as high as 15,000 as compared to 5 or 10 for polymer materials. A basic capacitor construction using ceramic dielectric materials is shown in figure 1.11

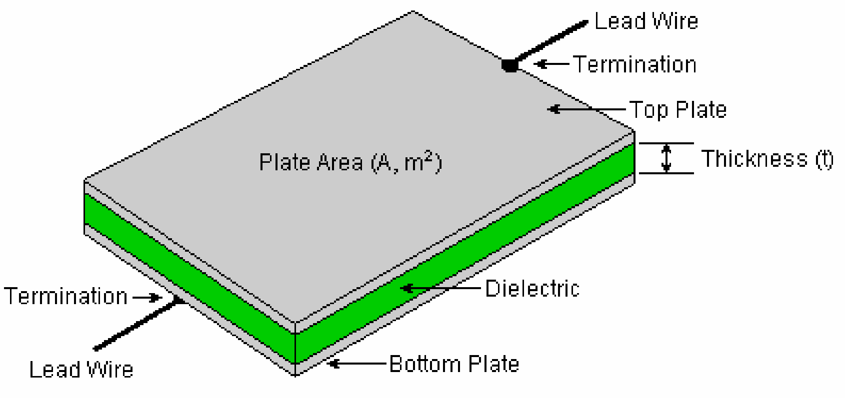

Figure 1.11 Basic Capacitor Construction

The volumetric efficiency can be further enhanced by stacking many layers of ceramic capacitors. Each individual dielectric layer contributes capacitance to the ceramic capacitor as electrodes terminate in a parallel configuration. Hence the effective equation for capacitors becomes

$$C = n.\frac{\varepsilon_o \varepsilon_r A}{d}$$

Where n is the number of dielectric layers. The advances in tape casting technology have made it possible to make dielectric layers, 20µm thick. This combined with the use of a high dielectric constant ceramic material allows large capacitance values to be achieved in relatively small volume capacitor devices. Ceramic capacitors are made by tape casting process. A slurry with a suitable binder/solvent system is first made from the dielectric ceramic powder. Thin green sheets of the ceramic are then made by the tap casting process. An ink consisting of an electrod and organics is screen printed on the dielectric sheets and then hundreds of sheets are stacked one on top of the other. A low pressure at a temperature between ~ 50 and70^{0}C is applied to laminate the sheets. The binder removal is accomplished by heating the green body very slowly to a temperature of ~ 300 – 400^{0}C. The ceramic capacitor is then sintered at a high temperature depending on the type of ceramic. After applying the terminations for the internal electrodes of the capacitors, the capacitor is mounted on the electrode substrate by soldering.

1.5 Research on advanced ceramics and Market analysis.

The development of ceramics with improved properties will open up an increasing number of demanding applications, like advanced electronic ceramic materials for Si electronics and automotive industries. Furthermore, increasing global demand for energy has led to a strong need for established and alternative energy sources. Advanced ceramics have played and will continue to play a critical role in all aspects of energy production, storage, distribution, conservation, and efficiency [19]. However, there are a number of issues which have to be addressed in terms of future needs for innovative and multifunctional ceramic material systems, robust and affordable manufacturing technologies, system level performance studies, system reliability and durability, and total life cycle cost. Finally, producers are always looking to improve the competitiveness and sustainability of manufacturing. This progress in advanced ceramics technology will not occur without the continuous support of ceramics fundamental research by government agencies and industry.

Advanced ceramics are prominently featured in passive electronic components and are providing key components for subsystems like printers, fine positioning, medical and optical devices, injection systems, actuators and sensors. In the microelectronics and high-power electronics industry they are utilized as components prepared by laminate and substrate technology. Ceramic packages are predicted on the long term for an integration of important optical functions, including light sources, light modulators, light sensors and light guides. These, in combination with electrical components will provide a complete optical information package (system in package, SIP).

Highly efficient thermoelectric energy converters are seen to be available for energy harvesting from process heat to provide energy-autonomous systems and for cooling of electronic components. For high-temperature electronics advanced ceramics are expected to play a stronger role as thick films, multilayers and tapes and as thin films for high-permittivity gate oxides in power semiconductors. Robust and flexible chemical sensors, especially gas sensors and biosensors are predicted to be available for combination of several sensor principles for increased sensitivity and selectivity. Ceramic micro-electromechanical systems (MEMS) are expected to gain momentum. Recent problems with electrostatic MEMS may hopefully be overcome using piezoelectric thin film drives. Therefore, increasingly multi-disciplinary approaches and R&D co-operations will be required including contributions, interfaces and leadership from the industrial side. To leverage the entire innovation potential of advanced ceramics along the complete value-added-chain requires major efforts which have to be shared between the academic and the industrial side. Also, research funding will be an essential part to sustain and support this ambitious but essential goal. Although high risk, they offer the opportunities for fundamental breakthroughs.

1.6 Objective and Scope of the present work

The aim of the present work is to synthesis some of technologically important niobium and tantalum based electroceramic compounds by novel hydroxide precursor technique for the first time and characterize these materials by various physico-chemical methods. This novel hydroxide precursor method has advantage of forming crystalline phase at much lower temperature as compared to samples prepared by the traditional solid-state method. Due to the fact that alkaline earth metal (Ba, Sr, Ca) carbonate or oxalate will decompose only at higher temperatures ($T > 800^{\circ}$ C), solid state methods using oxides, carbonates or oxalates do not produce electroceramics compound at low temperatures. Hence the present study aims for hydroxide precursor procedure to prepare ternary electroceramic compounds at relatively low temperature. There are very little or no literature for low temperature synthesis of ternary oxides. The present study minimizes the sintering temperature and duration for cost reduction and time saving. In the present study selected ternary oxides (ABO_3 and AB_2O_6) of alkali and alkali earth niobate, tantalate are synthesized by novel hydroxide precursor technique. Synthesized compounds are 1) $LiNbO_3$, 2) $LiTaO_3$, 3) $NaTaO_3$, 4) $NaNbO_3$, 5) $SrNb_2O_6$, and 6) $SrTa_2O_6$. The sequence of the reaction and phase evolution will also studied by the X-ray diffraction. The structures of these compounds were confirmed by XRD. The lattice parameters and phase content of these ceramic powders are analyzed by XRD. Least squares method is used to refine the lattice parameters. The composition analysis of sintered pellets will be done using Energy Dispersive analyzer(EDAX). Thermogravimetric analysis (TGA) is carried out to monitor the weight loss associated with the formation of niobates and tantalates from hydroxide precursor. Differential Scanning Calorimetric (DSC) analysis of samples prepared by hydroxide precursor method was carried out at 5 different heating rate (2.5, 5, 7.5, 10 and 15^0C/min) and activation energy is computed by Kissinger method. Impedance spectroscopy for all these compounds where thoroughly studies for Nyquist plot (Real vs Imaginary impedance), Bode plot – (1) Phase Angle vs frequency and 2)Impedance magnitude |Z| vs frequency, Dielectric Loss vs frequency. The morphology and the particle size is investigated using Transmission Electron Microscopy and Scanning Electron Microscopy.

The novel hydroxide precursor technique used in the synthesis of ternary electroceramic powders requires low sintering temperature and this process can avoid complex steps such as refluxing of alkoxides and high temperature sintering, resulting in less time consumption compared to other techniques.

1.7 Reference :

1. N. Ramadass, Materials Science and Engineering, 36 (1978) 231.
2. B. Jaffe, W. R. Cook and H. Jaffe, Piezoelectric Ceramics, Academic Press, New York, 1972.
3. H. Braver and E. Fenner, Siemens Rev., 3 (1965) 95.
4. H. Kaiser, Siemens Rev., 40 (1973) 475.
5. R. J. H. Vorehoeve, J. P. Remeika, P. E. Freeland and B. T. Mathias, Science, 177 (1972) 353.
6. C. S. Tedmon, Jr., H. S. Spacil and S. P. Mitoff, J. Electrochem. Soc., 116 (1969) 1170.
7. D. B. Meadowcroft, Nature (London), 226 (1970) 847.
8. F. S. Hickernell, J. Solid State Chem., 11 (1975) 225.
9. D. L. Staebler, J. Solid State Chem., 12 (1975) 177.
10. B. Cockayne, in B. Cockayne and D. W. Jones (eds.), Modern Oxide Materials, Academic Press, New York, 1972.
11. Chonghe Li, Kitty Chi Kwan Soh, Ping Wu, J. Alloys and Compounds 372 (2004) 40.
12. L.M. Feng, L.Q. Jiang, M. Zhu, H.B. Liu, X. Zhou, C.H. Li, J. Phy. and Chem. of Solids 69 (2008) 967.
13. W. Wersing in “High frequency ceramic dielectrics and their applications for microwave components” edited by B. C. H. Steele, Elsevier applied science, London, 1991.
14. Cristina Tealdi, M. Saiful Islam, Lorenzo Malavasi, Giorgio Flor, J. Solid State Chemistry 177 (2004) 4359.

15. YingChun Zhang, BaoJian Fu, Xiu Wang, J. Alloys and Compounds 478 (2009) 498.
16. I.S. Mulla, N. Natarajan, A.B. Gaikwad, V. Samuel, U.N. Guptha, V. Ravi, Materials Letters 61 (2007) 2127.
17. M. Thirumal, A. K. Ganguli, Progress in Crystal Growth and Characterization of Materials, 44 (2002) 147.
18. N. Setter, R. Waser, Electroceramic materials, Acta mater. 48 (2000) 151.
19. Jürgen Rödel, Alain B.N. Kounga, Marion Weissenberger-Eibl, Daniel Koch, Antje Bierwisch, Wolfgang Rossner, Michael J. Hoffmann, Robert Danzer, Gerhard Schneider, J. Eur. Ceram. Soc. 29 (2009) 1549.
20. C. B. Alcock, J. Alloys and Compounds, 197 (1993) 217.
21. R. Waser, U. Bo¨ttger, and S. Tiedke (eds.), Polar Oxides: Properties, Characterization, and Imaging. Wiley-VCH, Weinheim, 2005.
22. C. D. Chandler, C. Roger, and M. J. Hampden-Smith, Chem. Rev., 93 (1993) 1205.
23. N. Setter and R. Waser, Acta Mater., 48 (2000) 151.
24. M. Stech, P. Reynders, and J. Rodel, J. Am. Ceram. Soc., 83 (2000) 1889.
25. A. Arora, Adv. Eng. Mater., 6 (2004) 244.
26. M. Jansen, Angew. Chem. Int. Ed., 41 (2002) 3747.
27. D. Segal, J. Mater. Chem., 7 (1997) 1297.
28. R. W. Schwartz, T. Schneller, and R. Waser, C. R. Chimie, 7 (2004) 433.
29. B. L. Cushing, V. L. Kolesnichenko, and C. J. O'Connor, Chem. Rev., 104 (2004) 3893.
30. W. Heywang and H. Thomann, Annu. Rev. Mater. Sci., 14 (1984) 27.
31. C. B. Alcock, J. W. Fergus and Li Wang, Solid State electronics, 51 (1992) 291.

32. H. Iwahara, H. Uchida, K. Ono and K. Ogaki, J. Electrochem. Soc., 135 (1988) 529.
33. J.-P. Coutures, J.M. Badie, R. Berjoan, J. Coutures, R. Flammand and A. Rouanet, High Temp. Sci. 13 (1980) 331.
34. G.A. Smolensky, V.A. Isupov, A.I. Agranovskaya, N.N. krainic, Sov. Phys., Solid State 2 (1961) 2651
35. G.O. Jones, J. Kreisel, V. Jennings, M.A. Geday, P.A. Thomas, A. M. Glazer, Acta Crystallogr., B 58, (2002) 168.
36. H. Nagata, T. Shinya, Y Hiruma, T. Takenaka, Ceram. Trans. 167, (2005) 213.
37. G. Shirane, R. Newnham, R. Pepinsky, Phys. Rev. 96, (1954) 581.
38. K. Nakamura, T. Tokiwa, Y. Kawamura, J. Appl. Phys. 91 (2002) 9272
39. S. Wada, A. Seike, T. Tsurumi, Japanese J. Applied Physics 40, (2001) 5690.
40. V. M. Goldshmidt, Skr. Nor. Vidensk. Akad. Oslo, 2 (1926) 117.
41. Woodward D I, Reaney I M, Acta. Cryst.;B 61 (2005) 387.
42. Keer H V. Principles of the Solid State, New Age International (P) Ltd Publishers, 1993
43. Abdul Manan, Yaseen Iqbal, Mujeeb ur Rahman and Matiullah Khan, J Pak Mater Soc. 2 (2008) 10.
44. E.A. Wood, Acta Cryst. 4 (1951) 353.
45. M.L. Keith, R. Roy, Am. Miner. 39 (1954) 1.
46. J.M. Moreau, Mater. Res. Bull. 3 (1968) 427.
47. R.D. Shannon, Inorg. Chem. 6 (1967) 1474.
48. H. Muller-Buschbaum, C. Teske, Z. Anorg, Allg. Chem. 369 (1969) 249.
49. D. Babel, Structure and Bonding, vol. 3, Springer publisher, Berlin, 1967.
50. D. Babel, Z. Inorg. Allg. Chem. 369 (1969) 117.

51. A. Vedrine, J.P. Besse, G. Baud, M. Capestan, Rev. Chim. Miner. 7(1970) 593.
52. H.F. McMurdie, J. de Groot, M. Morris, H.E. Swanson, J. Res. Natl. Bur. Std. 73A (1969) 621.
53. A. S. Bhalla, R. Guo and R. Roy, Materials Research Innovations, 4 (2000) 3.
54. F.S. Galasso, Perovskites and High Tc Superconductors, Gordon and Breach Publisher, New York, 1990.
55. Z.L. Wang, Z.C. Kang, Functional and Smart Materials, Plenum Press, New York, 1998.
56. M.W. Lufaso, P.M. Woodward, Acta Cryst. B57 (2001) 726.
57. T. Scott Ercit, Michael A. Wise, Petr Cerny, American Mineralogist, 80 (1995) 613.
58. R.C. Pullar, K. Okeneme, N. McN. Alford, J. European Ceramic Society 23 (2003) 2479.
59. Gregory R. Lumpkin, Katherine L. Smith, Mark G. Blackford, J. Nuclear Materials, 289 (2001) 177.
60. Rolf L Romer, James E Wright, Geochimica et Cosmochimica Acta, 56 (1992) 2137.
61. Yi-Cheng Liou, Yueh-Lun Sung, Ceramics International 34 (2008) 371.
62. Supon Ananta, Rik Brydson and Noel W. Thomas, J. Eur. Ceram. Soc. 19 (1999) 355.
63. Yi-Cheng Liou, Jen-Hsien Chen, Ceramics International 30 (2004) 17.
64. Gregory R. Lumpkin, J. Nuclear Materials, 190 (1992) 302.
65. A. Chrysanthou, D. Macfarlane, O.S. Chinyamakobvu, J. Alloys and Compounds, 206 (1994) 77.
66. K.N. Singh, P.K. Bajpa, Physica B 405 (2010) 303.

67. R. de Almeida Silva, A. S. S. de Camargo, C. Cusatis, L. A. O. Nunes, J. P. Andreeta, J. Crystal Growth 262 (2004) 246.
68. Youhua Yu, Chude Feng, Chengen Li, Yi Yang, Wenlong Yao, Haixue Yan, Materials Letters, 51 (2001) 490.
69. P. Cerny, T.S. Ercit, Bull. Mineral. 108, (1989) 499.
70. P. Cerny, T.S. Ercit, M.A. Wise, Can. Mineral. 30, (1992) 587.
71. J.P. Mirao, M.O. Figueiredo, Chemical Geology 225 (2006) 402.
72. Yi-Cheng Liou, Yueh-Lun Sung, Ceramics International 34 (2008) 371.
73. M. Meada, T. Yamamura, T. Ikeda, Jpn. J. Appl. Phys. Supp. 26-2 (1987) 76.
74. H.J. Lee, I.T. Kim, K.S. Hong, Jpn. J. Appl. Phys. 36, part 2 (10A) (1997) 318.
75. H.J. Lee, K.J. Hong, S.J. Kim, I.T. Kim, Mater. Res. Bull. 32 (1997) 847.
76. C.S. Hsu, C.L. Huang, J.F. Tseng, C.Y. Huang, Mater. Res. Bull. 38 (2003) 1091.
77. M. S. Augsburger, J. C. Pedregosa, G. M. Sosa, R. C. Mercader, J. Solid State Chemistry 143 (1999) 219.
78. P. Cerny and T. S. Ercit, Bull. Mineral. 10 (1985) 499.
79. I. A. Komkov, Dokl. Akad. Nauk Earth Science Sect. 194 (1970) 434.
80. P. Cerny and A. C. Turnock, Can. Mineral. 10 (1971) 755.
81. T. S. Ercit, M. A. Wise, and P. Cerny, Am. Mineral. 80 (1995) 613.
82. M. Wenger, T. Armbruster, and C. A. Geiger, Am. Mineral. 76 (1991) 1897.
83. Matjaz Valant, Danilo Suvorov, Anton Meden, J. Am. Ceram. Soc., 82 (1999) 81.
84. Wang, C. L., Zhang, P. L., Zhong, W. L. and Zhao, H. S., J. Appl. Phys., 69 (1991) 2522.
85. Kus, C., Ptak, W. S. and Smiga, W., Ferroelectrics, 124 (1991) 249.
86. Dungan, R. H. and Golding, R. D., J. Am. Ceram. Soc., 47 (1964) 73.

87. Wang, C. L., Wang, Y. G., Zhang, P. L., Zhong, W. L. and Zhao, H. S., Solid State Comm., 85 (1993) 331.

88. Egerton, L. and Dillon, D. M, J. Am.Ceram. Soc., 42,(1959) 438.

89. Ahn, Z. S. and Schulze, W. A. J. Am. Ceram. Soc., 70 (1987) C18.

90. Kosec, M. and Kolar, D., Mat. Res. Bull., 10 (1975) 335.

91. Kus, C., Dambelkane, M. J. and Brante, I. V., Ferroelectrics, 81 (1988) 281.

92. Hardiman, B., Henson, R. M., Reeves, C. P. and Zeyfang, R. R., Ferroelectrics, 12 (1976) 157.

93. Henson, R. M., Zeyfang, R. R. and Kiehl, K. V., J. Am. Ceram. Soc., 60 (1977) 15.

94. A. Mergen, Ceramics International 35 (2009) 1151.

95. V.M. Vidojkovic, A.R. Brankovic, S.D. Milosevic, Mater. Lett. 31 (1997) 55.

96. V.V. Boldyrev, K. Tkacova, J. Mater. Synth. Process. 8 (2000) 121.

97. Y. Xia, Y. Zhou, M. Yoshio, J. Electrochem. Soc. 144 (1997) 2593.

98. R. Kanno, M. Yonemura, T. Kohigashi, Y. Kawamoto, M. Tabuchi, T. Kamiyama, J. Power Sour. 97 (2001) 423.

99. C. Wan, Y. Nuli, J. Zhuang, Z. Jiang, Mater. Lett. 56 (2002) 357.

100. Xian Ming Wu, Xin Hai Li, Zhuo Bing Xiao, Jianben Liu, Wen Bin Yan, Ming You Ma, Materials Chemistry and Physics 84 (2004) 182.

101. Li, W. and Currie, J. C., J. Electrochem. Soc., 144 (1997) 2773.

102. Chung-Hsin Lu, Hsien-Cheng Wang, J. Eur. Ceram. Soc. 24 (2004) 717.

103. Yen-Pei Fua, Cheng-Hsiung Lin, Yu-Hsiu Su, Jau-Ho Jean, She-Huang Wu, Ceramics International 30 (2004) 1953.

104. S.H. Ye, J.Y. Lv, X.P. Gao, F. Wu, D.Y. Song, Electrochimica Acta 49 (2004) 1623.

105. J.C. Hunter, J. Solid State Chem. 39 (1981) 142.

106. J.M. Tarascon, D. Guyomard, Electrochim. Acta 38 (1993) 1221.

107. T. Ohzuku, M. Kitagawa, T. Hirai, J. Electrochem. Soc. 137 (1990) 769.

108. J. Cho, G. Kim, Electrochem. Solid-State Lett. 2 (1999) 253.

109. K. Du , H. Zhang, J. Alloys and Compounds 352 (2003) 250.

110. S. Bach, M. Henry, N. Baffier, J. Livage, J. Solid State Chem. 88 (1990) 325.

111. J.P. Pereira-Ramos, J. Power Source 54 (1995) 120.

112. J.H. Choy, D.H. Kim, C.W. Kwon, S.J. Hwang, Y.I. Kim, J. Power Source 77 (1999) 1.

113. P. Barboux, J.M. Tarascon, F.K. Shokoohi, J. Solid State Chem. 94 (1991) 185.

114. W. Liu, G.C. Farrington, F. Chaput, B. Dunn, J. Electrochem. Soc. 143 (1996) 879.

115. L.I. Hill, R. Portal, A. Verbaere, D. Guyomard, Electrochem. Solid-State Lett. 4 (2001) 180.

116. L.I. Hill, R. Portal, A.L.G.L. Salle, A. Verbaere, D. Guyomard, Electrochem. Solid-State Lett. 4 (2001) 1.

117. J.D. Wright, N.A.J.M. Sommerdijk, Sol–Gel Materials Chemistry and Application, Gordon and Breach Science Publisher, Netherlands, 2001.

118. Zhan Jie Wang, Hirokazu Usuki, Toshihide Kumagai, Hiroyuki Kokawa, J. Crystal Growth 293 (2006) 68.

119. Heath, J.R.; LeGoues, F.K. Chem. Phys. Lett. 208 (1993) 263.

120. Li, Y.-D.; Duan, X.-F.; Qian, Y.-T.; Yang, L.; Ji, M.-R.; Li, C.-W. J. Am. Chem. Soc. 119 (1997) 7869.

121. Zhang, H.; Zuo, M.; Tan, S.; Li, G.; Zhang, S.; Hou, J. J. Phys. Chem. B.; 109 (2005) 10653.

122. Zhao, H.; Lei, M.; Yang, X.; Jian, J.; Chen, X., J. Am. Chem. Soc. 127 (2005) 15722

123. Zhibin Wu, Masahiro Yoshimura, Thin Solid Films 375 (2000) 46.

124. I. Porqueras, E. Bertran, Thin Solid Films 398 – 399 (2001) 41.

125. M.F. Al-Kuhaili, Vacuum 82 (2008) 623.

126. K. Byrappa and M. Yoshimura: Handbook of Hydrothermal Technology, Noyes Publications/William Andrew Publishing LLC, U.S.A, 2001.

127. Wojciech L. Suchanek and Richard E. Riman, Advances in Science and Technology, 45 (2006) 184.

128. R. Roy: J. Solid State Chem. 111 (1994) 11.

129. S. Sômiya: Hydrothermal Reactions for Materials Science and Engineering, Elsevier Science Publishers Ltd., U.K. 1989.

130. M. Yoshimura, W. L. Suchanek, and K. Byrappa, MRS Bull. 25 (2000) 17.

131. B. Gersten, M. Lencka and R. E. Riman: Chem. Mater. 14 (2002) 1950.

132. Jaffe H, J. Am. Ceram. Soc. 41 (1958) 494 .

133. R. C. Sherwood, J. P. Remeika , H. J. Williams, J. Appl. Phys., 30 (1959) 217

134. G.D. Raj, Solid State Physices, Ammol Publication, New Delhi(1995)

135. Uchino K, Amer. Ceram. Soc. Bull. 65 (1986) 647

136. Huybrechts B, Ishizaki K and Takata M, J. Mater. Sci. 30 (1995) 2463

137. Duran P and Moure C, J. Mater. Sci., 20 (1985) 827

138. Amin A, J. Amer. Ceram. Soc. 72 (1989) 369

139. Newnham R E, Rep. Prog. Phys. 52 (1989) 123

140. Uchino K, Mat. Res. Soc. Bull. XVIII, (1993) 42

141. J.F.Scott, L. Kammerdiner, M. Paris, S. Traynor, V. Ottenbacher, A. Shawabkeh and W.F. Oliver, J. Appl. Phy. 64 (1988) 1400.

142. J. F. Scott and C. A. Araujo, Science, 246 (1989) 140.

143. S.L. Swartz, IEEE Trans. Electrical Insulation, 25 (1990) 935

144. L.I. Maissel and R. Glang, Handbook of Thin film Technology, Mcgraw Hill, New York, 1970.

145. Xia, Y.; Yang, P.; Sun, Y.; Wu, Y.; Mayers, B.; Gates, B.; Yin, Y.; Kim, F.; Yan, H. Adv. Mater. 15 (2003) 353.

146. Wang, J.-G.; Tian, M.-L.; Mallouk, T. E.; Chan, M. H. W. Nano Lett., 4 (2004) 1313.

147. Cui, Y.; Duan, X.; Hu, J.; Lieber, C. M. J. Phys. Chem. B 104 (2000) 5213.

148. Gudiksen, M. S.; Lauhon, L. J.; Wang, J.; Smith, D. C.; Lieber, C. M, Nature, 415 (2002) 617.

149. Wang, Z. L. Materials Today, 7 (2004) 26.

150. Munnix, S.; Schmeits, M. Phys. Rev. B, 27 (1983) 7624.

151. Khalil El-Hami, Kazumi Matsushige, Ultramicroscopy 105 (2005) 143.

152. W. Lehmann, H. Skupin, C. Tolksdorf, E. Gebhard, R. Zentel, P. Kruger, M. Losche, F. Kremer, Nature 40 (2001) 447.

153. Q.M. Zhang, V. Bharti, X. Zhao, Science 280 (1998) 2101.

154. K. El-Hami, B. Gauthier, J. Appl. Phys. 77 (1995) 3987.

155. K. El-Hami, B. Gauthier, Sensors Actuators A, 64 (1998) 151.

156. T. Jaworek, D. Neher, G. Wegner, R.H. Wieringa, A.J. Schouten, Science, 279 (1998) 57

157. JingboZhao, Shaobo Qu, Hongliang Du, Yanju Zheng, Zhuo Xu, Materials Science and Engineering B 162 (2009) 9.

158. Rattikorn Yimnirun, Sylvie M. -L. Eury, V. Sundar, Paul J. Moses, Sei-Joo Jang, Robert E. Newnham, J. Eur. Ceram. Soc 19 (1999) 1269.

159. Sundar, V. and Newnham, R. E., Mater. Res. Bull, 31 (1996) 545.

160. Sundar, V. and Newnham, R. E., J. Science Letters, 13 (1994) 799.

161. Sundar, V., Li, J.-F., Viehland, D. and Newnham, R. E., Mater. Res. Bull., 31 (1996) 555.

162. J.-F. Vanhumbeeck, J. Proost, Electrochimica Acta 53 (2008) 6165.

163. Sylvie Eury, Rattikorn Yimnirun, V. Sundar, Paul J. Moses, Sei-Joo Jang, Robert E. Newnham, Materials Chemistry and Physics 61 (1999) 18.

164. Haertling G H, J. Am. Ceram. Soc. 82 (1999) 797.

165. J. F. Verweij, J. H. Klootw, Microelectronics Journal, 27 (1996) 611.

166. Kwan Chi Kao, Dielectric Phenomena in Solids, Elsevier Academic Press, 2004.

167. Yoon, D –S, and Roh J S, Critical Rev. Solid State Mat. Sci. 27 (2002) 143.

168. Maurice A K and Buchanan R C, Ferroelctrics 74 (1987) 61.

169. C.A-Paz de Araujo, J.D.Cuchiaro, L.D.Mcmillan, M.C.Scott, J.F.Scott, Nature 374 (2002) 627.

170. Werring W, Schnoller M and Wahl H, Ferroelctrics, 68 (1986) 145.

171. Heywang W, J. Mater. Sci., 6 (1971) 1214.

172. Park S M and Payne D A, Amer. Ceram. Soc. Bull. 58 (1979) 732.

173. A. D. Brailsford and E. M. Logothetis, Sensors and Actuators, 7 (1985) 39.

174. L. Yang, Z. Sui and C. Wang, Solid State Ionics, 50 (1992) 203.

175. E. M. Logothetis and R. E. Hetnick, Solid State Commun., 31 (1979) 167.

176. A. Baudrant, H. Vial and J. Daval, J. Crys. Growth, 43 (1978) 197.

177. C.E. Land, J. Sm. Ceram. Soc. 72 (1989) 2059.

178. Okazaki K and Hagata K, J. Am. Ceram. Soc. 56 (1973) 82.

179. Haertling G H, Photoelectronic effect in PLZT ceramics, Ceramic Transactions Vol. 14 Electrooptics and nonlinear optic materials, Edited by Bhalla A, Vigel E and Nair K, American Ceramic Society, Westervulle OH. (1990)

180. Cascales C and Zaldo C, J. Solid State Chem. 171 (2003) 262.

181. Mendez-B A, Rico M, Volkov V, Zaldo C and Cascales C, Mol. Phys. 101, (2003) 941.

182. Carlson D E and Wronski C R, Appl. Phys. Lett. 28 (1976) 671.

183. Alessandra Scognamiglio, Carlo Privato, Applied Energy 86 (2009) 1836.

184. Q. Qiao, K. Ma, Y.Q. Wang, G.C. Zhang, Z.R. Shi, G.H. Li, Applied Surface Science 256 (2010) 4656.

185. Thomas Surek, J. Crystal Growth 275 (2005) 292.

186. D.E. Carlson, C.R. Wronski, in: M.H. Brodsky (Ed.), Amorphous Silicon, Topics in Applied Physics, vol. 36, Springer, Berlin (1979).

187. J. Müller, B. Rech, J. Springer, M. Vanecek, Sol. Energy 77 (2004) 917.

188. H. Stiebig, F. Siebke, W. Beyer, C. Beneking, B. Rech, H. Wagner, Sol. Energy Mater. Sol. Cells 48 (1997) 351.

189. A. Shah, P. Torres, R. Tscharner, N. Wyrsch, H. Keppner, Science 285 (1999) 692.

190. W. Beyer, J. Hüpkes, H. Stiebig, Thin Solid Films 516 (2007) 147.

191. U. Kroll, J. Meier, S. Benagli, T. Roschek, J. Spitznagel, A. Huegli, D. Borello, M. Mohr, O. Kluth, D. Zimin, G. Monteduro, J. Springer, G. Androutsopoulos, C. Ellert,W. Stein, G. Buechel, A. Zindl, A. Buechel, D. Koch-Ospelt, Proc. 21st European Photovoltaic Solar Energy Conference, 4–8 Sept. 2006, Dresden (2006).

192. H. Stiebig, A. Kreisel, K.Winz, N. Schultz, C. Beneking, Th. Eickhoff, H. Wagner, M. Meer, Proceedings of the IEEE 1st World Conference on Photovoltaic Energy Conversion, 5–9 Dec. 1994, Hawaii, U.S.A., vol. 1, (1994) 603.

193. H. Stiebig, W. Reetz, C. Zahren, T. Repmann, B. Rech, Conference record of the 2006 IEEE 4th World Conference on Photovoltaic energy conversion, 7–12 May 2006, Hawaii, U.S.A., vol. 2, (2006) 1521.

194. Cheng-Liang Huang, Kuo-Hau Chiang, Mat. Sci. and Eng. A 474 (2008) 243.

195. H.C. Chang, C.C. Yeh, W.C. Ku, K.C. Tao, IEEE Trans. MTT-S Digest, WE2C (1996) 619.

196. T. Ishizaki, T. Uwano, IEEE Trans. MTT-S Digest, WEIC-4 (1994) 617.

197. H.J. Lee, K.S. Hong, S.J. Kim, Mater. Res. Bull. 32 (1997) 847.

198. M. Thirumala and A. K. Ganguli, Mater. Res. Bull. 36 (2001) 2421.

199. H.J. Lee, I.T. Kim, K.S. Hong, Jpn. J. Appl. Phys. 36 (1997) 1318

200. S. Mitsuda, H. Okano, S. Kobayashi, K. Prokes, J. Magn. Magn. Mater. 272 (2004) 993.

201. R.C. Pullar, K. Okeneme, N. McN. Alford, J. Eur. Ceram. Soc. 23 (2003) 2479.

202. V. Parvlescu, M. Ruwet, P. Grange, V.I. Parvlescu, Solid State Ionics, 101 (1997) 137.

203. S.C. Navale, A.B. Gaikwad, V. Ravi, Mater. Res. Bull. 41 (2006) 1353.

204. Cava R J, J. Am. Ceram. Soc. 83 (2000) 5.

205. Claes G. Granqvist, Renewable Energy, 5 (1994) 141.

206. M. Stanley Whittingham, Solid State Ionics 134 (2000) 169.

207. Yukio Sakabe, Current Opinion in Solid State and Materials Science, 2 (1997) 584.

208. Malti Goel, Ceramics International, 30 (2004) 1147.

209. Muralt. P, J. Am. Ceram. Soc. 91 (2008) 1385.

210. B. Su, D.H. Pearce, T.W. Button, J. Euro. Ceram. Soc. 21 (2001) 2005.

211. Frosch C J, Bell Lab. Rec., 32 (1954) 336.

212. Dienel H F, Bell Lab. Rec. 34 (1956) 407.

213. Matsuoka M, Masuyama T, and Iida Y, Jpn. J. Appl. Phys., 8 (1969) 1275.

214. Matsuoka M, Jpn. J. Appl. Phys. 10 (1971) 736.

Chapter 2

Experimental

The experimental process of synthesizing ternary oxides by novel hydroxide precursor method is discussed in this chapter. Also, the theory and experimental details of the techniques used in the present research work, viz. X-ray diffraction (XRD), Scanning Electron Microscopy (SEM), Energy Dispersive X-Ray Spectroscopy (EDX), Transmission Electron Microscopy (TEM), Impedance spectroscopy. This chapter also describes the thermal characterization techniques such as thermogravimetry analysis (TGA) and differential scanning calorimetery (DSC), which are used to study the thermal behaviour of the ternary oxides synthesised in the present study. This chapter also describes briefly about the mathematical techniques such as least squares method used for the lattice parameter refinement.

2.1 Introduction

There are different synthesis methods available for the synthesis of oxide ceramic materials [1-4]. The most common method is solid state method. In the present work, ternary oxide of niobates and tantales were syntheses by novel hydroxide precursor method. The synthesized compounds were (1) $LiNbO_3$, (2) $LiTaO_3$, (3) $NaNbO_3$, (4) $NaTaO_3$, (5) $SrNb_2O_6$, and (6) $SrTa_2O_6$. The other steps involved in making final products such as pelletizing, sintering, lapping, electroding and curing. The purity and source of the chemicals used for the synthesis are tabulated in Table 2.1.

The present study minimizes the sintering temperature and duration for cost reduction and time saving. Thermogravimetric analysis (TGA) is carried out to monitor the weight loss associated with the formation of niobates and tantalates from hydroxide precursor. The structures of these compounds were confirmed by XRD. Various other techniques such as SEM, TEM, EDX, DSC, Impedance spectra are used to characterise the samples prepared by hydroxide precursor method.

Table 2.1: Purity and source of the chemicals used.

Starting chemical used	Purity (%)	Source
Nb_2O_5	99.5	Aldrich, USA
Ta_2O_5	99.95	Spectrochem, India
Hydrofluoric acid	40%	Aldrich, USA
NaOH	97%	Loba Chemic, India
$Sr(OH)_2.8H_2O$	97.5%	Loba Chemic, India
LiOH	98%	Loba Chemic, India
Ammonia solution	30%	Merck, India

2.2 Synthesis of Niobates and Tantalates

2.2.1 Synthesis of Niobates by hydroxide precursor technique

Niobium (V) oxide is used as starting material for the synthesis of Niobates of Lithium, Sodium and Strontium. Niobium (V) oxide powders were dissolved in minium amount of hydrofluoric acid after heating on hot water bath at 90^0C for 10 h. To this NbF_5 solution, an excess of aqueous ammonia (30%) was added to precipitate niobium as hydroxide under basic conditions. The precipitate was then filtered and oven dried at 100^0 overnight. The required quantity of LiOH, NaOH and $Sr(OH)_2.2H_2O$ was separately mixed thoroughly with stoichiometric amount of $Nb(OH)_5$ and heated at various temperatures from 200 to 600^0C. XRD analysis were done at intermediate temperatures to confirm the formation of $LiNbO_3$, $NaNbO_3$ and $SrNb_2O_6$. These sintered pellet/pellets were characterized by various physico-chemical characterization techniques.

2.2.2 Synthesis of Tantalates by hydroxide precursor technique

Tantalum (V) oxide is used as starting material for the synthesis of tantalates of lithium, sodium and strontium. Tantalum (V) oxide powders were dissolved in minium amount of hydrofluoric acid after heating on hot water bath at 90^0C for 10 h. To this TaF_5 solution, an excess of aqueous ammonia (30%) was added to precipitate niobium as hydroxide under basic conditions. The precipitate was then filtered and oven dried at 100^0 overnight. The required quantity of LiOH, NaOH and $Sr(OH)_2.2H_2O$ was separately mixed thoroughly with stoichiometric amount of $Ta(OH)_5$ and heated at various temperatures from 200 to 600^0C. XRD analysis were done at intermediate temperatures to confirm the formation of $LiTaO_3$, $NaTaO_3$ and $SrTa_2O_6$. These sintered pellet/pellets were characterized by various physico-chemical characterization techniques.

2.3 X-ray Diffraction

X-rays are electromagnetic radiations with typical photon energies in the range of 100 eV-100 keV. These energetic X-rays can penetrate deep into the material and provide information about the structural arrangement of atoms and molecules [5]. X-rays are generated when a focused electron beam accelerated across a high voltage field bombards a stationary or rotating solid target. As electrons collide with atoms in the target and slow down, a continuous spectrum of X-rays are emitted, which are termed Bremsstrahlung radiation. The high-energy electrons also eject inner shell electrons in atoms through the ionization process. When a free electron fills the shell, an X-ray photon with energy characteristic of the target material is emitted. Common targets used in X-ray tubes include Cu and Mo, which emit 8 keV and 14 keV X-rays with corresponding wavelengths of 1.54 Å and 0.8 Å, respectively.

X-rays primarily interact with electrons in atoms, and during the coarse of interaction some photons from the incident beam will be deflected away from the direction where they originally travel, much like billiard balls bouncing off one anther. If the wavelength of these scattered X-rays does not change, the process is called elastic scattering (Thompson Scattering: only momentum has been transferred in the scattering process). The scattered X-rays carry information about the electron distribution in materials. However, in the inelastic scattering process (Compton Scattering), energy is transferred to the electrons and the scattered X-rays will have different wavelength than the incident X-rays. Diffracted waves from different atoms can interfere with each other and the resultant intensity distribution is strongly modulated by this interaction. If the atoms are arranged in a periodic fashion, as in crystals, the diffracted waves will consist of sharp interference maxima (peaks) with the same symmetry as in the distribution of atoms. X- ray diffraction is a well-known technique for structural identification of material and the determination of lattice parameters of material using Bragg’s law. For this it is practice to use analysis of X-ray diffraction pattern to identify phase and confirm formation of material. It is an indispensable tool for crystalline materials. X-ray diffraction experimental set up requires of an X-ray source, the sample under investigation and a detector to pick up X –rays. The radiation source may be monochromatic or polychromatic. Single crystal or polycrystalline samples can be used.

X-ray diffraction is useful nondestructive method of structure analysis. When an electromagnetic wave enters a crystal they get scattered by the electrons inside. But due to the periodicity associated with the arrangement of atoms of a crystal for certain angles of incidence (θ), there will be constructive interference between the different scatterers (plane of atoms). Nevertheless for most of the angles, destructive interferences leads to the cancellation of the differenced beam. With knowledge of the wavelength (λ) of the radiation and by measuring the angles at which the constructive interference occur (called Bragg angle θ_B). It is possible to understand the geometrical ordering of the atoms inside the crystal [6–9]. Measuring the diffraction pattern therefore allows one to deduce the distribution of atoms in a material. The peaks in an X-ray diffraction pattern are directly related to the atomic distances. Figure 2.1 shows incident X-ray beam interacting with the atoms in the two different planes.

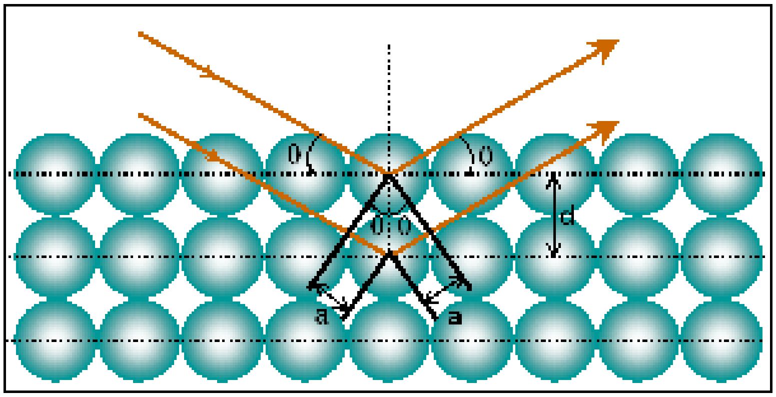

Figure 2.1. X-ray reflections from a crystal.

Consider parallel lattice planes spaced d apart. The radiation is incident in the plane of the paper. The path difference for rays reflected from adjacent planes is $2a = 2d\sin\theta$. Constructive interference of the radiation from successive planes occurs when $2d\sin\theta = n\lambda$, where $2\pi n$ is the difference in phase between reflections from successive planes. For a given set of lattice plane with an inter-plane distance of d, the condition for a diffraction (peak) to occur can be simply written as the Bragg's law given in *equation 2.1*:

$$2d\sin\theta = n\lambda \tag{2.1}$$

where, λ is the wavelength of the X-ray, θ the scattering angle, and n an integer representing the order of the diffraction peak. Whenever constructive interference occurs for a given set of plane, the angles of incidence θ is taken as θ_B of that planes. Bragg equation puts a limit to the maximum wavelength that can be used for diffraction as $\lambda \leq 2d$. This is the reason for using X-ray for crystal structure studies as the d values are typically in the range of few angstroms.

Conventionally, XRD has several limitations. A key disadvantage of XRD is that it is highly applicable to crystalline materials. Moreover, it is time-consuming and requires a large quantity of sample. Fortunately, synchrotron-based XRD is useful to circumvent these limitations. They offer exceptional resolution, even on very small samples containing only a few grains of a particular mineral.

The peak position is used for quantitative identification of phase, determination of unit cell parameters and symmetry of lattice. The profile or intensity is used for the structural refinement. The 'd' spacings are related to the lattice dimensions. Each reflection can be assigned by some hkl values that equate the interplaner spacing (d) with a unit cell parameter (a). The structure, crystallinity and the particle size are often measured using XRD [5].

Powder X-ray diffraction (XRD) patterns were recorded on a Philips PW 1710 diffractometer. The X-ray source of this diffractometer emits CuK$_\alpha$ radiation with wavelength of 1.5418 Å. The diffractometer is calibrated with reference to standard oriented Si wafer. For usual structural phase analysis a scan rate of 4 ° per min was used.

2.3.1 Crystallite size determination

A perfect crystal would extend in all directions to infinity, so we can say that no crystal is perfect due to its limited sizes. Such a deviation from perfect crystallinity will lead to broadening of the diffraction peak. However, this type of peak broadening is negligible when the crystallite size is larger than 200 nm. Crystallite size is a measure of the size of a coherently diffracting domain. Due to the presence of polycrystalline diffracting domain aggregates, crystallite size may not be the same thing as particle size.

Scherrer (1918) first observed that small crystallite size could give rise to peak broadening. He derived a well-known equation for relating the crystallite size to the peak width, which is called the Scherrer formula [10,11] given in *equation 2.2*

:

$$t = \frac{K\lambda}{\beta \cos\theta} \qquad (2.2)$$

where t is the averaged dimension of crystallites; K is the Scherrer constant, somewhat arbitrary value that falls in the range 0.87-1.0 (it is usually assumed to be 1); λ is the wavelength of X-ray radiation; and β is the integral breadth of a reflection (in radians 2θ) located at 2θ, i.e. full width at half maximum (FWHM).

The Scherrer equation is limited to nano-scale particles. It is not applicable to grains larger than about 0.1 μm, which precludes those observed in most metallographic and ceramographic microstructures. It is important to realize that the Scherrer formula provides a lower bound on the particle size. The reason for this is that a variety of factors can contribute to the width of a diffraction peak; besides crystallite size, the most important of these are usually inhomogeneous strain and instrumental effects. If all of these other contributions to the peak width were zero, then the peak width would be determined solely by the crystallite size and the Scherrer formula would apply. If the other contributions to the width are non-zero, then the crystallite size can be larger than that predicted by the Scherrer formula, with the "extra" peak width coming from the other factors.

2.3 Thermal Analysis

Thermal analysis (TA) has been defined as “a group of techniques in which a physical property of a substance and / or its reaction products is measured as a function of temperature while the substance is subjected to a controlled temperature programme” [12–14]. In brief, the measurement of change in any property as a material is being heated (or cooled) at a constant rate is called thermal analysis. Since all materials respond to heat in some way, TA has been applied to almost every field of science, with a strong emphasis on solving problems in materials science and engineering, as well as fundamental chemical investigations. TA is applicable whenever the primary interest is in determining the effect of heat upon a material, but the techniques can also be used as a means of probing a system to obtain other types of information, such as composition.

It is well recognized that the thermoanalytical techniques play an important role in the solution of a variety of problems in the ceramics. The utility of DSC and and TG has been documented in a number of studies, which concern electroceramics.

They are useful for investigation of phase transitions, problems concerning the evaporation of volatile components from heavy fractions, determination of the thermal stability, study of the pyrolysis and kinetics. The thermal analysis techniques as thermal gravimetric analysis (TGA) and Differential Scanning Calorimetry (DSC) provide a powerful tool to study the behaviour of ceramic materials during their thermal degradation.

2.4.1 Thermogravimetry Analysis

Thermogravimetry analysis (TGA) is used to measure variations in mass as a function of temperature (or time). TGA as a quick method of analysis, which was proved to be useful in distinguishing between ceramics and also provided significant information on the relative composition of these products, however TGA will not provide information about the elements present in the composition. This is a technique in which the change in weight of a substance with temperature over a period of time is followed. The temperature is increased at a constant rate for a known initial weight of the substance and changes in weight are accurately recorded at different times [15-17]. When the weights are plotted against temperature a curve characteristic of the substance studied is obtained. Such a curve is called a thermogravimetric curve or a thermogram. The schematic instrumentation of TGA setup is given in figure 2.2 Small sample weight and small uniform particle size are generally recommended to facilitate diffusion of gaseous products through the solid sample. Using small sample weight eliminates the existence of temperature gradient throughout the sample. This technique provides information in a wide variety of chemical investigations. Some of these are thermal stability, decomposition, vaporization, chemisorption, and purity check.

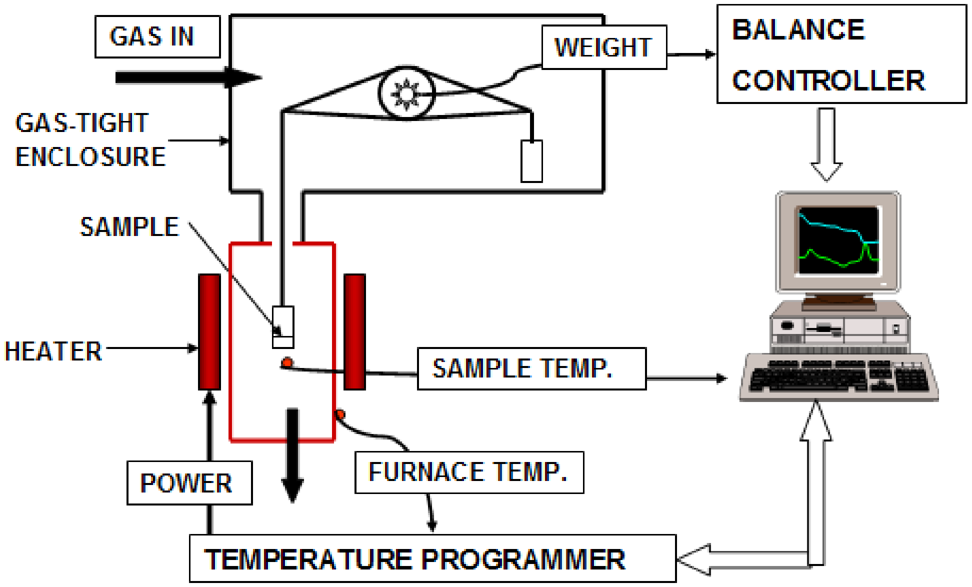

Figure 2.2 Instrumentation of TGA

2.4.2 Differential Scanning Calorimetry (DSC)

A differential scanning calorimeter (DSC) measures the heat transferred to or from a sample at constant pressure during a physical or chemical change. The peaks in a DSC thermogram represent the amount of electrical energy supplied to the system to keep the sample and reference at the same temperature. The area under the DSC peaks will be proportional to the enthalpy change of the reaction

The term “differential” refers to the fact that the behaviour of the sample is compared to that of a reference material that does not undergo a physical or chemical change during the analysis. The term “scanning” refers to the fact that the temperatures of the sample and reference material are increased or scanned systematically during the analysis.

A DSC consists of two small compartments that are heated electrically at constant rate. The temperature T at time t during a linear scan is

$$T = T_0 + \alpha t \tag{2.3}$$

where T_0 is the initial temperature

α is the temperature scan rate (in Kelvin per second Ks^{-1})

A computer controls the electrical power output in order to maintain the same temperature in the sample and reference compartments throughout the analysis and measures the difference in the amount of heat required to increase the temperature of a sample and reference as a function of temperature [18-21]. A schematic DSC instrumentation setup is given in figure 2.3. With a DSC, enthalpy changes may be determined in samples of masses a low as 0.5mg, which is a significant advantage over bomb or flame calorimeters, which require several grams of material. DSC is often used for the study of equilibria, heat capacities and kinetics of chemical reactions in the absence of phase change.

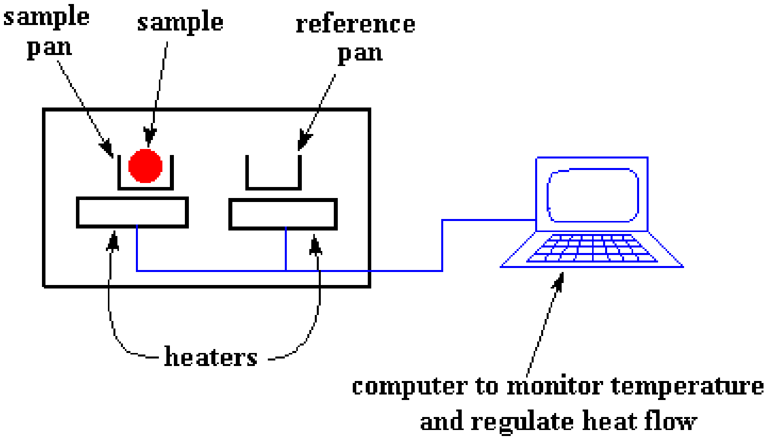

Figure 2.3. Schematic representation of DSC setup

2.4.3 Estimation of Activation Energy

Differential scanning calorimetry data is very useful in estimating the activation energy [22–26]. The activation energy is the threshold energy, or the energy that must be overcome in order for a chemical reaction to occur. Activation energy may otherwise be denoted as the minimum energy necessary for a specific chemical reaction to occur. The energy profile of a chemical reaction and reaction co-ordinates are illustrated in figure 4. In most of kinetic equations it is assumed that if close the value of correlation coefficient (r) is to the unity, the better would be the fit of the linear regression with respect to the results [25].

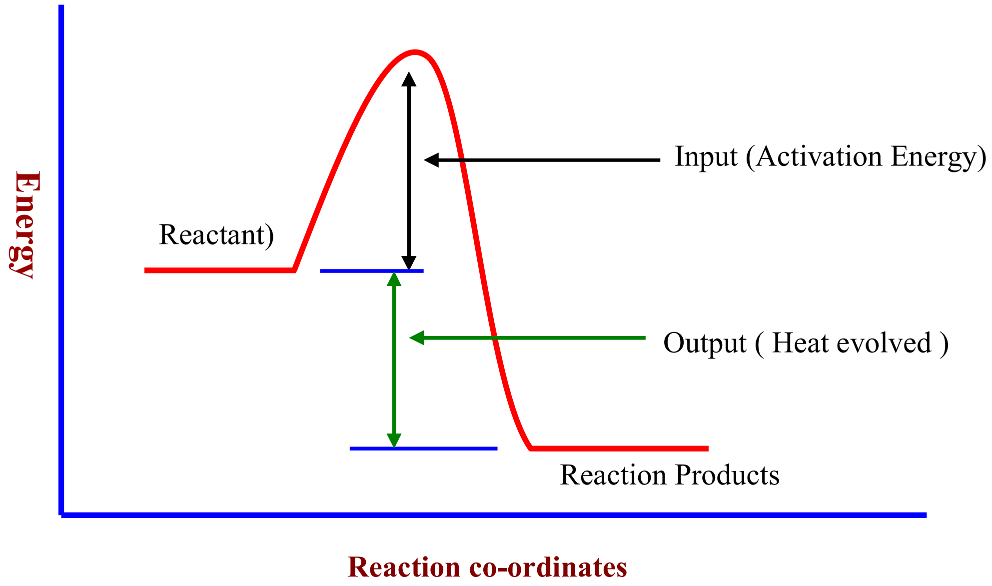

Figure 2.4 Energy profile of a chemical reaction and reaction co-ordinate

A popular method is for estimating activation energy is Kissinger method. It is based on the fact that shifts in the temperature (T_p) of the DSC peak, i.e. corresponding to the maximum rate of conversion.

$$\left[\frac{d}{dt}\left(\frac{d\alpha}{dt}\right)\right]_{T=T_p} = 0 \qquad (2.4)$$

According to Kissinger, appropriate approximations lead to the simple equation (2.5) derived from equation (2.4)

$$\ln\left(\frac{\beta}{T_p^2}\right) = -\frac{E}{RT_p} + Cte \tag{2.5}$$

Where β represents the heating rate associated with a linear rise in temperature, T = βt + T_0. The plotting of $\ln(\beta/T_p^2)$ in function of $1/T_p$ should result in a straight line, of slope –E/R. The schematic flow chart for the estimation of activation energy using Kissinger method is depicted in figure 2.5.

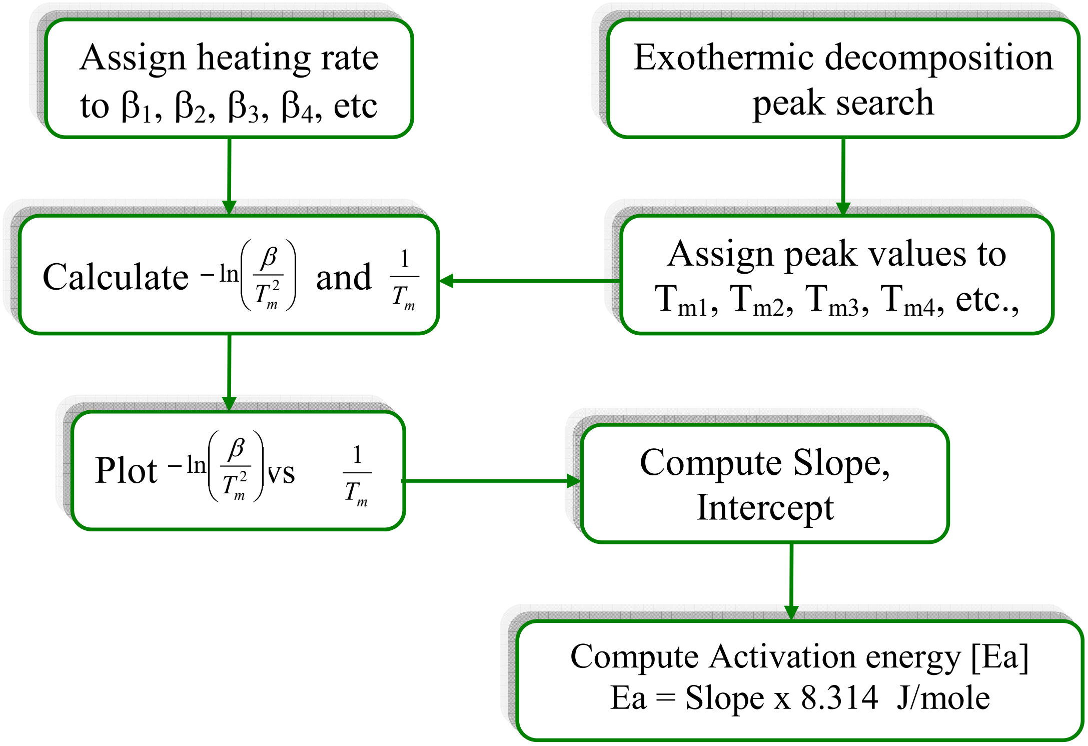

Figure 2.5. Flow chart for the estimation of activation energy using Kissinger method.

2.4.4 Least Squares method

The least squares method—a very popular technique—is used to compute estimations of parameters and to fit data. It is one of the oldest techniques of modern statistics as it was first published in 1805 by the French mathematician Legendre. Nowadays, the least square method is widely used to find or estimate the numerical values of the parameters to fit a function to a set of data and to characterize the statistical properties of estimates. The method of least squares assumes that the best-fit curve of a given type is the curve that has the minimal sum of the deviations squared (least square error) from a given set of data. Let $x_1, x_2, ..., x_n$ are the values of the independent variable X and $y_1, y_2, ..., y_n$ are the values of the dependent variable Y. The scatter diagram for the given data is shown below

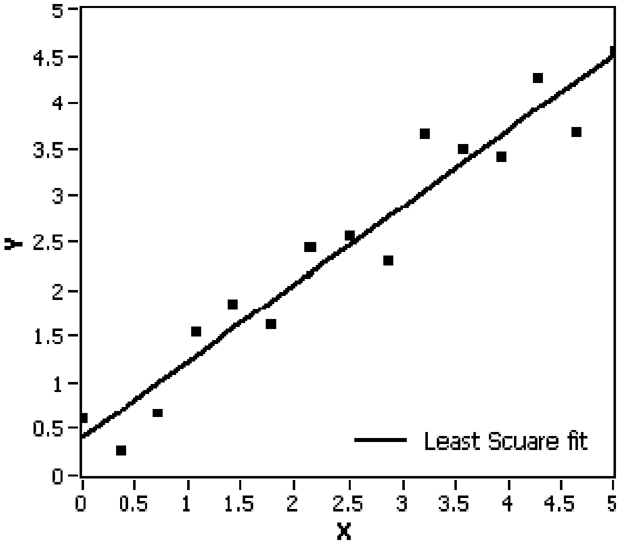

Figure 2.6. Scattered data points and Least square fit

In general curve fitting involves the determination of a continuous function

$$y = f(x) \tag{2.6}$$

which results in the most reasonable a best fit for the given set of values of (x_1,y_1), (x_2,y_2), ... (x_n,y_n). The computational techniques for linear least squares problems also make use of orthogonal matrix factorizations. The working procedure of least squares method consists of following steps to fit the least square equation

$$y = a + bx \tag{2.7}$$

(i) Form the normal equations

$$\Sigma y = na + b\Sigma x \tag{2.8}$$

$$\Sigma xy = a\Sigma x + b\Sigma x^2 \tag{2.9}$$

'n' be number of elements (data), i.e., no of x,y data available for summation (Σ)

(ii) Solve the above equations (2.8), (2.9) as simultaneous equations for a, b

(iii) Substitute the values of a, b in y = a + bx, which is the required straight line of best fit. The equations (2.8) & (2.9) can be solved using matrix method as below

$$\begin{bmatrix} n & \sum x \\ \sum x & \sum x^2 \end{bmatrix} \begin{bmatrix} a \\ b \end{bmatrix} = \begin{bmatrix} \sum y \\ \sum xy \end{bmatrix}$$

$$A\,X = B \tag{2.10}$$

If A is a non-singular matrix i.e., $|A| \neq 0$, then its inverse A^{-1} exists. Multiplying both sides of (2.10) by A^{-1}, we obtain

$$A^{-1}AX = A^{-1}B$$

$$IX = A^{-1}B$$

$$X = A^{-1}B \tag{2.11}$$

The left hand side of (6) is a column matrix and so also is right hand side. Equating the corresponding elements, we get the values of a and b. On substituting the values of a, b in equation (2.7), straight line equation is obtained, where 'a' is the intercept and 'b' is the slope of the straight line.

In this work, least square method is used for the estimation of activation energy for the computed data on $-\ln\left(\frac{\beta}{T_m^2}\right)$ vs $\frac{1}{T_m}$.

2.5 Energy Dispersive X-Ray Analysis

Energy Dispersive X-ray (EDX) analysis is a valuable tool for qualitative and quantitative element analysis. This method allows a fast and non-destructive chemical analysis with a spatial resolution in the micrometer regime [27]. It is based on the spectral analysis of the characteristic X-ray radiation emitted from the sample atoms upon irradiation by the focussed electron beam of a SEM. EDX Analysis stands for Energy Dispersive X-ray analysis. It is sometimes referred to also as EDS or EDAX analysis. It is a technique used for identifying the elemental composition of the specimen, or an area of interest thereof. It is mainly used for spatially resolved chemical analysis of bulk and thin film samples [28].

During EDX Analysis, the specimen is bombarded with an electron beam inside the scanning electron microscope. The bombarding electrons collide with the specimen atoms' own electrons, knocking some of them off in the process. A position vacated by an ejected inner shell electron is eventually occupied by a higher-energy electron from an outer shell. To be able to do so, however, the transferring outer electron must give up some of its energy by emitting an X-ray. The amount of energy released by the transferring electron depends on which shell it is transferring from, as well as which shell it is transferring to. Furthermore, the atom of every element releases X-rays with unique amounts of energy during the transferring process. Thus, by measuring the amounts of energy present in the X-rays being released by a specimen during electron beam bombardment, the identity of the atom from which the X-ray was emitted can be established. The EDX spectrum is just a plot of how frequently an X-ray is received for each energy level. An EDX spectrum normally displays peaks corresponding to the energy levels for which the most X-rays had been received. Each of these peaks are unique to an atom, and therefore corresponds to a single element. The higher a peak in a spectrum, the more concentrated the element is in the specimen.

An EDX spectrum plot not only identifies the element corresponding to each of its peaks, but the type of X-ray to which it corresponds as well. For example, a peak corresponding to the amount of energy possessed by X-rays emitted by an electron in the L-shell going down to the K-shell is identified as a K-Alpha peak. The peak corresponding to X-rays emitted by M-shell electrons going to the K-shell is identified as a K-Beta peak as illustrated in figure 2.7.

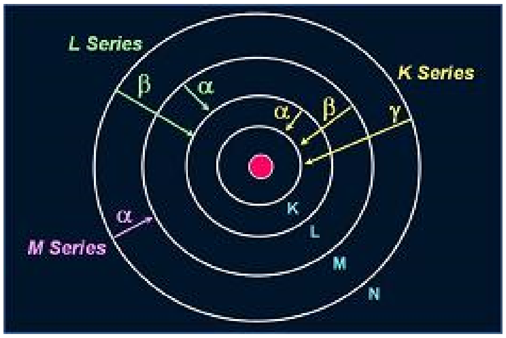

Figure 2.7. EDX spectrum shell identification schematic diagram

Atoms of different elements emit x-rays with different energies. However, no two elements emit an x-ray photon with exactly the same energy. It is so because the binding energy of the electrons is different for each element. This is a non-destructive analysis technique and the elements and their concentration in the sample can be determined reasonably accurately. EDX system doesn’t give any information about the chemical bonds in a compound. Since SEM has an in built source of electrons and a stage for handling the samples, EDX systems are mostly available as an attachment to a scanning electron microscope.

In this work, JEOL JED-2300 Energy dispersive X-ray analysis Station is used for the elemental analysis of sintered samples of Niobates and Tantalates. EDAX detector is operated at liquid nitrogen temperatures during measurements.

2.6 Surface Morphology

2.6.1 Scanning Electron Microscopy

In a typical scanning electron Conventional light microscope (SEM), electrons are thermionically emitted from a tungsten or lanthanum hexaboride (LaB_6) cathode, which fly towards an anode; alternatively electrons can be emitted via field emission (FE) [29]. Tungsten is used because it has the highest melting point and lowest vapour pressure of all metals, thereby allowing it to be heated for electron emission. The electron beam, which typically has an energy ranging from a few hundred eV to 50 keV, is focused by one or two condenser lenses into a beam with a very fine focal spot sized 1 nm to 5 nm. The beam passes through pairs of scanning coils in the objective lens, which deflect the beam in a raster fashion over a rectangular area of the sample surface. As the primary electrons strike the surface they are inelastically scattered by atoms in the sample. Through these scattering events, the primary electron beam effectively spreads and fills a teardrop-shaped volume, known as the interaction volume, extending about less than 100 nm to 5 µm depths into the surface. Interactions in this region lead to the subsequent emission of electrons which are then detected to produce an image. The most common imaging mode monitors low energy (<50 eV) secondary electrons. Due to their low energy, these electrons originate within a few nanometer from the surface. The electrons are detected by a scintillatorphotomultiplier device and the resulting signal is rendered into a two-dimensional intensity distribution that can be viewed and saved as a Digital image. The scanning electron microscope (SEM) is an incredible tool for seeing the unseen worlds of micro space. Conventional light microscopes use a series of glass lenses to bend light waves and create a magnified image. The scanning electron microscope creates the magnified images by using electrons instead of light waves [30–32]. Fig 2.8 shows the schematic block diagram of scanning electron microscope.

In this work, the microstructural features of samples were obtained using a scanning electron microscope (Leica Cambridge 440). The sintered pellets were fractured to expose the inner portion and mounted on specimen mounting stub. Silver paste was used to stick the sample to the stub and a thin layer of gold was coated on surface of sample using an ion beam sputtering system (Poloran equipment ltd., SEM coating unit E5000) to avoid charging the specimen.

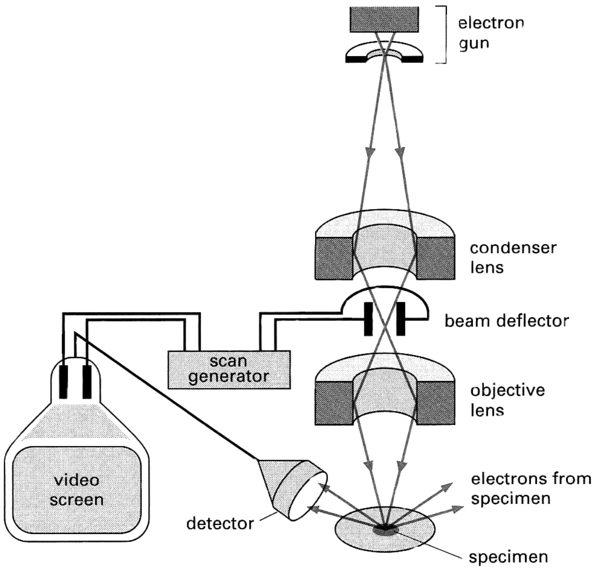

Figure 2.8 Schematic block diagram of Scanning Electron Microscope

2.6.2 Transmission Electron Microscopy

In transmission electron microscopy (TEM), a thin specimen is illuminated with electrons in which the electron intensity is uniform over the illuminated area [33]. As electrons travel through the specimen, they are either scattered by a variety of processes or they may remain unaffected by the specimen. The net result is that a non-uniform distribution of electrons emerges from the exit surface of the specimen that contains all the structural and chemical information about the specimen. Electron microscope is constructed to display this non-uniform distribution of electrons in two different ways. Based on similar principles of the conventional light microscope, the transmission electron microscope (TEM) is capable of magnification of 100,000 times an extreme resolution, far beyond the possibilities afforded by visible light. Unlike the scanning electron microscope, which uses reflected electrons, the TEM uses electrons passing through a very thin slice of the specimen. Magnetic lenses focus the electron beam and project the highly magnified image onto a phosphor screen or special photographic film. TEM is especially useful in studying the structure of cells, and in crystallography. TEM uses the electrons as light source and their much lower wavelength makes it possible to get a resolution a thousand times better than with a light microscope [34]. The possibility for high magnifications has made the TEM a valuable tool in medical, biological and materials research [33–38].

Angular distribution of scattering can be viewed in the form of scattering patterns, usually called diffraction patterns, commonly referred to as selected area electron diffraction (SAED). Spatial distribution of scattering can be observed as contrast in images of the specimen. The advantage of this arrangement is the possibility of directly viewing the area from which the diffraction pattern arises. Further, Kikuchi patterns obtained by inelastic scattering of electrons is also very useful for understanding the crystallographic orientation as these are rigidly attached to a crystal plane and therefore move in the diffraction pattern when the crystal is tilted.

Many materials require extensive sample preparation and thinning procedures to produce a sample thin enough to be electron transparent, and changes in the structure may be caused during this process. Also the field of view is relatively small, raising the possibility that the region analysed may not be characteristic of the whole sample. Also there is potential that the sample may be damaged by the electron beam, particularly in the case of biological materials. Despite these limitations, TEM has been the technique of choice due to atomic-level resolution leading direct visual information of size, shape, dispersion and structure.

The samples for TEM were prepared by drop coating on to a carbon coated copper TEM grid. TEM micrographs and selected area diffraction patterns were obtained on a JEOL, 1200 EX instrument operated at an accelerating voltage of 100 kV

2.7 Impedance Spectroscopy

Impedance spectroscopy is becoming a popular analytical tool in materials research and development because it involves a relatively simple electrical measurement that can readily be automated and whose results may often be correlated with many complex materials variables: from mass transport, rates of chemical reactions, corrosion and dielectric properties, to defects, microstructure and compositional influences on the conductance of solids. IS can predict aspects of the performance of chemical sensor and fuel cells, and it has been used extensively to investigate membrane behavior in living cells. It is useful as an empirical quality control procedure, yet it can contribute to the interpretation of fundamental electrochemical and electronic processes.

Impedance is a more general concept than resistance because it takes phase differences into account, and it has become a fundamental and essential concept in electrical engineering. Impedance spectroscopy (IS) is a relatively new and powerful method of characterizing many of the electrical properties of materials and their interfaces with electronically conducting electrodes [39, 40]. Impedance spectroscopy is a valuable technique used for the characterization of inhomogeneous (insulating, electrical and magnetic) materials exhibiting granular structures. To differentiate between the varying contributions from grains and grain boundaries, intergranular layers and electrode interface, ac impedance spectra are often used with great success [41 – 43]. Most common method of impedance analysis is to measure impedance directly in the frequency domain by applying a single frequency voltage to the interface and measuring the phase shift and amplitude (real and imaginary parts) of the resulting current at that frequency. This way the measurements was done in a large range of frequency (few Hz to Giga Hz). The concept of electrical impedance was first introduced by Oliver Heaviside in the 1980s and was soon after developed in terms of vector diagrams and complex representation by A.E.Kennelly and especially C.P. Steinmetz.

Impedance is a more general concept than resistance because it takes phase differences into account, and it has become a fundamental and essential concept in electrical engineering. In the impedance spectroscopy, a time dependent voltage $E(\omega) = \delta E \, \text{Sin} (\omega t)$ is applied across the ceramic sample. A sinusoidal current with the same angular frequency will then flow through the sample and the response is characterizes by complex impedance Z. Z will be a function of ω. The real and imaginary parts of their complex impedance Z (Z' and Z") can be recorded for a large range of frequencies using the impedance analyzer. When the data points are plotted in complex impedance plane (Z' and Z"), are usually along the arc of circles. An equivalent circuit based on a serial assembly of parallel resistances and capacitances can be then used to simulate the electrical behavior. Usually the values of the resistance and capacitance of each cell and therefore each arc can be assigned to a specific part of the ceramic sample: the grain interiors, grain boundaries, metal-ceramic interfaces etc. The chord of each arc of a circle is the resistance of that individual part of the ceramic. The time constant, Γ corresponding to each arc obeys the relation $\omega^*\Gamma = 1$, where ω^* corresponds to the top of the semicircular arc. The time constant corresponding to grains, grain boundaries, interfaces differ by one order of magnitude and hence well distinguished arcs corresponding to each part of the ceramic are usually obtained. A careful selection of the electrode is necessary to avoid the presence of an arc of a circle in the impedance spectrum, which can interfere with the grain-grain-boundary contributions.

For ac impedance measurements, sintered pellets of 10 mm diameter and 1 mm thickness were used after applying silver paste as top and bottom electrode. The impedance measurements were made with Impedance/gain-phase analyzer (Solartron model S1 1260 coupled with Solartron 1294 Impedance Interface) using frequency ranging from 0.1 Hz to 1 MHz with an ac amplitude voltage of 1 V. The dielectric loss spectrum is recorded using Hwelett Packard 4194 A, Impedance / Gain-Phase analyzer.

2.9 Reference:

1. Weiwei Hu, Yan Chen, Hongming Yuan, Ganghua Zhang, Guanghua Li, Guangsheng Pang, Shouhua Feng, J. Solid State Chemistry 183 (2010) 1582.
2. H. Zhang, X. Li, S. Li, Y. Xin and M. Zhao, NanoStructured Materials, 4 (1994) 285.
3. V.R. Choudhary, S. Banerjee, B.S. Uphade, Applied Catalysis A: General 197 (2000) 183.
4. Rao C N R, Chemical approaches to the synthesis of inorganic materials, Wiley Eastern Ltd. New Delhi, 1994.
5. B. D Cullity, Stock, S. R. Elements of X-ray Diffraction, 3rd Ed., Prentice Hall Pub. New Jersey, 2001.
6. C. Suryanarayana and M.Grant Norton, X-ray Diffraction, A Practical Approach, Plenum Press, New York, 1998.
7. R. Jenkins & R.L. Snyder, Introduction to X-ray Powder Diffractometry, John Wiley & Sons Inc., 1996.
8. H.P. Klug & L.E. Alexander, X-Ray Diffraction Procedures, 2nd Ed., John Wiley & Sons Inc., 1974.
9. B.E. Warren, X-Ray Diffraction, Addison-Wesley Publishing Co., 1969.
10. Klug H P and Alexander L E, *X-ray diffraction procedures*, John Wiley and sons New York, 1954.
11. A. L. Patterson, Phys. Rev. 56 (1939) 978.
12. J. O. Hill (ed.): "For Better Thermal Analysis and Calorimetry", 3rd Edition., International Confederation for Thermal Analysis and Calorimetry, 1991.
13. Helmut Günzler and Alex Williams, "Handbook of Analytical Techniques – Volume II", Wiley – Vch Publisher, Germany, 2002.

14. J. L. MacNaughton, Colin Trevor Mortimer, Differential scanning calorimetry, The Perkin-Elmer Corporation, 1976.
15. D. M. Price, D. J. Hourston & F. Dumont, “Thermogravimetry of Polymers”, R. A. Meyers (Ed.), Encyclopedia of Analytical Chemistry, John Wiley & Sons Ltd., Chichester (2000) 8094.
16. G. R. Heal,”Thermogravimetry & Derivative Thermogravimetry”, in P.J. Haines (ed.) Principles of Thermal Analysis & Calorimetry, ch. 4, Royal Society of Chemistry, Cambridge (2002) 10.
17. C. M. Earnest (Ed.), Compostional Analysis by Thermogravimetry, ASTM STP 97, American Society for Testing and Materials, 1988.
18. Günther Höhne, W. Hemminger, H.-J. Flammersheim, Differential scanning calorimetry, Springer-Verlag Berlin Heidelberg, 2003.
19. Mike Reading, Douglas J. Hourston, Modulated temperature differential scanning calorimetry, Springer, 2006.
20. Peter J. Haines, Principles of thermal analysis and calorimetry, The Royal Society of Chemistry, 2002.
21. Boris V. L'Vov, Thermal decomposition of solids and melts, Springer Publisher, Netherlands, 2007 .
22. R.N. Rogers and E.D. Morris, Analytical Chemistry, 30 (1966) 412.
23. Homer E. Kissinger, J. Research of the National Bureau of Standards, 57 (1956) 217.
24. S.Vyazokin, C.A.Wight, Annu. Rev. Phys. Chem. 48 (1997) 125.
25. F.Rodante, S. Vecchio, J Therm Anal Calorim, 63 (2001) 433.

26. Nobuyoshi Koga, "Reaction Kinetics in the Solid State", in "Comprehensive Handbook of Calorimetry & Thermal Analysis", edited by Michio Sorai, John Wiley & Sons, Ltd., 2004.
27. Anthony J. Garratt-Reed, David C. Bell , Energy-dispersive X-ray analysis in the electron microscope, BIOS Scientific Publishers Limited, Oxford, UK, 2003
28. Charles E. Lyman, Scanning electron microscopy, X-ray microanalysis, and analytical electron microscopy, Plenum Press, NewYork, 1990
29. Goldstein, J. I. et al., Scanning electron microscopy and X-ray microananalysis, Kluwer Academic/ Plenum Publishers, New York, 3rd ed., 2003.
30. Patrick Echlin, Handbook of sample preparation for scanning electron microscopy and x-ray, Springer Publishers, NewYork 2009.
31. Ian M. Watt, The principles and practice of electron microscopy, Cambridge University Press, UK, 1997.
32. Ludwig Reimer, Scanning electron microscopy: physics of image formation and microanalysis, Springer-Verlag, Berlin, Germany, 1998.
33. Williams, D. B.; Carter, C. B. Transmission Electron Microscopy, Vol I-III, Kluwer Academic, Plenum Publishers, 1996.
34. Fryer J R, Chemical application of Transmission Electron Microscopy, Academic press, San Diego, 1979.
35. Ludwig Reimer, Helmut Kohl, Transmission electron microscopy: physics of image formation, Springer Publisher, New York, 2008.
36. Marc De Graef, Introduction to conventional transmission electron microscopy, Cambridge University Press, 2003.
37. David Bernard Williams, C. Barry Carter, Transmission electron microscopy: a textbook for materials science, Springer Publisher, New York, 2009.

38. R. F. Egerton, Physical principles of electron microscopy: an introduction to TEM, SEM, and AEM, Springer Publisher, New York, 2005.
39. J. Ross Macdonald, Impedance Spectroscopy – Emphasizing solid materials and systems, Wiley Interscience Publisher, 1987.
40. Agilent Technologies Impedance Measurement Handbook, Agilent Technologies Co. Ltd, 2006.
41. Evgenij Barsoukov, James Ross Macdonald, Impedance spectroscopy: theory, experiment, and applications John Wiley & Sons, New Jersey, 2005.
42. Mark E. Orazem, Bernard Tribollet, Electrochemical impedance spectroscopy, John Wiley & Sons Inc, New Jersey, 2008.
43. John R. Scully, David C. Silverman, Martin W. Kendig, Electrochemical impedance: analysis and interpretation, American Society for testing and Materials, Philadelphia, 1993.

Chapter 3

Synthesis and Characterization of Lithium Niobate and Tantalate

This chapter comprised about the experimental synthesis procedures for Lithium Niobate and Lithium Tantalate followed by characterization of these two compounds. The characterization part of this chapter is divided into two vis for $LiNbO_3$ and $LiTaO_3$. Both the compounds were characterized for X-ray powder diffraction (XRD), Energy Dispersive X-Ray Analysis (EDAX), Transmission Electron Microscopy, Thermogravimetry Analysis (TGA), Differential Scanning Calorimetery (DSC) and Impedance Spectroscopy. Nyquist plot as well as Bode plot were constructed from Impedance data. Activation energy for the formation of $LiNbO_3$ and $LiTaO_3$ were estimated from DSC data using Kissinger method.

3.1 Introduction

Lithium Niobate ($LiNbO_3$) is an excellent material for electro-optic [1] and nonlinear-optic devices [2] such as optical waveguides [3–6], modulators, optical switches for gigahertz frequencies, surface acoustic wave devices and holographic memory [7] using photorefractive effect. Because of its good piezoelectric properties it's potential application increased greatly. Several methods for preparing $LiNbO_3$ been reported, including RF magnetron sputtering [3], pulsed laser deposition [8–10], chemical vapor deposition [4], liquid phase epitaxy, [5, 11] and the sol-gel method [12–27]. A new novel hydroxide precursor synthesis process was developed in this work and described in next section 3.2.1.

Lithium tantalite ($LiTaO_3$) exhibits unique electrooptical, acoustic, piezoelectric, pyroelectric and non-linear optical properties combined with good mechanical and chemical stability and wide transparency range and high optical damage threshold making it a suitable material for applications in electro-optical modulators, pyroelectric detectors, optical waveguide and SAW substrates, piezoelectric transducers, etc. [28–40]. For laser application, $LiTaO_3$ crystal has the advantage over $LiNbO_3$ crystal in its considerably higher threshold for photorefractive damage [41]. Although single crystals of $LiTaO_3$ find applications, there still are restrictions because of high cost and difficult fabrication. In contrast, polycrystalline $LiTaO_3$ ceramics can be made with a larger size and more complex shape.

3.2 Experimental

3.2.1 Synthesis of Lithium Niobate

For preparing Lithium Niobate ($LiNbO_3$), AR grade Niobium (V) oxide, lithium hydroxide and standard ammonia solution were used as starting materials. Required quantity of Nb_2O_5 was dissolved in HF (40 %) after heating in a hot water bath for 10 h. Then an aqueous ammonium hydroxide was added dropwise to the NbF_5 solution to precipitate Niobium as hydroxide under basic conditions. The precipitate was washed free of anions and dried at 100˚ C in an oven.

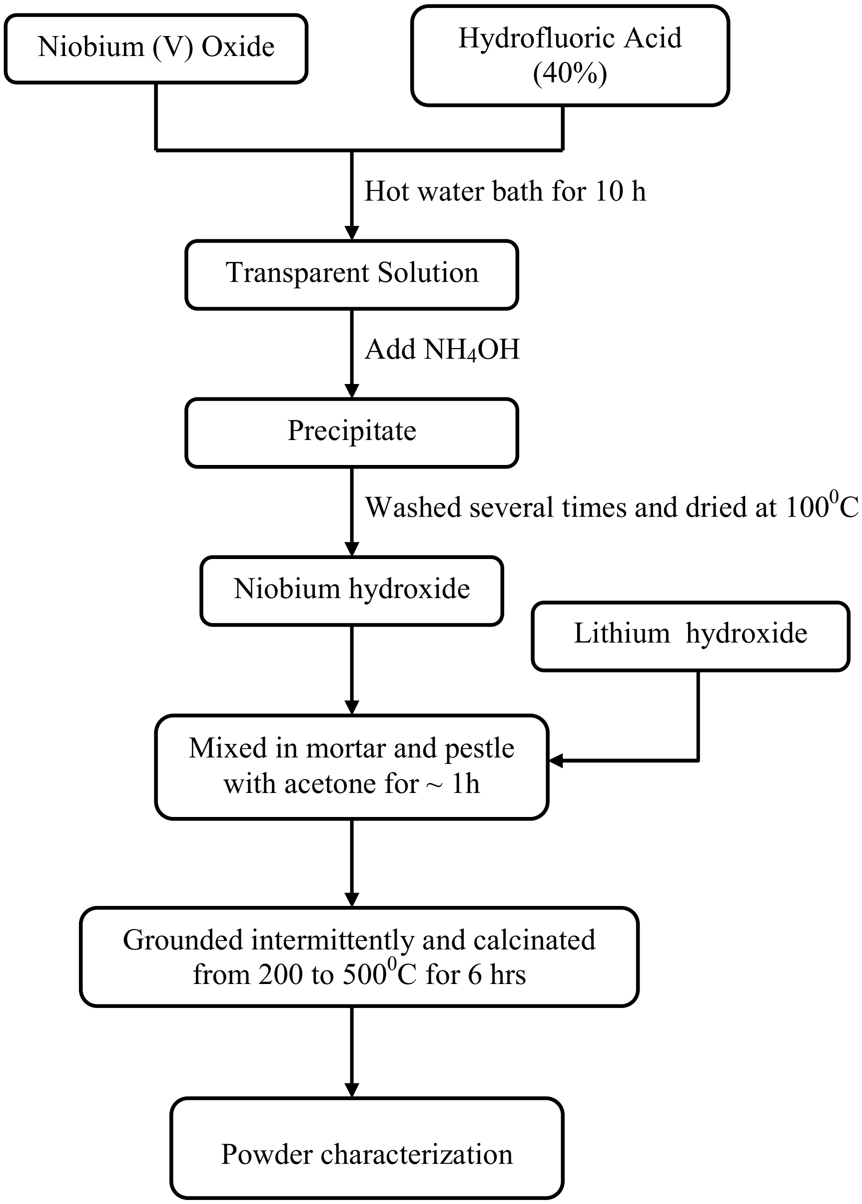

Figure 3.1 Flow chart for the preparation of $LiNbO_3$ by hydroxide precursor method

A stoichiometric amount of LiOH was mixed with $Nb(OH)_5.xH_2O$ and ground well for ~1 hour using acetone in a agate mortar. These powders were calcined at different temperatures from 200 to 500˚ C for 6 hours and characterized with XRD for

$LiNbO_3$ phase formation. The schematic flow chart for the preparation of $LiNbO_3$ by hydroxide precursor method is given in figure 3.1. The major chemical reaction involved in this process is given below

$$Nb_2O_5 + 10HF \xrightarrow{\Delta\ 90^0C,\ 10\ h} 2NbF_5 + 5H_2O \xrightarrow{NH_3OH} \underset{\text{Niobium hydroxide}}{Nb(OH)_5}$$

$$LiOH + Nb(OH)_5 \xrightarrow{\Delta\ 400^0C,\ 6\ h} LiNbO_3$$

3.2.2 Synthesis of Lithium Tantalate

For preparing Lithium Tantalate ($LiTaO_3$), AR grade (Loba chemie) tantalum (V) oxide, lithium hydroxide and standard ammonia solution were used as starting materials. Required quantity of Ta_2O_5 was dissolved in HF (40 %) after heating in a hot water bath for 10 h. Then an aqueous ammonium hydroxide was added dropwise to the TaF_5 solution to precipitate tantalum as hydroxide under basic conditions. The precipitate was washed free of anions and dried at 100° C in an oven. A stoichiometric amount of LiOH was mixed with $Ta(OH)_5.xH_2O$ and ground well for ~1 hour using acetone in a agate mortar. These powders were calcined at different temperatures from 200 to 500° C for 6 hours. Flow chart for the preparation of $LiTaO_3$ by hydroxide precursor method is given in figure 3.2. The powder X-ray pattern was recorded for all the samples calcined at different temperatures by using a Philips PW-1710 model X-ray diffractometer having Cu $K_\propto$ radiation. For lattice parameter and interplanar distance (d) calculation, the samples were scanned in the 2θ range of 10 – 80° for a period of 5s in the step scan mode. Silicon was used as an internal standard. The major chemical reaction involved in the formation of Lithium tantalate is given below

$$Ta_2O_5 + 10HF \xrightarrow{\Delta\ 90^0C,\ 10\ h} 2TaF_5 + 5H_2O \xrightarrow{NH_3OH} \underset{\text{Tantalum hydroxide}}{Ta(OH)_5}$$

$$LiOH + Ta(OH)_5 \xrightarrow{\Delta\ 450^0C,\ 6\ h} LiTaO_3$$

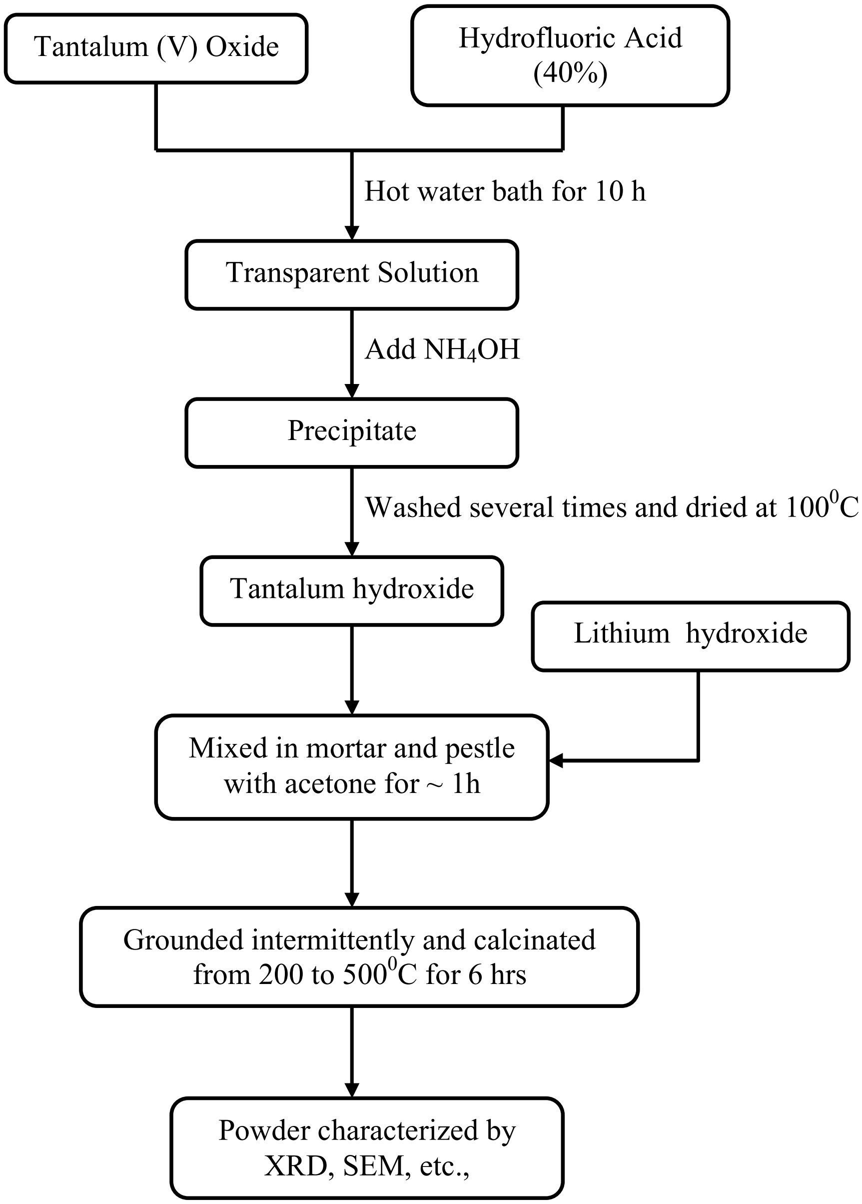

Figure 3.2 Flow chart for the preparation of $LiTaO_3$ by hydroxide precursor method

3.3 Characterization of Lithium Niobate

3.3.1 X-ray powder diffraction

The powder X-ray patterns were recorded for 2θ at 4^0/min for oven dried and samples calcined at various temperatures by using Philips PW-1710 model X-ray diffractometer using Cu Kα. Fig. 3.3 shows the XRD patterns of the powder calcined at 100, 200, 300 and 400 degree Celcius. XRD patterns for the powder calcined at 400°C for a duration of 4 hours, leads to the formation of major $LiNbO_3$ phase. This is the lowest temperature reported so far on the formation of $LiNbO_3$ phase. All the d-line peaks are similar to that reported in the literature. The $LiNbO_3$ has a hexagonal crystal structure (JCPDS-20-631). The calculated lattice parameters by least square fit are a=5.15 Å and c=13.86 Å.

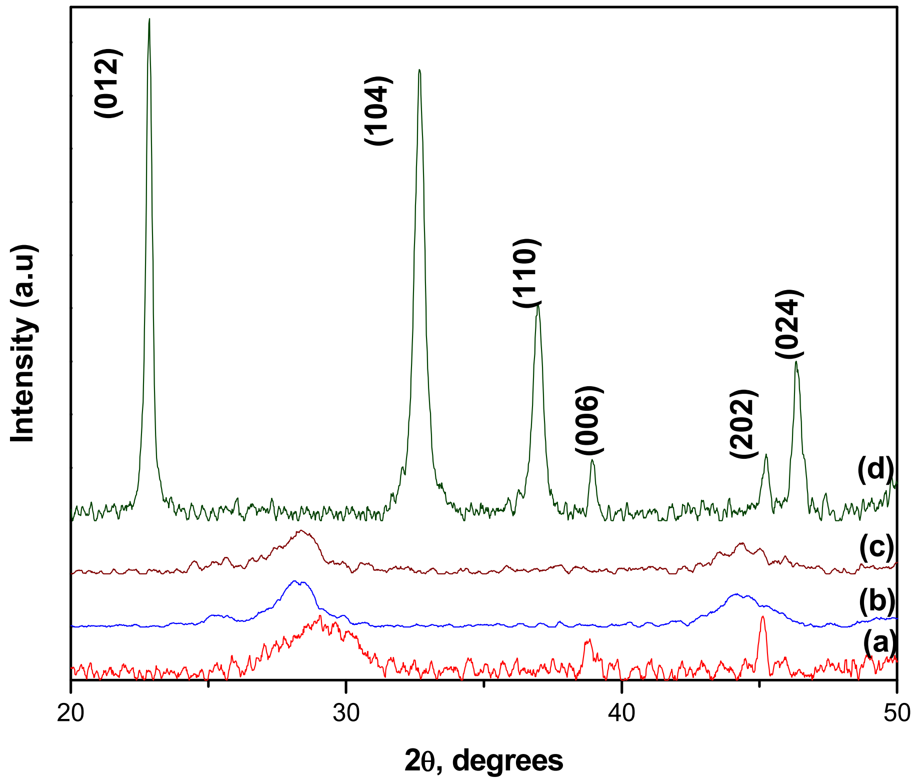

Figure 3.3. XRD of $LiNbO_3$ precursor powder (a) calcined at 100 °C, (b) calcined at 200 °C and (c) calcined at 300 °C and calcined at 400 °C for 4 h.

The conventional solid state method produces $LiNbO_3$ phase at 900 °C after prolonged firing. The average rystallite size of 80 nm was calculated from the Scherrer's formula

$$t = K\lambda/B\,Cos\theta_B$$

where t is the average size of the particles assuming particles to be spherical, K=0.9, λ is the wavelength of X-ray radiation, B is the full-width at half maximum of the diffracted peak and θB is the angle of diffraction.

3.3.2 Energy Dispersive X-Ray Analysis

The EDAX spectrum of $LiNbO_3$ prepared by hydroxide precursor method was scanned from 0 to 10keV and characteristics peaks for Niobium and Oxygen is observed at 2.166 keV and 0.525keV respectively in figure 2.3 and corresponding identified transition are tabulated in Table 1.

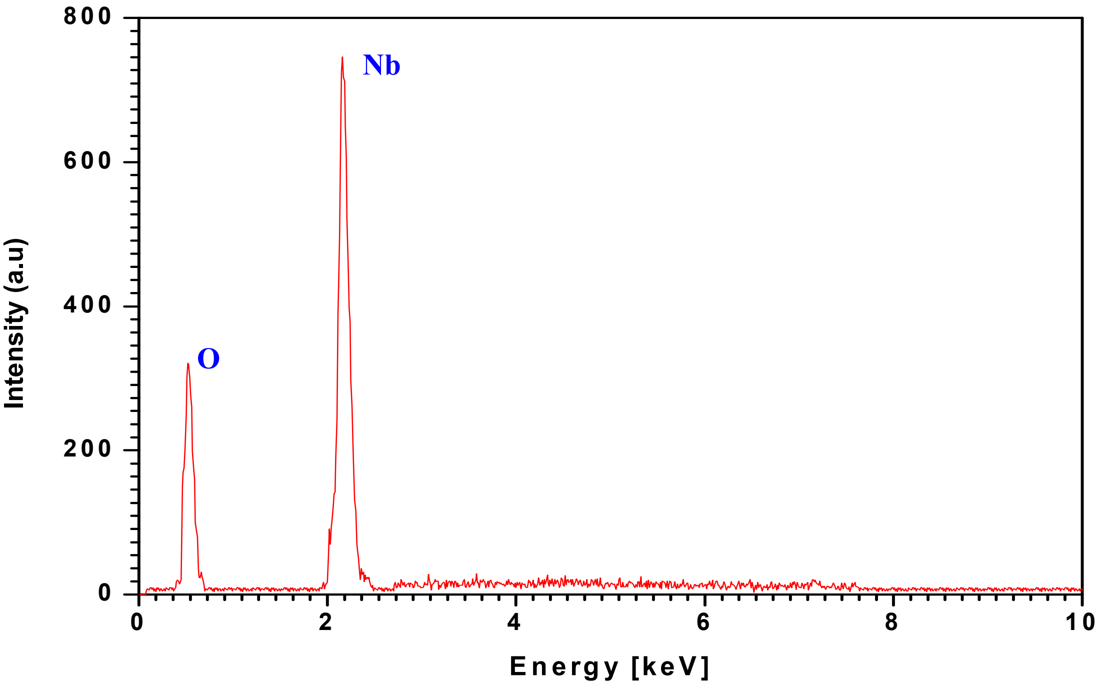

Figure 3.4. EDAX Spectrum of $LiNbO_3$ prepared by hydroxide precursor method

However, the EDAX of the matrix could not show the presence of lithium because of its light weight [42–44]. No other elements were monitored in EDAX shows the purity of product synthesized by hydroxide precursor method. JEOL JED-2300 Energy dispersive X-ray analysis Station is used for the elemental analysis of sintered samples of $LiNbO_3$

Table 3.1. EDAX spectrum peak observations for $LiNbO_3$

Sr No.	Element	Peak Observed	Transition
1	Oxygen	0.525 keV	K-alpha
2	Niobium	2.166 keV	L-alpha (L3M5)

3.3.3 Transmission Electron Microscopy

The samples for TEM were prepared by drop coating on to a carbon coated copper TEM grid. TEM micrographs and selected area diffraction patterns were obtained on a JEOL, 1200 EX instrument operated at an accelerating voltage of 100 kV. The particle size and morphology of the calcined powders were examined by transmission electron microscopy. The particle morphology of calcined powder (400 °C for 6 h) was irregular in shape, with an average primary particle size around 70 nm.

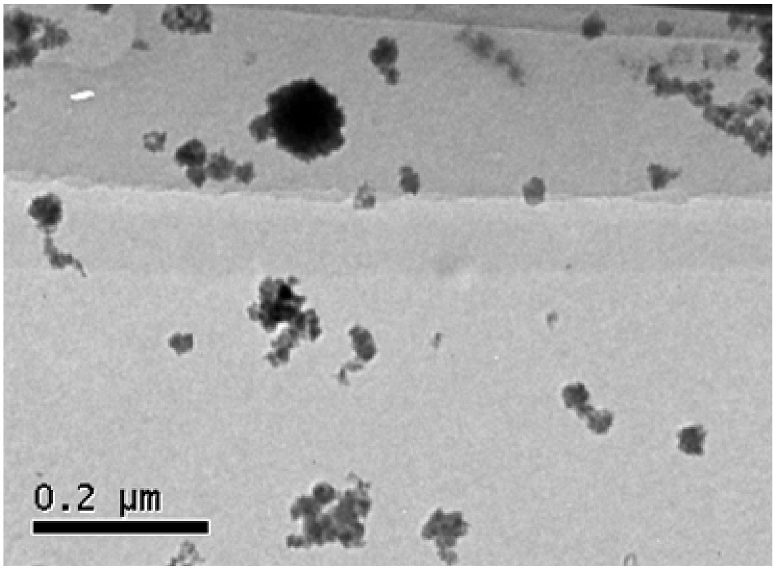

Fig. 3.5. Transmission Electron Microscopy image of LN calcined at 400 °C for 6 h.

3.3.4 Thermogravimetry Analysis

Stoichiometric amount of lithium hydroxide and Niobium hydroxide obtained from Niobium (V) oxide with HF is mixed well thoroughly and thermogravimetric analysis of this mixture is carried out at 10 different heating rate (2.5, 5, 7.5, 10, 12.5, 15, 17.5, 20, 22.5 and 25^0C/min) and observation is given in figure 3.6. Around 8 to 14 mg of mixture is used for TGA analysis. Inert nitrogen gas at 40mL/min is used as a purge gas during Thermogravimetric analysis. Irrespective of heating rate, figure 3.6 clearly shows at around 380 to 400^0C there is a dip in mass profile, which is an indication of solid state reaction takes place with release of hydroxyl ions from the precursors. XRD also conforms the structural formation $LiNbO_3$ at 400^0C.

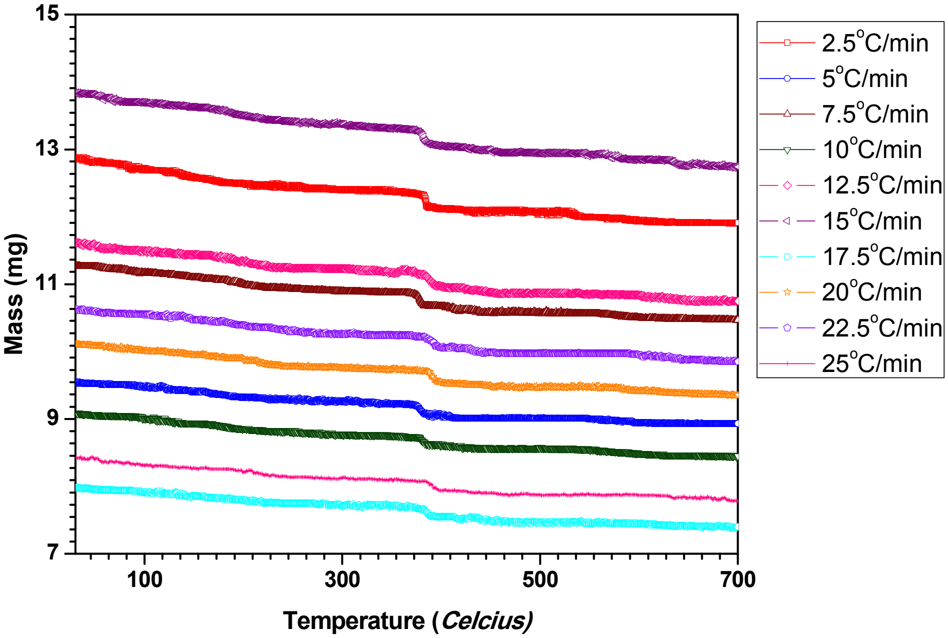

Figure 3.6. TGA profile of $LiNbO_3$ formation at different heating rate

3.3.5 Differential Scanning Calorimetery

Differential Scanning Calorimetric (DSC) analysis of $LiNbO_3$ precursor powders was carried out at 5 different heating rate (2.5, 5, 7.5, 10 and 15^0C/min) and presented in figure 3.7. Stoichiometric amount of Lithium hydroxide and Niobium hydroxide obtained from Niobium (V) oxide with HF is mixed well thoroughly. Around 20 mg of mixture is used for DSC analysis. Inert Nitrogen gas is used as a purge gas during DSC analysis of mixture. The onset DSC peeks were observed at around 380^0C and the peak shifts with heating rate and tabulated in Table 3.2 for the computation of activation energy by Kissinger method. From the table 3.2, Kissinger plot was constructed (figure 3.8) to find the linear equation, from the slope of the equation the activation energy for the formation of $LiNbO_3$ by hydroxide precursor method is 275.63 kJ.

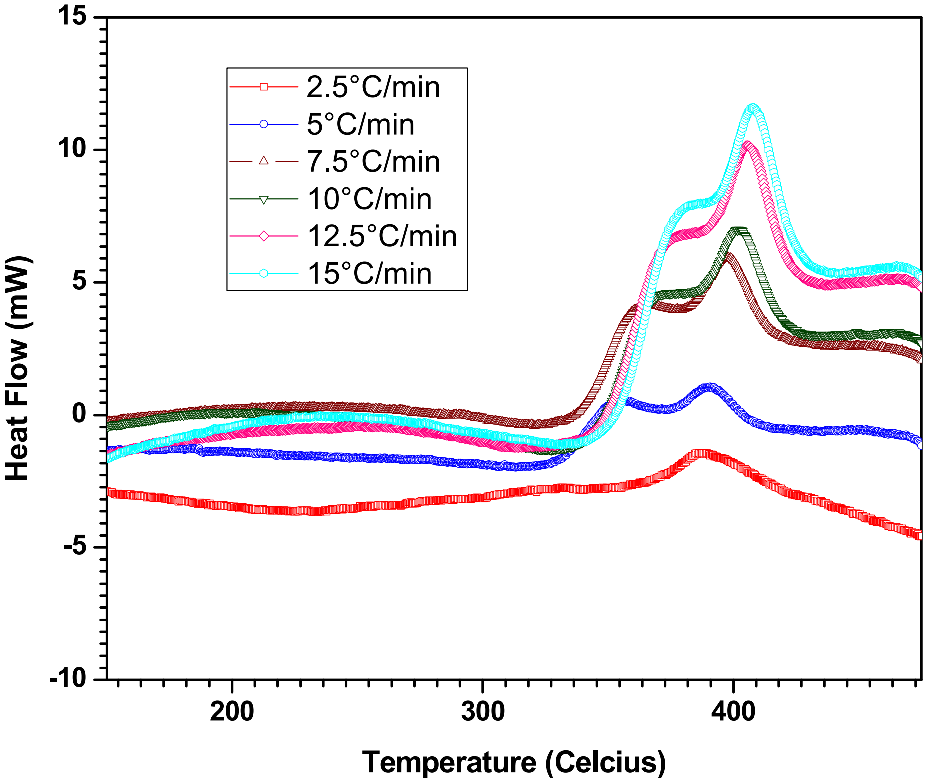

Figure 3.7. DSC profile of $LiNbO_3$ formation at different heating rate

Table 3.2. DSC data on $LiNbO_3$ at various heating rates (Kissinger method).

Heating rate β (°C)	Peak T_{max} (°C)	Peak T_{max} (K)	T^2_{max}	$\frac{1}{T_{max}}$	$\frac{\beta}{T^2_{max}}$	$-\ln\left(\frac{\beta}{T^2_{max}}\right)$	Slope	Activation Energy (kJ/mol)
2.5	386.56	659.71	435217	0.001515	5.7442E-06	12.067	33153.6355	275.63
5	390.83	663.98	440869	0.001506	1.1341E-05	11.387		
7.5	397.3	670.45	449503	0.001491	1.6685E-05	11.001		
10	402.58	675.73	456611	0.001479	2.1900E-05	10.729		
12.5	405.88	679.03	461082	0.001472	2.7110E-05	10.515		
15	407.77	680.92	463652	0.00146	3.2351E-05	10.338		

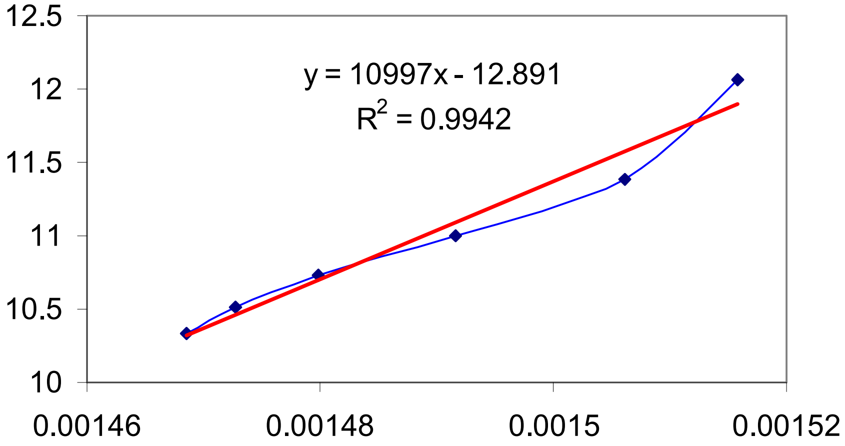

Fig. 3.8. Kissinger Plot for $LiNbO_3$ for computing activation energy.

3.3.6 Impedance Spectroscopy

The variation of real (Z') and Imaginary (Z") part or Nyquist plot of impedance with frequency for $LiNbO_3$ samples sintered at 750^0C for 30, 60, 90 and 120 minutes is shown in figure 3.9. A single semicircular arc is appeared for all samples, however for the sample sintered for 120 min, one additional semicircular arc is appeared at high frequency as shown in figure 3.10. One semicircle in the high frequency range and the other in the low frequency range for $LiNbO_3$ sintered at 750^0C for 120 minute may correspond to oxygen migration in the bulk and across grain boundaries.

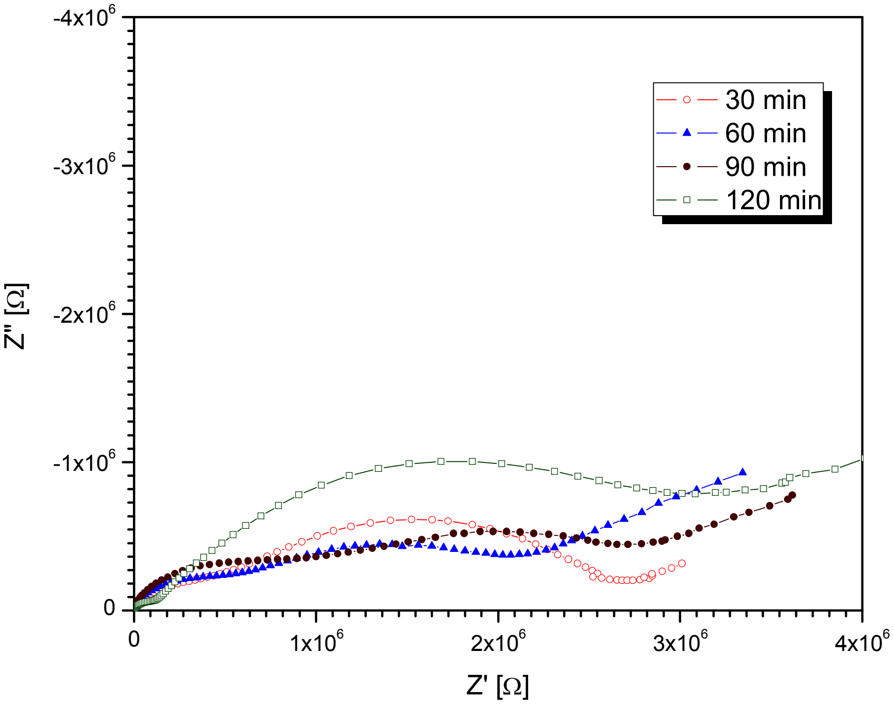

Figure 3.9. Nyquist plot of $LiNbO_3$ Sintered at 750^0C for 30, 60, 90 and 120 min

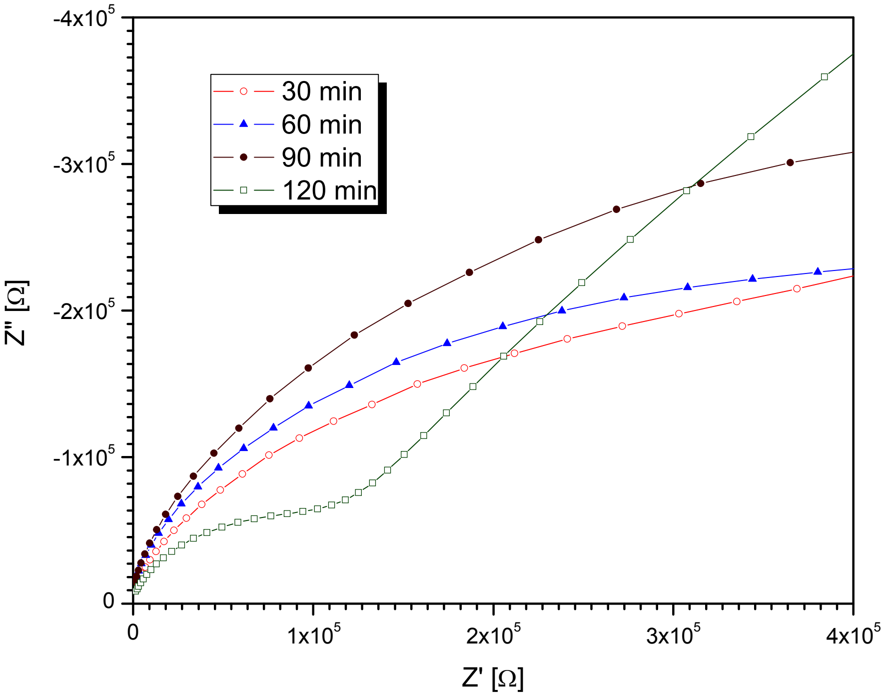

Figure 3.10. Nyquist plot at high frequency observed for $LiNbO_3$ Sintered at 750^0C for 30, 60, 90 and 120 min

Bode plot was constructed for the for $LiNbO_3$ samples sintered at 750^0C for 30, 60, 90 and 120 minutes with frequency vs magnitude of impedance as shown in figure 3.11 and frequency vs phase angle as shown in 3.12. Figure 3.11 shows the decrease in magnitude of impedance drastically with increase in frequency. The frequency dependence of phase angle is observed in figure 3.12 for $LiNbO_3$ samples sintered at 750^0C .

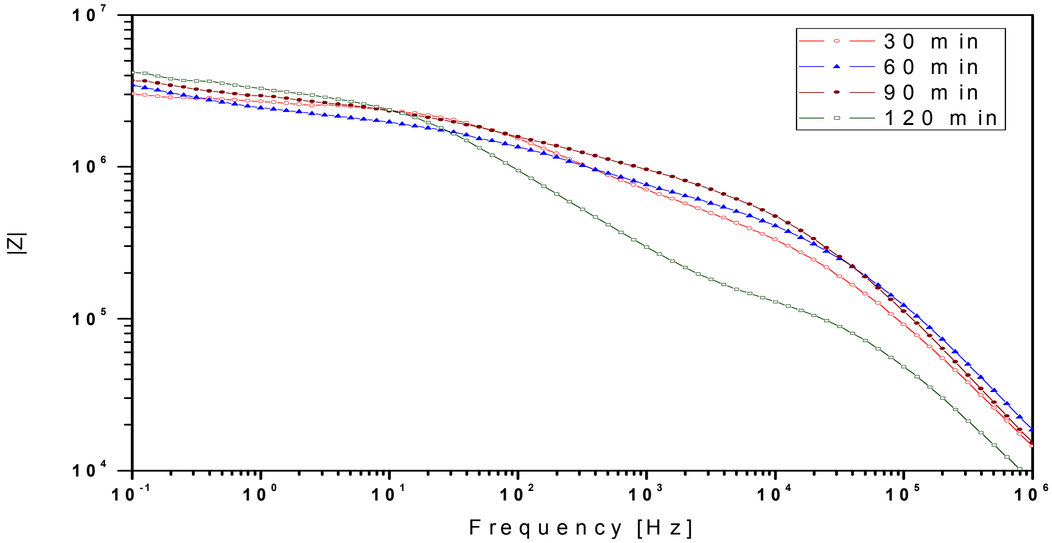

Figure 3.11. Bode plot – Impedance magnitude |Z| vs frequency of $LiNbO_3$ Sintered at

750^0C for 30, 60, 90 and 120 min

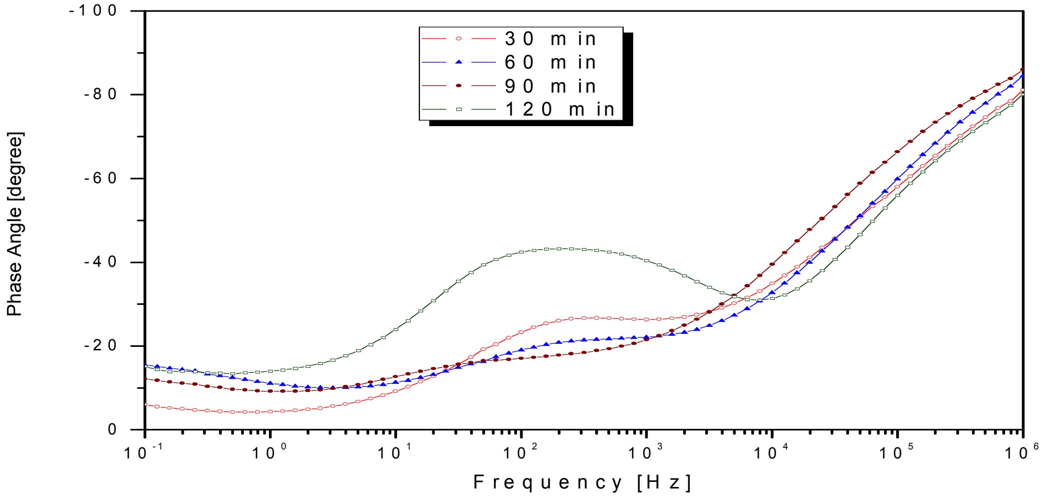

Figure 3.12. Bode plot – Phase Angle vs frequency of $LiNbO_3$ Sintered at 750^0C for 30, 60, 90 and 120 min

The variation of real (Z') and Imaginary (Z") part or Nyquist plot of impedance with frequency for $LiNbO_3$ samples sintered at 1000^0C for 30, 60, 90 and 120 minutes is shown in figure 3.13. A single semicircular arc is appeared for all samples, however for the sample sintered for 120 min, one additional semicircular arc is appeared at high frequency as shown in figure 3.10. One semicircle in the high frequency range and the other in the low frequency range for $LiNbO_3$ sintered at 1000^0C for 30 and120 min may correspond to oxygen migration in the bulk and across grain boundaries

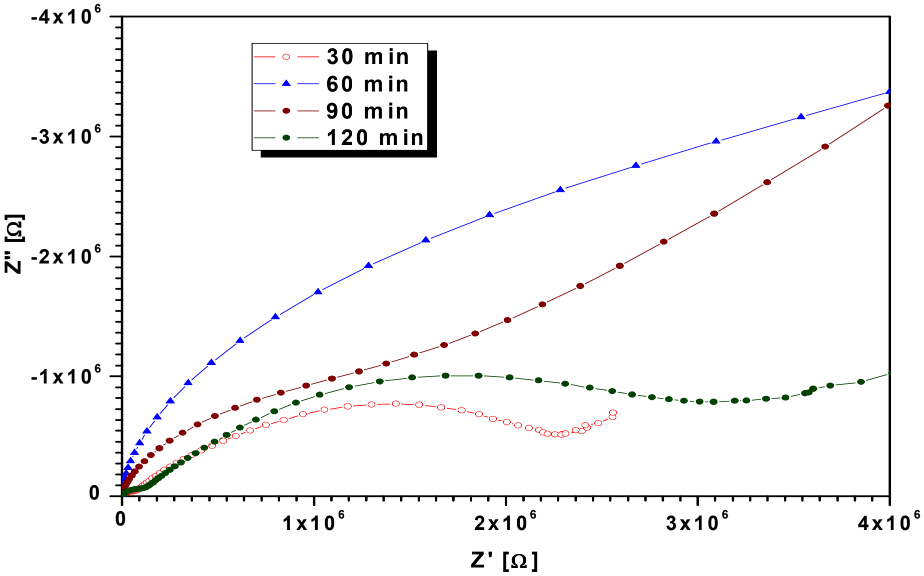

Figure 3.13. Nyquist plot of $LiNbO_3$ Sintered at 1000^0C for 30, 60, 90 and 120 min

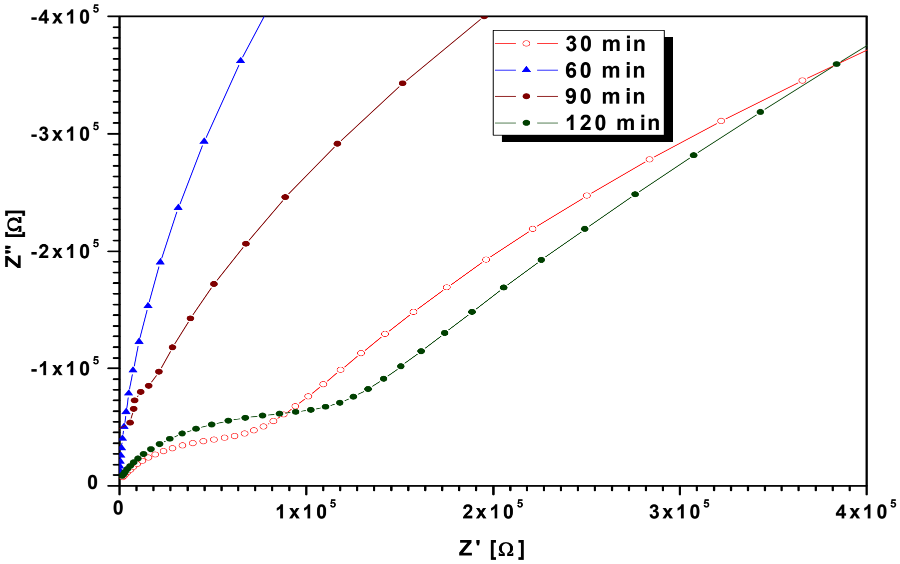

Figure 3.14. Nyquist plot at high frequency observed for $LiNbO_3$ Sintered at 1000^0C for 30, 60, 90 and 120 minutes

Bode plot was constructed for the for $LiNbO_3$ samples sintered at 1000^0C for 30, 60, 90 and 120 minutes is with frequency vs magnitude of impedance as shown in figure 3.15 and frequency vs phase angle as shown in figure 3.16. The sample sintered for 30 minute shows lower impedance |Z| as compared to samples sintered for longer duration. Both the figures show the frequency dependence of impedance parameters for $LiNbO_3$ samples.

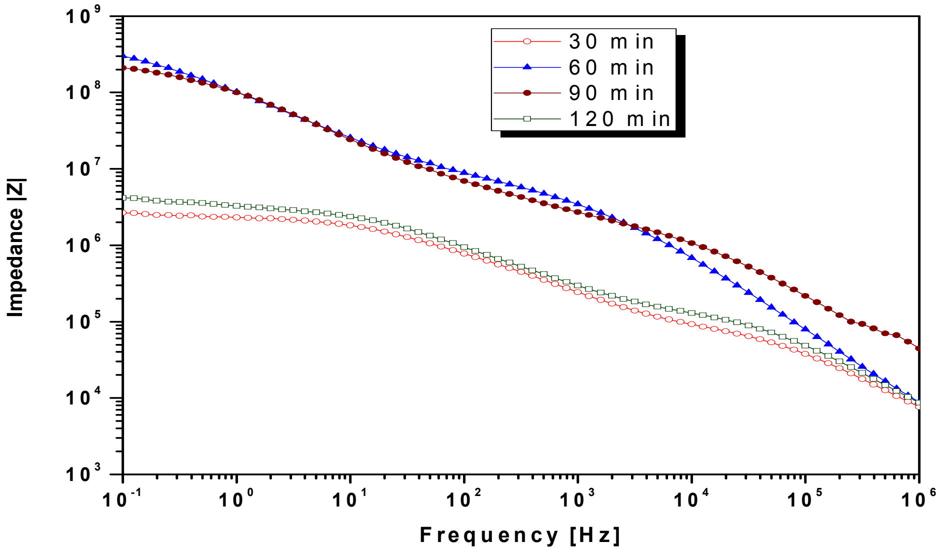

Figure 3.15. Bode plot – Impedance magnitude |Z| vs frequency of $LiNbO_3$ Sintered at 1000^0C for 30, 60, 90 and 120 minutes

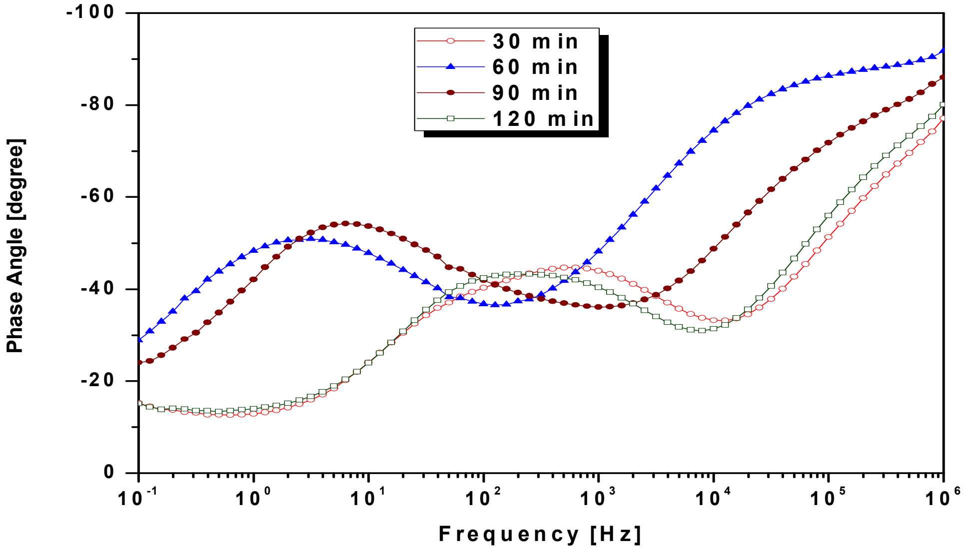

Figure 3.16. Bode plot – Phase Angle vs frequency of $LiNbO_3$ Sintered at 1000^0C for 30, 60, 90 and 120 min

Dielectric Loss vs frequency of $LiNbO_3$ Sintered at 750^{0}C and 1000^{0}C were measured upto 40MHz and plotted in figure 3,17 and 3.18 respectively. It is observed that the the dielectric loss of $LiNbO_3$ decreases with increase in frequency and becomes stable after 10^{6}Hz. $LiNbO_3$ samples sintered for 30 min duration shows higher dielectric loss as compared to samples sintered for longer duration. Since the dielectric loss of $LiNbO_3$ is very less at high frequency, it has potential application in high frequency devices.

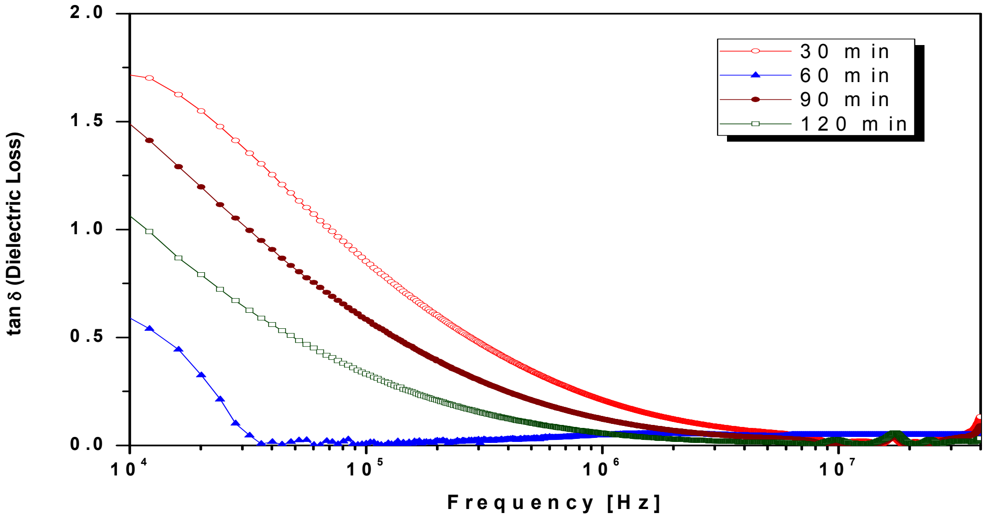

Figure 3.17. Variation of dielectric loss as a function of frequency for $LiNbO_3$ samples sintered at 750^{0}C for 30, 60, 90 and 120 minutes

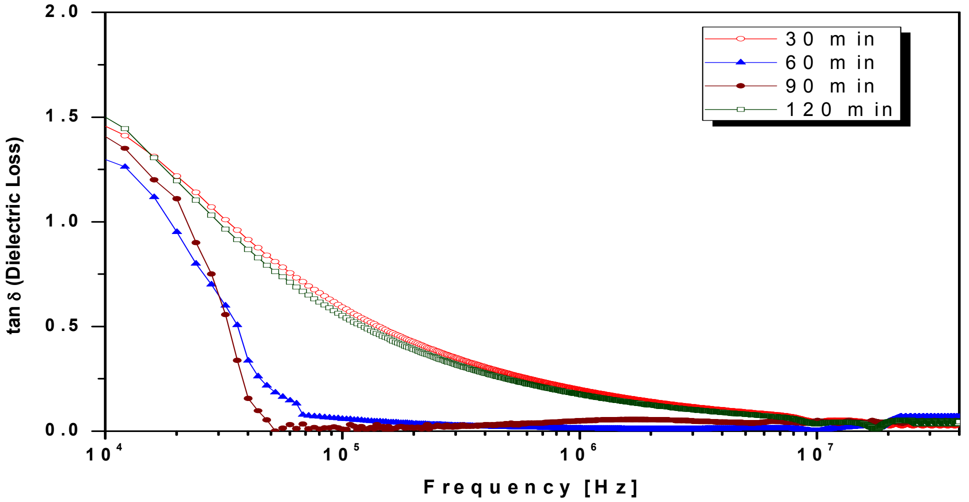

Figure 3.18. Variation of dielectric loss as a function of frequency for $LiNbO_3$ samples sintered at 1000^{0}C for 30, 60, 90 and 120 minutes

3.4 Characterization of Lithium Tantalate

3.4.1 X-ray powder diffraction

The powder X-ray patterns were recorded for 2θ at 4^0/min for oven dried and samples calcined at various temperatures by using Philips PW-1710 model X-ray diffractometer using Cu Kα. Fig 3.8 shows the XRD patterns of the powder calcined at different temperatures. The powders heated at 200˚ C consists of many intermediates of varying composition and authentically could not indexed. However, when calicination temperature was 450˚ C and duration of ~ 6 hours, it leads to formation of major $LiTaO_3$ phase. This is the lowest temperature reported so far for the formation of LT phase. All the d-line peaks are similar to that reported in the literature. The crystal structure of LT is hexagonal and all the d-line patterns match with reported values (JCPDS-29-836). The calculated lattice parameters by least squares fit are a = 5.154 Å and c = 13.756 Å. The conventional solid state method gives LT phase at 900˚C after prolonged firing. The average particle size of 45 nm was calculated from Scherrer's formula $t = K\lambda/B\cos\theta_B$ where t is the average size of the particles assuming particles to be spherical, K=0.9, λ is the wavelength of X-ray radiation, B is the full width at half maximum of the diffracted peak and θ_B is the angle of diffraction.

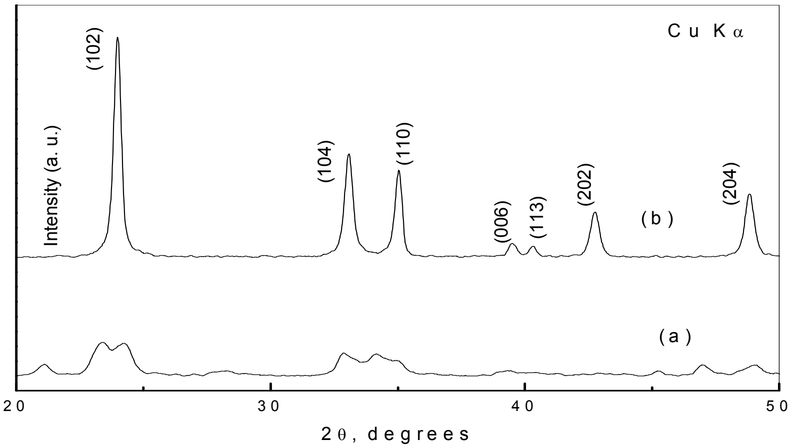

Fig 3.19 XRD of LT precursor powder calcined at (a) 200^0C and (b) 450^0C for 6 hr

3.4.2 Energy Dispersive X-Ray Analysis

The elemental analysis of the synthesized $LiTaO_3$ was carried out using the EDAX attachment to the SEM system. During measurements, EDAX detector is operated at liquid nitrogen temperatures.

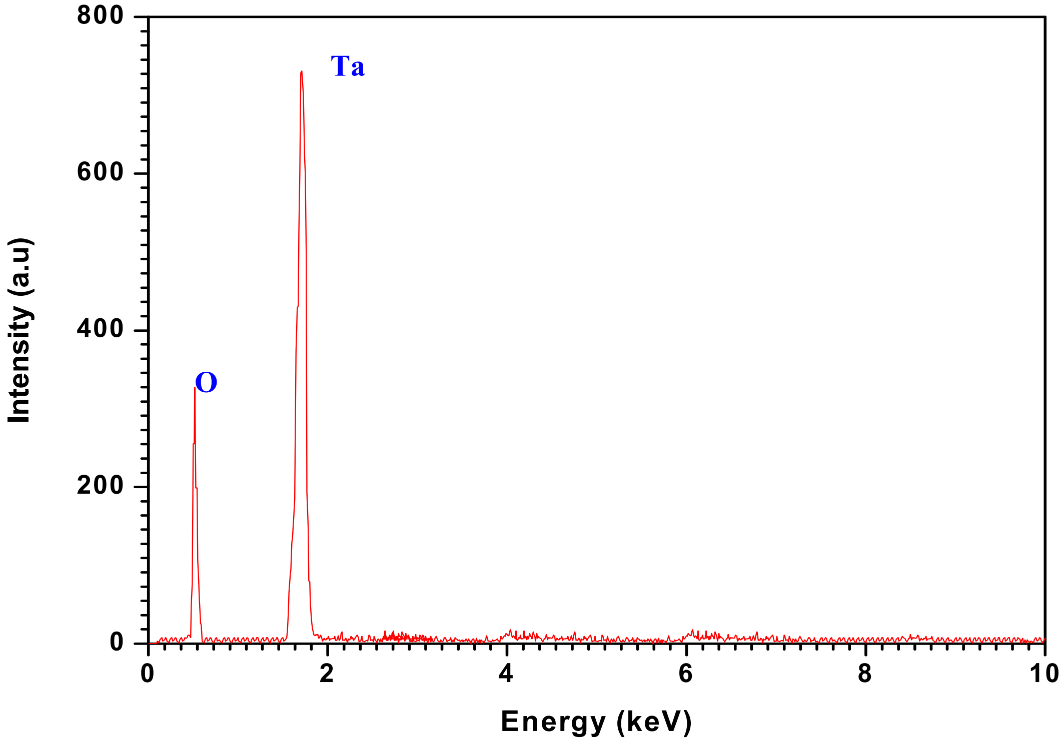

Figure 3.20. EDAX Spectrum of $LiTaO_3$ prepared by hydroxide precursor method

The EDAX spectrum of $LiTaO_3$ prepared by hydroxide precursor method was scanned from 0 to 10keV and characteristics peaks for Oxygen is observed at 0.525 keV respectively. The characteristic M-alpha peak for Tantalum as observed by F. Piret et al [45] and other researchers [46–49] is also observed at 1.709 keV. The composition of synthesized materials was confirmed through EDAX studies and the resulting spectra are tabulated in Table 3.3

Table 3.3. EDAX spectrum peaks observed for $LiNbO_3$

Sr No.	Element	Peak Observed	Transition
1	Oxygen	0.525 keV	K-alpha
2	Tantalum	1.709 keV	M-alpha

The peak for Lithium is not observed in EDAX spectrum due to the instrument limitation of JEOL JED-2300 Energy dispersive X-ray analysis Station.

3.4.3 Transmission Electron Microscopy

The particle size and morphology of the calcined powders were examined by transmission electron microscopy. TEM observations were made with a JEOL model 1200 EX instrument at the accelerating voltage of 100 kV. All the powders were dispersed in amyl acetate on a carbon coated TEM copper grid. The particle morphology of calcined powder (450˚C for 6h) was irregular in shape, with an average primary particle size around 50nm

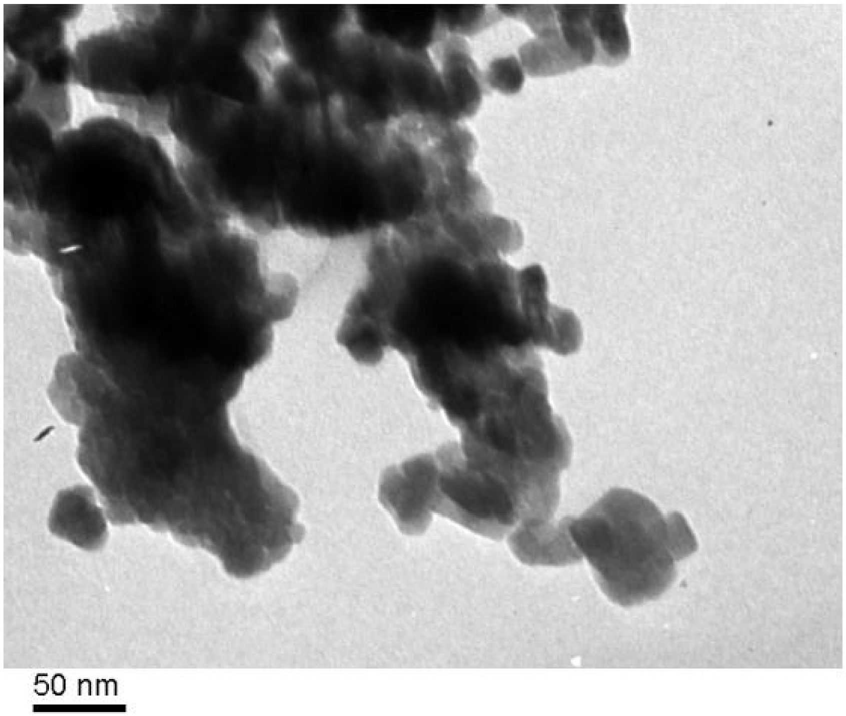

Fig 3.21 TEM image of LT powder calcined at 450^0C for 6 h

3.4.4 Thermogravimetry Analysis

Stoichiometric amount of lithium hydroxide and Tantalum hydroxide obtained from Tantalum (V) oxide with HF is mixed well thoroughly and thermogravimetric analysis of this mixture is carried out at 5, 7.5, 10, 12.5, 15 and 17.5, 20, 22.5 and 25^0C/min and depicted in figure 2. Around 18 to 24 mg of mixture is used for TGA analysis. Irrespective of heating rate, figure 1 clearly shows gradual dip in mass upto 450C and then stable profile, which is an indication of solid state reaction takes place with release of hydroxyl ions from the precursors. XRD also conforms the structural formation $LiTaO_3$ at 450^0C.

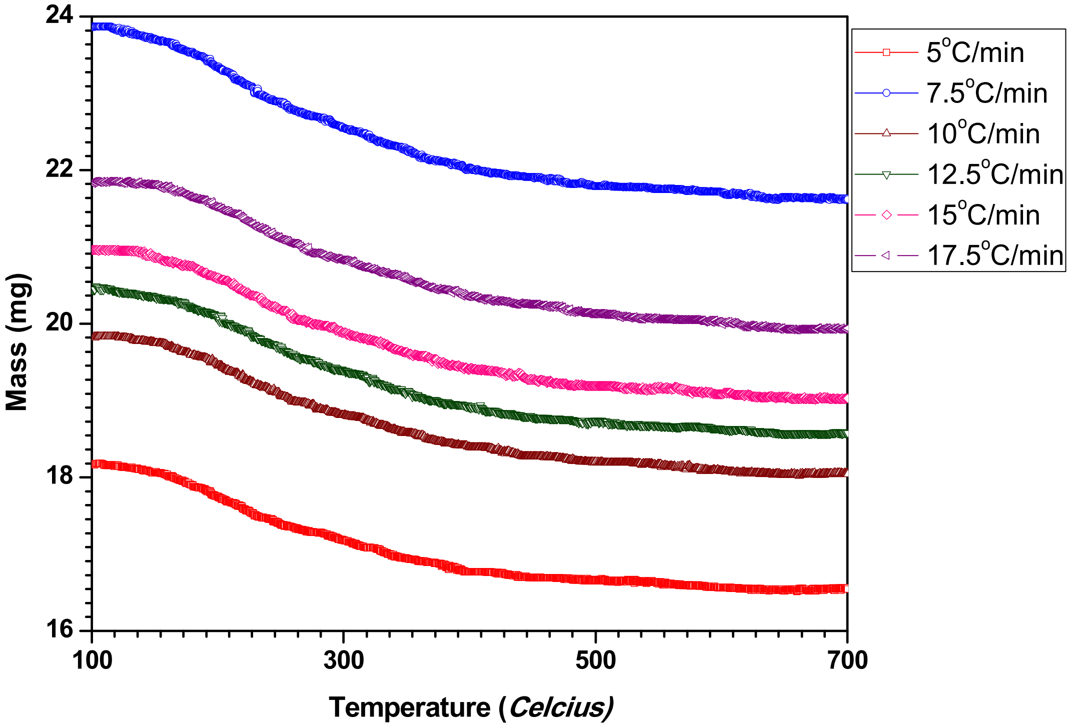

Figure 3.22. TGA profile of $LiTaO_3$ formation at different heating rate

3.4.5 Differential Scanning Calorimetery

Differential Scanning Calorimetric (DSC) analysis of $LiTaO_3$ precursor powder was carried out at 6 different heating rate (2.5, 5, 7.5, 10 and 15^0C/min). Stoichiometric amount of Lithium hydroxide and Tantalum hydroxide obtained from Tantalum (V) oxide with HF is mixed well thoroughly. Around 20 mg of mixture is used for DSC analysis. Inert Nitrogen gas is used as a purge gas during DSC analysis of mixture.

The onset DSC peeks were observed at around 430^{0}C and the peak shifts with heating rate and tabulated in table 3.4 for the computation of activation energy by Kissinger method. From the table 3.4, Kissinger plot was constructed to find the linear equation, from the slope of the equation the activation energy for the formation of $LiTaO_3$ by hydroxide precursor method is 177.16 kJ.

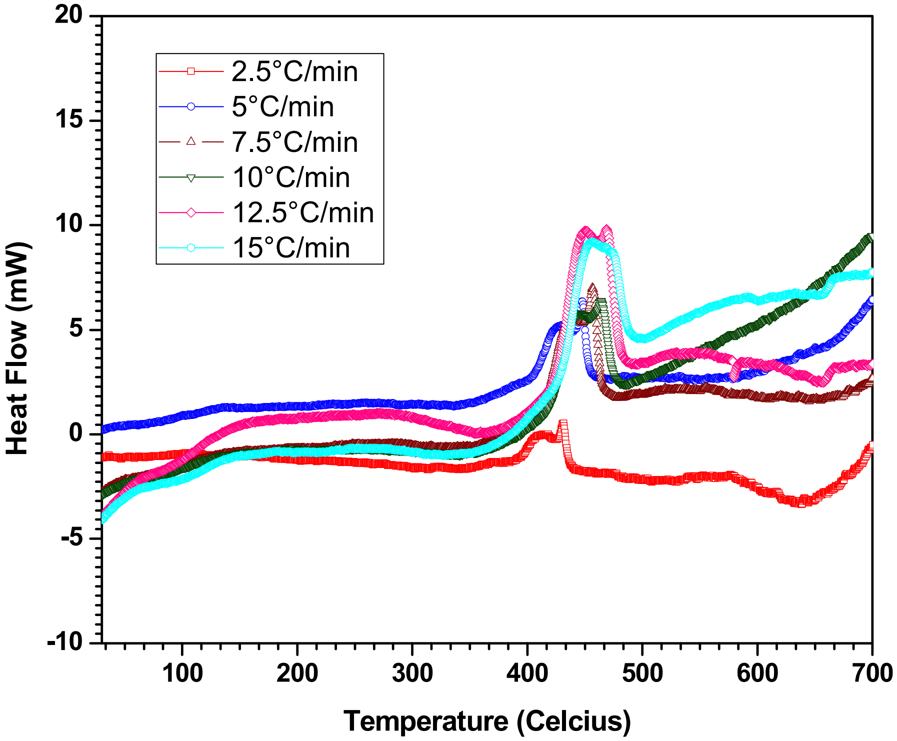

Figure 3.23. DSC profile of $LiTaO_3$ formation at different heating rate

Table 3.4. DSC data on $LiTaO_3$ at various heating rates (Kissinger method).

Heating rate β (°C)	Peak Tmax (°C)	Peak Tmax (K)	T_{max}^2	$\frac{1}{T_{max}}$	$\frac{\beta}{T_{max}^2}$	$-\ln\left(\frac{\beta}{T_{max}^2}\right)$	Slope	Activation Energy (kJ/mol)
2.5	431.41	704.56	496405	0.001419	5.0362E-06	12.198	21308.6432	177.16
5	447.56	720.71	519423	0.001387	9.6260E-06	11.551		
7.5	456.66	729.81	532623	0.001370	1.4081E-05	11.170		
10	463.92	737.07	543272	0.001356	1.8407E-05	10.902		
12.5	468.59	741.74	550178	0.001348	2.2719E-05	10.692		
15	472.6	745.75	556143	0.001340	2.6971E-05	10.520		

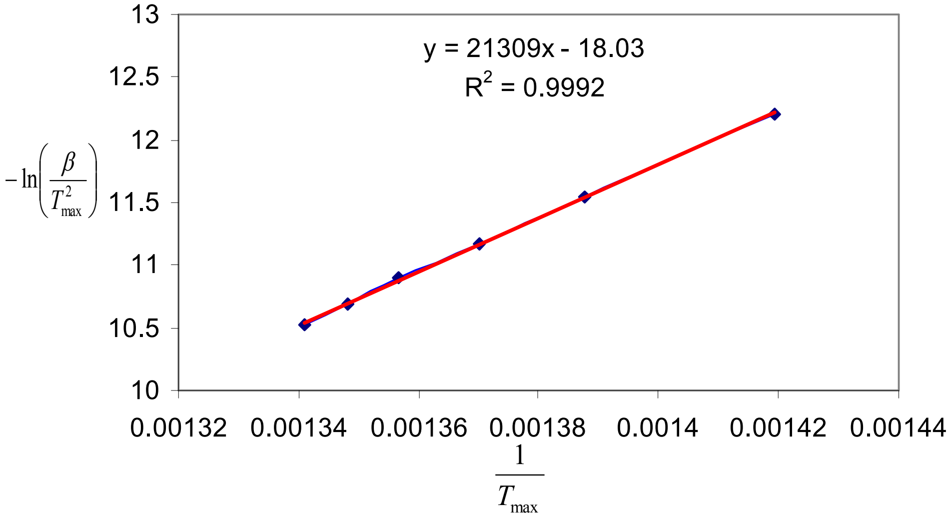

Fig. 3.24. Kissinger Plot for $LiTaO_3$ for computing activation energy.

3.4.6 Impedance Spectroscopy

The variation of real (Z') and Imaginary (Z") part or Nyquist plot of impedance with frequency for $LiTaO_3$ samples sintered at 750^0C for 30, 60, 90 and 120 minutes is shown in figure 3.25. A single semicircular arc is appeared for all samples, however for the sample sintered for 30 min, one additional semicircular arc is appeared at high frequency as shown in figure 3.26. One semicircle in the high frequency range and the other in the low frequency range for $LiTaO_3$ sintered at 750^0C for 30 minute may correspond to oxygen migration in the bulk and across grain boundaries.

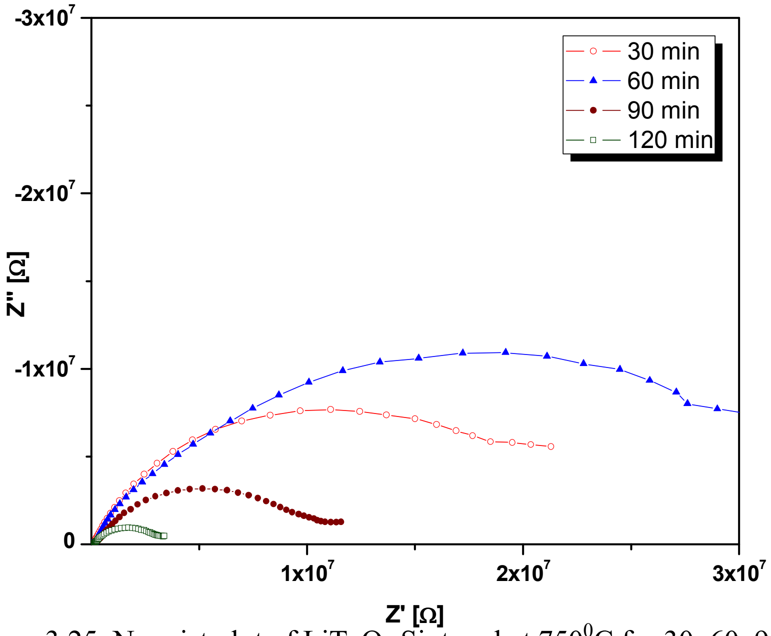

Figure 3.25. Nyquist plot of $LiTaO_3$ Sintered at 750^0C for 30, 60, 90 and 120 min

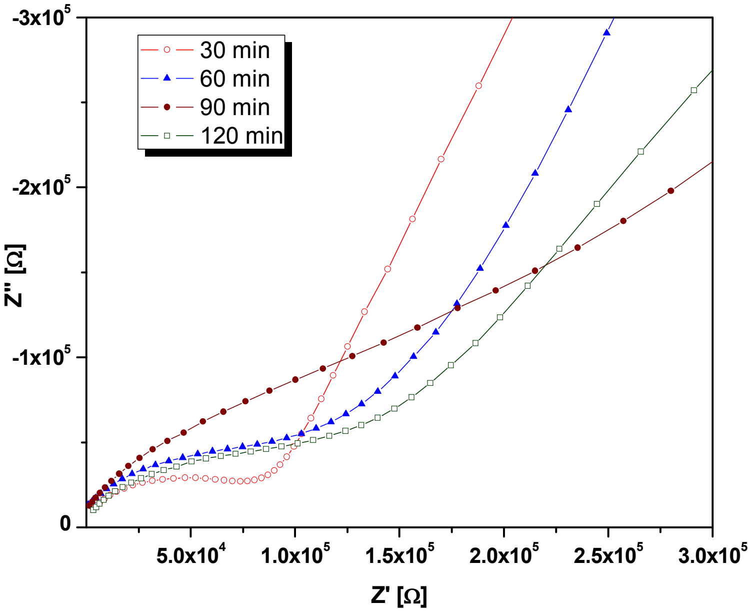

Figure 3.26. Nyquist plot at high frequency observed for $LiTaO_3$ Sintered at 750^0C for 30, 60, 90 and 120 min

Bode plot was measured for the for $LiTaO_3$ samples sintered at 750^0C for 30, 60, 90 and 120 minutes with frequency vs magnitude of impedance as shown in figure 3.27 and frequency vs phase angle as shown in figure 3.28. Figure 3.27 shows the decrease in magnitude of impedance drastically with increase in frequency. The frequency dependence of phase angle is observed in figure 3.28 for $LiTaO_3$ samples sintered at 750^0C

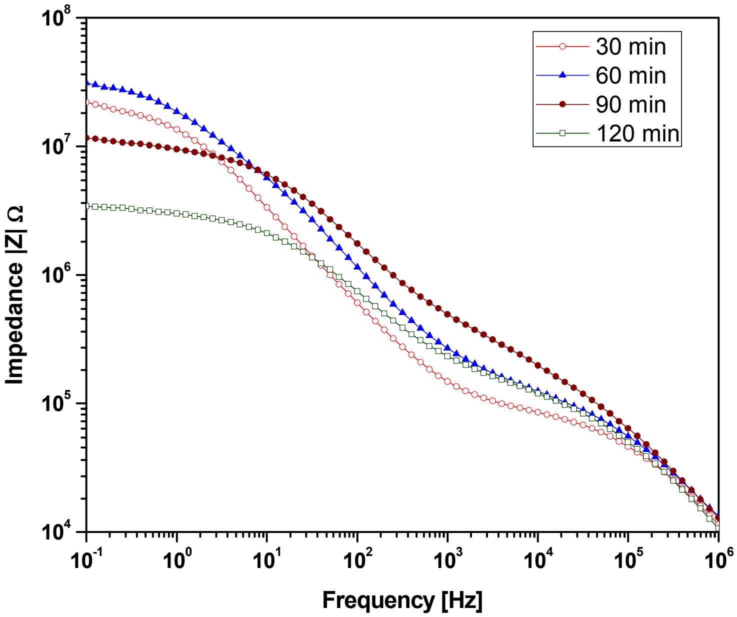

Figure 3.27. Bode plot – Impedance magnitude |Z| vs frequency of $LiTaO_3$ Sintered at 750^0C for 30, 60, 90 and 120 min

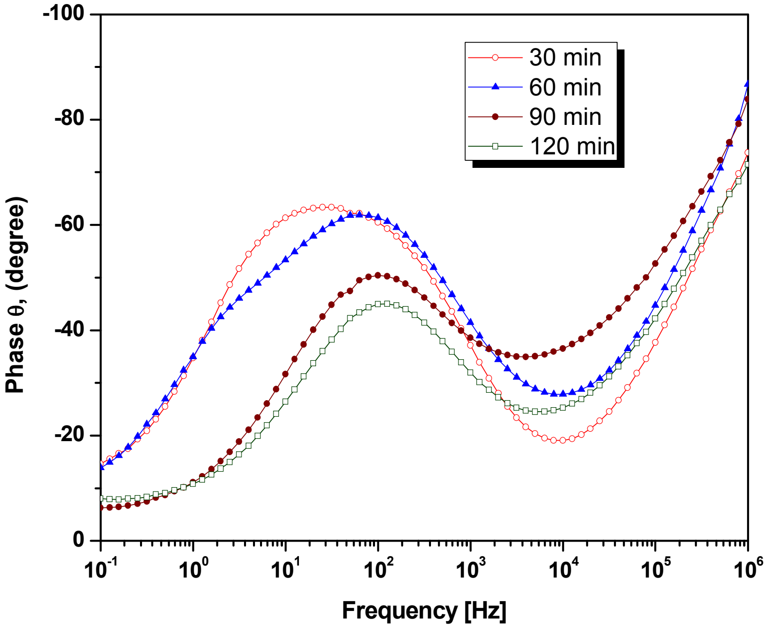

Figure 3.28. Bode plot – Phase Angle vs frequency of $LiTaO_3$ Sintered at 750^0C for 30, 60, 90 and 120 min

The variation of real (Z') and Imaginary (Z") part or Nyquist plot of impedance with frequency for $LiTaO_3$ samples sintered at 1000^0C for 30, 60, 90 and 120 minutes is shown in figure 3.29. A single semicircular arc is appeared for all samples even at high frequency as shown in figure 3.30. The semicircle at low frequency relates grain boundary, secondary phase segregated at grain boundary and sometimes effect of electrode.

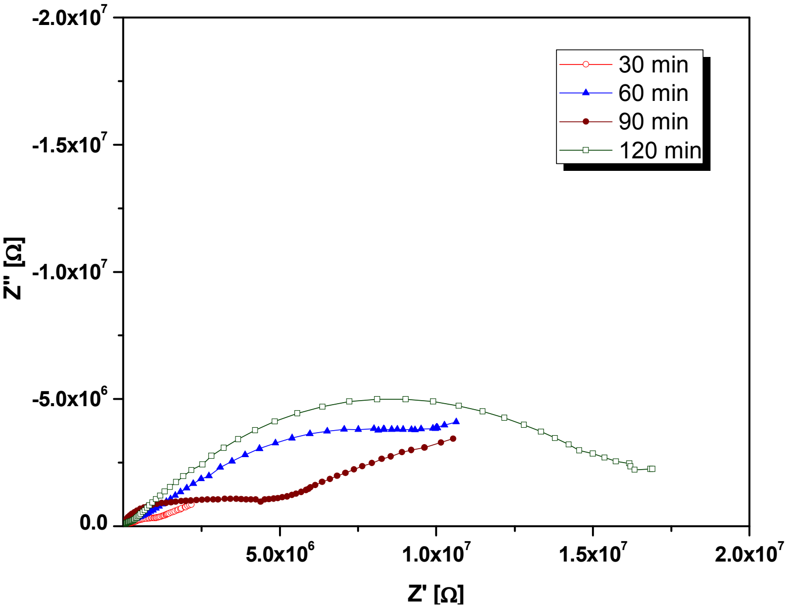

Figure 3.29. Nyquist plot of $LiTaO_3$ Sintered at 1000^0C for 30, 60, 90 and 120 min

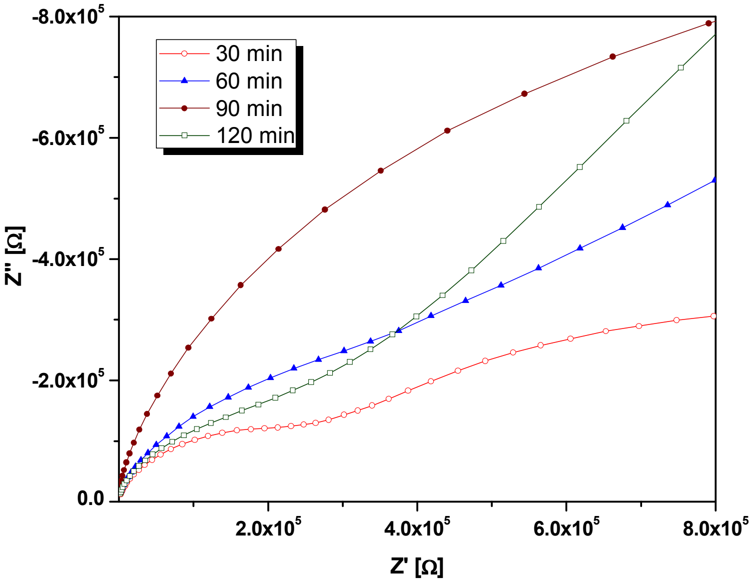

Figure 3.30. Nyquist plot at high frequency observed for $LiTaO_3$ Sintered at 1000^0C for 30, 60, 90 and 120 min

Bode plot was constructed for the for $LiTaO_3$ samples sintered at 1000^0C for 30, 60, 90 and 120 minutes is with frequency vs magnitude of impedance as shown in figure 3.31 and frequency vs phase angle as shown in figure 3.32. Both the figures shows the frequency dependence of impedance parameters for $LiTaO_3$ samples. The sample sintered for 30 minute shows lower impedance |Z| as compared to samples sintered for longer duration.

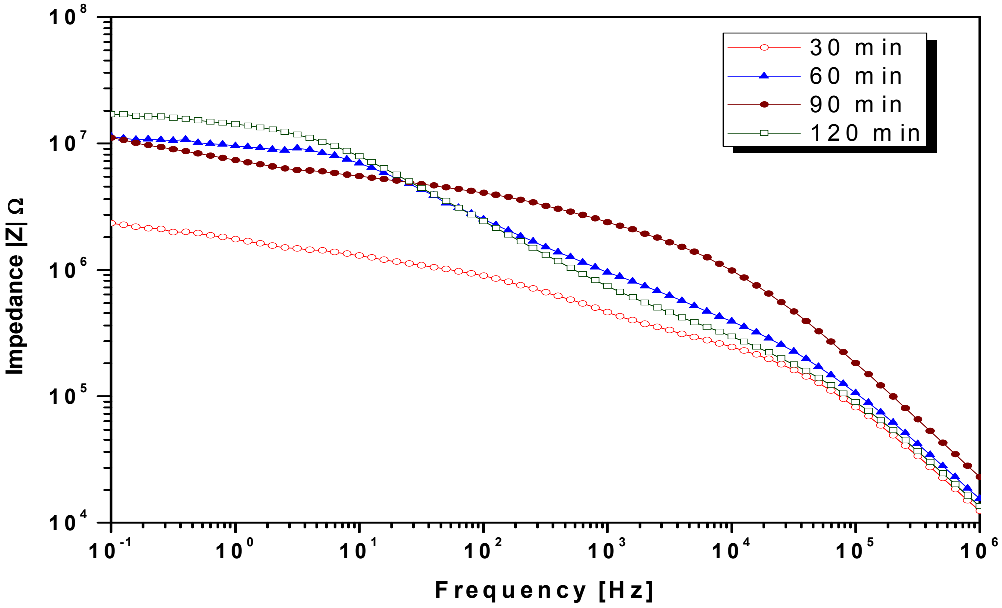

Figure 3.31. Bode plot – Impedance magnitude |Z| vs frequency of $LiTaO_3$ Sintered at 1000^0C for 30, 60, 90 and 120 min

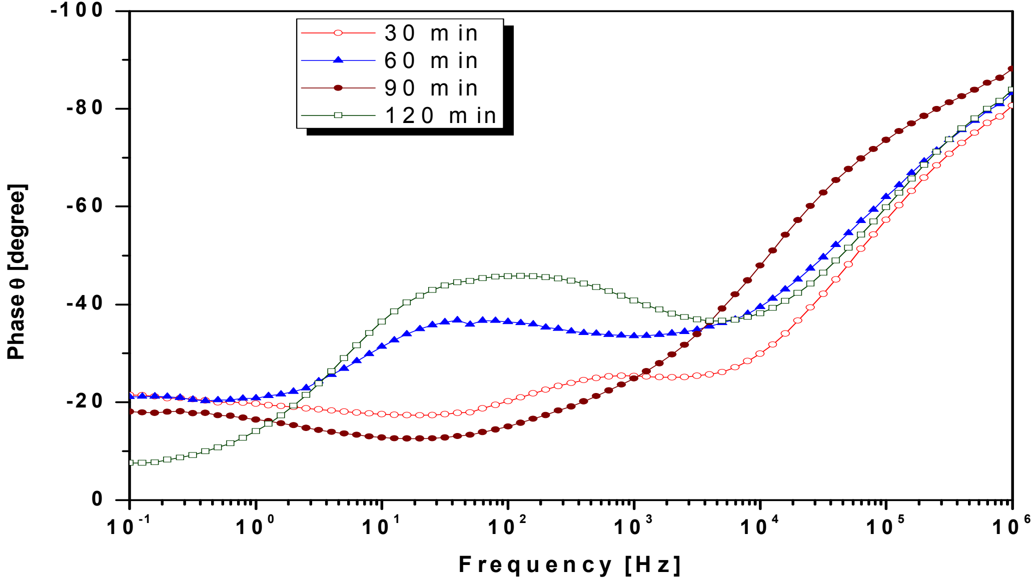

Figure 3.32. Bode plot – Phase Angle vs frequency of $LiTaO_3$ Sintered at 1000^0C for 30, 60, 90 and 120 min

Dielectric Loss vs frequency of LiTaO3 Sintered at 750^{0}C and 1000^{0}C were measured upto 40MHz and plotted in figure 3,33 and 3.34 respectively. It is observed that the the dielectric loss of $LiTaO_3$ decreases with increase in frequency. Since the dielectric loss of $LiTaO_3$ is very less at high frequency, it has potential application in high frequency devices

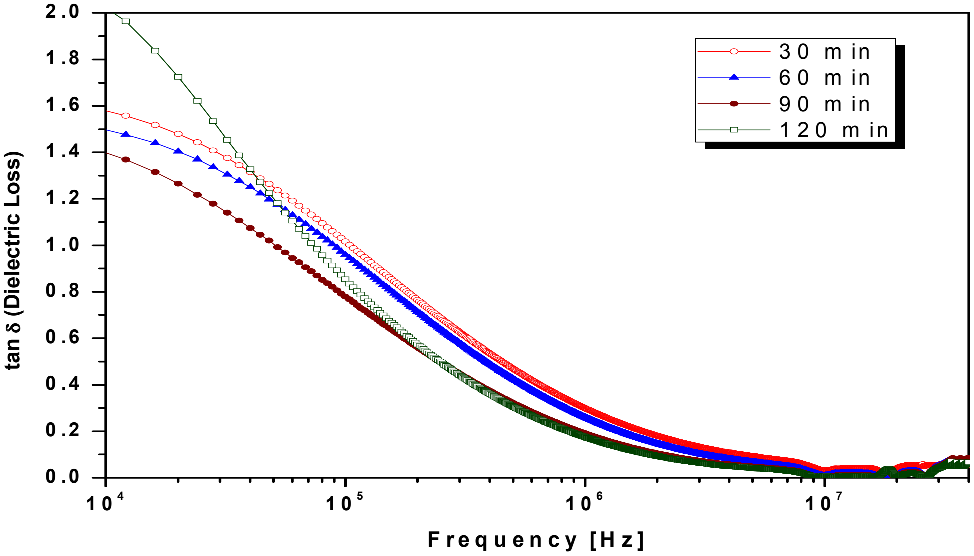

Figure 3.33. Dielectric Loss vs frequency of $LiTaO_3$ Sintered at 750^{0}C for 30, 60, 90 and 120 min

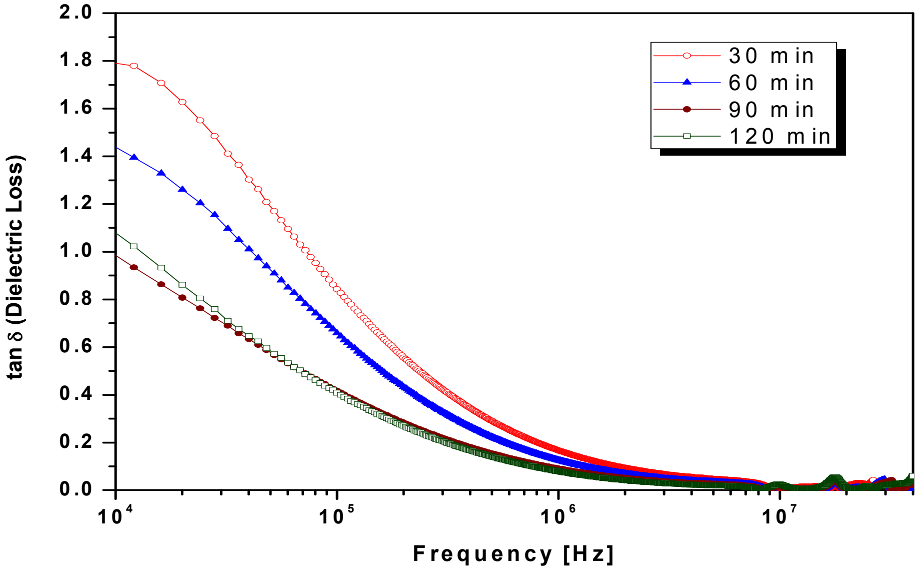

Figure 3.34. Dielectric Loss vs frequency of $LiTaO_3$ Sintered at 1000^{0}C for 30, 60, 90 and 120 min

3.5 Summary

A novel hydroxide precursors procedure for the preparation of ultrafine particles of Lithium niobate and Lithium tantalate was elucidated. The conventional solid state method produces $LiNbO_3$ phase at 900 °C after prolonged firing. However the new novel hydroxide precursor method produces $LiNbO_3$ at 400^0C.

Lithium tantalate ($LiTaO_3$) has the same crystallographic structure as lithium niobate ($LiNbO_3$) and a very similar electronic structure [50]. Both crystals are piezo-, pyro- and ferro-electric, photorefractive and nonlinear with large electro-optic and nonlinear coefficients [51–53]. Since, microstructure affects critically the optical properties, the synthesis of LN ceramic powders with good sinterability and compositional homogeneity is necessary. Traditionally LT is prepared by solid state reaction which leads to inhomogeneity in composition and coarse particles. The wet chemical methods have their own advantages when compared with the traditional solid state method. The advantages include nanocrystalline size, homogeneity in composition, high reactivity and surface area, narrow particle size distribution and low sintering temperature. The wet- chemical methods include coprecipitation, hydrothermal, combustion, alkoxide and citrate gel methods. Recently microwave hydrothermal technique was also used for the preparation of complex oxides.

EDAX shows the purity of product synthesized by hydroxide precursor method, since no other element peaks are observed in EDAX spectrum. Irrespective of heating rate, TGA profile of $LiNbO_3$ clearly shows at around 380 to 400^0C there is a dip in mass profile, which is an indication of solid state reaction takes place with release of hydroxyl ions from the precursors. XRD also conforms the structural formation $LiNbO_3$ at 400^0C

Differential scanning calorimetry provide the information about the activation energy for the formation of $LiNbO_3$ by hydroxide precursor method is 275.63 kJ and activation energy for the formation of $LiTaO_3$ is 177.16 kJ. Nyquist plot as well as Bode plot provide the information about the variation of its impedance parameters with frequency. The real as well as imaginary part of impedance of $LiNbO_3$ is higher than $LiTaO_3$. For both LiNbO3 and LiTaO3, the samples sintered at 1000^0C for 30 min shows lower impedance |Z| as compared to samples sintered for longer duration. As dielectric loss of $LiNbO_3$ is very less at high frequency, it has potential application in high frequency devices.

3.6 References

1. K. Terabe, A. Gruverman, Y. Matsui, N. Iyi and K. Kitamura, J. Mater. Res. 11 (1996) 3152.
2. H. Xie, W.-Y. Hsu and R. Raj, J. Appl. Phys 77 7 (1995) 3420.
3. M. Shimizu, Y. Furushima, T. Nishida and T. Shiosaki, Jpn. J. Appl. Phys. 32 (1993) 4111.
4. H. Tamada, A. Yamada and M. Saitoh, J. Appl. Phys 70 5 (1991) 2536.
5. A. Yamada, H. Tamada and M. Saitoh, J. Appl. Phys 76 3 (1994) 1776.
6. S. Ono, T. Takeo and S. Hirano, J. Am. Ceram. Soc. 79 5 (1996) 1343.
7. S. Hirano, T. Yogo, W. Sakamoto, Y. Takeichi, S. Ono, J. Eur. Ceram. Soc. 24 (2004) 435.
8. A.M. Marsh, S.D. Harkness, F. Qian and R.K. Singh, Appl. Phys. Lett. 62 (1993) 952.
9. S.B. Ogale, R. Nawathey-Dikshit, S.J. Dikshit and S.M. Kanetkar, J. Appl. Phys 71 (1992) 5718.
10. A.A. Wernberg, H.J. Gysling, A.J. Filo and T.N. Blaton, Appl. Phys. Lett. 62 (1993) 946.
11. S. Hirano and K. Kato, Adv.Ceram. Mater. 2 (1987) 142.
12. S. Hirano and K. Kato, J. Non-Cryst. Solids, 100 (1988) 538.
13. S. Hirano and K. Kato, Solid State Ionics 32 (1989) 765.
14. S. Hirano, T. Hayashi, K. Nosaki and K. Kato, J. Am. Ceram. Soc. 72 (1989) 707.
15. S. Hirano, K. Kikuta and K. Kato, Mater. Res. Symp. Proc 200 (1990) 3.
16. T. Yogo, Y. Takeichi, K. Kikuta and S. Hirano, J. Am. Ceram. Soc. 78 (1995) 1649.

17. K. Kikuta, Y. Isobe, T. Yogo, S. Ono and S. Hirano, J. Am. Ceram. Soc. 79 (1996) 2289.
18. S. Hirano, T. Yogo, K. Kikuta, Y. Isobe and S. Ono, J. Mater. Sci. 28 (1993) 4188.
19. S. Ono and S. Hirano, J. Am. Ceram. Soc. 80 10 (1997) 2533.
20. S. Ono and S. Hirano, J. Am. Ceram. Soc. 80 11 (1997) 2869.
21. S. Ono, O. Böse, W. Unger, Y. Takeichi and S. Hirano, J. Am. Ceram. Soc. 81 (1998) 1749.
22. S. Ono and S. Hirano, J. Mater. Res. 16 (2001) 1155.
23. J.-G. Yoon and K. Kim, Appl. Phys. Lett. 68 (1996) 2523.
24. K. Nashimoto, H. Moriyama and E. Osakabe, Jpn. J. Appl. Phys 35 (1996) 4936.
25. K. Nashimoto, M.J. Cima, P.C. McIntyre and W.E. Rhine, J. Mater. Res. 10 (1995) 2564.
26. P.G. Clem and D.A. Payne, Mater. Res. Soc. Symp. Proc 361 (1995) 179.
27. P.G. Clem, Z. Xu and D.A. Payne, Mater. Res. Soc. Symp. Proc 401 (1996) 249.
28. D.C. Sinclair, A.R. West, Physical Review B 39 (1989) 13486.
29. S.M. Kostritskii, Yu.N. Korkishko and V.A. Fedorov, J. Appl. Phys. 91 (2002) 930.
30. A. Rauber, Current Topics in Materials Science, North-Holland Press, Amsterdam (1978).
31. Y. Kuwano, T. Yokoo and K. Shibita, Jpn. J. Appl. Phys. 20 (1981) 221.
32. M.C. Kao, M.S. Lee, C.M. Wang, H.Z. Chen and Y.C. Chen, Jpn. J. Appl. Phys. 41 (2002) 2982.
33. Y. Saito and T. Shiosaki, Jpn. J. Appl. Phys. 30 (1991) 2004.
34. S. Hirano and K. Kato, Bull. Chem. Soc. Jpn. 62 (1989) 249.

35. X.L. Guo, Z.G. Liu, S.N. Zhu, T. Yu, S.B. Xiong and W.S. Hu, J. Cryst. Growth 165 (1997) 187.
36. L.S. Hung, J.A. Agostinelli, J.M. Mir and L.R. Zheng, Appl. Phys. Lett. 62 (1993) 3071.
37. J.A. Agostinelli, G.H. Braunstein and T.N. Blanton, Appl. Phys. Lett. 63 (1993) 123.
38. K. Nashimoto, Mater. Res. Soc. Symp. Proc. 310 (1993) 293.
39. P.J. Retuert, P.G. Kueuer, O. Wittke, R.E. Avila and G.J. Piderit, J. Mater. Res. 10 (1995) 2797.
40. S.I. Hirano and K. Kato, Mater. Res. Soc. Symp. Proc. 155 (1989) 181.
41. A. Askin, G.D. Boyd, J.M. Dziedzic, et al., Appl. Phys. Lett 9 (1966) 72.
42. A. Fini, G. Fazio, M.A. Holgado, M.J.F. Herva, Int. J. Pharm. 171 (1998) 45.
43. Y. Kojima, K. Suzuki, Y. Kawai, J. Power Sources, 155 (2006) 325.
44. G. Bhaskar Kumar, S. Buddhudu, Ceramics International, 35 (2009) 521.
45. F. Pireta, M. Singh, C.G. Takoudis, B.L. Sua, Chem. Phys. Lett, 453 (2008) 87.
46. Qinghui Li, Yuki Ono, Yoshikazu Homma, Izumi Nakai, Katsutoshi Fukuda, Takayoshi Sasaki, Keiichi Tanaka, and Satoshi Nakayama, J. Electron Microscopy 58 (2009) 1.
47. D. Hrunskia, B. Schroederb, M. Scheibc, R.M. Merzd, W. Bockd and C. Wagnerd, Thin Solid Films, 516 (2008) 818.
48. E. Opila, S. Levine and J. Lorincz, J. Materials Science, 39 (2004) 5969.
49. Elizabeth J. Opila, Jim Smith, Stanley R. Levine, Jonathan Lorincz and Marissa Reigel, The Open Aerospace Engineering Journal, 3 (2010) 41.
50. I. Inbar, R.E. Cohen, Phys. Rev. B 53 (1996) 1193.
51. R.C. Miller, W.A. Nordland, Phys. Rev. B 2 (1970) 4896.

52. G.L. Tangonan, M.K. Barnoski, J.F. Lotspeich, A. Lee, Appl. Phys. Lett. 30 (1977) 238.

53. S.-H. Lee, T.W. Noh and J.-H. Lee, Appl. Phys. Lett. 68 (1996) 472.

Chapter 4

Synthesis and Characterization of Sodium Niobate and Tantalate

This chapter comprised about the preparation of Sodium Niobate and Sodium Tantalate and its structural confirmation using X-ray powder diffraction.. The characterization part of this chapter is divided into two vis for $NaNbO_3$ and $NaTaO_3$. Thermal behaviour of both the compounds were analysed for Thermogravimetry Analysis (TGA), Differential Scanning Calorimetery (DSC) and activation energy is estimated for the phase formation. Impedance Spectroscopy. Nyquist plot as well as Bode plot were constructed from Impedance data. The average particle size and morphology of the compounds were studied using scanning electron microscopy and the elemental analysis of the compound was carried out using EDAX.

4.1 Introduction

$NaNbO_3$ and $NaTaO_3$ are well-known pervoskite oxides (ABO_3) which possess attractive physical properties such as low density, high sound velocity and are useful for ferroelectric and piezoelectric applications [1–7]. The sodium resides on the twelve coordinated A site, and the Nb/Ta metal occupies the octahedral B site. For $NaTaO_3$, there is only one crystallographic sodium site present, which is surrounded by 12 oxygen atoms whereas for $NaNbO_3$, two distinct crystallographic Na sites are present.

$NaNbO_3$ has been attracting increasing interests for its applications in lead-free piezoelectric ceramics [8–11]. Ferroelectric and piezoelectric ceramics made from $NaNbO_3$ based solid solutions have great potential applications in electromechanical and nonlinear optical devices [12–15]. One striking example showed that $NaNbO_3$ was one of the important components of the environmentfriendly, lead-free piezoelectric ceramics that could most likely replace the widely used lead zirconium titanate (PZT) [16].

Alkali niobate systems have been investigated to obtain materials with low dielectric loss, greater stability and improved performance. However, the electric properties of polycrystalline niobates depend on microstructure, which is strongly influenced by the preparation method and the sintering process [17]. Alkali metal niobate powders are usually prepared via a solid-state reaction between Nb_2O_5 and alkali metal carbonates. This classical method involves high temperatures and long reaction times, produces the volatilization of the alkali metal, leads to poor compositional homogeneity and provides products with large particles [18]. Alternative routes need to be developed to facilitate the production of desired materials in a controllable way. Ceramic syntheses using chemical [19], hydrothermal

[20–23], polymeric precursors [24] and mechanochemical activation [25–27] have been described in the literature to facilitate the reactions. However, the processes are generally complicated and most of these chemistry-based routes require high purity inorganic or organometallic reactants, more expensive than the widely available oxides and carbonates [28].

$NaTaO_3$ is a member of the perovskite family having the chemical formula ABO_3 are the subject of extensive investigations because of their technical importance[29] and luminescence[30], photocatalytic activity [31–33]. $NaTaO_3$ attracts our attention because it attains the highest photocatalytic quantum yield for water splitting into H_2 and O_2 under UV irradiation among all known materials [34]. Also the photocatalytic decomposition of H_2O into H_2 and O_2 using solar energy is one of such systems in which clean and high energy-containing H_2 is directly obtained [35].

The solid-state synthesis method was widely used to prepare the vast majority of the tantalates acting as photocatalysts [36–43]. A few studies developed other synthetic routes for the tantalates [43, 44], hydrothermal method[34,35]. The solid-state method requires high-temperature (1420 K) [37] and long-duration calcination, leading to grain growth (thus small surface area) and loss of stoichiometry of the products [44]. Moreover, the high temperature heat treatment may result in the large grain growth (thus the reduction in surface areas), which may lead to low photocatalytic activities [35]. The sol–gel method has been used in syntheses of nanosized materials with considerably larger surface area [45, 46].

Traditionally $NaNbO_3$ and $NaTaO_3$ have been synthesized via solid state reaction of alkali metal carbonates and Nb_2O_5/Ta_2O_5 at temperatures of 800^0C or above which sometimes leads to inhomogeneity in composition and coarse particles [47, 48]. The aim of present study was to prepare of $NaNbO_3$ and $NaTaO_3$ at low temperature.

4.2 Experimental

4.4.1 Synthesis of Sodium Niobate

The schematic flow chart for the preparation of sodium niobate is given in figure 4.1. For preparing $NaNbO_3$, AR grade niobium (V) oxide, sodium hydroxides, hydrofluric acid (HF (40 %)) and standard ammonia solution were used as starting materials.

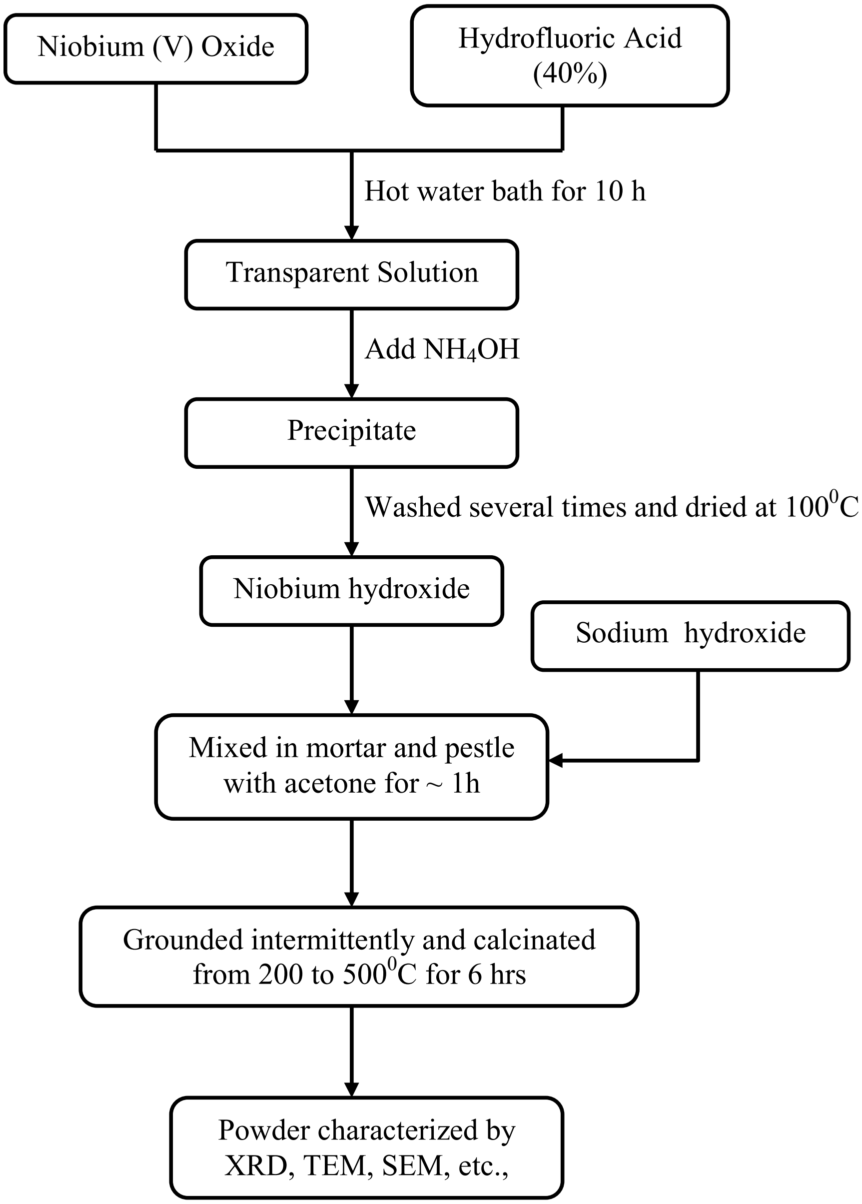

Figure 4.1 Flow chart for the preparation of $NaNbO_3$ by hydroxide precursor method

Required quantity of Nb_2O_5 was dissolved in HF (40 %) after heating in a hot water bath for 10 h. Then an aqueous ammonium hydroxide was added dropwise to the NbF_5 solution to precipitate niobium as hydroxide under basic conditions. The precipitate was washed free of anions and dried at 100˚ C in an oven. A stoichiometric amount of NaOH was mixed with $Nb(OH)_5.xH_2O$ and ground well for ~1 hour using acetone in a agate mortar. These powders were calcined at different temperatures from 200 to 500˚ C for 6 hours. The chemical reaction takes place in the formation of NaNbO3 by hydroxide precursor method is given below

$$Nb_2O_5 + 10HF \xrightarrow{\Delta\ 90^0C,\ 10\ h} 2NbF_5 + 5H_2O \xrightarrow{NH_3OH} \underset{\text{Niobium hydroxide}}{Nb(OH)_5}$$

$$NaOH + Nb(OH)_5 \xrightarrow{\Delta\ 400^0C,\ 6\ h} NaNbO_3$$

4.2.2 Synthesis of Sodium Tantalate

For preparing $NaTaO_3$, AR grade tantalum (V) oxide, sodium hydroxides, hydrofluric acid (HF (40 %)) and standard ammonia solution were used as starting materials. Required quantity of Ta_2O_5 was dissolved in HF (40 %) after heating in a hot water bath for 10 h. Then an aqueous ammonium hydroxide was added dropwise to the TaF_5 solution to precipitate niobium as hydroxide under basic conditions. The precipitate was washed free of anions and dried at 100˚ C in an oven. A stoichiometric amount of NaOH was mixed with $Ta(OH)_5.xH_2O$ and ground well for ~1 hour using acetone in a agate mortar. These powders were calcined at different temperatures from 200 to 500˚ C for 6 hours. The schematic of overall procedure to synthesis $NaTaO_3$ is given in figure 4.2 as a flow chart format. The major chemical reaction involved in the formation of Sodium tantalate is given below

$$Ta_2O_5 + 10HF \xrightarrow{\Delta\ 90^0C,\ 10\ h} 2TaF_5 + 5H_2O \xrightarrow{NH_3OH} \underset{\text{Tantalum hydroxide}}{Ta(OH)_5}$$

$$NaOH + Ta(OH)_5 \xrightarrow{\Delta\ 450^0C,\ 6\ h} NaTaO_3$$

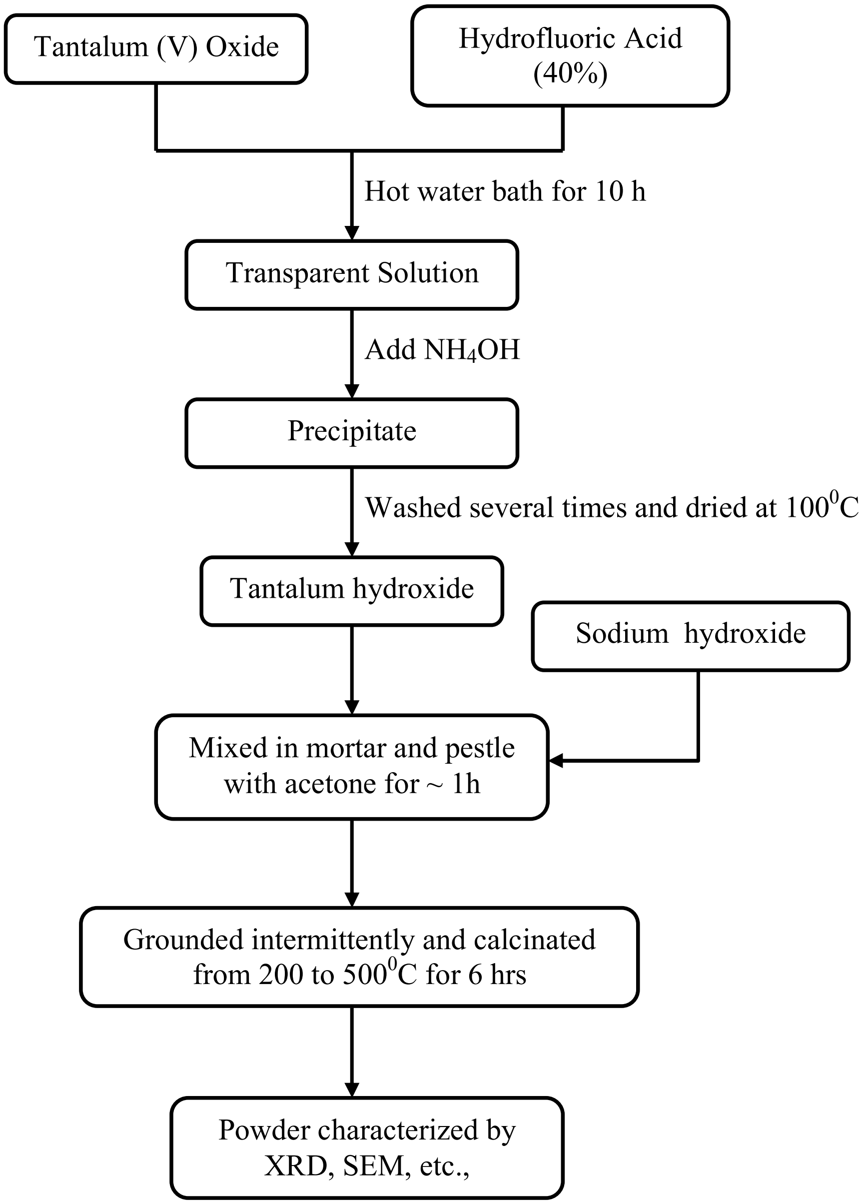

Figure 4.2 Flow chart for the preparation of $NaTaO_3$ by hydroxide precursor method

4.3 Characterization of Sodium Niobate

4.3.1 X-ray powder diffraction

The powder X-ray pattern was recorded for all the samples calcined at 200^0C by using a Philips PW-1710 model X-ray diffractometer and Cu K_∞ radiation. For lattice parameter and interplanar distance (d) calculation, the samples were scanned in the 2θ range of 20 – 60^o for a period of 5s in the step scan mode. Silicon was used as an internal standard. Least squares method was used to determine the lattice parameters. Fig 4.3 shows the XRD pattern of the $NaNbO_3$ powder calcined at 200° C. All the d-line peaks are similar to that reported in the literature. This is the lowest temperature reported so far for the formation of $NaNbO_3$ phase. The crystal structure of $NaNbO_3$ is orthorhombic (JCPDS: 14- 603). The calculated lattice parameters by least squares fit are a = 5.511 Å, b = 5.557 Å and c = 15.540 Å.

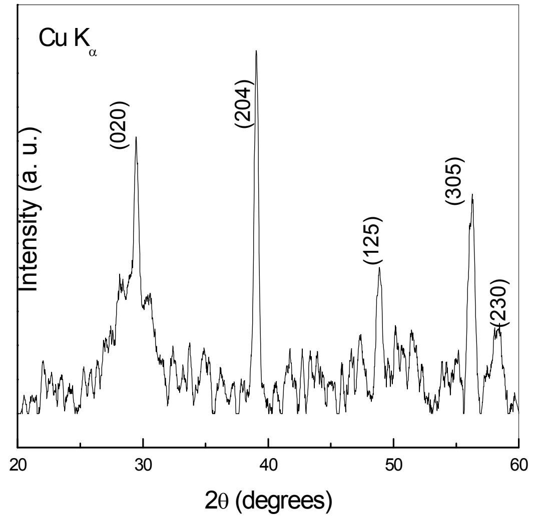

Fig. 4.3. XRD of NN precursor powder calcined at (a) 200°C

4.3.2 Energy Dispersive X-Ray Analysis

EDAX profile of $NaNbO_3$ ceramic powder synthesized by hydroxide precursor method is measured using JEOL JED-2300 Energy dispersive X-ray analysis Station and presented in Fig. 4.4 to validate the presence of Sodium, Niobium and Oxygen.

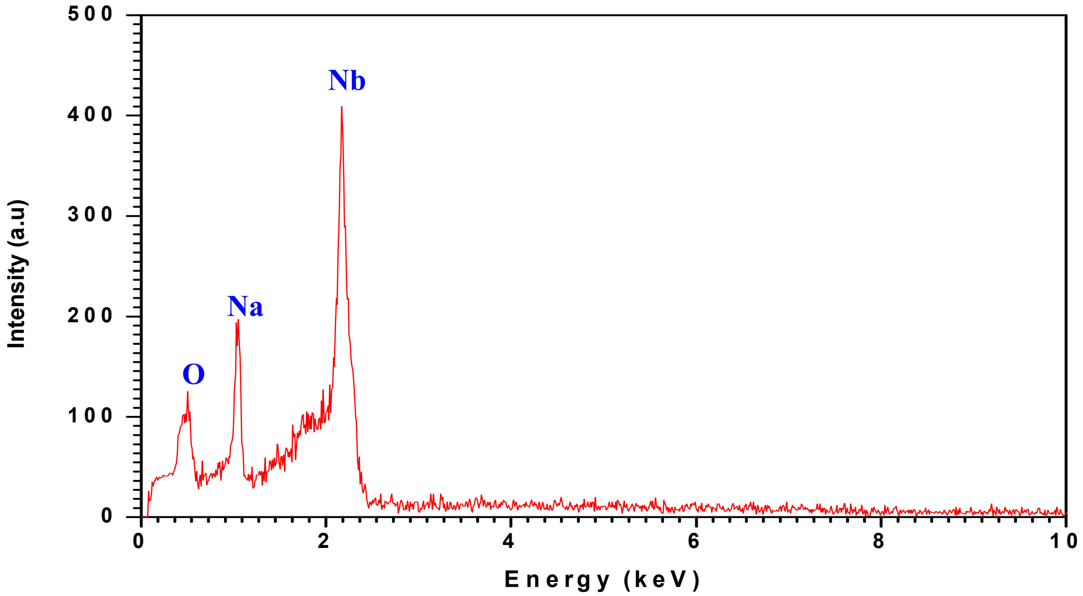

Figure 4.4. EDAX Spectrum of $NaNbO_3$ prepared by hydroxide precursor method

The EDAX spectrum of $NaNbO_3$ prepared by hydroxide precursor method was scanned from 0 to 10keV and characteristics peaks for Sodium, Niobium and Oxygen is observed at 1.041 keV, 2.166 keV and 0.525keV respectively and corresponding identified transition are tabulated in Table 4.1.

Table 4.1. EDAX spectrum peaks observed for $NaNbO_3$

Sr No.	Element	Peak Observed	Transition
1	Oxygen	0.525 keV	K-alpha
2	Sodium	1.041 keV	K-alpha
3	Niobium	2.166 keV	L-alpha (L3M5)

4.3.3 Scanning Electron Microscopy

The SEM images were observed using a Leica Cambridge 440 microscope. All the powders were dispersed in amyl acetate for SEM studies. The average particle size and morphology of these calcined powders of $NaNbO_3$ were examined by scanning electron microscopy. Fig. 4.5 shows the SEM images for $NaNbO_3$ calcined at 400^0C .

In the case of $NaNbO_3$, there was not much agglomeration with an average particle size of 70 nm (Fig.4.5).

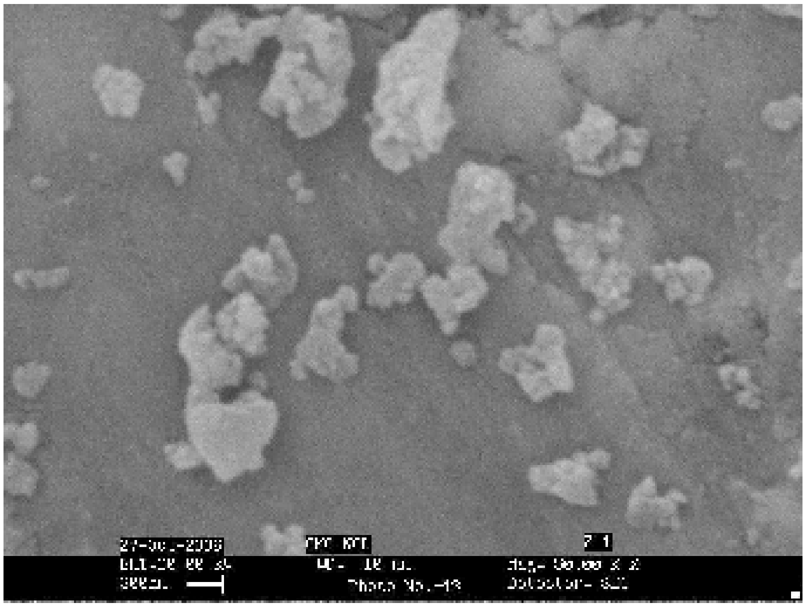

Fig. 4.5. SEM image of NN powder calcined at 400°C

4.3.4 Thermogravimetry Analysis

Stoichiometric amount of Sodium hydroxide and freshly prepared Niobium hydroxide is mixed well thoroughly and thermogravimetric analysis of this mixture is carried out at 10 different heating rate (2.5, 5, 7.5, 10, 12.5, 15, 17.5, 20, 22.5 and 25^0C/min) and depicted in figure 4.6. Around 7 to 16 mg of mixture is used for TGA analysis. Irrespective of heating rate, figure 4.6 clearly shows gradual dip in mass upto 200^0C and then stable profile, which is an indication of solid state reaction takes place with release of hydroxyl ions from the precursors. XRD also conforms the structural formation $NaNbO_3$ at 200^0C.

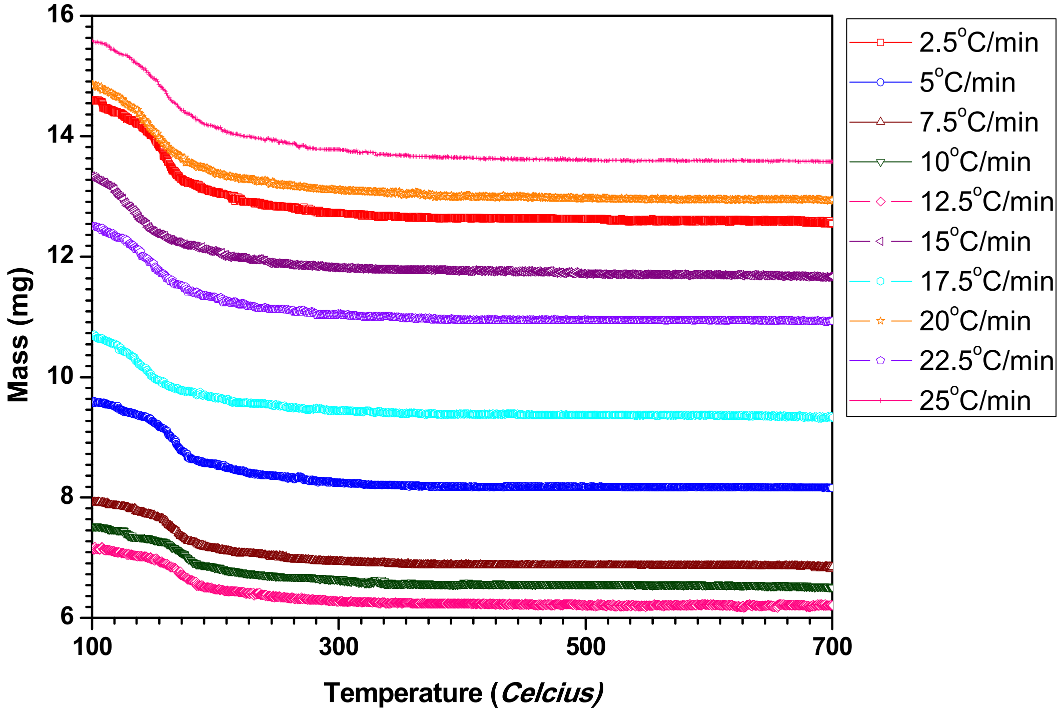

Figure 4.6. TGA profile of $NaNbO_3$ formation at different heating rate

4.3.5 Differential Scanning Calorimetery

Differential Scanning Calorimetric (DSC) analysis of $NaNbO_3$ was carried out at 5 different heating rate (2.5, 5, 7.5, 10 and 15^0C/min). Stoichiometric amount of Sodium hydroxide and freshely prepared Niobium hydroxide are mixed well thoroughly. Around 20 mg of mixture is used for DSC analysis. Inert Nitrogen gas is used as a purge gas during DSC analysis of mixture. The exothermic DSC peeks were observed at around 180^0C and the peak shifts with heating rate and tabulated in Table 1 for the computation of activation energy by Kissinger method. From the table 4.2, Kissinger plot was constructed to find the linear equation, from the slope of the equation the activation energy for the formation of $NaNbO_3$ by hydroxide precursor method is 91.42 kJ.

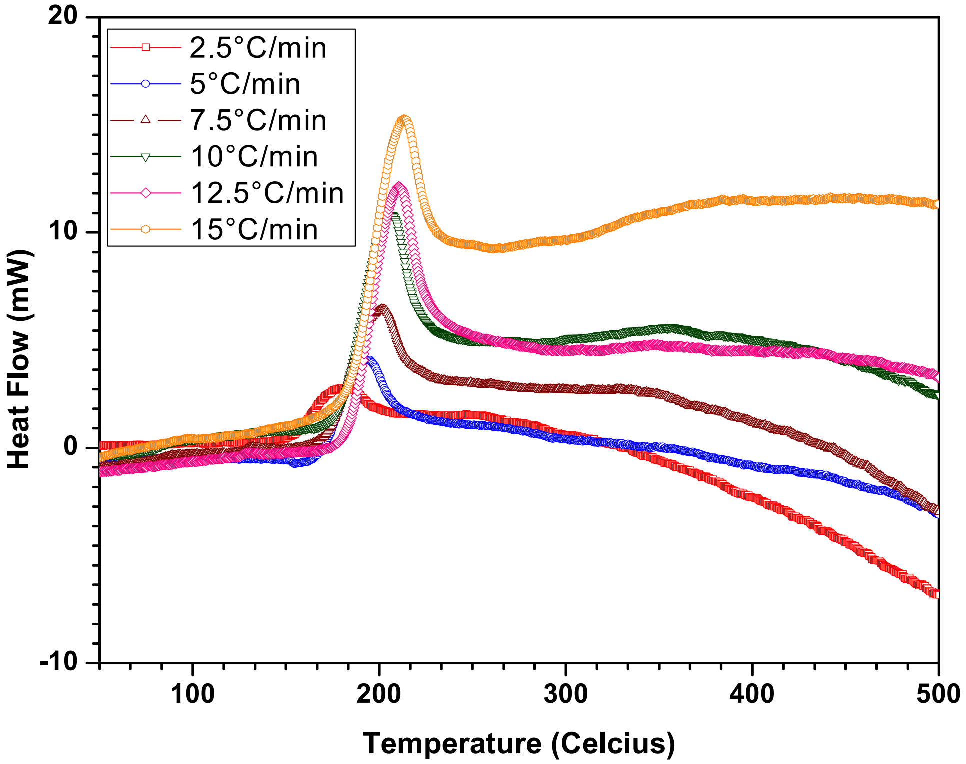

Figure 4.7. DSC profile of $NaNbO_3$ formation at different heating rate

Table 4.2. DSC data on $NaNbO_3$ at various heating rates (Kissinger method).

Heating rate β (^{0}C)	Peak Tmax (^{o}C)	Peak Tmax (K)	T_{max}^2	$\frac{1}{T_{max}}$	$\frac{\beta}{T_{max}^2}$	$-\ln\left(\frac{\beta}{T_{max}^2}\right)$	Slope	Activation Energy (kJ/mol)
2.5	180.19	453.34	205517	0.00220	1.216E-05	11.316	10996.7416	91.42
5	194.59	467.74	218781	0.00213	2.285E-05	10.686		
7.5	201.42	474.57	225217	0.00210	3.330E-05	10.309		
10	206.59	479.74	230150	0.00208	4.344E-05	10.043		
12.5	210.52	483.67	233937	0.00206	5.343E-05	9.8370		
15	213.20	486.35	236536	0.00205	6.341E-05	9.6658		

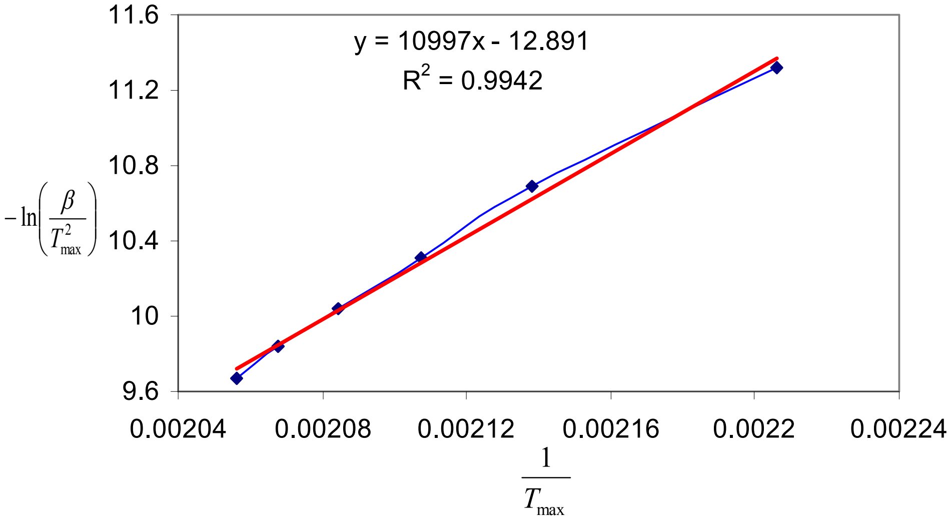

Fig. 4.8. Kissinger Plot for $NaNbO_3$ for computing activation energy.

4.3.6 Impedance Spectroscopy

The impedance measurement from 0.1Hz to 1 MHz using Solartron SI-1260 Impedance/Gain Phase Analyser with Solartron 1294 Impedance Interface for PC is presented in this section. Impedance spectrum were also recorded from 100 Hz to 40 MHz at different bias voltage -40 Volt to + 40 Volt using HP Impdeance analyzer to study the influence of bias voltage from -40 V to + 40 V. However no noticeable change is profile is observed and hence the data is discarded in this thesis. The Nyquist plot for $NaNbO_3$ prepared by hydroxide precursor method is graphically plotted in figure 4.9 for the frequency to 10^6 Hz. Figure 4.9 shows single semi-circle formation for $NaNbO_3$ samples sintered at 750 degree Celsius for 30, 60, 90 and 120 minutes. Nyquist plot for higher frequency is shown in figure 4.10 and it doesn’t show any additional semicircle arc formation at higher frequency. In the Nyquist plot the semicircle at low frequency relates grain boundary, secondary phase segregated at grain boundary and sometimes effect of electrode.

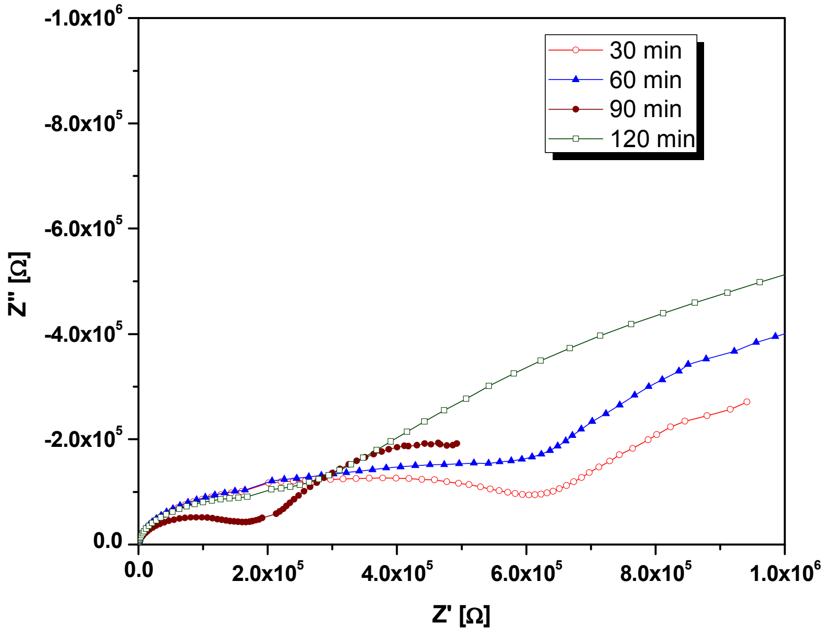

Figure 4.9. Nyquist plot of $NaNbO_3$ Sintered at 750^0C for 30, 60, 90 and 120 min

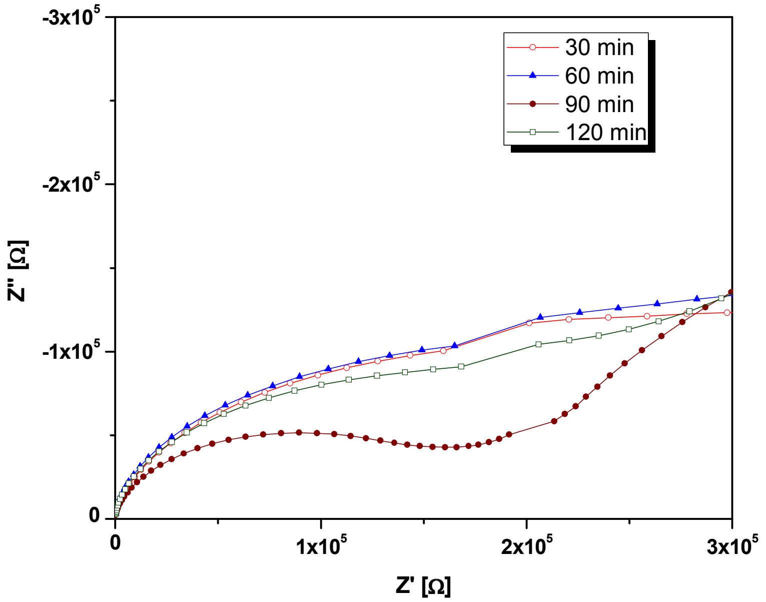

Figure 4.10. Nyquist plot at high frequency observed for $NaNbO_3$ Sintered at 750^0C for 30, 60, 90 and 120 min

Bode plot was graphically ploted for the for $NaNbO_3$ samples sintered at 750^0C for 30, 60, 90 and 120 minutes with frequency vs magnitude of impedance as shown in figure 4.11 and frequency vs phase angle as shown in 5.12. Figure 5.11

shows the decrease in magnitude of impedance drastically with increase in frequency. The frequency dependence of phase angle is observed in figure 4.12 for $NaNbO_3$ samples sintered at 750^0C. The sample sintered for 120 min shows higher impedance |Z| as compared to samples sintered for smaller duration.

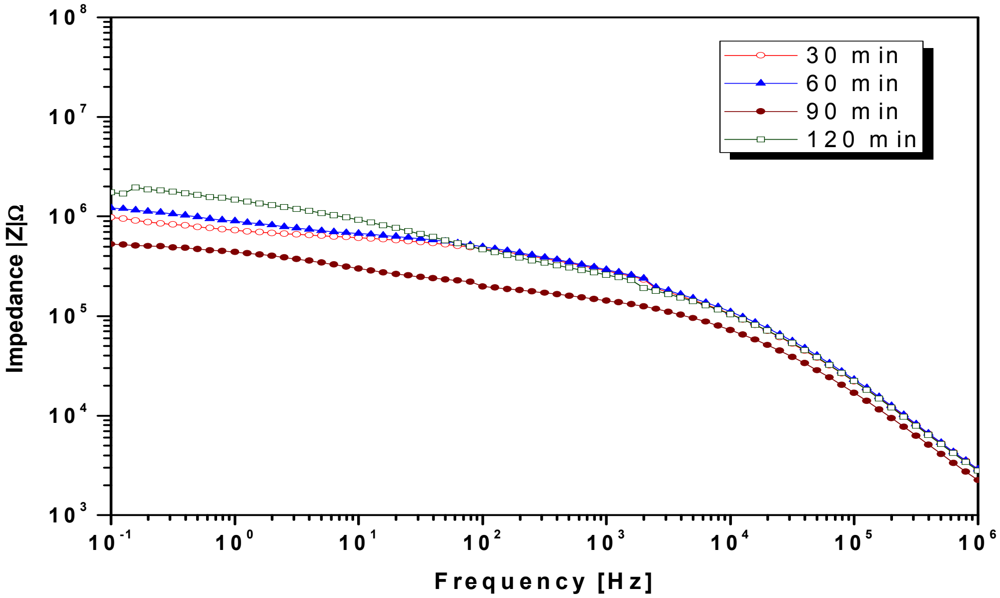

Figure 4.11. Bode plot – Impedance magnitude |Z| vs frequency of $NaNbO_3$ Sintered at 750^0C for 30, 60, 90 and 120 minutes

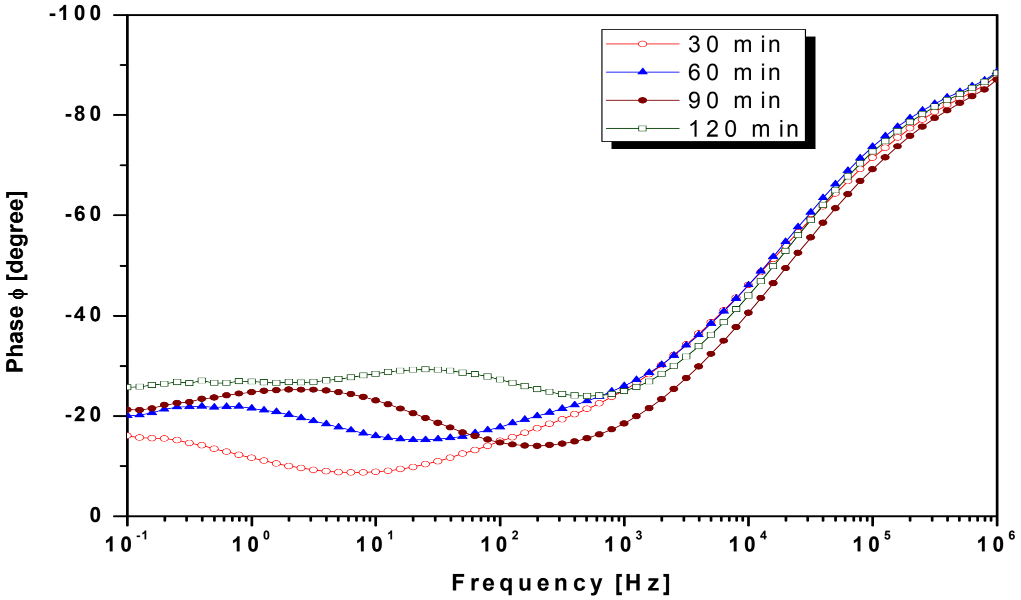

Figure 4.12. Bode plot – Phase Angle vs frequency of $NaNbO_3$ Sintered at 750^0C for 30, 60, 90 and 120 min

The variation of real (Z') and Imaginary (Z") part or Nyquist plot of impedance with frequency for $NaNbO_3$ samples sintered at 1000^0C for 30, 60, 90 and 120 min is shown in figure 4.13. A single semicircular arc is appeared for all samples, even high frequency Nyquist plot presented in figure 4.14 also doesn't show any additional semicircular arc. The semicircle at low frequency for $NaNbO_3$ samples sintered at 1000^0C relates grain boundary, secondary phase segregated at grain boundary and sometimes effect of electrode.

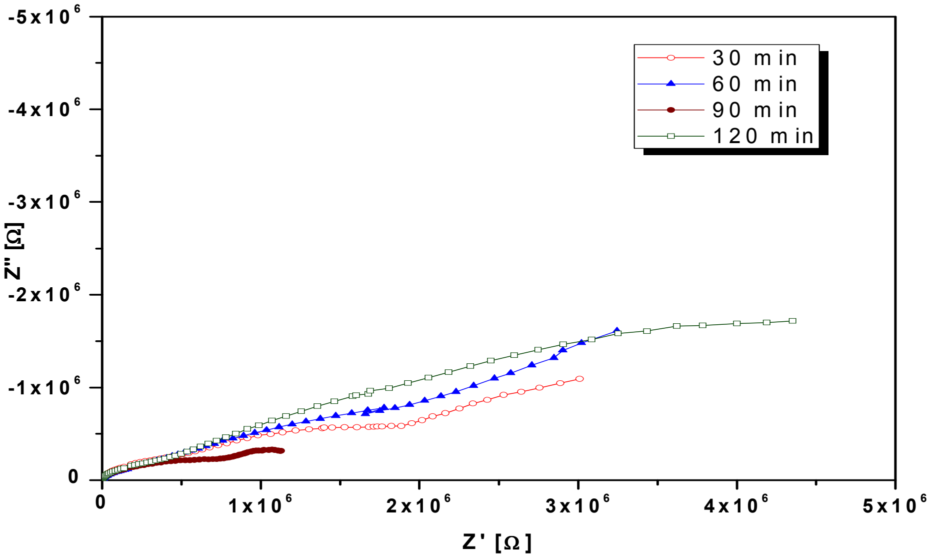

Figure 4.13. Nyquist plot of $NaNbO_3$ Sintered at 1000^0C for 30, 60, 90 and 120 min

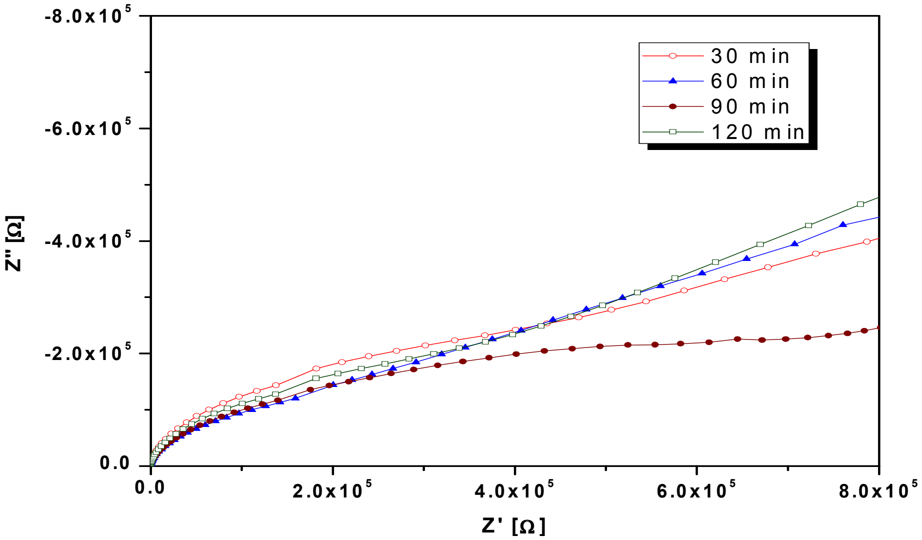

Figure 4.14. Nyquist plot at high frequency observed for $NaNbO_3$ Sintered at 1000^0C for 30, 60, 90 and 120 min

Bode plot was constructed for the for $NaNbO_3$ samples sintered at 1000^0C for 30, 60, 90 and 120 min is with frequency vs magnitude of impedance as shown in figure 4.15 and frequency vs phase angle as shown in figure 4.16. Both the figures shows the frequency dependence of impedance parameters for $NaNbO_3$ samples

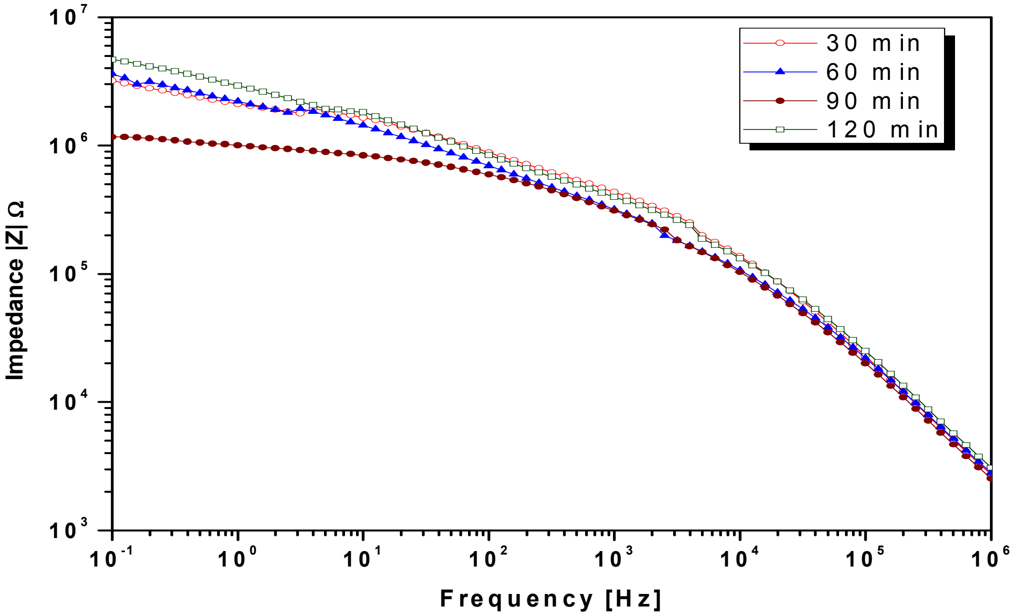

Figure 4.15. Bode plot – Impedance magnitude |Z| vs frequency of $NaNbO_3$ Sintered at 1000^0C for 30, 60, 90 and 120 min

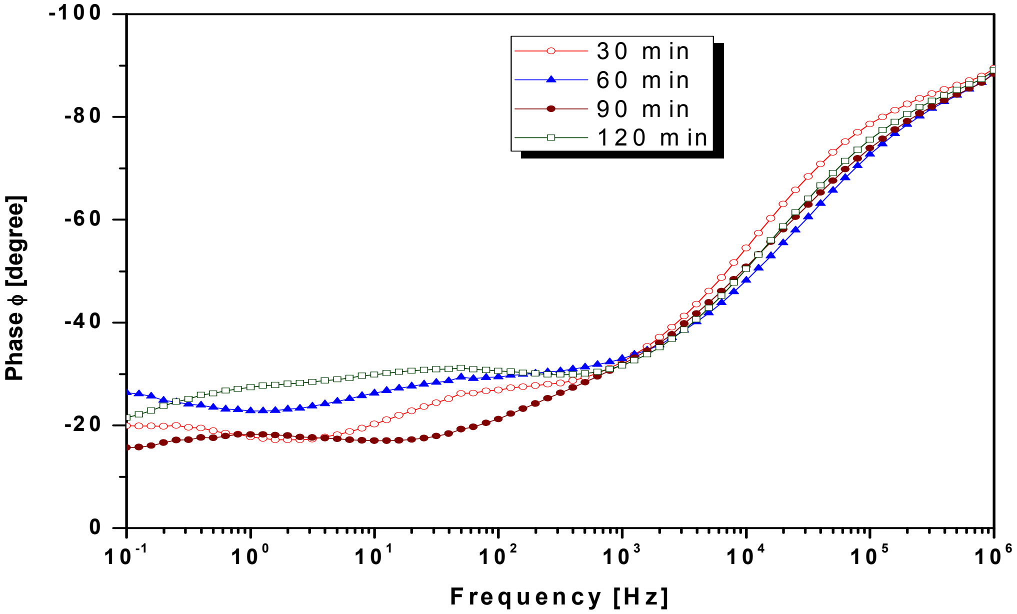

Figure 4.16. Bode plot – Phase Angle vs frequency of $NaNbO_3$ Sintered at 1000^0C for 30, 60, 90 and 120 min

Dielectric Loss vs frequency of $NaNbO_3$ Sintered at 750^0C and 1000^0C were measured upto 40MHz and plotted in figure 4.17 and 4.18 respectively. It is observed that the dielectric loss of $NaNbO_3$ decreases with increase in frequency, however an abnormal high dielectric loss peak is absorbed at around 20MHz. Presence of dislocations or voids can also influence the dielectric loss of the bulk sample. The dielectric loss observed for the samples sintered at 750^0C is higher than the samples sintered at 1000^0C.

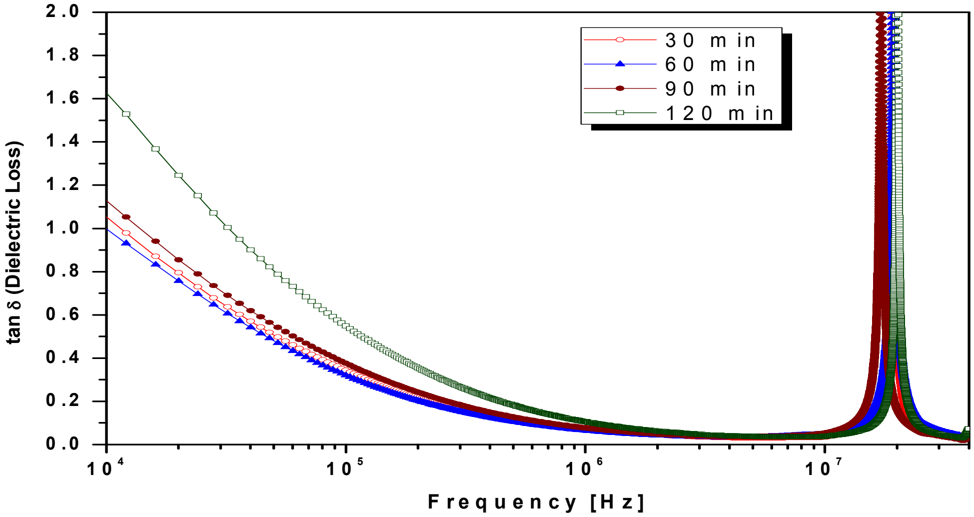

Figure 4.17. Dielectric Loss vs frequency of NaNbO3 Sintered at 750^0C for 30, 60, 90 and 120 min

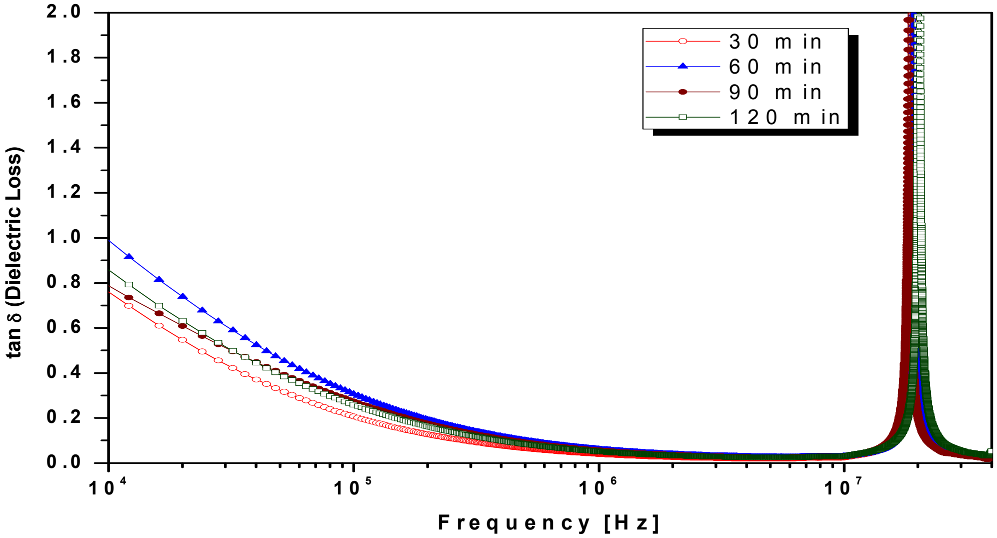

Figure 4.18. Dielectric Loss vs frequency of $NaNbO_3$ Sintered at 1000^0C for 30, 60, 90 and 120 min

4.4 Characterization of Sodium Tantalate

4.4.1 X-ray powder diffraction

X-ray powder diffraction patterns of the $NaTaO_3$ precursor powder calcined at 100, 200, 300 and 400 degree Celcius is shown in Fig. 4.19. XRD patterns for the powder calcined at 400 °C for a duration of 4 hours, leads to the formation of major $NaTaO_3$ phase. This is the lowest temperature reported so far on the formation of $NaTaO_3$ phase.

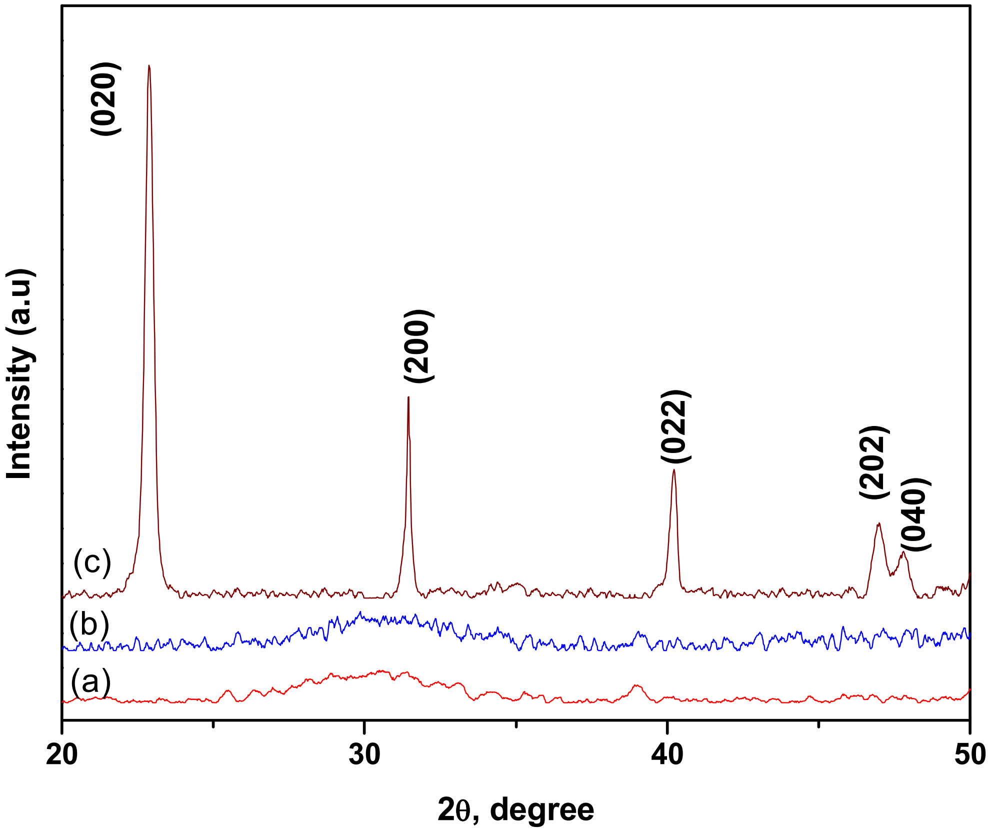

Figure 4.19. XRD of $NaTaO_3$ precursor powder (a) calcined at 100 °C, (b) calcined at 200 °C and calcined at 500 °C for 4 h.

All the d-line peaks are similar to that reported in the literature. The $NaTaO_3$ has a orthorhombic body-centered crystal structure (JCPDS-25-0863). The calculated lattice parameters by least square fit are a=5.513 Å, b= 7.75Å and c=5.494 Å. The conventional solid state method produces $NaTaO_3$ phase at 1000 °C after prolonged firing. The average crystallite size of 85 nm was calculated from the Scherrer's formula

$$t = K\,\lambda/B\,\mathrm{Cos}\theta_B$$

where t is the average size of the particles assuming particles to be spherical,K=0.9, λ is the wavelength of X-ray radiation, B is the full-width at half maximum of the diffracted peak and θB is the angle of diffraction.

4.4.2 Energy Dispersive X-Ray Analysis

The elemental compositions of the synthesized $NaTaO_3$ samples were confirmed by Energy Dispersive X-ray Spectroscopic Analysis (EDAX) using an X-ray detector attached to the SEM and presented in figure 4.20. EDAX detector is operated at liquid nitrogen temperatures during measurements.

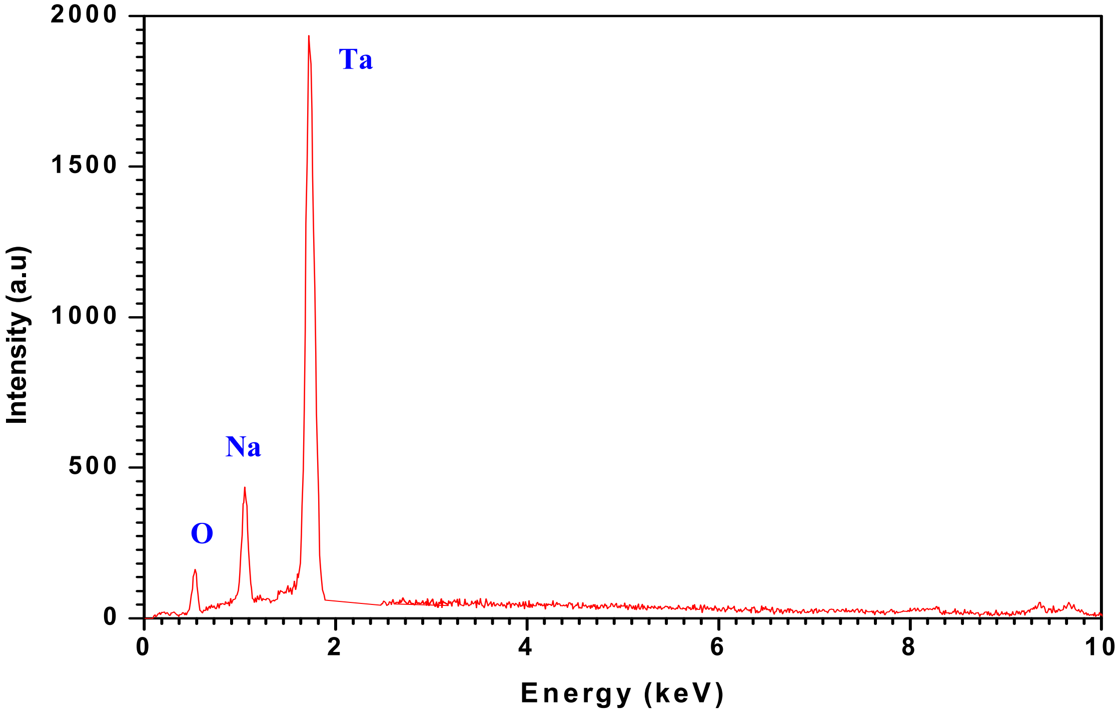

Figure 4.20. EDAX Spectrum of $NaTaO_3$ prepared by hydroxide precursor method

The EDAX spectrum of $NaTaO_3$ prepared by hydroxide precursor method was scanned from 0 to 10keV. The characteristic M-alpha peak for Tantalum and K-alpha peak for Oxygen are observed at 1.709 keV 0.525 keV. The characteristic K-alpha peak for Sodium at 1.041keV is also observed in the EDAX spectrum as reported for sodium in literature [49–54]. The summary of EDAX peaks observed for $NaTaO_3$ and corresponding identified transition are tabulated in Table 4.3

Table 4.3 EDAX spectrum peaks observed for $NaTaO_3$

Sr No.	Element	Peak Observed	Transition
1	Oxygen	0.525 keV	K-alpha
2	Sodium	1.041 keV	K-alpha
3	Tantalum	1.709 keV	M-alpha

4.4.3 Scanning Electron Microscopy

The SEM images were observed using a Leica Cambridge 440 microscope. All the powders were dispersed in amyl acetate for SEM studies. Silver paste was used to stick the sample to the stub and a thin layer of gold was coated on surface of sample using an ion beam sputtering system (Poloran equipment ltd., SEM coating unit E5000) to avoid charging the specimen. The morphology of calcined powders of $NaTaO_3$ were examined by scanning electron microscopy. Fig. 4.21 shows the SEM images for $NaTaO_3$ calcined at 500^0C . The average particle size of about 80nm is observed scanning electron microscopy for $NaTaO_3$.

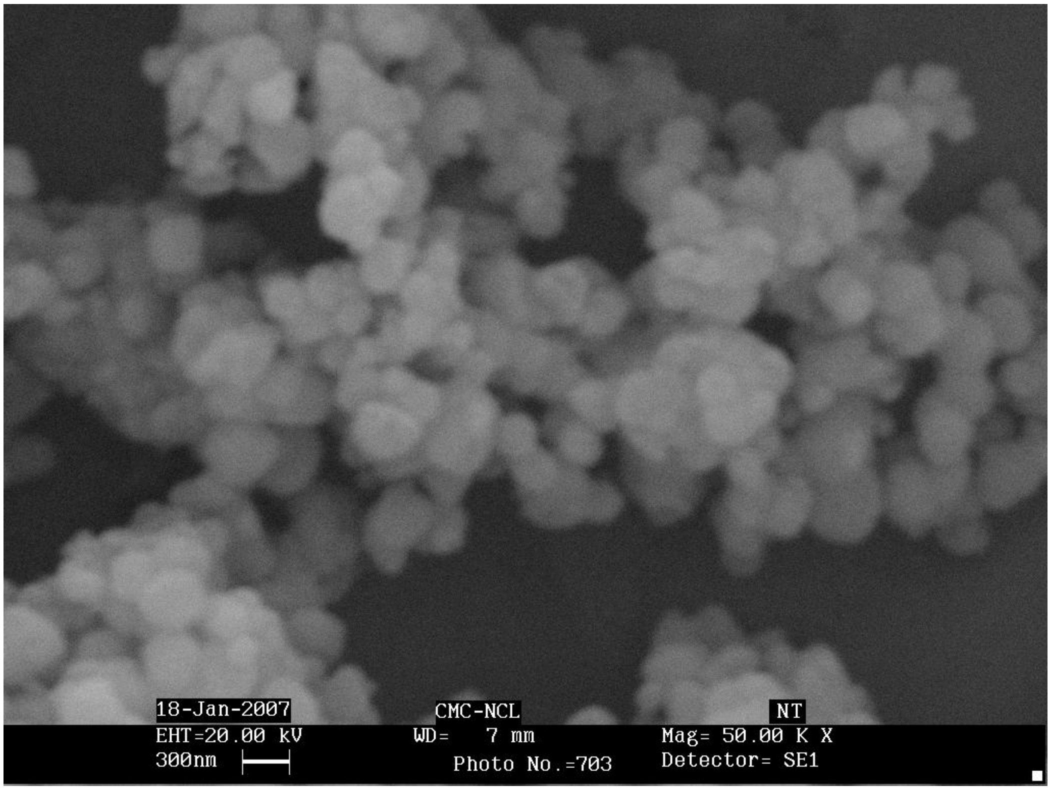

Fig. 4.21. SEM image of $NaTaO_3$ powder calcined at 500˚C

4.4.4 Thermogravimetry Analysis

Stoichiometric amount of Sodium hydroxide and freshly prepared Tantalum hydroxide obtained are mixed well thoroughly and thermogravimetric analysis of this mixture is carried out at 5, 7.5, 10, 12.5, 15 and 17.5, 20, 22.5 and 25^0C/min and depicted in figure 4.22. Around 13 to 22 mg of mixture is used for TGA analysis. Irrespective of heating rate, figure 1 clearly shows a sudden dip at around 100^0C followed by a gradual dip in mass upto 500C and then stable profile, which is an indication of solid state reaction takes place with release of hydroxyl ions from the precursors. XRD also conforms the structural phase formation $NaTaO_3$ at 500^0C.

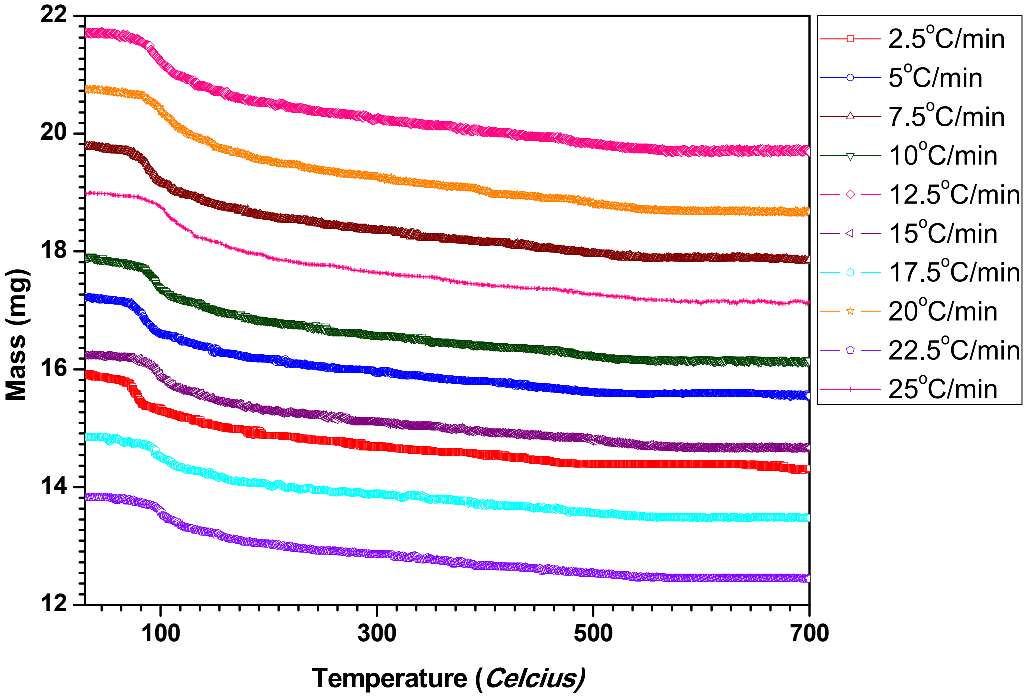

Figure 4.22. TGA profile of $NaTaO_3$ formation at different heating rate

4.4.5 Differential Scanning Calorimetery

Differential Scanning Calorimetric (DSC) analysis of $NaTaO_3$ was carried out at 5 different heating rate (2.5, 5, 7.5, 10 and 15^0C/min) and presented in figure 4.23. Stoichiometric amount of Sodium hydroxide and freshly prepared Tantalum hydroxide are mixed well thoroughly. Around 20 mg of mixture is used for DSC analysis. Inert Nitrogen gas is used as a purge gas during DSC analysis of mixture. The exothermic DSC peeks were observed at around 465^0C and the peak shifts with heating rate and tabulated in Table 4.4 for the computation of activation energy by Kissinger method. From the table 4.4, Kissinger plot (figure 4.24) was constructed to find the linear equation, from the slope of the equation the activation energy for the formation of $NaTaO_3$ by hydroxide precursor method is 113.82 kJ.

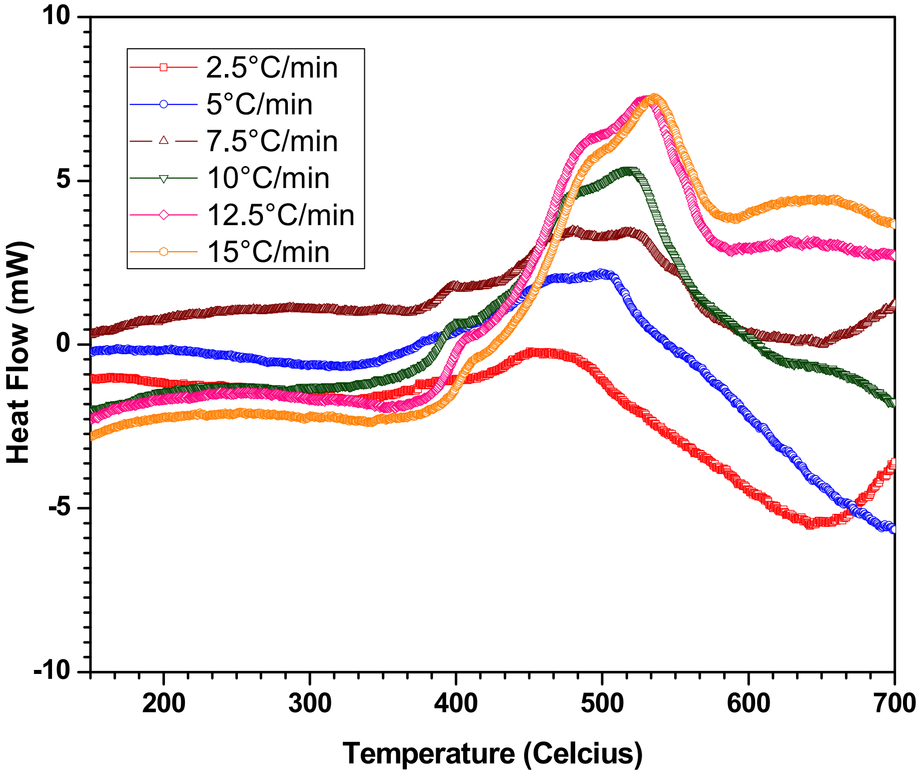

Figure 4.23 DSC profile of $NaTaO_3$ formation at different heating rate

Table 4.4 DSC data on $NaTaO_3$ at various heating rates (Kissinger method).

Heating rate β (^{0}C)	Peak Tmax (^{o}C)	Peak Tmax (K)	T^2_{max}	$\frac{1}{T_{max}}$	$\frac{\beta}{T^2_{max}}$	$-\ln\left(\frac{\beta}{T^2_{max}}\right)$	Slope	Activation Energy (kJ/mol)
2.5	465.59	738.74	545737	0.001353	4.580E-06	12.293	13690.6725	113.82
5	498.79	771.94	595891	0.001295	8.390E-06	11.688		
7.5	516.08	789.23	622884	0.001267	1.204E-05	11.327		
10	520.61	793.76	630055	0.001259	1.587E-05	11.050		
12.5	530.44	803.59	645757	0.001244	1.935E-05	10.852		
15	535.02	808.17	653139	0.001237	2.296E-05	10.681		

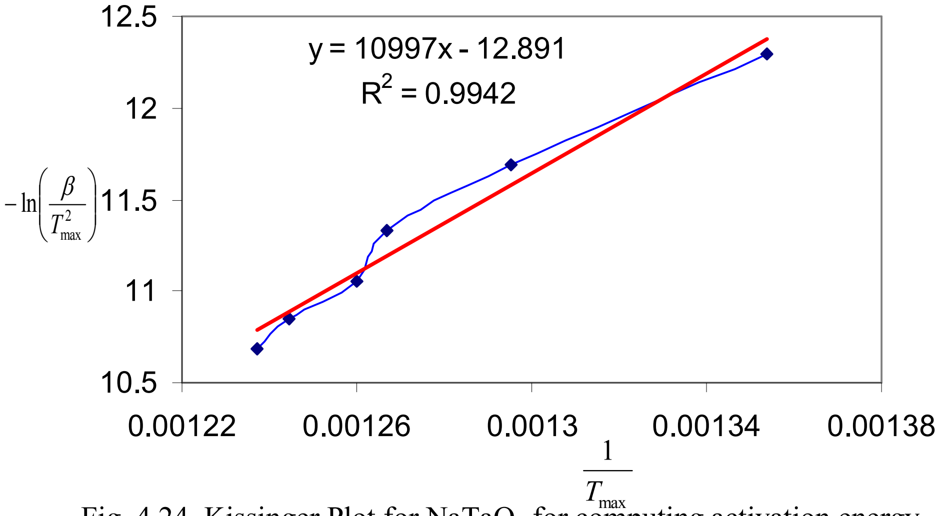

Fig. 4.24. Kissinger Plot for $NaTaO_3$ for computing activation energy.

4.4.6 Impedance Spectroscopy

The variation of real (Z') and Imaginary (Z") part or Nyquist plot of impedance with frequency for $NaTaO_3$ samples sintered at 750^0C for 30, 60, 90 and 120 minutes is shown in figure 4.25. A single semicircular arc is appeared for all samples, however for the sample sintered for 30, 60 and 90 min, an additional semicircular arc is appeared at high frequency as shown in figure 4.26. One semicircle in the high frequency range and the other in the low frequency range for $NaTaO_3$ sintered at 750^0C for 30, 60 and 90 min may correspond to oxygen migration in the bulk and across grain boundaries.

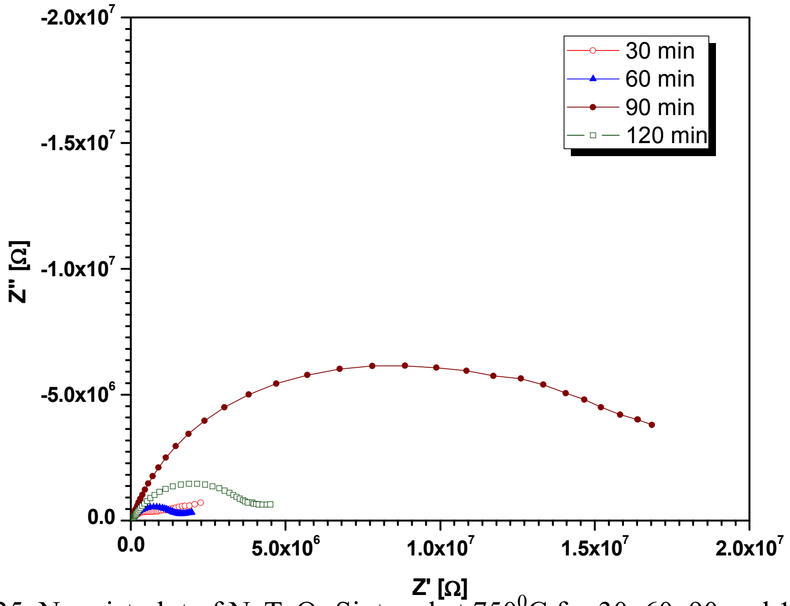

Figure 4.25. Nyquist plot of $NaTaO_3$ Sintered at 750^0C for 30, 60, 90 and 120 minutes

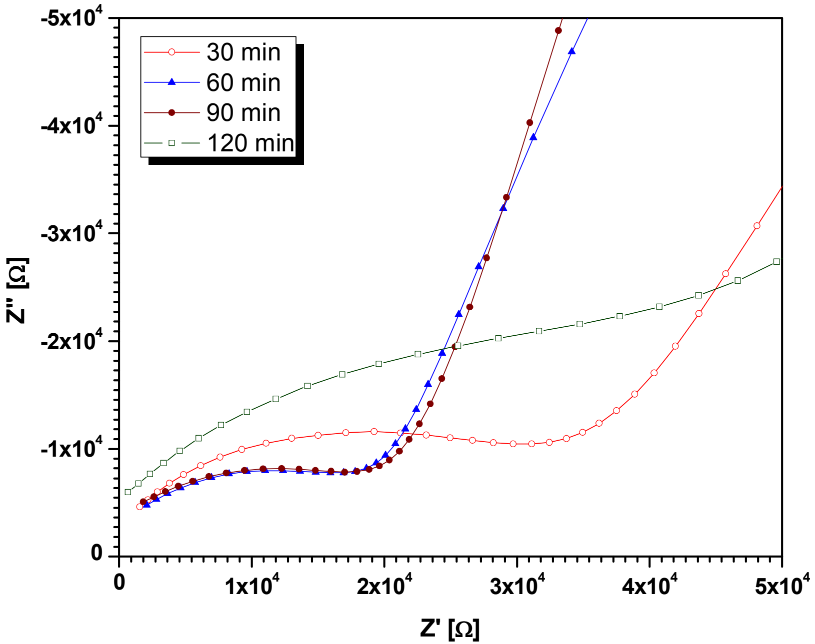

Figure 4.26 Nyquist plot at high frequency observed for $NaTaO_3$ Sintered at 750^{0}C for 30, 60, 90 and 120 min

Bode plot was measured for the for $NaTaO_3$ samples sintered at 750^{0}C for 30, 60, 90 and 120 min with frequency vs magnitude of impedance as shown in figure 3.27 and frequency vs phase angle as shown in figure 4.28. Figure 4.27 shows the decrease in magnitude of impedance drastically with increase in frequency. The frequency dependence of phase angle is observed for $NaTaO_3$ samples sintered at 750^{0}C

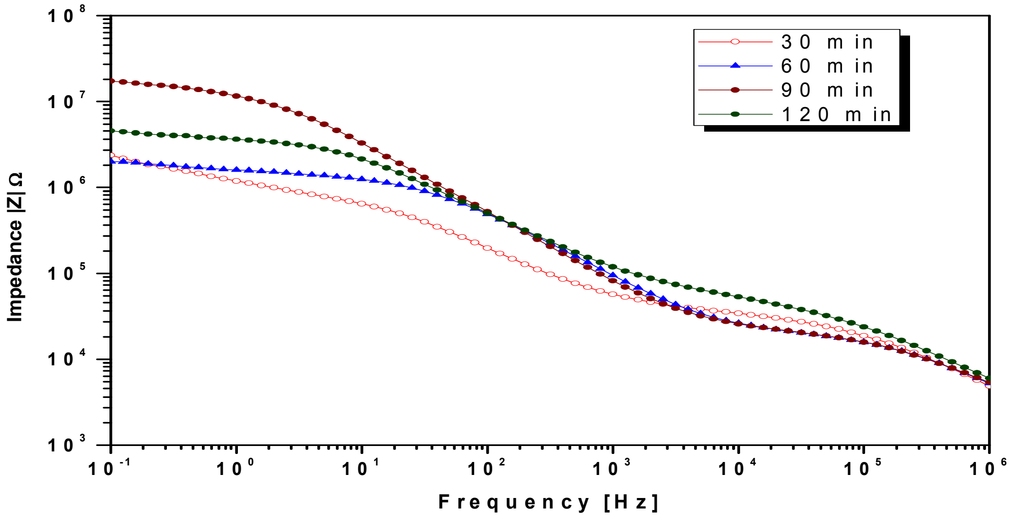

Figure 4.27. Bode plot – Impedance magnitude |Z| vs frequency of $NaTaO_3$ Sintered at 750^{0}C for 30, 60, 90 and 120 min

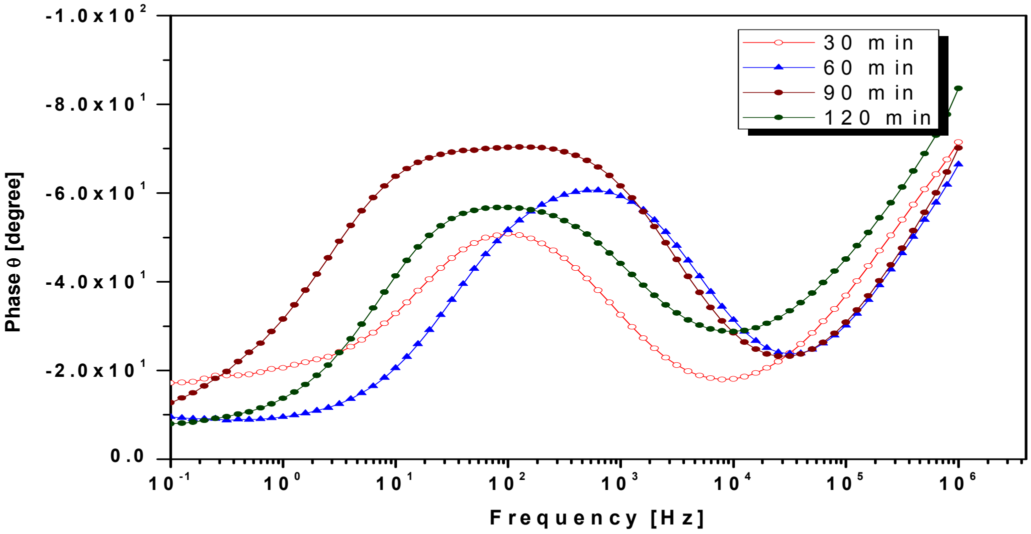

Figure 4.28 Bode plot – Phase Angle vs frequency of $NaTaO_3$ Sintered at 750^0C for 30, 60, 90 and 120 minutes

The variation of real (Z') and Imaginary (Z") part or Nyquist plot of impedance with frequency for $NaTaO_3$ samples sintered at 1000^0C for 30, 60, 90 and 120 minutes is shown in figure 4.29. A single semicircular arc is appeared for all samples even at high frequency as shown in figure 4.30. Semicircles observed at high frequency of Nyquist plot corresponds to grain relaxation of $NaTaO_3$ sintered samples.

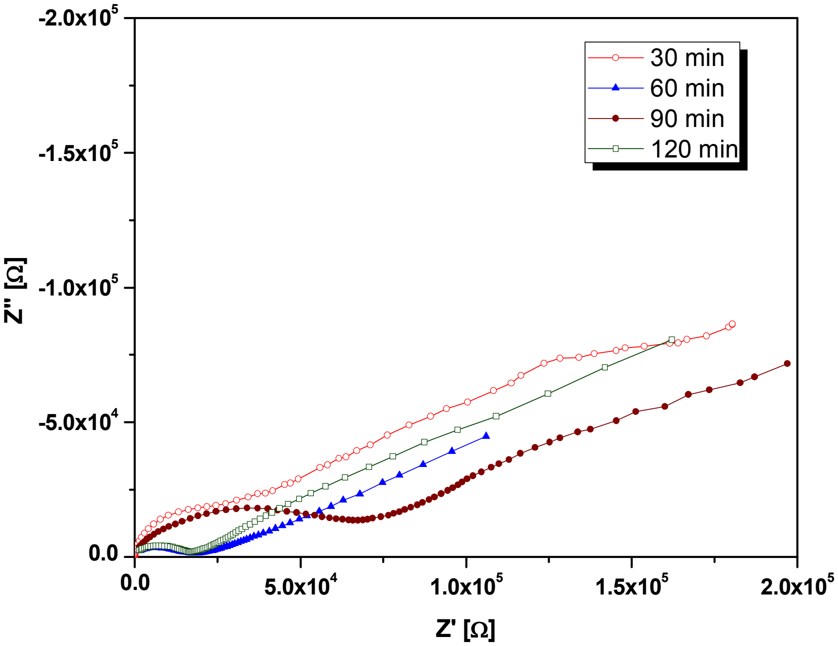

Figure 4.29. Nyquist plot of $NaTaO_3$ Sintered at 750^0C for 30, 60, 90 and 120 minutes

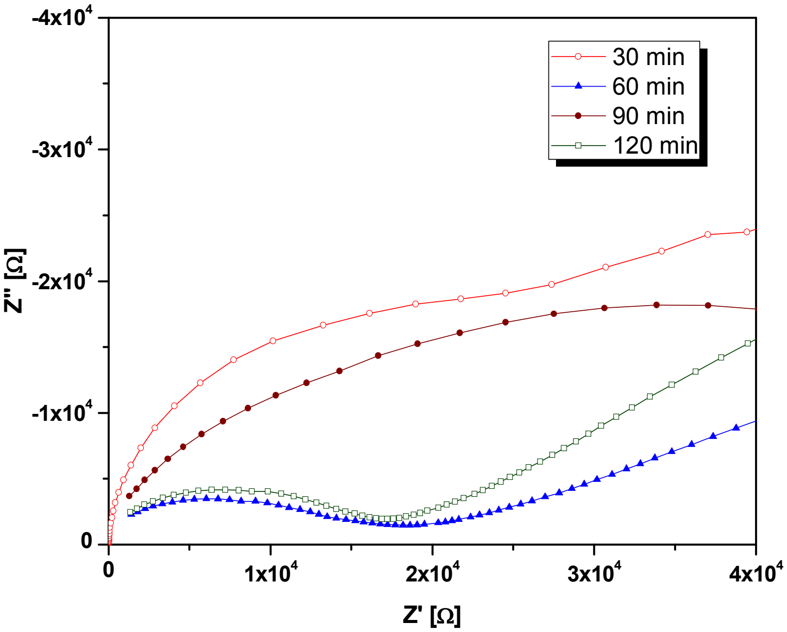

Figure 4.30. Nyquist plot at high frequency observed for $NaTaO_3$ Sintered at 1000^0C for 30, 60, 90 and 120 min

Bode plot was constructed for the for $NaTaO_3$ samples sintered at 1000^0C for 30, 60, 90 and 120 minutes is with frequency vs magnitude of impedance as shown in figure 4.31 and frequency vs phase angle as shown in figure 4.32. Both the figures shows the frequency dependence of impedance parameters for NaTaO3 samples. The sample sintered for 30 minute shows lower impedance |Z| as compared to samples sintered for longer duration.

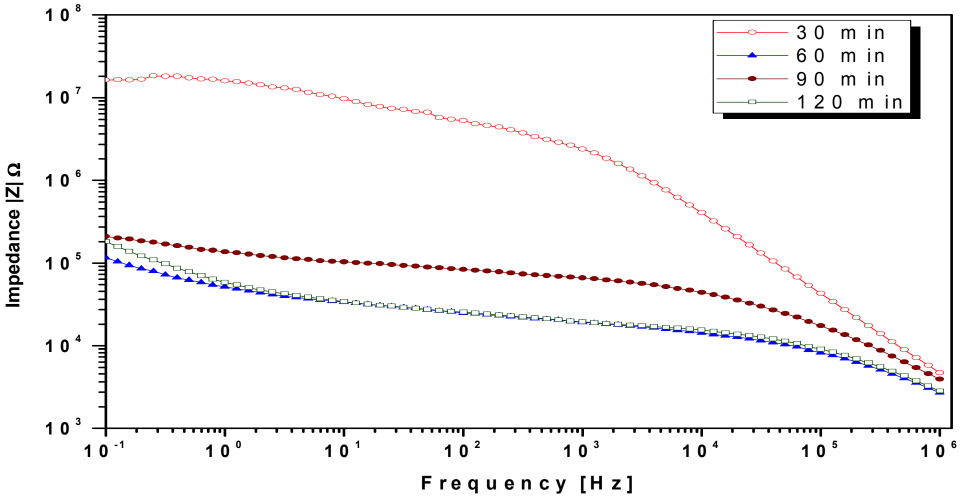

Figure 4.31. Bode plot – Impedance magnitude |Z| vs frequency of $NaTaO_3$ Sintered at 1000^0C for 30, 60, 90 and 120 min

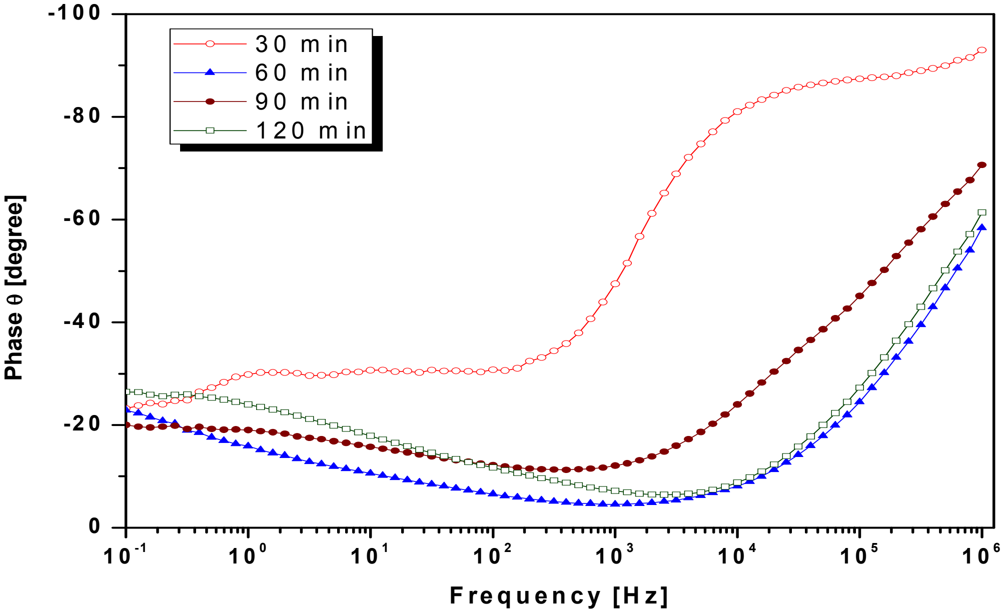

Figure 4.32. Bode plot – Phase Angle vs frequency of $NaTaO_3$ Sintered at 1000^0C for 30, 60, 90 and 120 min

Dielectric Loss vs frequency of $NaTaO_3$ Sintered at 750^0C and 1000^0C were measured upto 40MHz and plotted in figure 4.33 and 4.34 respectively. It is observed that the dielectric loss of $NaTaO_3$ decreases with increase in frequency, however an abnormal high dielectric loss peak is absorbed at around 20MHz.

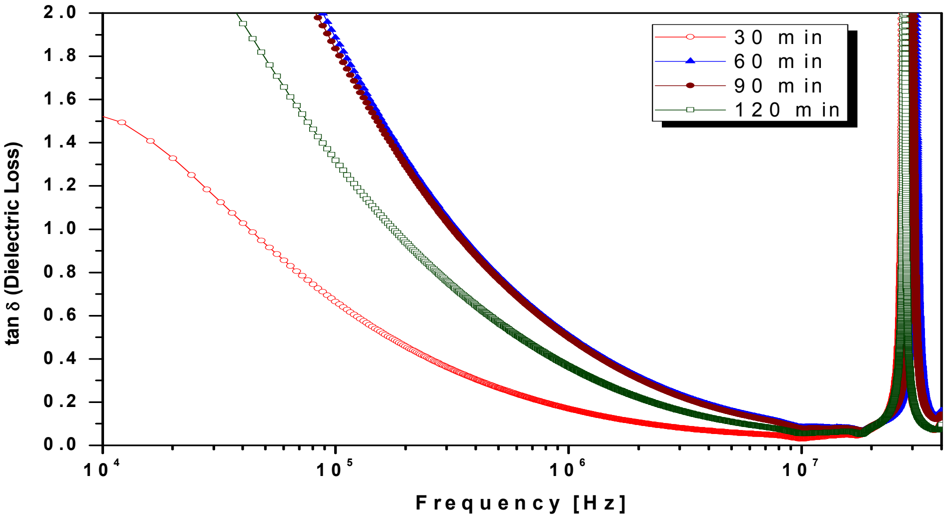

Figure 4.33. Dielectric Loss vs frequency of NaTaO3 Sintered at 750^0C for 30, 60, 90 and 120 minutes

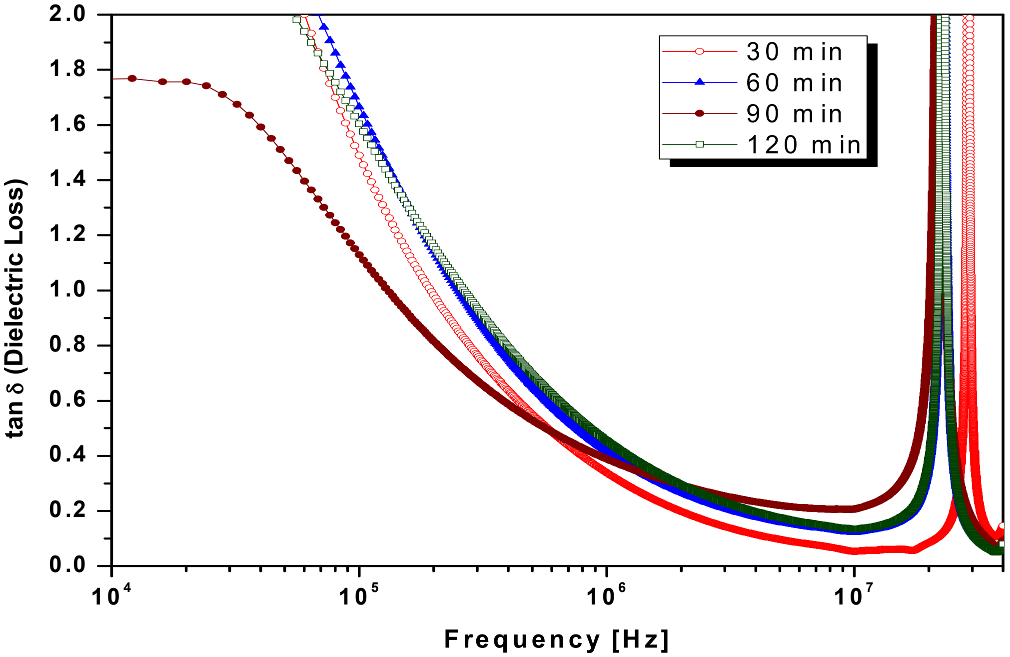

Figure 4.34. Dielectric Loss vs frequency of $NaTaO_3$ Sintered at 1000^0C for 30, 60, 90 and 120 min

4.5 Summary

A simple procedure of using hydroxide precursors for the preparation of ultrafine particles of $NaNbO_3$ and $NaTaO_3$ was elucidated. The formation of $NaNbO_3$ phase occurs at 200°C. and the formation of $NaTaO_3$ is observed at 500^0C. EDAX spectrum shows the purity of product synthesized by hydroxide precursor method, since no other element peaks are observed in EDAX spectrum. Sodium niobate and Sodium tantalate shows the characteristic K-α peak at 1.041keV in the EDAX spectrum. Differential scanning calorimetry provide the information about the activation energy for the formation of $NaNbO_3$ by hydroxide precursor method is 91.42 kJ and activation energy for the formation of $NaTaO_3$ is 113.82 kJ. Nyquist plot, Bode plot, and dielectric loss provide the information about the variation of its impedance parameters with frequency. Semicircles in Nyquist plot at high frequency corresponds to grain relaxation and at low frequency relate grain boundary, secondary phase segregated at grain boundary and sometimes effect of electrode. It is observed that, the dielectric loss for both $NaNbO_3$ and $NaTaO_3$ decreases with increase in frequency, however an abnormal high dielectric loss peak is absorbed at around 20MHz. Presence of dislocations or voids can also influence the dielectric loss of the bulk sample.

4.6 References

1. Vishnu Shanker, Saroj L. Samal, Gopal K. Pradhan, Chandrabhas Narayana, Ashok K. Ganguli, Solid State Sciences 11 (2009) 562.
2. Y. Saito, H. Takao, T. Tani, T. Nonoyama, K. Takatori, T. Homma, T. Nagaya, M. Nakamura, Nature 432 (2004) 84.
3. L.A. Reznitchenko, N.V. Dergunova, G.A. Geguzina, O.N. Razumovskaya, L.A. Shilkina, L.S. Ivanova, Inorg. Mater. 33 (1997) 1277.
4. L.A. Reznitchenko, N.V. Dergunova, G.A. Geguzina, O.N. Razumovskaya, L.A. Shilkina, L.S. Ivanova, Ferroelectrics 214 (1998) 241.
5. G.A. Geguzina, L.A. Reznitchenko, N.V. Dergunova, Ferroelectrics 214 (1998) 261.
6. L.A. Reznitchenko, A.V. Turik, E.M. Kuznetsova, V.P. Sakhnenko, J. Phys.: Condens. Matter 13 (2001) 3875.
7. S. Lanfredi, M.H. Lente, J.A. Eiras, Appl. Phys. Lett. 80 (2002) 2731.
8. G. Shirane, R. Newnham, R. Pepinsky, Phys. Rev. 96 (1954) 581.
9. L.A. Reznitchenko, A.V. Turik, E.M. Kuznetsova, V.P. Sakhnenko, J. Phys.: Condens. Matter. 13 (2001) 3875.
10. H.D. Megaw, Ferroelectrics 7 (1974) 87.
11. Krzysztof Konieczny, Materials Science and Engineering B60 (1999) 124.
12. E. Hollenstein, D. Damjanovic, N. Setter, J. Eur. Ceram. Soc. 27 (2007) 4093.
13. H.L. Du, F.S. Tang, D.J. Liu, D.M. Zhu, W.C. Zhou, S.B. Qu, Mater. Sci. Eng. B 136 (2007) 165.
14. K. Singh, V. Lingwal, S.C. Bhatt, N.S. Panwar, Mater. Res. Bull. 36 (2001) 2365.
15. I.P. Raevski, S.A. Prosandeev, J. Phys. Chem. Solids 63 (2002) 1939.

16. Y. Saito, H. Takao, T. Tani, T. Nonoyama, K. Takatori, T. Homma, T. Nagaya, M. Nakamura, Nature 432 (2004) 84.
17. S. Ding, J. Shen, J. Am. Ceram. Soc. 73 (1990) 1449.
18. T. Nitta, J. Am. Ceram. Soc. 51 (1968) 626.
19. S. Lanfredi, L. Dessemond, A.C.M. Rodrigue, J. Eur. Ceram. Soc. 20 (2000) 983.
20. G.K.L. Goh, F.F. Lange, S.M. Haile, C.G. Levi, J. Mater. Res. 18 (2003) 338.
21. Huawei Song, Wenhui Ma, Ceramics International 37 (2011) 877.
22. Guoqiang Li, Tetsuya Kako, Defa Wang, Zhigang Zou, Jinhua Ye, J. Physics and Chemistry of Solids 69 (2008) 2487.
23. Shu Ya Wu, Xiao Qiang Liu, Xiang Ming Chen, Ceramics International 36 (2010) 871.
24. M. A. L. Nobre, E. Longo, E. R. Leite, J. A. Varela, Materials Letters, 28 (1996) 215.
25. T. Hungrıa, L. Pardo, A. Moure, A. Castro, J. Alloys Compd. 395 (2005) 166.
26. A. Castro, B. Jim´enez, T. Hungr´ıa, A. Moure, L. Pardo, J. Eur. Ceram. Soc. 24 (2004) 941.
27. T. Rojac, O. Masson, R. Guinebretière, M. Kosec, B. Malic, J. Holc, J. Eur. Ceram. Soc, 27 (2007) 2265.
28. Yu-Jen Hsiao, Yen-Hwei Chang, Yee-Shin Chang, Te-Hua Fang, Yin-Lai Chai, Guo-Ju Chen, Tzu-Wei Huang, Materials Science and Engineering B 136 (2007) 129.
29. Y.X.Wang, W.L.Zhong, C.L.Wang, P.L.Zhang, Solid State Communications, 120 (2001) 137.
30. M. Wiegel, M. H. J. Emond, E. R. Stobbe, G. Blasse, J. Phys. Chem. Solids, 55 (1994) 773.

31. Kato, H. and Kudo, A., Chem. Phys. Lett., 295 (1998) 487.
32. Yamakata, A., Ishibashi, T.-A., Kato, H., Kudo, A. and Onishi, H., J. Phys. Chem. B, 107 (2003) 14383.
33. Che-Chia Hu, Hsisheng Teng, Applied Catalysis A: General 331 (2007) 44.
34. Nayara G. Teixeira, Anderson Dias, R.L. Moreira, J. Eur. Ceram. Soc 27 (2007) 3683.
35. J.W. Liu G. Chen, Z.H. Li, Z.G. Zhang, J. Hydro. Energy 32 (2007) 2269.
36. H. Kato, K. Asakura, A. Kudo, J. Am. Chem. Soc. 125 (2003) 3082.
37. A. Kudo, H. Kato, Chem. Phys. Lett. 331 (2000) 373.
38. T. Ishihara, H. Nishiguchi, K. Fukamachi, Y. Takita, J. Phys. Chem. B 103(1999)1.
39. H. Kato, A. Kudo, J. Phys. Chem. B 105 (2001) 4285.
40. H. Kato, H. Kobayashi, A. Kudo, J. Phys. Chem. B 106 (2002) 12441.
41. H. Kato, A. Kudo, Catal. Today 78 (2003) 561.
42. A. Iwase, H. Kato, A. Kudo, Chem. Lett. 34 (2005) 946.
43. D.G. Porob, P.A. Maggard, J. Solid State Chem. 179 (2006) 1727.
44. M. Yoshino, M. Kakihana, W.S. Cho, H. Kato, A. Kudo, Chem. Mater. 14 (2002) 3369.
45. C.C. Tsai, H.S. Teng, J. Am. Ceram. Soc. 87 (2004) 2080.
46. W.H. Lin, C. Cheng, C.C. Hu, H.S. Teng, Appl. Phys. Lett. 89 (2006) 211904.
47. C. An, K. Tang, C. Wang, G. Shen, Y.T. Qian, Mater. Res. Bull. 37 (2002) 1791.
48. G.S. Maciel, N. Rakov, C.B. de Araujo, A.A. Lipovskii, D.K. Tagantsev, Appl. Phys. Lett. 79 (2001) 584.
49. Kayoko Nakamura, Hirotake Orii, Anal. Chem., 52 (1980) 532.

50. Izabela Michalak, Katarzyna Chojnacka and Krzysztof Marycz, Microchim Acta 172 (2011) 65.
51. Kuniaki Fukuda, Minoru Tanaka, Hisao Tanase, Experimental and Molecular Pathology 40 (1984) 21.
52. Ricky W. Chuang and Chin C. Lee J. Lightwave Technology, 20 (2002) 1590.
53. Chin C. Lee, Ricky W. Chuang, Materials Science and Engineering: B, 111 (2004) 40.
54. Heather C. Allen, J. M. Laux, Rainer Vogt, Barbara J. Finlayson-Pitts, and John C. Hemminger, J. Phys. Chem., 100 (1996) 6371.

Chapter 5

Synthesis and Characterization of Strontium Niobate and Tantalate

This chapter comprised about the synthesis and characterization of Strontium Niobate and Strontium Tantalate. The characterization part of this chapter is divided into two secitons for $SrNb_2O_6$ and $SrTa_2O_6$. Impedance Spectroscopy. of these compounds were studied by Nyquist plot and Bode plot. Both the compounds were discussed and characterized for X-ray powder diffraction (XRD). Elements in the compounds were studied by Energy Dispersive X-Ray Analysis (EDAX). Average particle size and morphology were analyzed using Scanning Electron Microscopy. Thermal analysis of both the compounds were carried out using Thermogravimetry Analysis (TGA), Differential Scanning Calorimetery (DSC) and activation energy for the formation of $SrNbO_3$ and $SrTaO_3$ were estimated from DSC data using Kissinger method.

5.1 Introduction

Compounds with the general formula AB_2O_6 (where A and B include many main group and transition metal cations) have been of special interest for a long time and the physical properties of many of them were studied in detail [1]. Divalent columbite niobate ceramics with general formula ANb_2O_6 (A = divalent cations) have very interesting characteristics as excellent dielectric property, quality factor and temperature coefficient of resonant frequency [2–4]. Therefore, they have been characterized for the application point of view in microwave resonators. Many attempts have been done to get single columbite phase in these materials but it is found very difficult because of corundum like phase, and requires prolonged heating [5]. Most of the ANb_2O_6 compounds also exhibit polymorphism; however, each can exist as an isomorphous orthorhombic phase with the columbite structure, except for the Sr, Ba, Pb analogues which crystallize in a different orthorhombic structures [6].

$SrNb_2O_6$ is traditionally synthesized by solid-state reaction route[7–9], combustion method [10], and microwaves technique [11]. $SrNb_2O_6$ has been extensively studied for enhanced photocatalytic activity [9, 12–14], lead free piezoceramics [15, 16] and photoluminescence [10]. The Photocatalysis has been proposed as a promising means of eliminating organic pollutants from environments [17–20]. $SrNb_2O_6$ is also used as a precursor in the synthesis of SBN which has many technological applications such as electro-optic [21,22] pyroelectric, [23,24] piezoelectric [25] and photorefractive devices [26,27].

The miniaturization of electronic devices requires very thin SiO_2 insulators, whose minimal thickness is limited by the leakage current due to electron tunneling through the barrier. To overcome this problem, high-k dielectric constant material is needed to replace the conventional SiO_2. Recently it has been reported that $SrTa_2O_6$ is a promising candidate for gate oxide applications because of its high dielectric constant (up to 110), low leakage current density, and superior thermal stability with silicon [28–33]. Strontium tantalite is also widely studied for its photocatalytic activity [34–39]. Several methods have been reported in literature for the synthesis of $SrTa_2O_6$ such as sol–gel technique [30], atomic layer deposition (ALD) [37] or plasmaenhanced ALD [28, 29], liquid source misted chemical deposition (LSMCD) [41, 42] and metalorganic chemical vapor deposition (MOCVD) [43–45].

In the present work a novel hydroxide precursors to synthesize $SrNb_2O_6$ and $SrTa_2O_6$ powders at lower temperatures thereby without using carbonate source for strontium. Thus this method has advantage over co-precipitation process in which alkali earth elements are precipitated as carbonates or oxalates.

5.2 Experimental

5.4.1 Synthesis of Strontium Niobate

For preparing $SrNb_2O_6$, niobium (V) oxide and strontium hydroxide were used as starting materials and they were of AR grade. The Nb_2O_5 powders were dissolved in minimum amount of HF (60%) after heating on a hot water bath at 90 °C for 10 h. To this NbF_5 solution, an excess of aqueous ammonia (30%) was added to precipitate niobium as hydroxide under basic conditions. The precipitate was then filtered and oven dried at 100 °C overnight.. The required quantity of $Sr(OH)2\cdot 2H_2O$ was mixed thoroughly with stoichiometric amount of $Nb(OH)_5$ and heated at various temperatures from 200 to 600 °C for 6 h. The schematic flow chart for the preparation of strontium niobate by hydroxide precursor method is presented in figure 5.1.The major chemical reaction involved in this process is given below

$$Nb_2O_5 + 10HF \xrightarrow{\Delta\ 90^0C,\ 10\ h} 2NbF_5 + 5H_2O \xrightarrow{NH_3OH} \underset{\text{Niobium hydroxide}}{Nb(OH)_5}$$

$$Sr(OH)_2{\cdot}2H_2O + 2Nb(OH)_5 \xrightarrow{\Delta\ 500^0C,\ 6\ h} SrNb_2O_6 + 8H_2O$$

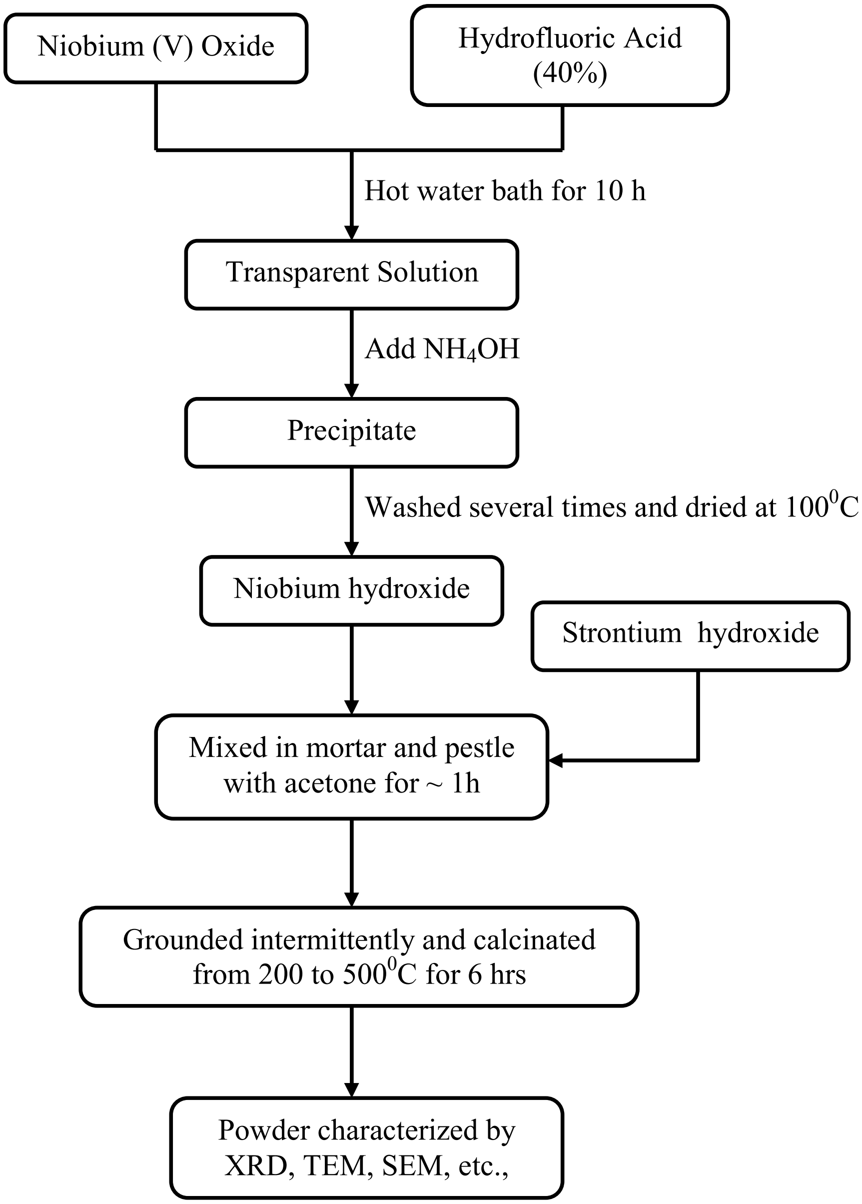

Figure 5.1 Flow chart for the preparation of $SrNb_2O_6$ by hydroxide precursor method

5.2.2 Synthesis of Strontium Tantalate

The major chemical reaction involved in the formation of strontium tantalate is given below

$$Ta_2O_5 + 10HF \xrightarrow{\Delta\ 90^0C,\ 10\ h} 2TaF_5 + 5H_2O \xrightarrow{NH_3OH} \underset{\text{Tantalum hydroxide}}{Ta(OH)_5}$$

$$Sr(OH)_2\cdot 2H_2O + 2Ta(OH)_5 \xrightarrow{\Delta\ 500^0C,\ 6\ h} SrTa_2O_6 + 8H_2O$$

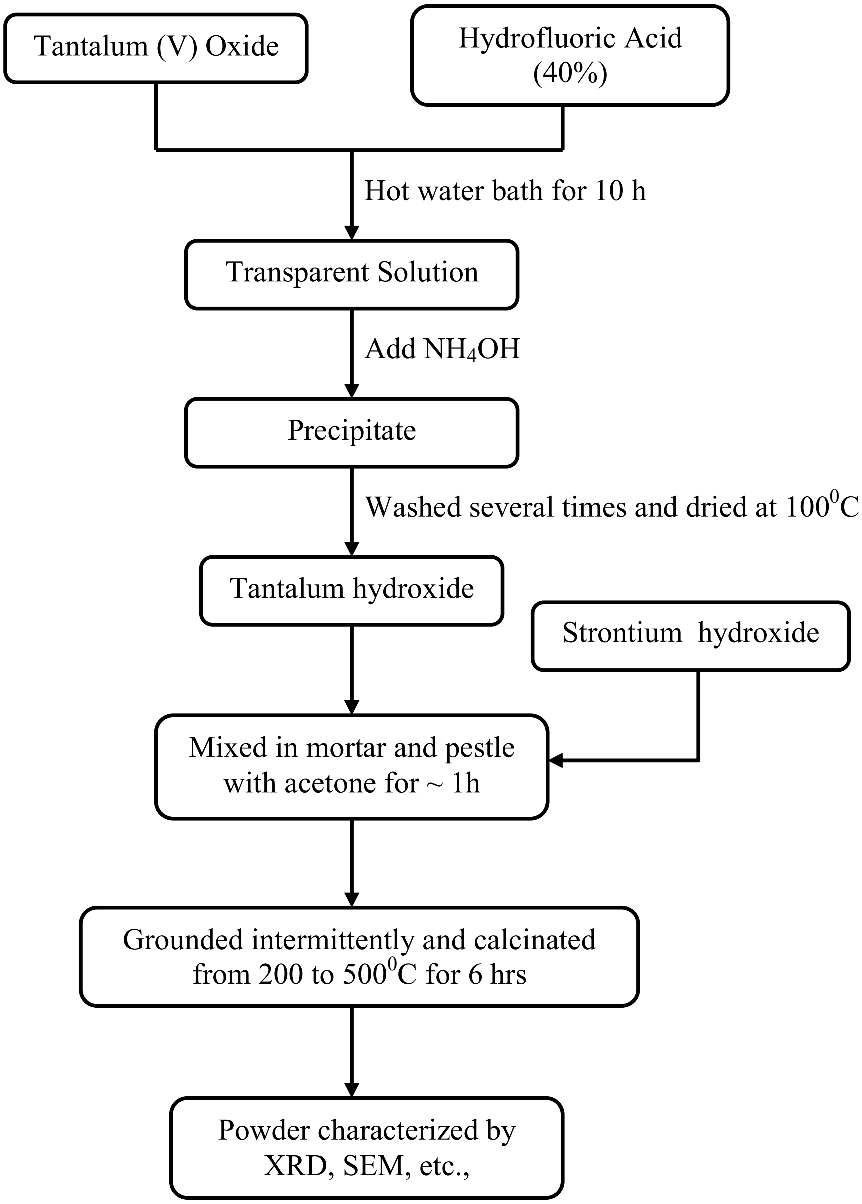

Figure 5.2 Flow chart for the preparation of $SrTa_2O_6$ by hydroxide precursor method

For preparing $SrTa_2O_6$, tantalum (V) oxide and strontium hydroxide were used as starting materials and they were of AR grade. The Ta_2O_5 powders were dissolved in minimum amount of HF (60%) after heating on a hot water bath at 90 °C for 10 h. To this TaF_5 solution, an excess of aqueous ammonia (30%) was added to precipitate niobium as hydroxide under basic conditions. The precipitate was then filtered and oven dried at 100 °C overnight.. The required quantity of $Sr(OH)_2 \cdot 2H_2O$ was mixed thoroughly with stoichiometric amount of $Ta(OH)_5$ and heated at various temperatures from 200 to 600 °C for 6 h. The schematic of overall procedure to synthesis $SrTa_2O_6$ is given in figure 5.2 as a flow chart format.

5.3 Characterization of Strontium Niobate

5.3.1 X-ray powder diffraction

Figs. 5.3 and 5.4 show XRDs of $SrNb_2O_6$ hydroxide precursor powder heat treated at different temperatures ranging from 200 to 600°C. When temperature is at 400°C the incipient product phase was found to be formed along with some intermediate phases which cannot be authentically indexed. However the formation of product phase was completed at 500°C. The XRD pattern of the sample remains the same when calcination temperature was increased to 600 °C. For lattice parameter and interplanar distance (d) calculation, the samples were scanned in a 2θ range of 10–80° in step scan mode at 5 s/step. Silicon was used as an internal standard. The crystal structure of $SrNb_2O_6$ is orthorhombic and all lines in the diffractogram match with reported values (JCPDS: 28-1243). The calculated lattice parameters by least square fit are a=11.03 Å, b=7.707 Å and c=5.607 Å. There is a little difference in the calculated lattice parameters from literature values which may be attributed to change in preparative conditions. This is the lowest temperature reported so far for the formation of $SrNb_2O_6$ phase in the literature.

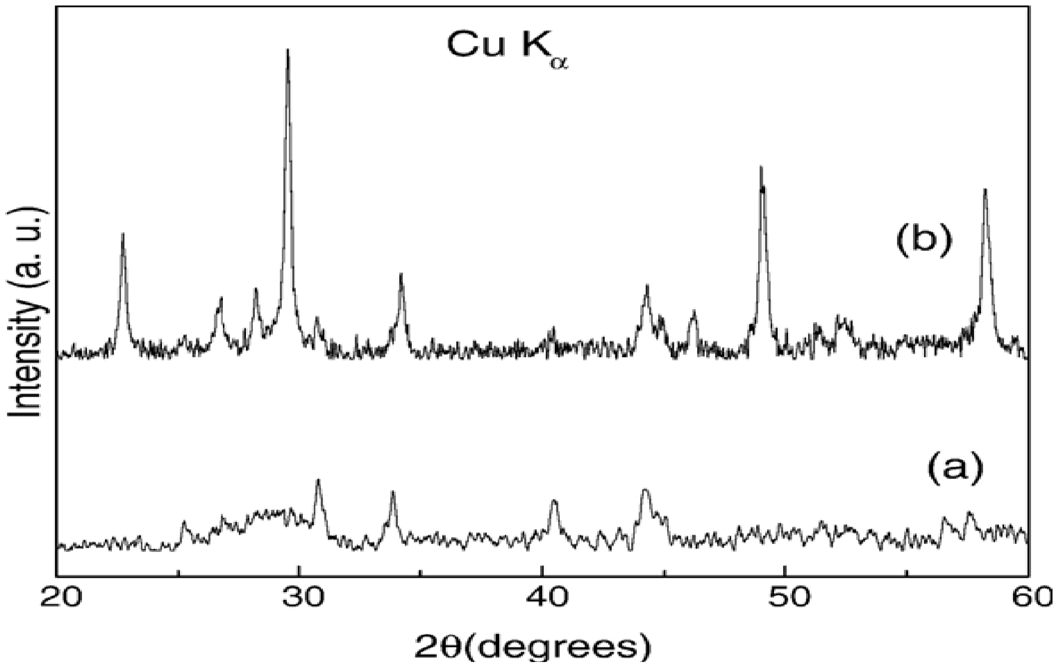

Fig. 5.3. The XRD of $SrNb_2O_6$ hydroxide precursor powders after heating at (a) 200 and (b) 400 °C.

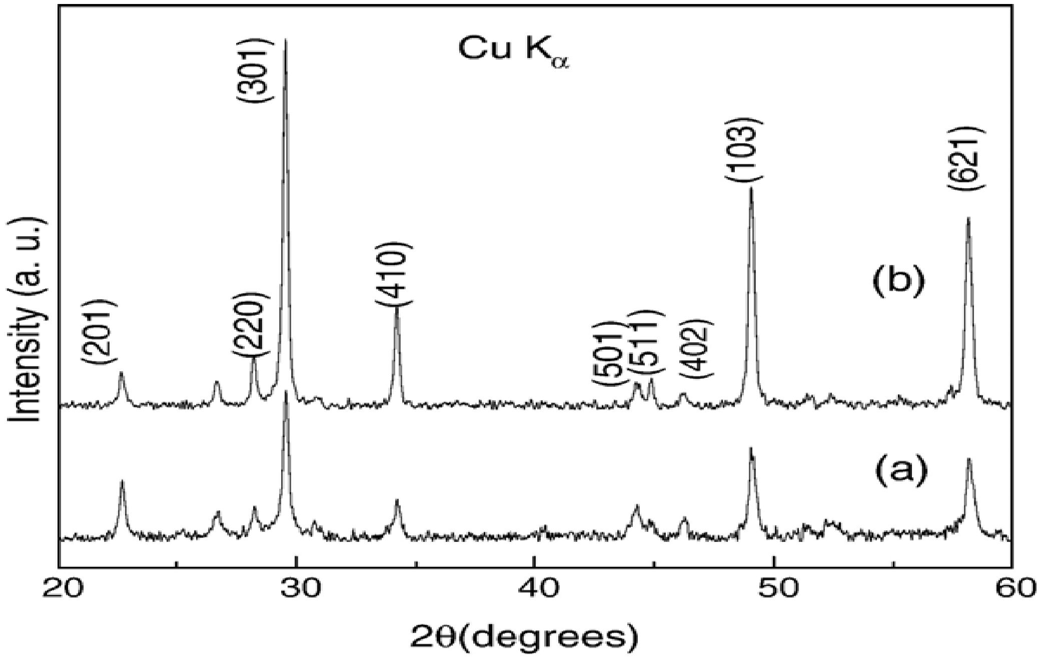

Figure 5.4. The XRD of $SrNb_2O_6$ hydroxide precursor powders after heating at (a) 500 °C and (b) 600 °C.

The particle size calculated from Scherrer's formula (t=K λ/B cosθB) where t is the average size of the particles, assuming particles are spherical, K=0.9, λ is the wavelength of X-ray radiation, B is the full width at half maximum of the diffracted peak and θB is the angle of diffraction) is 120 nm

5.3.2 Energy Dispersive X-Ray Analysis

The EDAX was scanned from 0 to 10keV for $SrNb_2O_6$. The characteristics L-alpha (L3M5) peak for Strontium is observed at 1.806 keV as reported in literature [46–52]. A peak at 0.525 keV on EDAX spectrum is identified as the contribution of Oxygen. The characteristic niobium contribution at 2.166 keV is due to a L-alpha (L_3M_5) emission [53]. Experimentally observed EDAX spectrum of $SrNb_2O_6$ prepared by hydroxide precursor method is given in figure 5.5. The EDAX peaks observed for $SrNb_2O_6$ and corresponding identified transition are tabulated in Table 5.1.

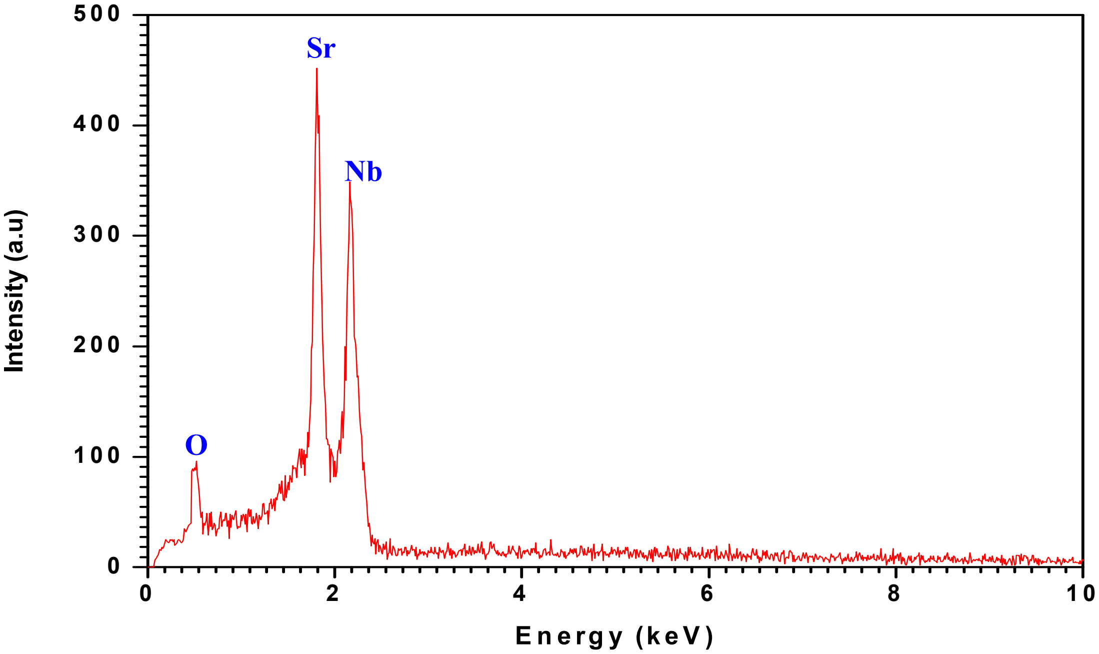

Figure 5.5. EDAX Spectrum of $SrNb_2O_6$ prepared by hydroxide precursor method

Table 5.1 EDAX spectrum peaks observed for $SrNb_2O_6$

Sr No.	Element	Peak Observed	Transition
1	Oxygen	0.525 keV	K-alpha
2	Strontium	1.806 keV	L3M5
3	Niobium	2.166 keV	L-alpha (L3M5)

5.3.3 Scanning Electron Microscopy

The SEM images were observed using a Leica Cambridge 440 microscope. All the powders were dispersed in amyl acetate for SEM studies.

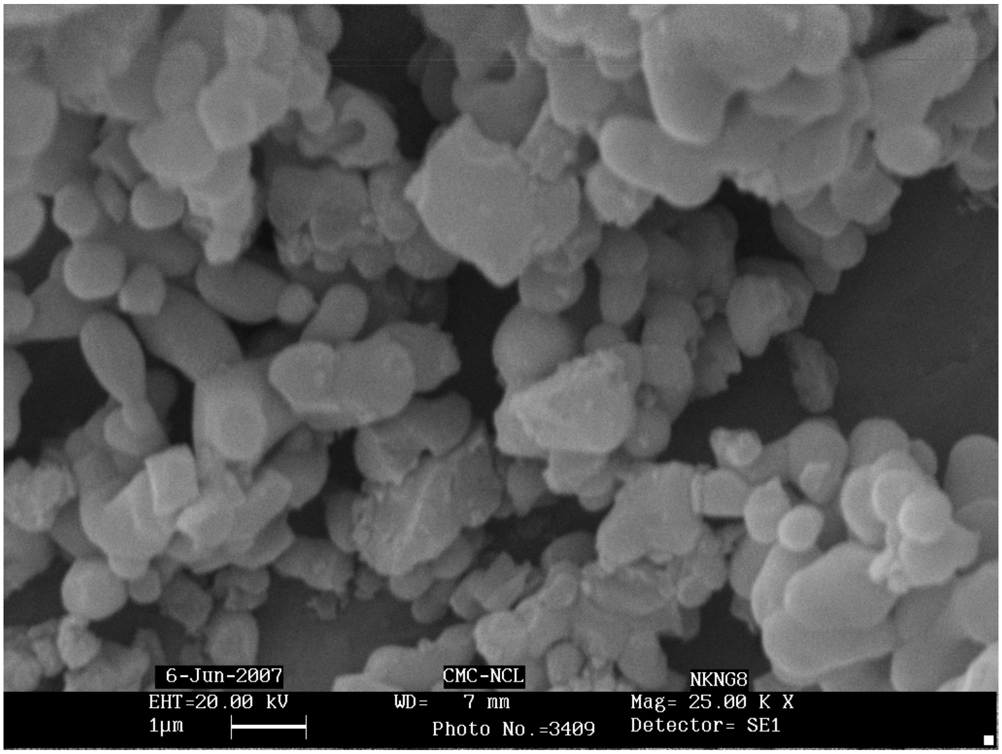

Figure 5.6 The SEM micrographs of $SrNb_2O_6$ powders calcined at 500 °C.

The average particle size and morphology of these calcined powders were examined by scanning electron microscopy and shown in figure 5.6 . The calcined powders

(500°C for 6 h) prepared by hydroxide precursor technique have spherical to elliptical in shape and agglomerated, with an average primary particle size ~300 nm.

5.3.4 Thermogravimetry Analysis

Stoichiometric amount of Strontium hydroxide and freshly prepared Niobium hydroxide are mixed well thoroughly and thermogravimetric analysis of this mixture is carried out at 10 different heating rate (2.5, 5, 7.5, 10, 12.5, 15, 17.5, 20, 22.5 and 25^{0}C/min) and depicted in figure 5. Around 7 to 14 mg of mixture is used for TGA analysis. Irrespective of heating rate, figure 5 clearly shows gradual dip in mass upto 500^{0}C and then stable profile, which is an indication of solid state reaction takes place with release of hydroxyl ions from the precursors. XRD also conforms the structural formation $SrNb_2O_6$ at 500^{0}C

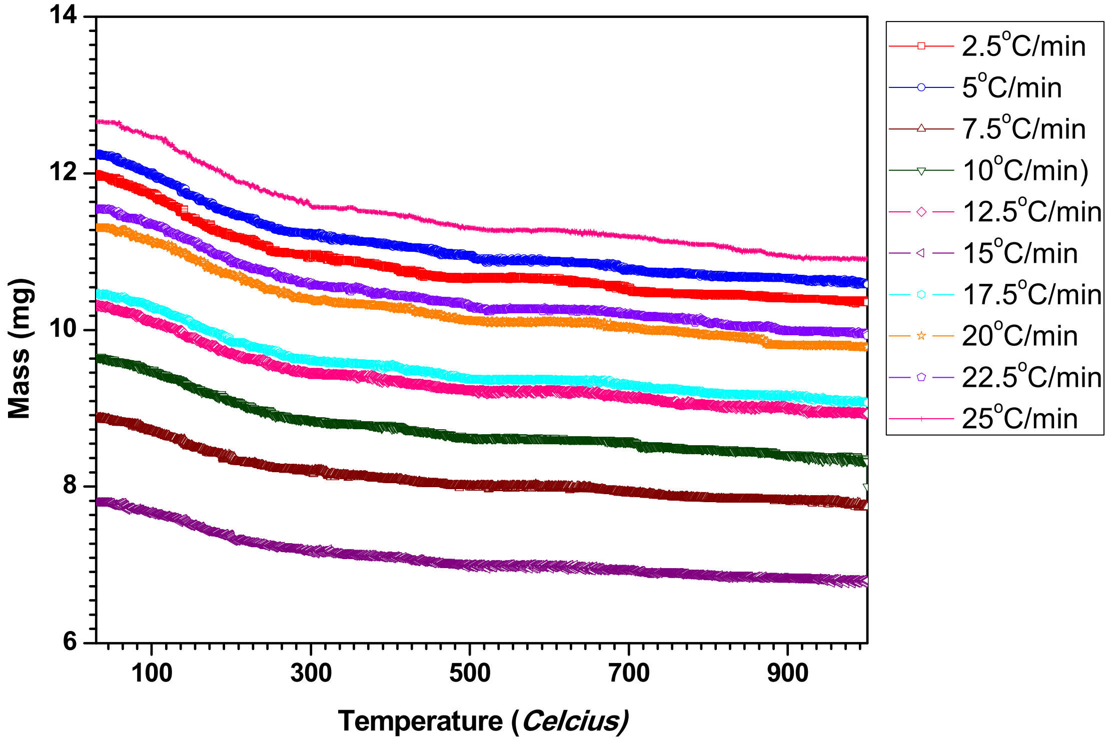

Figure 5.7 TGA profile of $SrNb_2O_3$ formation at different heating rate

5.3.5 Differential Scanning Calorimetery

Differential Scanning Calorimetric (DSC) analysis of $SrNb_2O_6$ was carried out at 6 different heating rate (2.5, 5, 7.5, 10 and 15^0C/min) and shown in figure 5.8. Stoichiometric amount of Strontium hydroxide and freshly prepared Niobium hydroxide obtained from Niobium (V) oxide with HF is mixed well thoroughly. Around 20 mg of mixture is used for DSC analysis. Inert Nitrogen gas is used as a purge gas during DSC analysis of mixture. The exothermic DSC peeks were observed at around 478^0C to 508^0C and the peak shifts with heating rate are tabulated in Table 5.2 for the computation of activation energy by Kissinger method. From the table 5.2, Kissinger plot (figure 5.9) was constructed to find the linear equation, from the slope of the equation the activation energy for the formation of $SrNb_2O_6$ by hydroxide precursor method is 270.28 kJ.

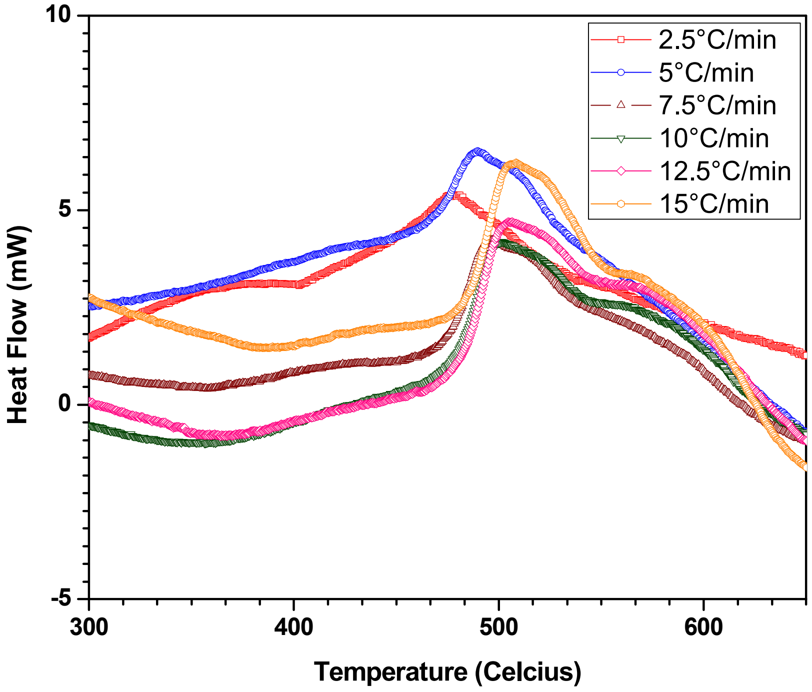

Figure 5.8. DSC profile of $SrNb_2O_6$ formation at different heating rate

Table 5.2 DSC data on $SrNb_2O_6$ at various heating rates (Kissinger method).

Heating rate β (^0C)	Peak T_{max} (^oC)	Peak T_{max} (K)	T^2_{max}	$\frac{1}{T_{max}}$	$\frac{\beta}{T^2_{max}}$	$-\ln\left(\frac{\beta}{T^2_{max}}\right)$	Slope	Activation Energy (kJ/mol)
2.5	478.25	751.40	564602	0.001330	4.4279E-06	12.327	32509.46674	270.28
5	489.62	762.77	581818	0.001311	8.59375E-06	11.664		
7.5	497.63	770.78	594102	0.001297	1.26241E-05	11.279		
10	501.49	774.64	600067	0.001290	1.66648E-05	11.002		
12.5	506.66	779.81	608104	0.001282	2.05557E-05	10.792		
15	508.51	781.66	610992	0.001279	2.45502E-05	10.614		

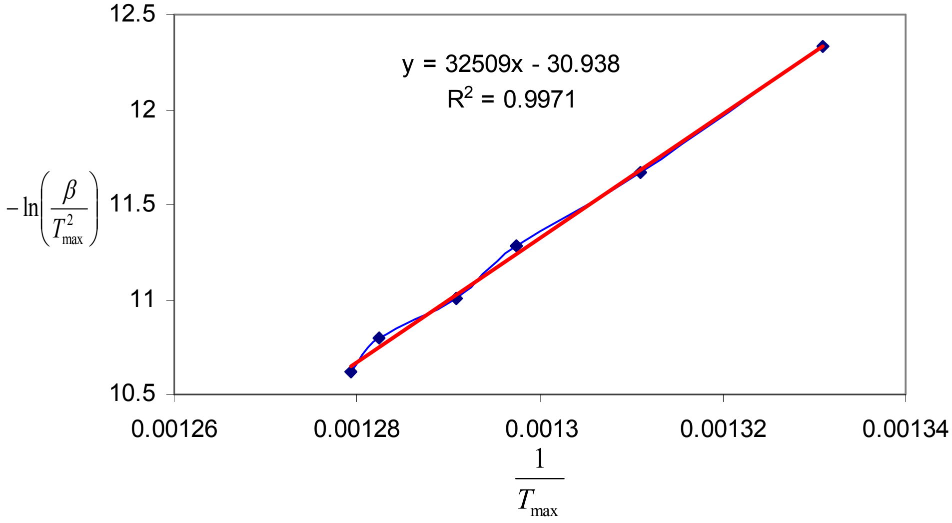

Fig. 5.9 Kissinger Plot for $SrNb_2O_6$ for computing activation energy.

5.3.6 Impedance Spectroscopy

The impedance measurement from 0.1Hz to 1 MHz using Solartron SI-1260 Impedance/Gain Phase Analyser with Solartron 1294 Impedance Interface for PC is presented in this section. The Nyquist plot for $SrNb_2O_6$ prepared by hydroxide precursor method is graphically plotted in figure 5.10 for the frequency to 10^6 Hz. Figure 4.9 shows single semi-circle formation for $SrNb_2O_6$ samples sintered at 750 degree Celsius for 30, 60, 90 and 120 minutes. From figure 5.10 and Nyquist plot for higher frequency as shown in figure 5.11 it is observed that all the samples shows a semicircle arc at high frequency as well as forming another semicircle arc at lower frequency. One semicircle in the high frequency range and the other in the low frequency range for $SrNb_2O_6$ sintered at 750^0C may correspond to oxygen migration in the bulk and across grain boundaries. Also semicircles in Nyquist plot at high frequency corresponds to grain relaxation and at low frequency relate grain boundary, secondary phase segregated at grain boundary and sometimes effect of electrode.

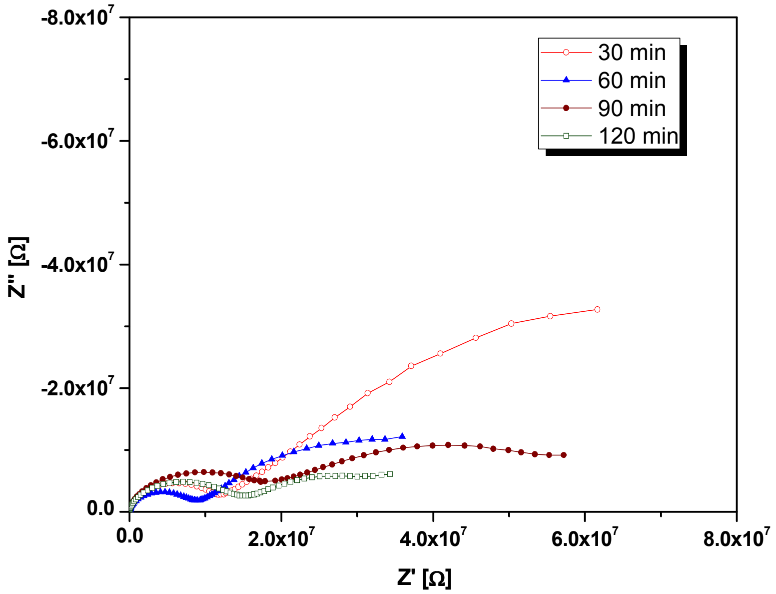

Figure 5.10 Nyquist plot of $SrNb_2O_6$ Sintered at 750^0C for 30, 60, 90 and 120 min

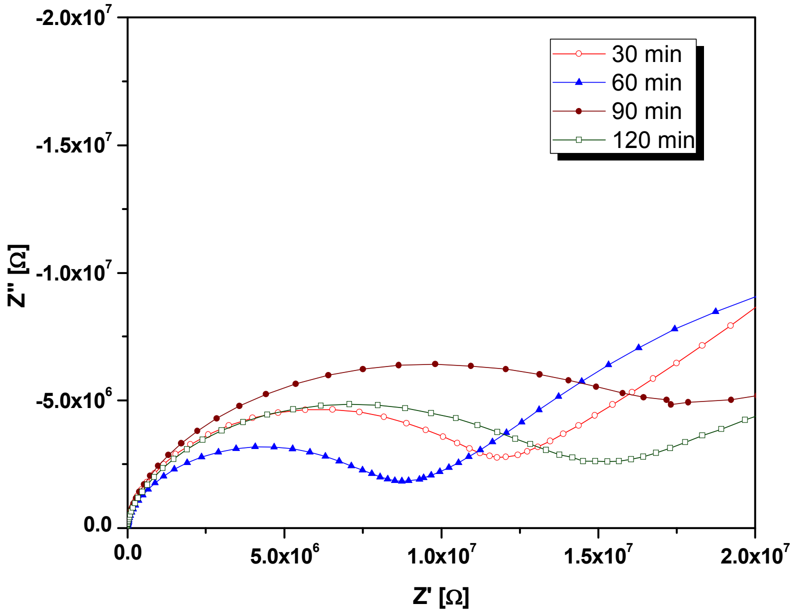

Figure 5.11 Nyquist plot at high frequency observed for $SrNb_2O_6$ Sintered at 750^0C for 30, 60, 90 and 120 min

Bode plot was graphically ploted for the for $SrNb_2O_6$ samples sintered at 750^0C for 30, 60, 90 and 120 minutes with frequency vs magnitude of impedance as shown in figure 5.12 and frequency vs phase angle as shown in 5.13. Figure 5.12 shows the decrease in magnitude of impedance drastically with increase in frequency. The frequency dependence of phase angle is observed in figure 5.13 for $SrNb_2O_6$ samples sintered at 750^0C. All the samples shows similar trend in the phase angle shift with increase in frequency.

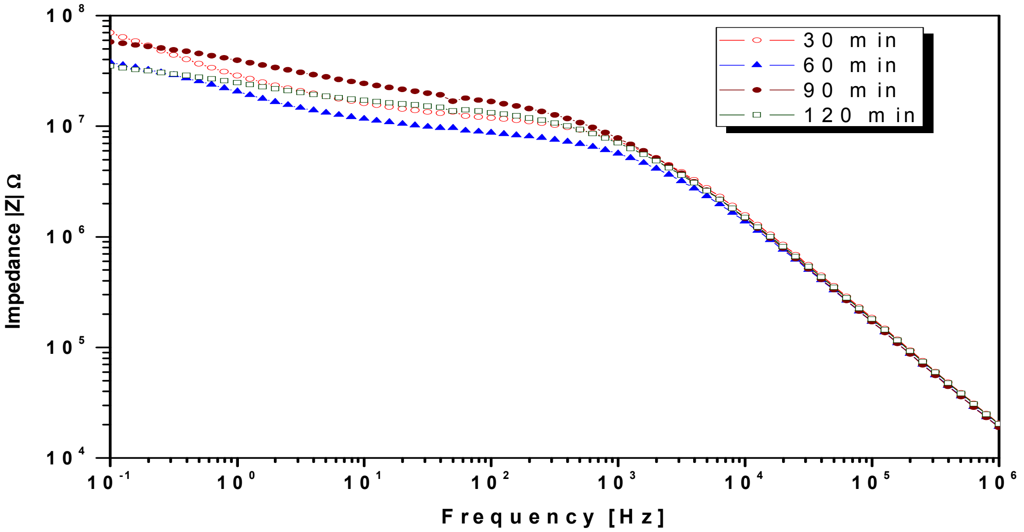

Figure 5.12 Bode plot – Impedance magnitude |Z| vs frequency of $SrNb_2O_6$ Sintered at 750^0C for 30, 60, 90 and 120 min

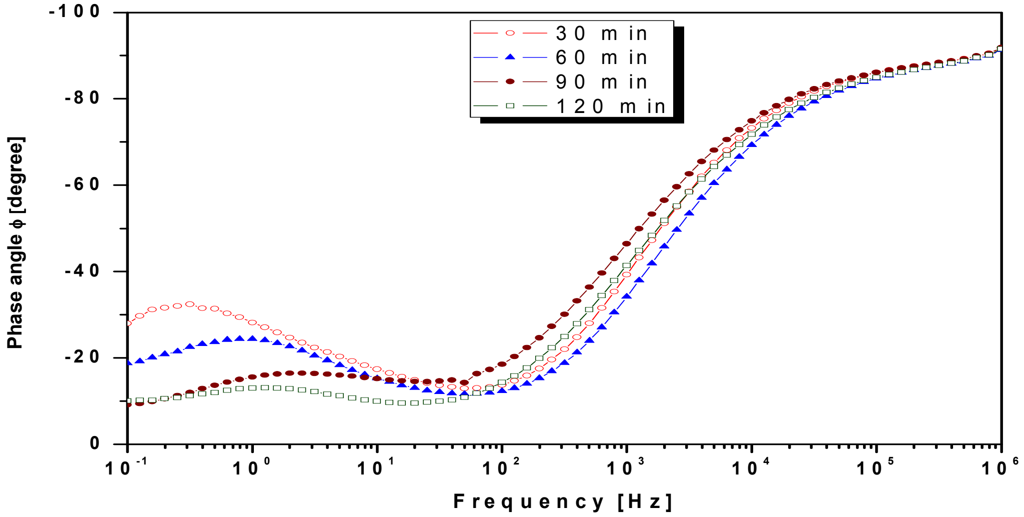

Figure 5.13. Bode plot – Phase Angle vs frequency of $SrNb_2O_6$ Sintered at 750^0C for 30, 60, 90 and 120 min

The variation of real (Z') and Imaginary (Z") part or Nyquist plot of impedance with frequency for $SrNb_2O_6$ samples sintered at 1000^0C for 30, 60, 90 and 120 minutes is shown in figure 5.14. A single semicircular arc is appeared for all samples. The semicircle at low frequency relates grain boundary, secondary phase segregated at grain boundary and sometimes effect of electrode.

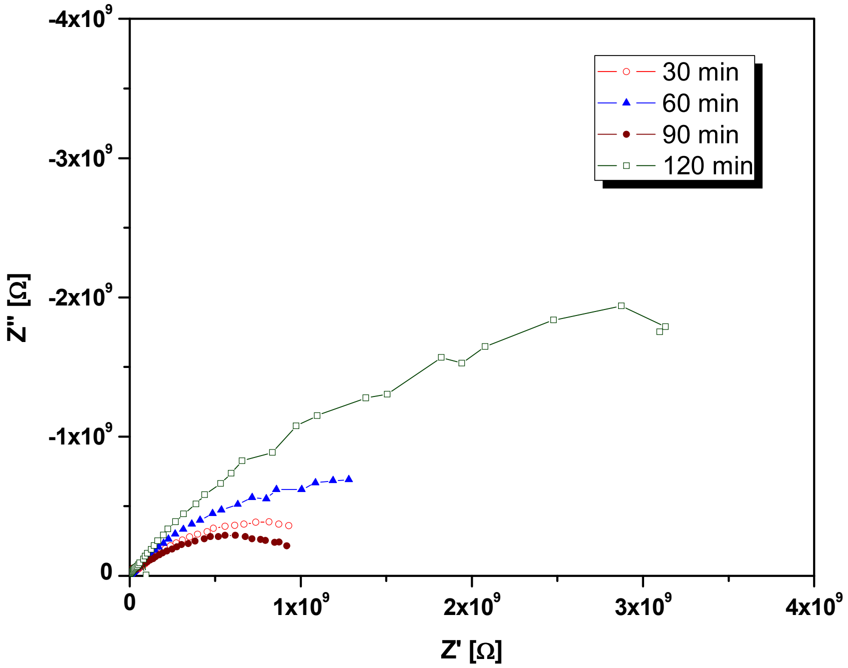

Figure 5.14 Nyquist plot at high frequency observed for $SrNb_2O_6$ Sintered at 1000^0C for 30, 60, 90 and 120 min

Bode plot was constructed for the for $SrNb_2O_6$ samples sintered at 1000^0C for 30, 60, 90 and 120 minutes is with frequency vs magnitude of impedance as shown in figure 5.15 and frequency vs phase angle as shown in figure 5.16. Both the figures shows the frequency dependence of impedance parameters for $SrNb_2O_6$ samples. The sample sintered for 120 minute shows higher impedance |Z| as compared to samples sintered for smaller duration.

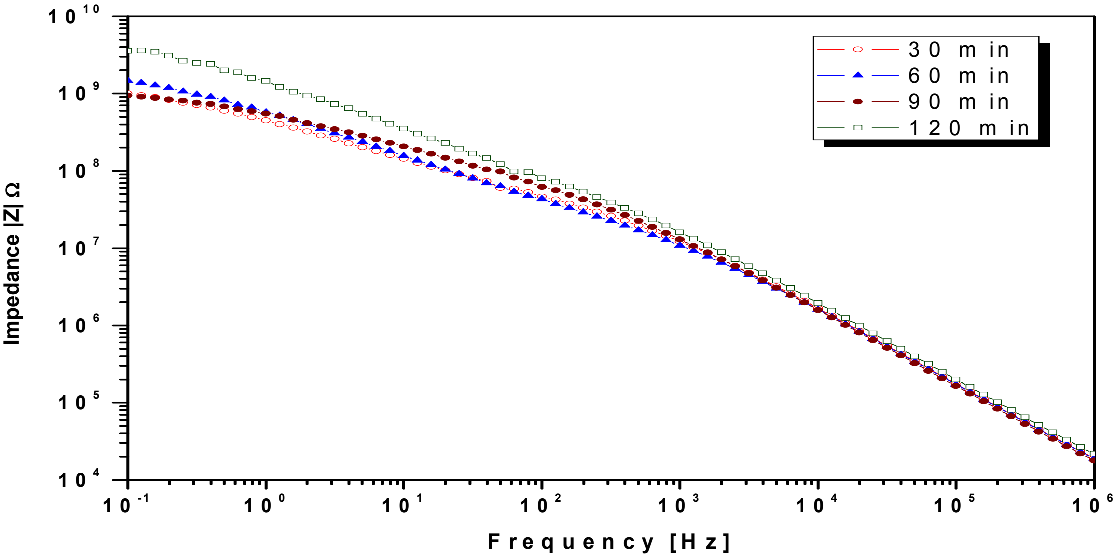

Figure 5.15. Bode plot – Impedance magnitude |Z| vs frequency of $SrNb_2O_6$ Sintered at 1000^0C for 30, 60, 90 and 120 min

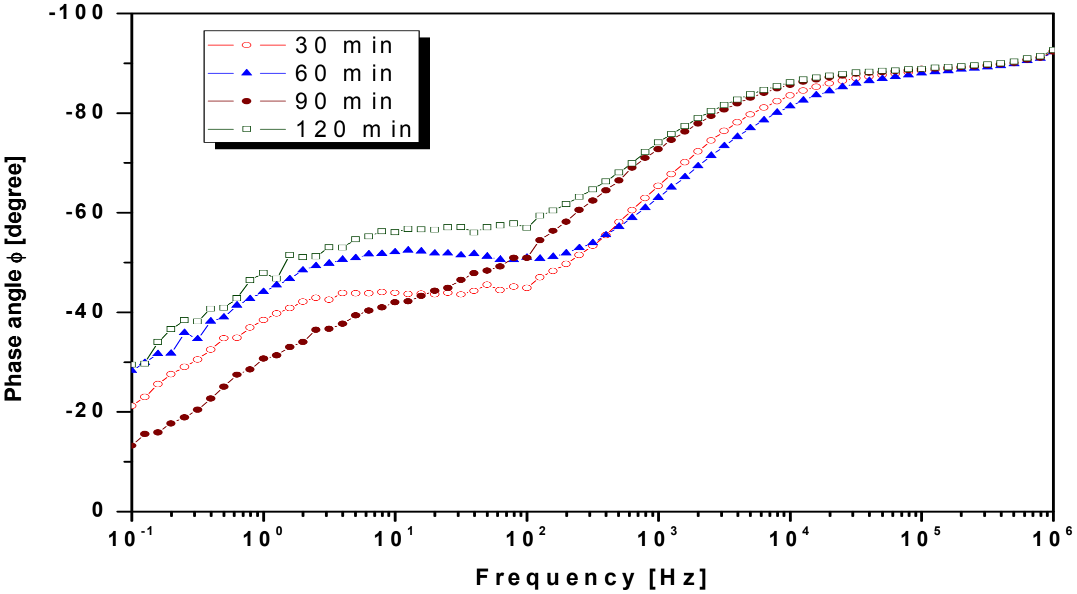

Figure 5.16. Bode plot – Phase Angle vs frequency of $SrNb_2O_6$ Sintered at 1000^0C for 30, 60, 90 and 120 min

Dielectric Loss vs frequency of $SrNb_2O_6$ Sintered at 750^0C and 1000^0C were measured upto 10MHz and plotted in figure 5.17 and 5.18 respectively. It is observed that the dielectric loss of $SrNb_2O_6$ decreases with increase in frequency, however an abnormal high dielectric loss peak is absorbed at near 10MHz for all the samples. Presence of dislocations or voids can also influence the dielectric loss of the bulk sample.

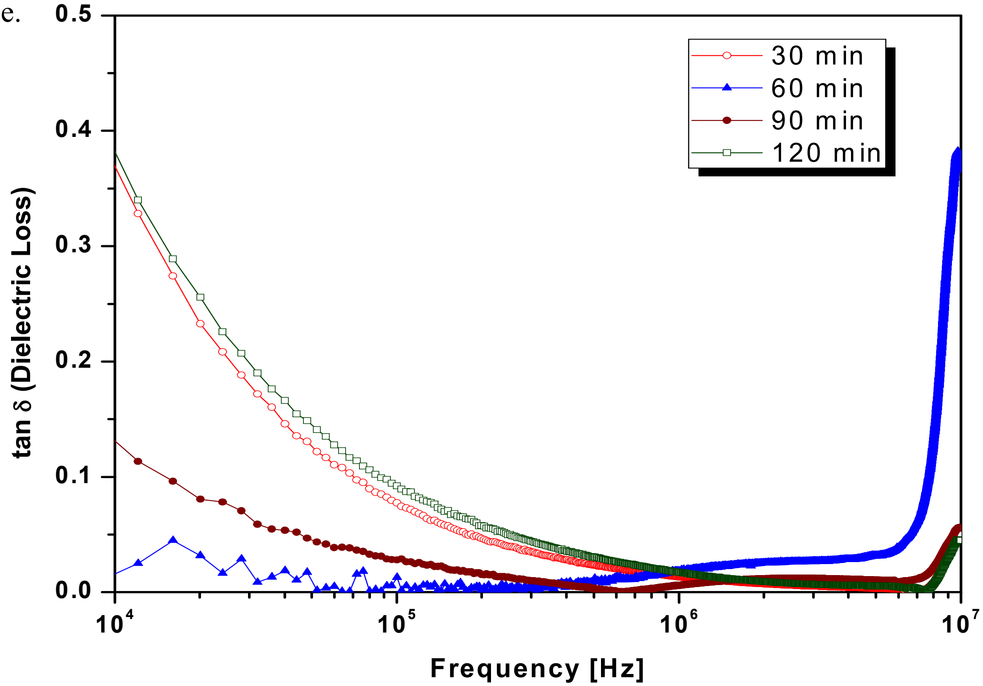

Figure 5.17 Dielectric Loss vs frequency of $SrNb_2O_6$ Sintered at 750^0C for 30, 60, 90 and 120 min

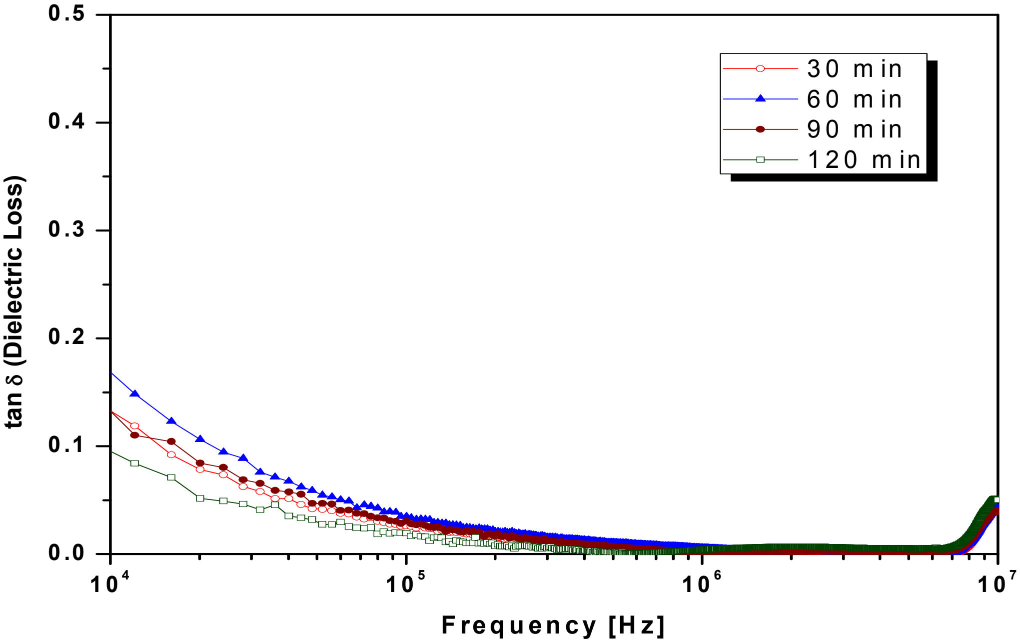

Figure 5.18 Dielectric Loss vs frequency of $SrNb_2O_6$ Sintered at 1000^0C for 30, 60, 90 and 120 minutes

5.4 Characterization of Strontium Tantalate

5.4.1 X-ray powder diffraction

The powder X-ray patterns were recorded for 2θ at 40/min for oven dried and samples calcined at various temperatures by using Philips PW-1710 model X-ray diffractometer using Cu Kα. Fig. 5.19 illustrates the XRDs of $SrTa_2O_6$ hydroxide precursor powders calcined at different temperatures ranging from 200 to 500 °C for 6h. Unlike in the case of $SrNb_2O_6$, the XRDs of these powders do not show good crystallinity until the samples were heat treated at 400 °C for 6 h. However the formation of product phase was completed at 500 °C. For lattice parameter and interplanar distance (d) calculation, the samples were scanned in a 2θ range of 10–80° in step scan mode at 5 s/step. Silicon was used as an internal standard.

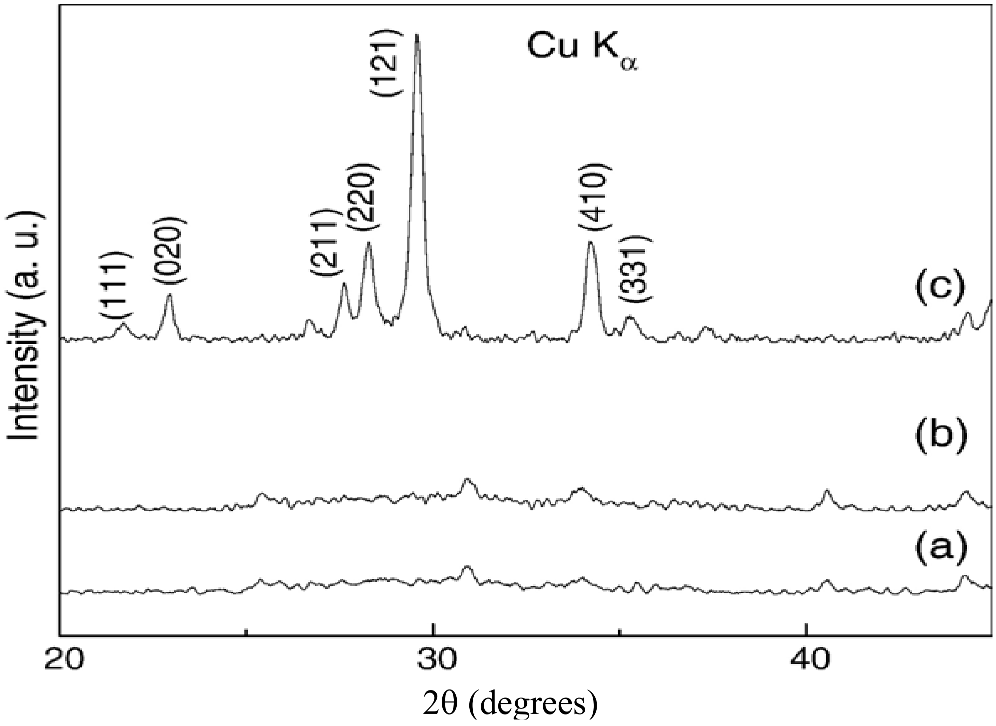

Fig. 5.19 The XRD of $SrTa_2O_6$ hydroxide precursor powders after heating at (a) 200 and (b) 400 and (c) 500 °C.

The crystal structure of $SrTa_2O_6$ is orthorhombic and all lines in the diffractogram match with reported values (JCPDS: 38-0828). The calculated lattice parameters by least squares fit are a=11.01 Å, b=7.6370 Å and c=5.617 Å. The particle size calculated from Scherrer's formula ($t=K\ \lambda/B\ \cos\theta B$) where t is the average size of the particles, assuming particles are spherical, K=0.9, λ is the wavelength of X-ray radiation, B is the full width at half maximum of the diffracted peak and θB is the angle of diffraction) is 80 nm

5.4.2 Energy Dispersive X-Ray Analysis

Experimentally observed EDAX spectrum of $SrTa_2O_6$ prepared by hydroxide precursor method is depicted in figure 5.20 The EDAX was scanned from 0 to 10keV and characteristics peaks for Strontium, and Oxygen is observed at 1.806 keV and 0.525 keV respectively. The tantalum element characteristic contribution at 1.709 keV is due to a M-alpha emission [53–57]. The EDAX peaks observed for $SrTa_2O_6$ and corresponding identified transition are tabulated in Table 5.3.

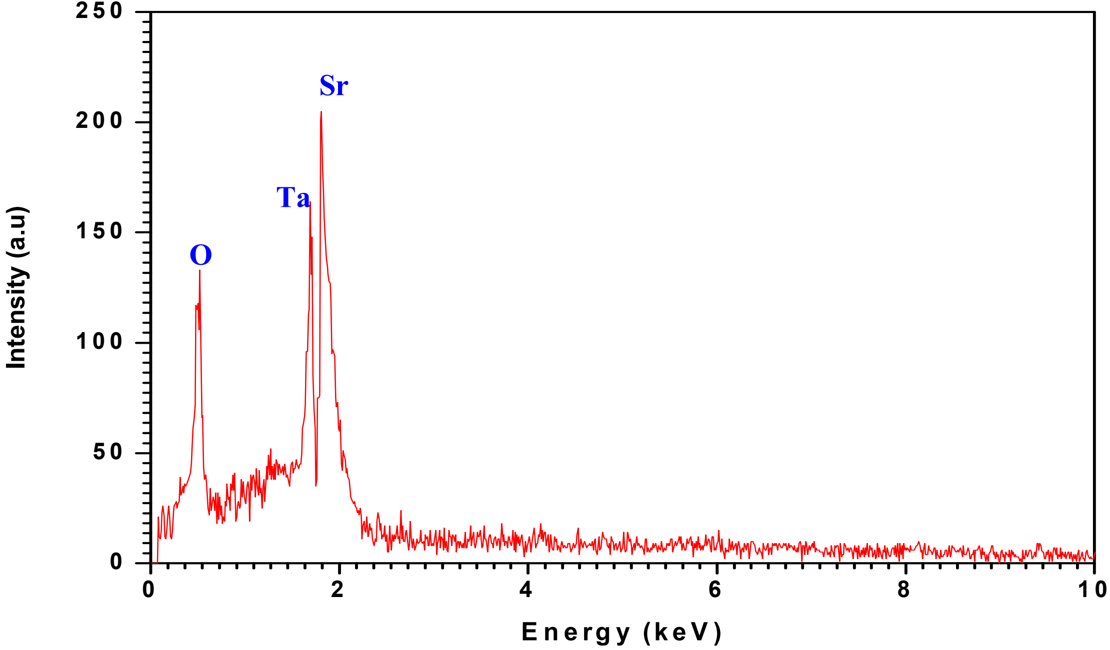

Figure 5.20. EDAX Spectrum of $SrTa_2O_6$ prepared by hydroxide precursor method

Table 5.3 EDAX spectrum peaks observed for $SrTa_2O_6$

Sr No.	Element	Peak Observed	Transition
1	Oxygen	0.525 keV	K-alpha
2	Strontium	1.806 keV	L3M5
3	Tantalum	1.709 keV	M-alpha

5.4.3 Scanning Electron Microscopy

The average particle size and morphology of these calcined powders were examined by scanning electron microscopy is shown in figure 5.21. The calcined powders (500 °C for 6 h) prepared by hydroxide precursor technique have spherical to elliptical in shape and agglomerated, with an average primary particle size ~90 nm. The SEM images were observed using a Leica Cambridge 440 microscope. All the powders were dispersed in amyl acetate for SEM studies.

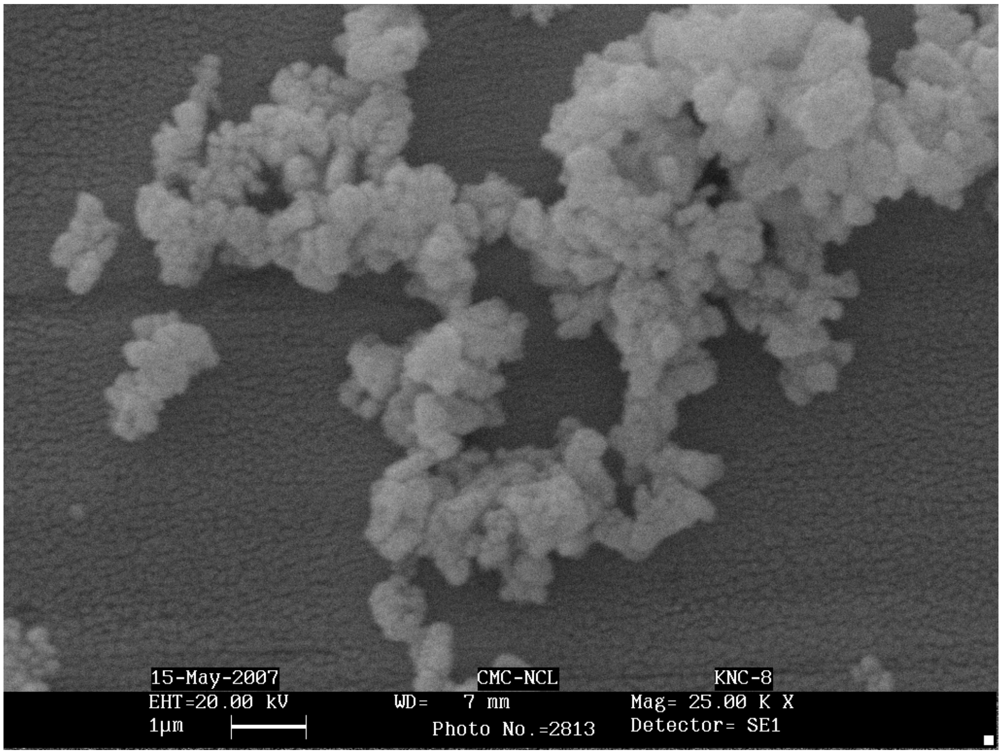

Figure 5.21 The SEM micrographs of $SrNb_2O_6$ powders calcined at 500 °C.

5.4.4 Thermogravimetry Analysis

Stoichiometric amount of Strontium hydroxide and Tantalum hydroxide obtained from Tantalum (V) oxide with HF is mixed well thoroughly and thermogravimetric analysis of this mixture is carried out at 10 different heating rate (2.5, 5, 7.5, 10, 12.5, 15, 17.5, 20, 22.5 and 25^0C/min) and depicted in figure 5.22. Around 8 to 16 mg of mixture is used for TGA analysis. Irrespective of heating rate, figure 6 clearly shows gradual dip in mass upto 500C and then stable profile, which is an indication of solid state reaction takes place with release of hydroxyl ions from the precursors. XRD also conforms the structural formation $SrTa_2O_6$ at 500^0C

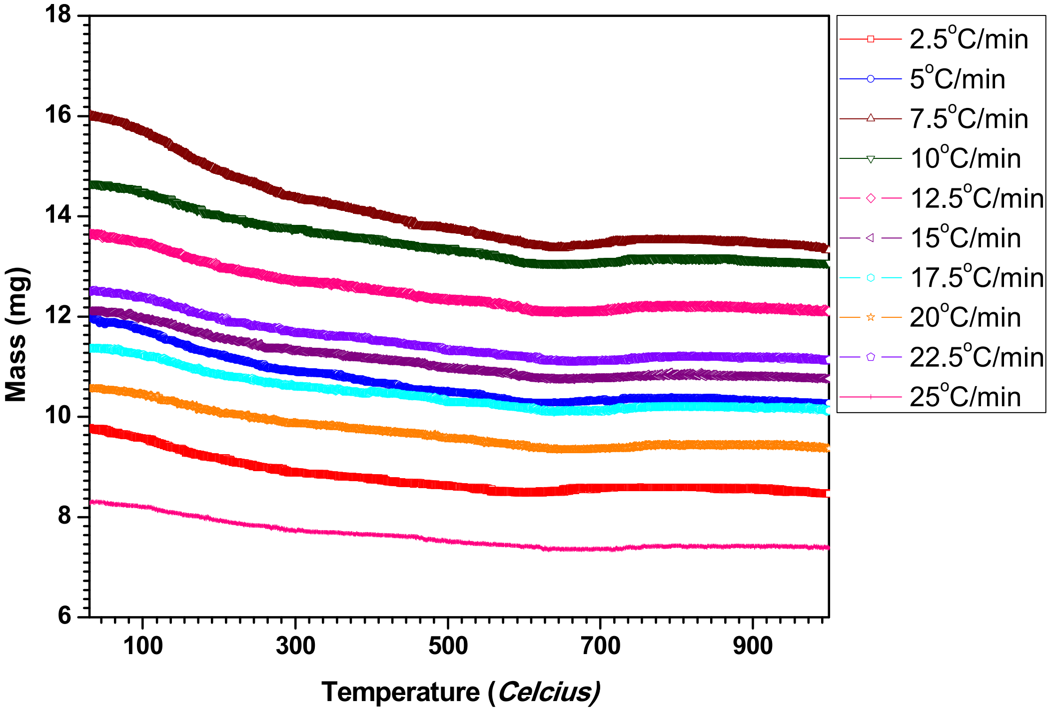

Figure 5.22. TGA profile of $SrTa_2O_3$ formation at different heating rate

5.4.5 Differential Scanning Calorimetery

Differential Scanning Calorimetric (DSC) analysis of $SrTa_2O_6$ was carried out at 6 different heating rate (2.5, 5, 7.5, 10 and 15^0C/min) and shown in figure 5.23. Stoichiometric amount of Strontium hydroxide and freshly prepared tantalum hydroxide are mixed well thoroughly. Around 20 mg of mixture is used for DSC analysis. Inert Nitrogen gas is used as a purge gas during DSC analysis of mixture. The exothermic DSC peeks were observed at around 455^0C to 510^0C range and the peak shifts with heating rate and tabulated in Table 5.4 for the computation of activation energy by Kissinger method. From the table 5.4, Kissinger plot (figure 5.24) was constructed to find the linear equation, from the slope of the equation the activation energy for the formation of $SrTa_2O_6$ by hydroxide precursor method is 142.92 kJ.

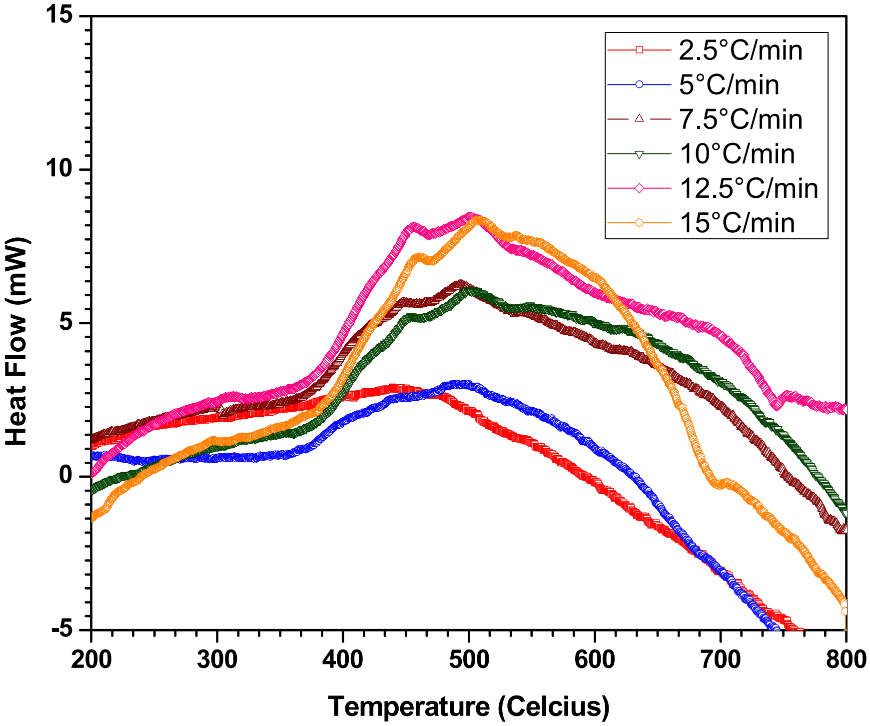

Figure 5.23. DSC profile of $SrTa_2O_6$ formation at different heating rate

Table 5.4 DSC data on $SrTa_2O_6$ at various heating rates (Kissinger method).

Heating rate β (^{0}C)	Peak Tmax (^{o}C)	Peak Tmax (K)	T^2_{max}	$\frac{1}{T_{max}}$	$\frac{\beta}{T^2_{max}}$	$-\ln\left(\frac{\beta}{T^2_{max}}\right)$	Slope	Activation Energy (kJ/mol)
2.5	455.60	728.75	531077	0.001372	4.707E-06	12.266	17190.9552	142.92
5	490.96	764.11	583864	0.001308	8.563E-06	11.667		
7.5	493.91	767.06	588381	0.001303	1.274E-05	11.270		
10	499.14	772.29	596432	0.001294	1.676E-05	10.996		
12.5	503.69	776.84	603480	0.001287	2.071E-05	10.784		
15	510.03	783.18	613371	0.001276	2.445E-05	10.618		

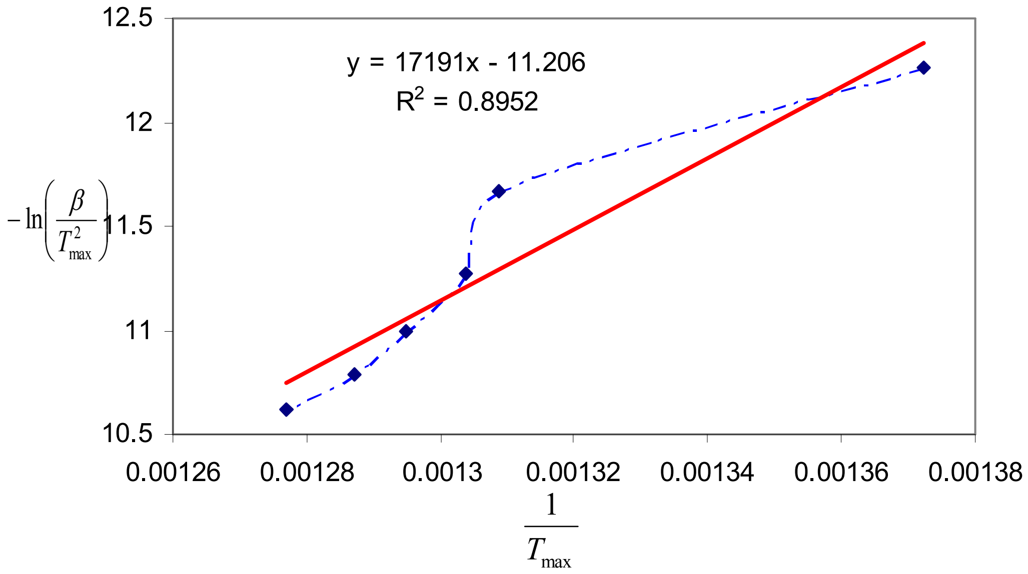

Fig. 5.24. Kissinger Plot for $SrTa_2O_6$ for computing activation energy.

5.4.6 Impedance Spectroscopy

The variation of real (Z') and Imaginary (Z") part or Nyquist plot of impedance with frequency for $SrTa_2O_6$ samples sintered at 750^{0}C for 30, 60, 90 and 120 minutes is shown in figure 4.25. Figure 4.25 shows single semi-circle formation for $SrTa_2O_6$ samples sintered at 750 degree Celsius for 30, 60, 90 and 120 minutes. Nyquist plot for higher frequency is shown in figure 4.26 and it doesn't show any additional semicircle arc formation at higher frequency. The semicircle at low frequency relates grain boundary, secondary phase segregated at grain boundary and sometimes effect of electrode.

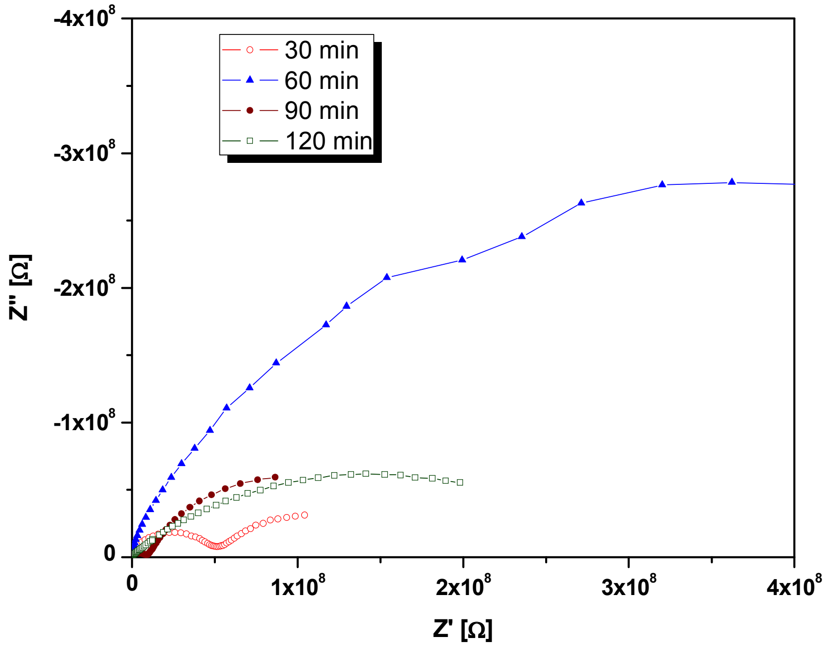

Figure 5.25. Nyquist plot of $SrTa_2O_6$ Sintered at 750^0C for 30, 60, 90 and 120 min

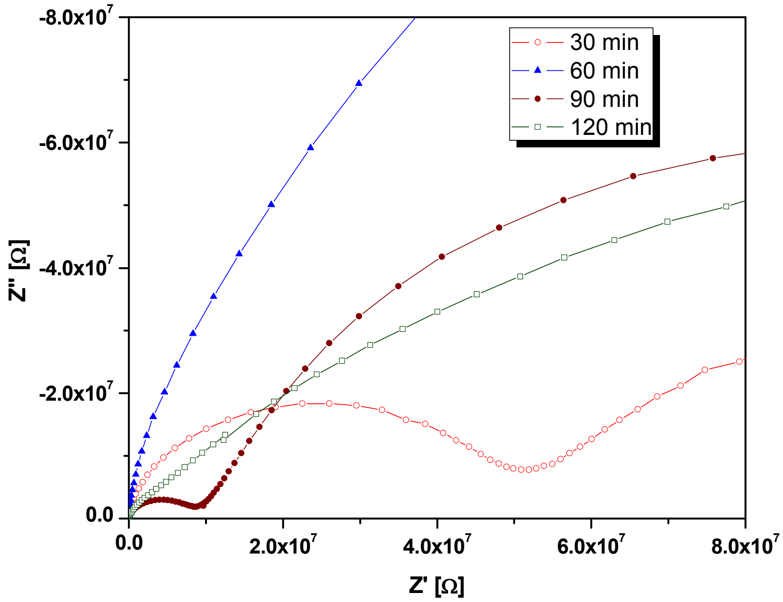

Figure 5.26. Nyquist plot at high frequency observed for $SrTa_2O_6$ Sintered at 750^0C for 30, 60, 90 and 120 min

Bode plot was measured for the for $SrTa_2O_6$ samples sintered at 750^0C for 30, 60, 90 and 120 min with frequency vs magnitude of impedance as shown in figure 5.27 and frequency vs phase angle as shown in figure 5.28. Figure 5.27 shows the decrease in magnitude of impedance drastically with increase in frequency. The frequency dependence of phase angle is observed for $SrTa_2O_6$ samples sintered at 750^0C. The sample sintered for 60 minute shows higher impedance |Z| as compared to samples sintered for other durations.

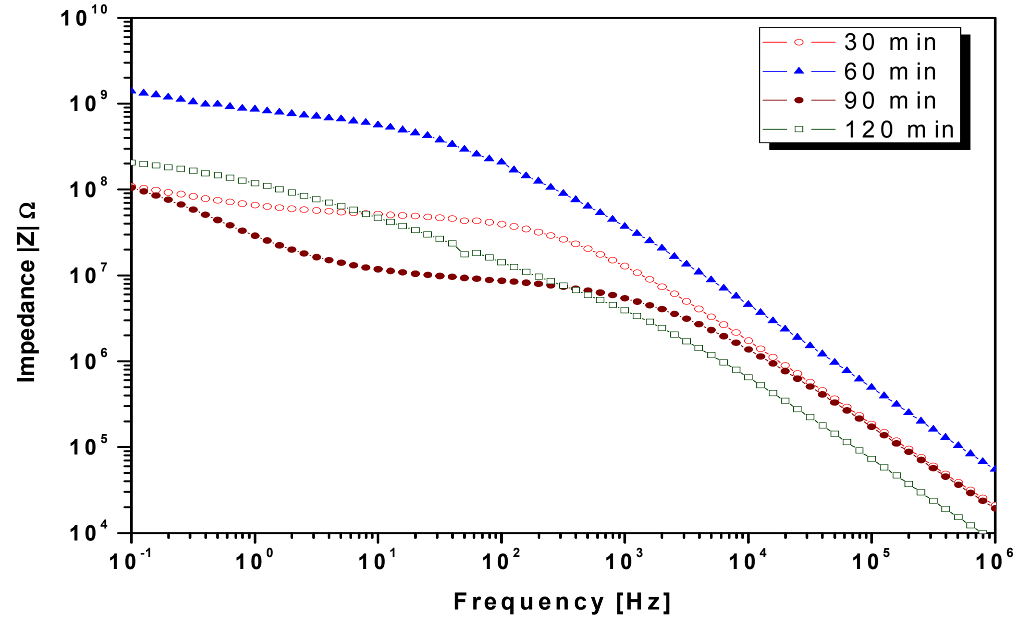

Figure 5.27. Bode plot – Impedance magnitude |Z| vs frequency of $SrTa_2O_6$ Sintered at 750^0C for 30, 60, 90 and 120 min

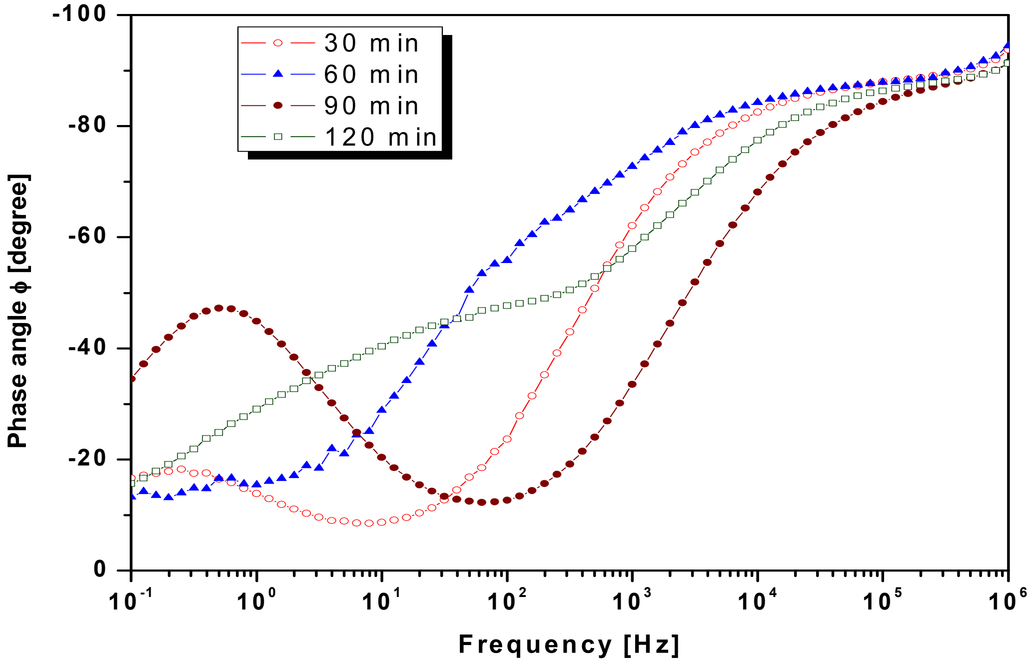

Figure 5.28. Bode plot – Phase Angle vs frequency of $SrTa_2O_6$ Sintered at 750^0C for 30, 60, 90 and 120 min

The variation of real (Z') and Imaginary (Z") part or Nyquist plot of impedance with frequency for $SrTa_2O_6$ samples sintered at 1000^0C for 30, 60, 90 and 120 minutes is shown in figure 5.29. A single semicircular arc is appeared for all samples, however for the sample sintered for 30 and 60 min, an additional semicircular arc is appeared at high frequency as shown in figure 5.30. One semicircle in the high frequency range and the other in the low frequency range for $SrTa_2O_6$ sintered at 750^0C for 30 and 60 min may correspond to oxygen migration in the bulk and across grain boundaries. Also Semicircles in Nyquist plot at high frequency corresponds to grain relaxation and at low frequency relate grain boundary, secondary phase segregated at grain boundary and sometimes effect of electrode.

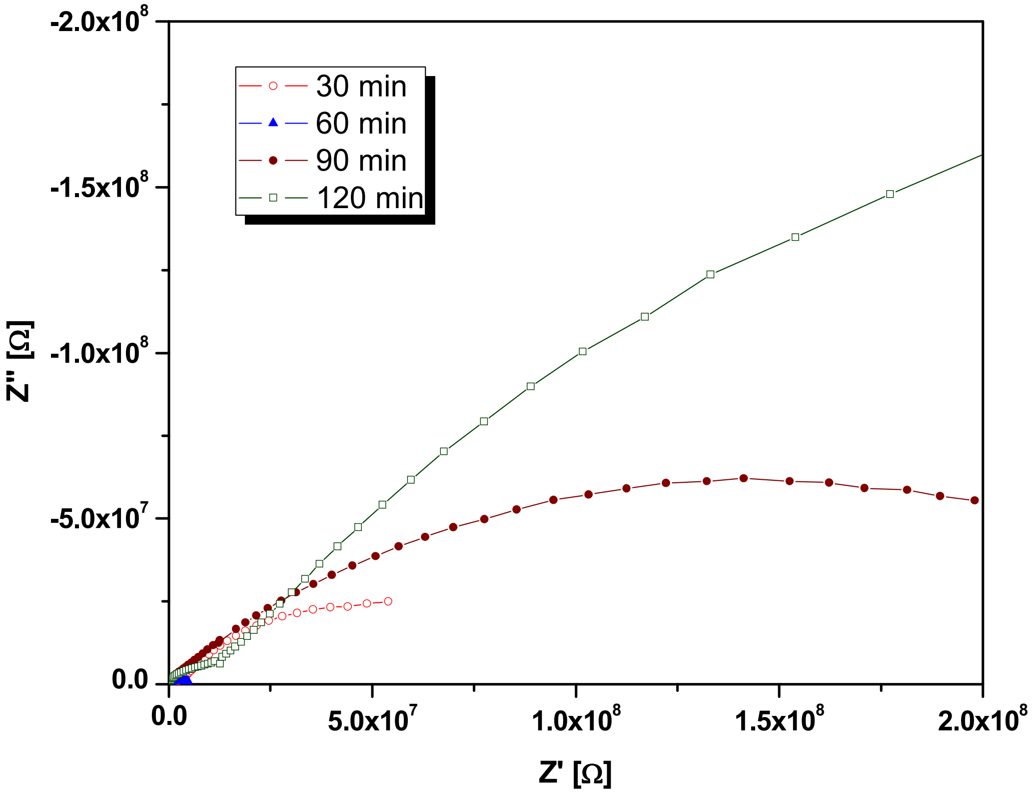

Figure 5.29. Nyquist plot at high frequency observed for $SrTa_2O_6$ Sintered at 1000^0C for 30, 60, 90 and 120 min

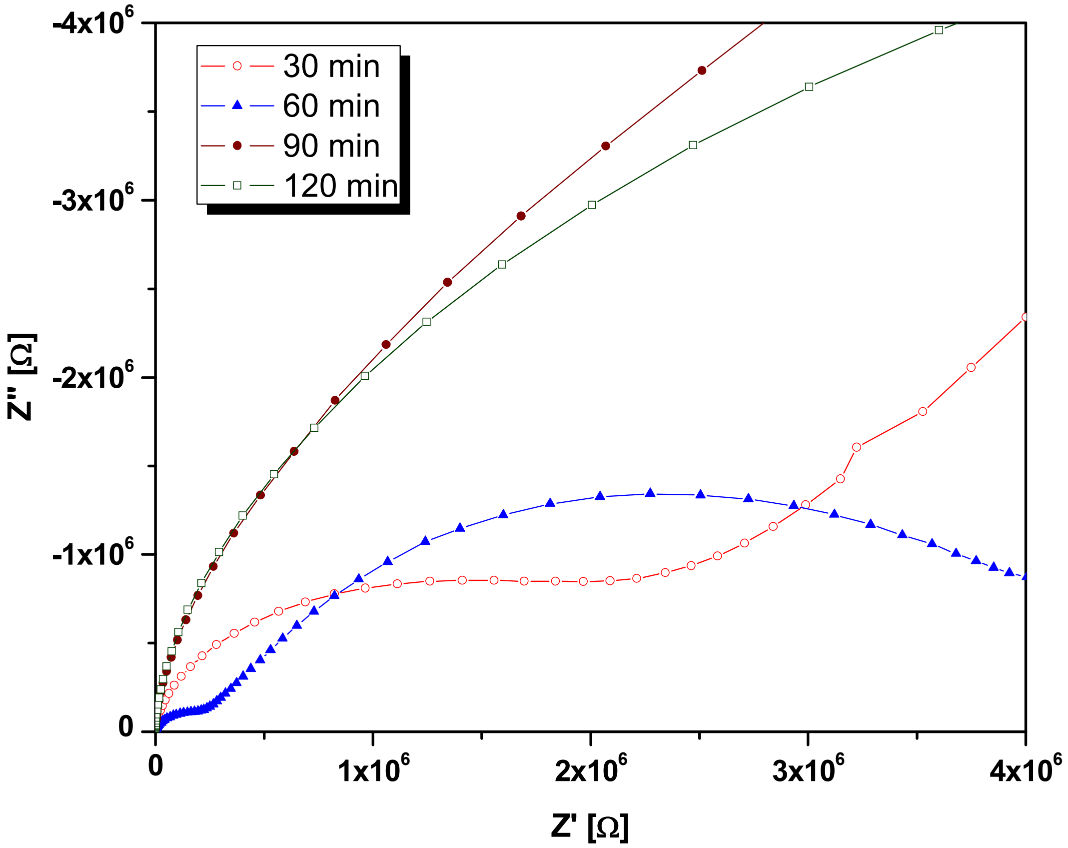

Figure 5.30. Nyquist plot at high frequency observed for $SrTa_2O_6$ Sintered at 1000^0C for 30, 60, 90 and 120 min

Bode plot was constructed for the for $SrTa_2O_6$ samples sintered at 1000^0C for 30, 60, 90 and 120 minutes is with frequency vs magnitude of impedance as shown in figure 5.31 and frequency vs phase angle as shown in figure 5.32. Both the figures shows the frequency dependence of impedance parameters for $SrTa_2O_6$ samples. The sample sintered for 60 minute shows lower impedance |Z| as compared to samples sintered for other duration. Presence of dislocations or voids can also influence the dielectric electric and impedance properties of the bulk sample.

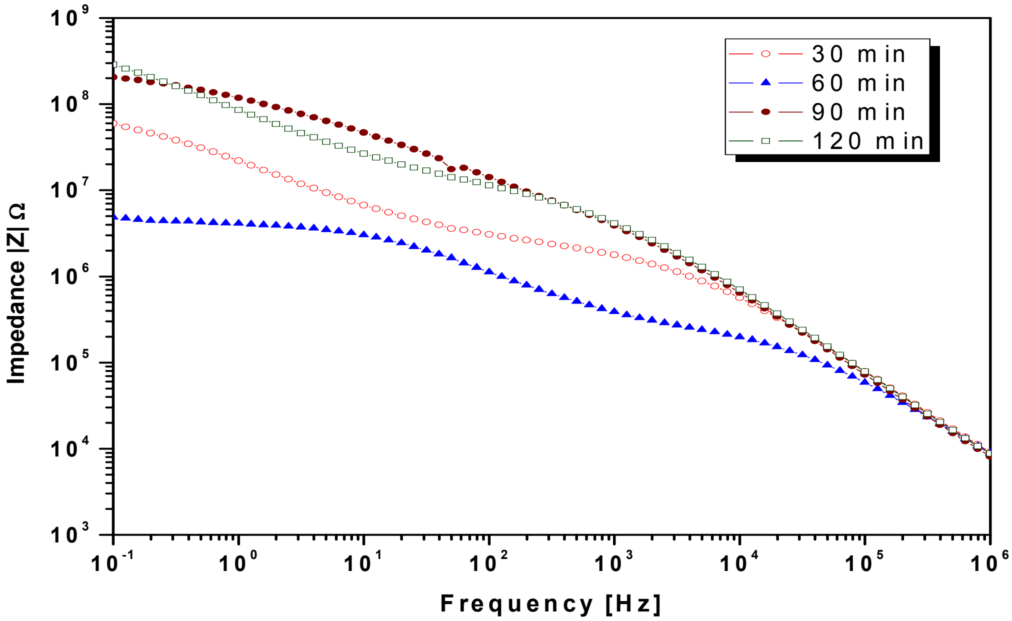

Figure 5.31. Bode plot – Impedance magnitude |Z| vs frequency of $SrTa_2O_6$ Sintered at 1000^0C for 30, 60, 90 and 120 min

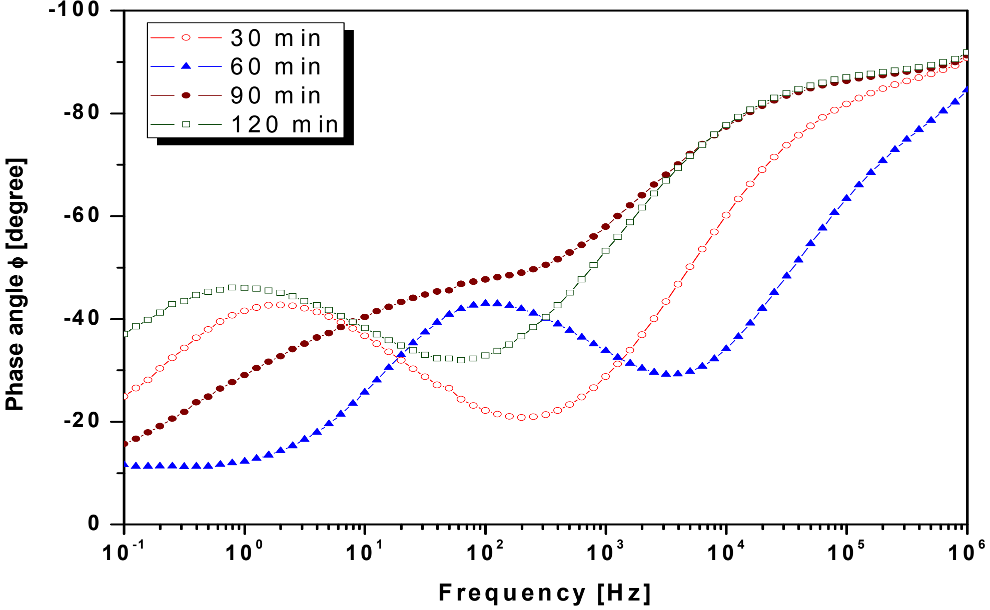

Figure 5.32. Bode plot – Phase Angle vs frequency of $SrTa_2O_6$ Sintered at 1000^0C for 30, 60, 90 and 120 min

Dielectric Loss vs frequency of $SrTa_2O_6$ Sintered at 750^0C and 1000^0C were measured upto 10MHz and plotted in figure 5.33 and 5.34 respectively. It is observed that the dielectric loss of $SrTa_2O_6$ decreases with increase in frequency and becomes stable after 10^6Hz. $SrTa_2O_6$ samples sintered at 705^0C as well as 1000^0C.

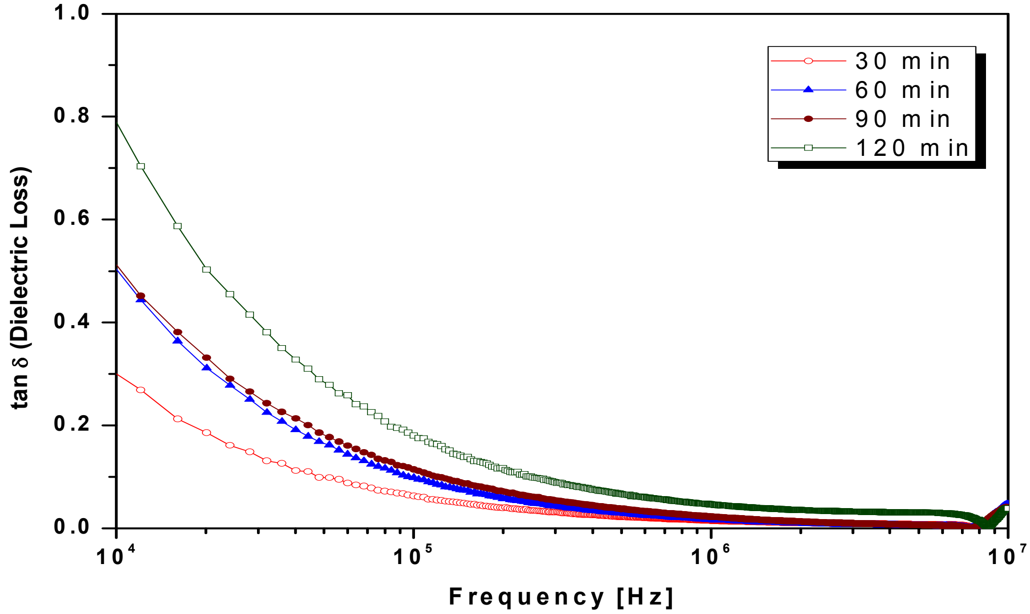

Figure 5.33. Dielectric Loss vs frequency of $SrTa_2O_6$ Sintered at 750^0C for 30, 60, 90 and 120 min

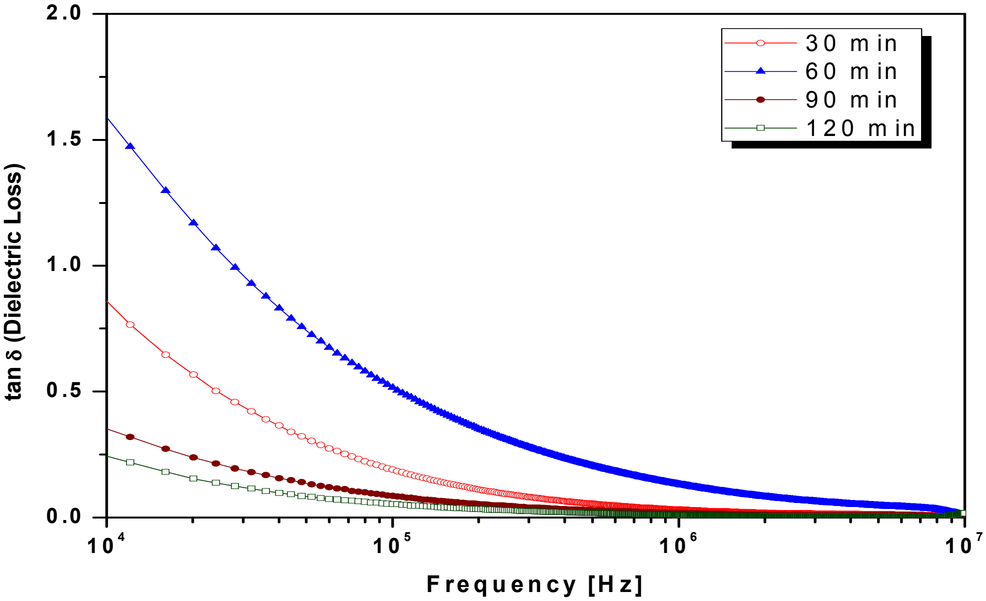

Figure 5.34. Dielectric Loss vs frequency of $SrTa_2O_6$ Sintered at 1000^0C for 30, 60, 90 and 120 min

5.5 Summary

The conventional solid state method forms $SrNb_2O_6$ or $SrTa_2O6$ at 900 °C after prolonged heating (12 h). The purpose of this study was to investigate the possibility of lowering temperature of formation of strontium niobate and strontium tantalate phases. The procedure consists of preparing corresponding hydroxides and mixing thoroughly and subsequent heating to formation of strontium niobate and strontium tantalate powders. This procedure is quite novel and can be used for large scale production of these powders.

The properties of ceramics are greatly affected by the important characteristics of the powder such as particle size, morphology, purity and chemical composition. The traditional solid state methods lead to poor compositional homogeneity and high sintering temperatures. The average particle size and morphology of these calcined powders were examined by scanning electron microscopy. Thermogravimetry analysis was carried out to probe the thermal profile during the formation of $SrNb_2O_6$ and $SrTa_2O_6$. Differential scanning calorimetry for $SrNb_2O_6$ as well as $SrTa_2O_6$ were carried out at 6 different heating rate to estimate the activation energy by Kissinger method and the estimated activation energy for the formation of $SrNb_2O_6$ and $SrTa_2O_6$ by hydroxide precursor method is 270.28 kJ and 142.92 kJ respectively. Nyquist plot and Bode plot was constructed to study the impedance characteristics of Strontium niobate and Strontium tantalate. In the impedance spectroscopy, the frequency dependence of phase angle is observed for both $SrNb_2O_6$ and $SrTa_2O_6$ samples sintered at 750^0C and 1000^0C. The dielectric loss of $SrNb_2O_6$ decreases with increase in frequency, however an abnormal high dielectric loss peak is absorbed at near 10MHz. In case of $SrTa_2O_6$ it is observed that the dielectric loss of $SrTa_2O_6$ drastically decreases with increase in frequency.

5.6 References

1. Horst P. Beck, Hyun Seup-Ra, Robert Haberkorn, Holger Kohlmann, Matthias Eul, Z. Anorg. Allg. Chem., 636 (2010) 1069.
2. H.J. Lee, K.S. Hong, S.J. Kim, I.T. Kim, Mater. Res. Bull. 32 (1997) 847.
3. R.C. Pullar, J.D. Breeze, N. McN. Alford, J. Am. Ceram. Soc. 88 (2005) 2466.
4. Y.C. Zhang, Z.X. Yue, Z. Gui, L.T. Li, Mater. Lett. 57 (2003) 4531.
5. A. Ananta, R. Brydson, N.W. Thomas, J. Eur. Ceram. Soc. 19 (1999) 355.
6. H. Brusset, H. Gillier-Pandraud, S.D. Voliotis, Mater. Res. Bull. 6 (1971) 5.
7. M. Pastor, S. Goenka, S. Maiti, K. Biswas, I. Manna, Ceramics International 36 (2010) 1041.
8. J. Leitner, M. Hampl, K. Ruzicka, M. Straka, D. Sedmidubsky and P. Svoboda, J. Thermal Analysis and Calorimetry, 91 (2008) 985.
9. In-Sun Cho, Shin Tae Bae, Dong Hoe Kim, Kug Sun Hong, Int. J. Hydrogen Energy, 35 (2010) 12954.
10. Yuanyuan Zhou, Qian Ma, Mengkai Lü, Zifeng Qiu, Aiyu Zhang, Zhongsen Yang, Materials Science and Engineering B 150 (2008) 66.
11. Wen-Jiung Lee and Tsang-Tse Fang, J. Am. Ceram. Soc., 81 (1998) 193.
12. Xinping Lin, Fuqiang Huang, Jingcheng Xing, Wendeng Wang, Fangfang Xu, Acta Materialia 56 (2008) 2699.
13. Tao Huang, Xinping Lin, Jingcheng Xing, Wendeng Wang, Zhichao Shan, Fuqiang Huang, Materials Science and Engineering B 141 (2007) 49.
14. Jingcheng Xing, Zhichao Shan, Kaiqiang Li, Jianjiang Bian, Xinping Lin, Wendeng Wang, Fuqiang Huang, J. Phys. and Chem. of Solids 69 (2008) 23.
15. P. K. Panda, J Mater Sci 44 (2009) 5049.
16. Lili Zhao & Xiangchun Liu & Changsheng Tian, J Electroceram 21 (2008) 782.

17. I. Rosenberg, J.R. Brock, A. Heller, J. Phys. Chem. 96 (1992) 3423.
18. Y. Ohko, K. Hashimoto, A. Fujishima, J. Phys. Chem. A 101 (1997) 8057.
19. K. Sunada, Y. Kikuchi, K. Hashimoto, A. Fujishima, Environ. Sci. Technol. 32 (1998) 726.
20. X. Lin, F. Huang, W. Wang, Y. Wang, Y. Xia, J. Shi, Appl. Catal. A 313 (2006) 218.
21. P. V. Lenzo, E. G. Spencer, and A. A. Ballman, Appl. Phys. Lett., 11(1967) 23.
22. S. Ducharme, J. Feinberg, and R. R. Neurgaonkar, IEEE, J. Quantum Electron., 23 (1987) 2116.
23. A. M. Glass, J. Appl. Phys., 40 (1969) 4699.
24. R. B. Maciolek and S. T. Liu, J. Electron. Mater., 2 (1973) 191.
25. R. R. Neurgaonkar, M. H. Kalisher, T. C. Lim, E. J. Staples, and K. L. Leester, Mater. Res. Bull., 15 (1980) 1235.
26. J. B. Thaxter, Appl. Phys. Lett., 15 (1969) 210.
27. R. R. Neurgaonkar and W. K. Cory, J. Opt. Soc. Am. B: Opt. Phys., 3 (1986) 274.
28. Chae B-G, Lee WJ, You IK, Ryu SO, Yung MY, Yu BG. Jpn J Appl Phys, 41 (2002) 729.
29. Cho KI, Yoon SG, Lee CS. Jpn J Appl Phys 40 (2001) 6941.
30. Tokumitsu E, Fujii G, Ishiwara H. Appl Phys Lett 75 (1999) 575.
31. Ruzyllo J, Lee DO, Roman P, Horn MP, et al. IEEE international symposium on semiconductor manufacturing conference, Proceedings, 2 (2001) 71.
32. Regnery S, Thomas R, Ehrhart P, Waser R. J Appl Phys 97 (2005) 73521.
33. K. Chang, K. Shanmugasundaram, D. O. Lee, P. Roman, C. -T. Wu, J. Wang, J. Shallenberger, P. Mumbauer, R. Grant, R. Ridley, G. Dolny, J. Ruzyllo, Microelectronic Engineering 72 (2004) 130.

34. Kohtaro Yoshioka, Valery Petrykin, Masato Kakihana, Hideki Kato, Akihiko Kudo, J. Catalysis 232 (2005) 102.
35. Hideki Kato, Akihiko Kudo, Catalysis Today 78 (2003) 561.
36. Akihiko Kudo, International J. Hydrogen Energy 31 (2006) 197.
37. Akira Fujishima, Xintong Zhang, Donald. A. Tryk, Int. J. Hydrogen Energy 32 (2007) 2664.
38. Gaoke Zhang, Wei Jiang, Shujie Yu, Mater. Res. Bull. 45 (2010) 1741.
39. J.W. Liu, G. Chen, Z.H. Li, Z.G. Zhang, Int. J Hydrogen Energy 32 (2007) 2269.
40. Vehkamaki M, Ritala M, Leskela M, Jones A, Davies H, Sajavaara T, Rauhala E. J Electrochem Soc151 (2004) 69.
41. Jiang J, Awadelkarim OO, Lee D-O, Roman P, Ruzyllo J. Solid-State Electron 46 (2002) 1991.
42. D.O. Lee, P. Roman, C. -T. Wu, W. Mahoney, M. Horn, P. Mumbauer, M. Brubaker, R. Grant, J. Ruzyllo, Microelectronic Engineering 59 (2001) 405.
43. Condorelli GG, Baeri A, Fragala IL, Lauretta V, Smerlo G. Mater Sci Semicond Proc 5 (2002) 135.
44. M. Silinskas, M. Lisker, B. Kalkofen, E.P. Burte, Materials Science in Semiconductor Processing, 9 (2006) 1102.
45. D. -O. Lee, P. Roman, C. -T. Wu, P. Mumbauer, M. Brubaker, R. Grant, J. Solid-State Electronics 46 (2002) 1671.
46. Seher Kinikoğlu, and Müzeyyen Mar oğlub, J. Eur. Ceram. Soc, 14(1994) 45.
47. L. Lu and A.K. Dahle, Materials Science and Engineering: A, 435 (2006) 288.
48. Elizabeth Cruwysa, Ken Robinsona and Norman R. Davis, Polar Record 30 (1994) 49.

49. Chi-Shen Lee, Katja M. Kleinke and Holger Kleinke, Solid State Sciences, 7 (2005) 1049.
50. T. A. Vijayan, R. Chandramohan, S. Valanarasu, J. Thirumalai and S. P. J Mater Sci 43 (2008) 1776.
51. F. H. Samuel, A. M. Samuel, P. Ouellet and H. W. Doty, Metallurgical and Materials Transactions A, 32 (2001) 2061.
52. Pusit Pookmanee, Sukon Phanichphan, J. Ceramic Processing Research. 11 (2010) 384.
53. F. Pireta, M. Singh, C.G. Takoudis, B.L. Sua, Chem. Phy. Lett. 453(2008) 87.
54. Qinghui Li, Yuki Ono, Yoshikazu Homma, Izumi Nakai, Katsutoshi Fukuda, Takayoshi Sasaki, Keiichi Tanaka, and Satoshi Nakayama, J. Electron Microscopy 58(1) (2009) 1.
55. D. Hrunskia, B. Schroederb, M. Scheibc, R.M. Merzd, W. Bockd and C. Wagnerd, Thin Solid Films 516 (2008) 818.
56. E. Opila, S. Levine and J. Lorincz, J. Materials science 39 (2004) 5969.
57. Elizabeth J. Opila, Jim Smith, Stanley R. Levine, Jonathan Lorincz and Marissa Reigel, The Open Aerospace Engineering Journal, 3 (2010) 41.

Chapter 6

Summary and Discussion

This chapter summarise the results of selected ternary oxides synthesised in the present work namely (1) $LiNbO_3$, (2) $LiTaO_3$, (3) $NaNbO_3$, (4) $NaTaO_3$, (5) $SrNb_2O_6$, and (6) $SrTa_2O_6$. X-ray diffraction pattern of compounds synthesised by novel hydroxide precursor method confirms the final product can be synthesised at lower temperature as compared to conventional solid state ceramic method using carbonates or oxides as precursors. A brief evaluation of thermal behaviour of ternary oxides studied in the present work using TGA and DSC are discussed in this chapter. The estimated activation energy for the phase formation of compounds using differential scanning calorimetry is summarised in this chapter.

Summary and Discussion

Traditionally alkali metal niobates powders are usually synthesized via a solid state reaction route using sodium and/or lithium carbonates and niobium pentoxide [1–4]. One of the characteristics of this classical method is that it is rather difficult to achieve an homogeneous mixture of the components. Moreover, high sintering temperatures are required because of the low surface area of raw powders. Indeed, this method does not always allow for the production of dense, homogeneous single phase ceramics. High sintering temperatures can also enhance the volatilization of the alkali metal, which leads to stoichiometric variations in the sintered material. Increased sinterability of mixed powders and higher densification rate of green compacts were attained through pressure sintering and/or by adding selected sintering additives [5–8]. Fired densities ranging from 94 to 98% of the theoretical ones were thus reached. The firing temperature was decreased by one hundred degrees using pressure sintering. However, a calcination step at a temperature of around 900^0C and a subsequent annealing in an oxygen flow were sometimes required [9,10].

A method to prepare transparent ferroelectric glass-ceramics based on metal alkali niobates by a direct crystallization of a batch of oxides was recently proposed [11]. The reported results suggest that as-prepared materials are suitable for electrooptical applications,but the temperatures required exceed 1350^0C. In recent years, a wide variety of chemical routes for powder synthesis have been developed and optimized for preparing niobate-based electroceramics. The most popular routes are coprecipitation and sol-gel processes [12]. Other alternative methods to prepare ceramic powders have been described in the literature, such as hydrothermal synthesis [13] and a polymeric precursor process derived from the Pechini method [13–16]. However the hydroxide precursor method used in the present work produces niobates and tantalates at lower temperature and this process can avoid complex steps such as refluxing of alkoxides and high temperature sintering, resulting in less time consumption compared to other techniques. These samples were characterised by various physico-chemical techniques. Since the electrical and optical properties of dielectric ceramics strongly depend on their microstructure [17, 18] which is mainly influenced by the powder synthesising method and sintering process [19]. The list of compounds synthesized in the present work and their phase formation temperature confirmed by X-ray powder diffraction and calculated lattice parameters by least squares method is given in Table 6.1. The matching JCPDS reference for all the characterized compounds also given in Table 6.1

Table 6.1. Compounds synthesized and their phase formation temperature

Sr No.	Compound synthesized	Phase formation temperature	Identified phase	Lattice parameters	JCPDS Reference
1	Lithium Niobate	400^0C	Hexagonal	a=5.15 Å c=13.86 Å	20-0631
2	Lithium Tantalate	450^0C	Hexagonal	a = 5.154 Å c=13.756 Å	29-0836
3	Sodium Niobate	200^0C	Orthorhombic	a = 5.511 Å b = 5.557 Å c= 15.540 Å	14- 0603
4	Sodium Tantalate	500^0C	Orthorhombic	a = 5.513 Å b = 7.75Å c = 5.494 Å	25-0863
5	Strontium Niobate	500^0C	Orthorhombic	a=11.03 Å b=7.707 Å c=5.607 Å	28-1243
6	Strontium Tanatlate	500^0C	Orthorhombic	a=11.01 Å b=7.6370 Å c=5.617 Å.	38-0828

The elemental analysis of the synthesized compounds was carried out using the Energy Dispersive X-Ray Analysis (EDAX) attachment to the Scanning Electron Microscopy (SEM) system. During measurements, EDAX detector is operated at liquid nitrogen temperatures. EDAX results are used to validate the presence of required elements in the synthesized compounds and eliminate the presence of impurity elements in the compounds synthesized by hydroxide precursor methods. EDAX spectrum peaks observed in the present work from corresponding compounds are listed in Table 6.2 However, the EDAX spectrum of the lithium niobate and lithium tantalate could not show the presence of lithium because of its light weight [20 – 22].

Table 6.2 EDAX spectrum peaks observed in the present work and respective

Sr No.	Element	Compounds	Peak Observed	Transition	Reference
1	Oxygen	$LiNbO_3$, $LiTaO_3$ $NaNbO_3$, $NaTaO_3$ $SrNb_2O_6$, $SrTa_2O_6$	0.525 keV	K-alpha	23 – 29
2	Sodium	$NaNbO_3$, $NaTaO_3$	1.041 keV	K-alpha	30 – 35
3	Tantalum	$LiTaO_3$, $NaTaO_3$, $SrTa_2O_6$	1.709 keV	M-alpha	36 – 40
4	Strontium	$SrNb_2O_6$, $SrTa_2O_6$	1.806 keV	L3M5	41 - 47
5	Niobium	$LiNbO_3$, $NaNbO_3$, $SrNb_2O_6$	2.166 keV	L-alpha (L3M5)	48 - 52

Using impedance spectroscopy, Nyquist plot as well as bode plots were constructed and bode plots shows the frequency dependence of impedance parameters for all the synthesized compounds in the present work. Semicircles in Nyquist plot at high frequency corresponds to grain relaxation and at low frequency relate grain boundary, secondary phase segregated at grain boundary and sometimes effect of electrode.

Thermogravimetric analysis of compounds synthesized in the present work at different heating rate shows a dip in mass loss during the phase formation of the compounds formed by hydroxide precursor method and then the mass is quite stable over wide range of temperature. Differential Scanning Calorimetric (DSC) analysis of all the thoroughly mixed precursors was carried out at 5 different heating rate (2.5, 5, 7.5, 10 and 15^0C/min). . Inert Nitrogen gas is used as a purge gas during DSC analysis of mixture. From the exothermic peak shift observed in the DSC profile of each compound the activation energy required for the phase formation is estimated using Kissinger method and tabulated in table 6.3.

Table 6.3 Estimated activation energy by Kissinger method for synthesized compounds

Sr No.	Compound synthesized	Estimated Activation Energy
1	Lithium Niobate ($LiNbO_3$)	275.63 kJ/mol
2	Lithium Tantalate ($LiTaO_3$)	177.16 kJ/mol
3	Sodium Niobate ($NaNbO_3$)	91.42 kJ/mol
4	Sodium Tantalate ($NaTaO_3$)	113.82 kJ/mol
5	Strontium Niobate ($SrNb_2O_6$)	270.28 kJ/mol
6	Strontium Tanatlate ($SrTa_2O_6$)	142.92 kJ/mol

From the observation of table 6.3, it is found that the sodium niobate ($NaNbO_3$) requires very low activation energy for the phase formation by hydroxide precursor technique, also the X-ray powder diffraction studies $NaNbO_3$ precursors calcined different temperature shows, hexagonal crystal structure is formed at lower temperature (200^0C). The novel hydroxide precursor method used in this present work is an excellent way to prepare stoichiometric, homogeneous and fine ceramic powders at lower temperatures.

Reference:

1. Wang, C. L., Zhang, P. L., Zhong, W. L. and Zhao, H. S., J. Appl. Phys., 69 (1991) 2522.
2. Kus, C., Ptak, W. S. and Smiga, W., Ferroelectrics, 124 (1991 249.
3. Dungan, R. H. and Golding, R. D., J. Am. Ceram. Soc., 47 (1964) 73.
4. Wang, C. L., Wang, Y. G., Zhang, P. L., Zhong, W. L. and Zhao, H. S., Solid State Comm., 85 (1993) 331.
5. Egerton, L. and Dillon, D. M., J. Am. Ceram. Soc., 42 (1959) 438.
6. Ahn, Z. S. and Schulze, W. A., J. Am. Ceram. Soc., 70 (1987) 18.
7. Kosec, M. and Kolar, D., Mat. Res. Bull., 10 (1975) 335.
8. Kus, C., Dambelkane, M. J. and Brante, I. V.,.Ferroelectrics, 81 (1988) 281.
9. Hardiman, B., Henson, R. M., Reeves, C. P. and Zeyfang, R. R., Ferroelectrics, 12 (1976) 157.
10. Henson, R. M., Zeyfang, R. R. and Kiehl, K. V., J. Am. Ceram. Soc., 60 (1977) 15.
11. Todorovic, M. and Radonjic, Lj., Electrical and optical properties of ferroelectric glass-ceramics based on $LiNbO_3$ and its solid solution crystals.. In Fourth Euro-Ceramics, vol. 5, ed. G. Gusmano and E. Traversa. Gruppo Editoriale Faenza Editrice SpA, Faenza, (1995) 253.
12. Johson Jr., D. W., Am. Ceram. Soc. Bull., 60 (1981) 221
13. Dawson, W. J., Hydrothermal synthesis of advanced ceramic powders. Am. Ceram. Soc. Bull., 67 (1988) 1673.
14. Nobre, M. A. L., Longo, E., Leite, E. R. and Varela, J. A., Mat. Letters,, 28 (1996) 215.

15. Zagheto, M. A., Paiva Santos, C. O., Varela, J. A., Longo, E. and Mascarenhas, Y. P., J. Am. Ceram. Soc., 75 (1992) 2088.
16. Miot, C., Proust, C. and Husson, E., J. Eur. Ceram., 15 (1995) 1163.
17. Kimura, T., Miyamoto, S. and Yamaguchi, T., J. Am. Ceram. Soc., 73 (1990) 127.
18. Ding, S. and Shen, J., J. Am. Ceram. Soc., 73 (1990) 1449.
19. S. Lanfredi, L. Dessemond, A.C. Martins Rodrigues, J. Eur. Ceram. Soc 20 (2000) 983.
20. A. Fini, G. Fazio, M.A. Holgado, M.J.F. Herva, Int. J. Pharm. 171 (1998) 45.
21. Y. Kojima, K. Suzuki, Y. Kawai, J. Power Sources 155 (2006) 325.
22. G. Bhaskar Kumar, S. Buddhudu, Ceramics International 35 (2009) 521.
23. V.K. Tomar and D.K. Gautam, Materials Science in Semiconductor Processing 10 (2007) 200.
24. V K Tomar, D S Patil and D K Gautam, Semicond. Sci. Technol. 22 (2007) 43.
25. Alessio Varesano, Lorenzo Dall'Acqua, Claudio Tonin, Polymer Degradation and Stability 89 (2005) 125.
26. Z Saghi, X Xu, Y Peng, B J Inkson and G Möbus, Microscopy and Microanalysis 13 (2007) 438.
27. Noriaki Wakabayashi, Masayuki Takeichi, Hiroyuki Uchida, and Masahiro Watanabe, J. Phys. Chem. B, 109 (2005) 5836.
28. Khan, Aurangzeb; Khan, Saima N.; Jadwisienczak, Wojciech. M.; Kordesch, Martin E., Science of Advanced Materials, 1 (2009) 236.
29. B. K. Sonawane, M. P. Bhole and D. S. Patil, Opt Quant Electron 41 (2009) 17.
30. Kayoko Nakamura, Hirotake Orii, Anal. Chem., 52 (1980) 532.
31. Izabela Michalak, Katarzyna Chojnacka and Krzysztof Marycz, Microchim Acta 172 (2011) 65.

32. Kuniaki Fukuda, Minoru Tanaka, Hisao Tanase, Yasuyoshi Muramatsu and Vinci Mizuhira, Experimental and Molecular Pathology 40 (1984) 21.
33. Ricky W. Chuang and Chin C. Lee , Low-Loss Deep Glass, J. Lightwave Technology, 20 (2002) 1590
34. Chin C. Lee, Ricky W. Chuang, Materials Science and Engineering: B, 111 (2004) 40.
35. Heather C. Allen, J. M. Laux, Rainer Vogt, Barbara J. Finlayson-Pitts, and John C. Hemminger, J. Phys. Chem., 100 (1996) 6371.
36. F. Pireta, M. Singh, C.G. Takoudis, B.L. Sua, Chemical Physics Letters 453 (2008) 87.
37. Qinghui Li, Yuki Ono, Yoshikazu Homma, Izumi Nakai, Katsutoshi Fukuda, Takayoshi Sasaki, Keiichi Tanaka, and Satoshi Nakayama, J. Electron Microscopy 58 (2009) 1.
38. D. Hrunskia, B. Schroederb, M. Scheibc, R.M. Merzd, W. Bockd and C. Wagnerd, Thin Solid Films 516 (2008) 818.
39. E. Opila, S. Levine and J. Lorincz, J. Materials Science 39 (2004) 5969.
40. Elizabeth J. Opila, Jim Smith, Stanley R. Levine, Jonathan Lorincz and Marissa Reigel, The Open Aerospace Engineering Journal, 3 (2010) 41.
41. Seher Kinikoğlu, and Müzeyyen Mar oğlub, J. Eur. Ceram. Soc, 14 (1994) 45.
42. L. Lu and A.K. Dahle, Materials Science and Engineering: A, 435 (2006) 288.
43. Elizabeth Cruwysa, Ken Robinsona and Norman R. Davis, Polar Record, 30 (1994) 49.
44. Chi-Shen Lee, Katja M. Kleinke and Holger Kleinke, Solid State Sciences, 7 (2005) 1049.

45. T. A. Vijayan, R. Chandramohan, S. Valanarasu, J. Thirumalai and S. P. Subramanian, J Mater Sci 43 (2008) 1776.
46. F. H. Samuel, A. M. Samuel, P. Ouellet and H. W. Doty, Metallurgical and Materials Transactions A, 32 (2001) 2061.
47. Pusit Pookmanee, Sukon Phanichphan, J. Ceramic Processing Research. 11 (2010) 384.
48. Daisy Bayot, Bernard Tinant, and Michel Deviller, Inorg. Chem., 44 (2005) 1554.
49. Petra Alén Mikko Ritala, Kai Arstila, Juhani Keinonen and Markku Leskelä, Thin Solid Films, 491 (2005) 235.
50. W. D. MacDonald, G. J. C. Carpenter and S. Saimoto, Materials Science and Engineering A, 190 (1995) 33.
51. Mikko Ritala, Timo Asikainen, Markku Leskelä, Janne Jokinen, Reijo Lappalainen, Mikko Utriainen, Lauri Niinistö, Eero Ristolainen, Applied Surface Science 120 (1997) 199.
52. Edward R. Doering, George J. Havrilla and Thomasin C. Miller, Disilicide J. Nondestructive evaluation, 23 (2004) 95.

List of Research Publications

1. "Low temperature synthesis of $SrNb_2O_6$ and $SrTa_2O_6$ using hydroxide precursor", **H. Muthurajan**, H.H. Kumar, N. Koteswara Rao, Sivaram Prasad, R.K.Jha, V. Ravi, Materials Letters 62 (2008) 892-894
2. "A Novel Technique to Prepare $LiTaO_3$ at Low Temperature", **H. Muthurajan**, HH Kumar, N.Natarajan, V Ravi, Ceramic International 34 (2008) 669–670
3. "Novel Hydroxide precursors to prepare $NaNbO_3$ and $KNbO_3$", **H. Muthurajan,** HH Kumar, V. Samuel, U.N. Gupta and V.Ravi, Ceramic International 34 (2008) 671–673
4. "Novel Hydroxide Precursors For Low Temperature Synthesis of Selected Ternary Oxides", **H. Muthurajan**, N. Koteswara Rao, U.N. Gupta, Sivaram Pradhan, R.K. Jha, H.H. Kumar, S.A. Mirji, V. Ravi, Materials Research Bulletin 43 (2008) 1842–1849.
5. "A co-precipitation technique to prepare $BiTaO_4$ powders", **H. Muthurajan**, U.N. Gupta, B. Rituraj, N. Koteswara rao, Sivaram Pradhan, R. Radha, V. Ravi, Materials Letters 62 (2008) 501–503.
6. "Novel Synthesis of $SrBi_2Nb_2O_9$ Powders From Hydroxide Precursors", **H. Muthurajan**, N. Koteswara Rao, U.N. Gupta, Sivaram Pradhan, R.K. Jha, V. Ravi, International Journal of Applied Ceramic Technology, 5 [1] (2008) 101-104.
7. "Synthesis of LSMO at low temperature by novel hydroxide precursor technique", U.N. Gupta, **H. Muthurajan**, H.H. Kumar, N. Koteswara Rao, S.P. Gokhale, V. Ravi, Materials Letters 62 (2008) 527 – 529.

8. "A Co-precipitation Technique of Preparing $LaNbO_4$ Powders", U. N. Gupta, Sivaram Pradhan, **H. Muthurajan**, H. H. Kumar, D. K. Kharat, V. Ravi, Journal of American Ceram. Soc., 90 [8] (2007) 2661–2663
9. "A Co-precipitation method for preparation of Bi_3TiNbO_9 Powders", U.N. Gupta, V. Samuel, **H.Muthurajan**, H. H Kumar, S.D. Patil and V. Ravi, Ceramic International 34 (2008) 675–677.
10. "A co-precipitation technique to prepare $BiNbO_4$ powders", R. Radha, U.N. Gupta, V. Samuel, **H. Muthurajan**, H.H. Kumar, V. Ravi, Ceramic International 34 (2008) 1565–1567.
11. "Low Temperature Synthesis and Characterization of $BiNbO_4$ Powders Materials Characterization", R. Radha, **H. Muthurajan**, N. Koteswara Rao, Sivaram Pradhan , U. N. Gupta, R. K. Jha, S. A. Mirji, and V. Ravi, Materials Characterization, 59 (2008) 1083 – 1087

Symposium

12. "Low Temperature Synthesis of $BiNbO_4$ for Microwave dielectric resonator application", **H. Muthurajan**, HH Kumar, DK Kharat, V Ravi, Proceedings of 10th National Symposium on Antennas and Propagation at Department of Electronics, Cochin University of Science & Technology, Kochi, 14-16 December 2006